An Investigation of Nanoparticle Toxicity Mechanisms against Environmentally Relevant Bacteria and the Potential for Sustainable Agriculture Applications

A DISSERTATION
SUBMITTED TO THE FACULTY OF THE
UNIVERSITY OF MINNESOTA
BY

Joseph Thomas Buchman

IN PARTIAL FULFILLMENT OF THE REQUIREMENTS
FOR THE DEGREE OF
DOCTOR OF PHILOSOPHY

Christy L. Haynes, Adviser

May 2019

Acknowledgements

Throughout my journey in grad school, I have been fortunate to be surrounded by support from all angles. First and foremost, I am so thankful to my advisor, Christy Haynes, whose guidance has molded me into the scientist I am. While grad school can be a very challenging endeavor, Christy would always encourage me and push me to meet the challenges; I always left my meetings with her feeling energized and ready to tackle the science! I am so honored to have gotten to work with her.

In the Haynes lab, I feel that I've made many lasting friendships, and am grateful to group members past and present for making every day at work an enjoyable one, even when experiments weren't being the most cooperative. Specifically, I am thankful to Solaire Finkenstaedt-Quinn, who is so supportive and can always make me laugh – she continues to do so despite the distance that now separates us. Sarah Gruba could always be counted on for both help and distractions, even though there was "always more work to get done." I value the time that I spent with Victoria Szlag, Nathan Klein, and Katie Hurley, and for the many fruitful discussions we had about varying topics like our current experiments or Doctor Who and River Song. As the go-to person for her expertise in nanotoxicity, I am thankful to Autumn Qiu, who was always willing to give advice, even when she was quite busy. I'm grateful to my first mentor in the Haynes lab, Hattie Ring, who taught me many important lab skills and was an inspiration for my presentation style. I have enjoyed the many discussions that I have with Natalie Hudson-Smith, Becky Rodriguez, Peter Clement, Hyunho Kang, Amani Lee, Tana O'Keefe, and Jiayi He that have helped propel our science forward as well as open my eyes to many other topics. Beyond the Haynes lab, I feel fortunate to have been integrated into a larger research family in the form of the Center for Sustainable Nanotechology. There are too many people in the CSN to name who have been instrumental along my path, but I am grateful for them all. I also feel lucky to have had the opportunity to intern at Abbott Laboratories during my graduate studies, where I am glad to have worked with Amanda DeGraw, Joelle Rolfs, Elise Wignall, and Ian Manion, who have taught me so much and have become close friends.

I am also very thankful for my undergraduate research advisor, Vivian Feng, with whom I had the unique experience of working with at the graduate level while she did her sabbatical in the Haynes lab and as a collaborator as part of the Center for Sustainable

Nanotechnology. Vivian has never ceased to provide help and support, as well as to be someone that I know I can always turn to, and for that I am eternally grateful.

While much of graduate school happens within the lab and with collaborators, my network extends beyond those I have directly worked with. To my other friends from the department of chemistry, Amanda Oehrlein, Sarah Harris, Alyssa Cassabaum, Emily Keller, Tom Webber, and Zach Degregorio, I'm grateful for the times that we distracted each other from the stress of grad school. To my Augsburg crew, namely, Zach and Brittany Stevens, Spencer Miller, Teresa Niebur, Austin Wagner, Erik and Shannon Grindal, Charlie Olson, Peter and Kendra Schmit, and Joan Kunz, I'm thankful (and, quite frankly, impressed) that we managed to continue having our monthly board game nights throughout all of my time in grad school. Our friendship will clearly stand the test of time. To my close friends, Kane Dietz, Jim Kranz, and Brandon Guy, I'm grateful for all of the fun times, the many laughs, and the deep conversations that we've had. You've all been a shoulder for me when I've needed it.

Finally, anyone who knows me knows of the incredibly supportive extended family I've grown up with, and I'm close with so many of them, that I cannot name them all here, but they all know how much I appreciate them. As the saying goes "it takes a village to raise a child," and all my grandparents, my Auntie Dawnie, and my Auntie Gale essentially helped raise me alongside my parents, and have always been there for me and cheered me on throughout my journey. I'm also thankful for my cousins, Laura and Bert Nijssen, who often gave me advice throughout grad school, and took my mind off the stress with our Fancy Feast Fridays. To my two brothers, Michael and Brad Buchman, we have always had each other's backs, and we know that, despite our near-constant teasing and nicknames, we will always be super close. Thank you for your moral support through all these years. I am so grateful for everything that my parents, Kay and Bob Buchman, have done for me, they've definitely gone above and beyond in offering their support and helping me to achieve my goals. There is no way I'd be where I am now without their tender care and encouragement. What follows are acknowledgements for the technical assistance and funding for each chapter.

Chapter One

This work was supported by the National Science Foundation under the Center for Sustainable Nanotechnology, CHE-1503408. The CSN is part of the Centers for Chemical Innovation Program. J.T.B. and N.V.H.-S. acknowledge support by a National Science

Foundation Graduate Research Fellowship (grant number 00039202). We gratefully acknowledge Dr. Amanda N. Oehrlein for helpful discussion.

Chapter Two

This work was supported by the National Science Foundation under the Center for Sustainable Nanotechnology, CHE-1503408. J.T.B. was supported by the University of Minnesota Biotechnology Training Grant Program through the National Institutes of Health under grant number 5 T32 GM 8347-24. K.M.L. was supported by a University of Minnesota UROP award. We are grateful to Tian (Autumn) Qiu for her work with the fluorescamine assay. The authors gratefully acknowledge Dr. Michael P. Schwartz, Dr. Joel A. Pedersen, and Dr. Franz M. Geiger for helpful discussion. The TEM work in this study was carried out in the Characterization Facility, University of Minnesota, which receives partial support from NSF through the MRSEC program. We thank Fang Zhou for microtome sectioning of the resin-embedded bacteria samples for TEM analysis. The authors are grateful for the University of Minnesota's University Flow Cytometry Resource for flow cytometric analysis.

The computing resources necessary for this research were provided in part by the National Science Foundation through XSEDE resources on Bridges under grant number TG-CTS090079. Additional computing resources were provided by the Maryland Advanced Research Computing Center (MARCC).

Chapter Three

This work was supported by the National Science Foundation under the Center for Sustainable Nanotechnology, CHE-1503408. The CSN is part of the Centers for Chemical Innovation Program. J.T.B. was supported by a National Science Foundation Graduate Research Fellowship (grant number 00039202). TEM imaging in this study was carried out in the Characterization Facility, University of Minnesota, which receives partial support from the National Science Foundation through the MRSEC program. The authors gratefully acknowledge Fang Zhou at the Characterization Facility for microtome preparation of resin-embedded samples for TEM. The authors thank Elizabeth Lundstrom for ICP-MS analysis of the ion dissolution samples in bacterial medium as part of the University of Minnesota Earth Sciences Department. The authors acknowledge the Trace Element Research Group at the UW-Madison, Wisconsin State Laboratory of Hygiene (WSLH) for their analytical services (magnetic-sector ICPMS) for the ion dissolution samples in daphnid medium. The authors are thankful to Tianlei Yan for his contributions to NMC synthesis. This research was supported in part through computational resources

provided by the University of Iowa, Iowa City, Iowa. This work used the Extreme Science and Engineering Discovery Environment (XSEDE), which is supported by National Science Foundation grant number ACI-1548562 through allocation ID TG-GEO160006.

Chapter Four

This work was supported by the National Science Foundation under the Center for Sustainable Nanotechnology, CHE-1503408. The CSN is part of the Centers for Chemical Innovation Program. J.T.B. acknowledges support by a National Science Foundation Graduate Research Fellowship (grant number 00039202). TEM imaging in this study was carried out in the Characterization Facility, University of Minnesota, which receives partial support from the National Science Foundation through the MRSEC program. The authors are grateful to Fang Zhou at the Characterization Facility for microtome preparation of resin-embedded samples for TEM. The authors gratefully acknowledge Elizabeth Lundstrom for ICP-MS analysis of the NP binding samples as well as the iron dissolution samples as part of the University of Minnesota Earth Sciences Department. The authors thank Dr. Erin Carlson for use of her iQ5 real-time PCR detection system.

Chapter Five

This work was supported by the National Science Foundation under the Center for Sustainable Nanotechnology, CHE-1503408. The CSN is part of the Centers for Chemical Innovation Program. J.T.B. and N.V.H.-S. acknowledge support by a National Science Foundation Graduate Research Fellowship (grant number 00039202).

Dedication

This thesis is dedicated to my parents, Kay and Bob, whose constant love, support, and encouragement have always inspired me to give everything my best effort.

Abstract

Due to the unique physicochemical properties of nanoparticles, largely due to their high surface area-to-volume ratio, they are being increasingly used in consumer products. At any time during the manufacture, use, and ultimately, disposal of these products, there is a reasonable likelihood of nanoparticle release into the environment. Once released, their impact on the environment are less well-understood. Therefore, there is a growing emphasis to understand the impacts of nanoparticles on the environment, by understanding how the nanoparticles interact with ubiquitous organisms that have important ecological roles. Beyond looking solely at whether nanoparticle introduction will kill these organisms, the molecular-level mechanisms of their toxicity have been studied. By understanding the mechanisms, the goal is to be able to predict the toxicity of nanoparticles prior to their mass production, and to inform a more sustainable design and use of nanomaterials.

Chapter One of this work reviews the understanding of molecular-level toxicity mechanisms to organisms in the environment, with an emphasis on beneficial bacteria. It also describes different strategies that have been employed to redesign nanoparticles that reduce the impact of these toxicity mechanisms. Chapter Two illustrates the importance of using more than one organism when doing studies of nanoparticle toxicity. Not all organisms respond equally, and there are some that are not impacted by a given nanoparticle type, so use of multiple species that cover a range of complexities improves the chances that a nanoparticle will not be incorrectly labeled as “nontoxic”. By using multiple organisms, those that are most impacted can also be identified for follow-on research to investigate the mechanism of toxicity.

Chapter Three assesses the toxicity mechanism of an important nanomaterial often used in energy storage applications that is made of the complex oxide, lithium nickel manganese cobalt oxide, across a range of industrially-relevant stoichiometries. While for equimolar stoichiometries of this material, the importance of nickel and cobalt release has been implicated as the main toxicity driver to *Shewanella oneidensis* MR-1, this work demonstrates that even at increased nickel concentrations in the material, the toxicity remained the same due to increased material stability leading to a similar dissolution profile. For another important environmental organism, *Daphnia magna*, the toxicity did increase with increasing nickel content, indicating that a material redesign will not necessarily have the same impact on different organisms. Chapter Four investigates the impact of iron oxide nanoparticles to *S. oneidensis*, which showed that these nanoparticles

improved bacterial survival, mostly due to the release of beneficial iron ions. Since changing bacterial populations can perturb an environment, a mesoporous silica coating was applied to the iron oxide nanoparticles to reduce their dissolution and their impact on the bacteria.

While more understanding of the mechanisms by which nanoparticles can exhibit toxicity is being gained, there are many nanoparticles for which there is a low toxicity to organisms. In Chapter Five, we apply silica nanoparticles, which have been found to be largely nontoxic, to our plant model, *Citrullus lanatus*. Through dissolution, silica nanoparticles are capable of serving as a source of silicic acid, an important micronutrient, for plants. These nanoparticles benefit healthy plants by increasing their biomass and improving the overall fruit yield. This work demonstrates a way to apply nanoparticle toxicity knowledge to proactively utilize nanoparticles to improve sustainability in agriculture.

Table of Contents

List of Tables

Chapter 2

Chapter 3

Chapter 4

List of Figures

Chapter 1

Chapter 2

Chapter 3

Chapter 4

Chapter 5

List of Abbreviations

ANOVA	Analysis of variance
APF	4’-Aminophenyl fluorescein
AUDPC	Area under the disease progress curve
BET	Brunauer-Emmett-Teller
BSA	Bovine serum albumin
CA-QD	Cysteamine-coated QDs
cDNA	Complementary deoxyribonucleic acid
CTAB	n-Cetyltrimethylammonium bromide
DFT	Density functional theory
DLS	Dynamic light scattering
DMSO	Dimethylsulfoxide
DPBS	Dulbecco’s phosphate-buffered saline
DPPH•	2,2-Diphenyl-1-picrylhydrazyl
E_F	Fermi level
EDS	Energy-dispersive X-ray spectroscopy
H_2DCF-DA	2’,7’-Dichlorofluorescin diacetate
HEPES	4-(2-Hydroxyethyl)-1-piperazineethanesulfonic acid
HPLC	High-performance liquid chromatography
HRP	Horseradish peroxidase
ICP-MS	Inductively coupled plasma mass spectrometry
ICP-OES	Inductively coupled plasma optical emission spectroscopy
IONP	Iron oxide nanoparticle
LB	Luria-Bertani
LPS	Lipopolysaccharide
MARCC	Maryland Advanced Research Computing Center
MBC	Minimum bactericidal concentration
MHRW	Moderately hard reconstituted water
MPA	3-Mercaptopropionic acid
$MPNH_2$	3-Mercaptopropylamine
msIONP	Mesoporous silica-coated iron oxide nanoparticle
MSN	Mesoporous silica nanoparticle
NMC	Nickel manganese cobalt oxide
NP	Nanoparticle

OD	Optical density
O-*TM*-O	Transition metal oxide
PAH	Polyallylamine hydrochloride
PDDA	Poly(diallyldimethylammonium chloride)
PDOS	Projected density of states
PEG	Polyethylene glycol
PEG-silane	2-[Methoxy(polyethyleneoxy)$_{9\text{-}12}$propyl]-trimethoxysilane
PMMA	Poly(methyl methacrylate)
PVP-10	Polyvinylpyrrolidone average molecular weight 10,000 g/mol
QD	Quantum dot
qPCR	Quantitative polymerase chain reaction
RNA	Ribonucleic acid
ROS	Reactive oxygen species
RPM	Revolutions per minute
SAM	Spectral angle mapper
SEM	Scanning electron microscopy
SHE	Standard hydrogen electrode
SLB	Supported lipid bilayer
TEM	Transmission electron microscopy
TEOS	Tetraethylorthosilicate
TGA	Thermogravimetric analysis
XRD	X-ray diffraction
XSEDE	Extreme Science and Engineering Discovery Environment
ZPE	Zero-point energy

Chapter 1

Understanding Nanoparticle Toxicity Mechanisms to Inform Redesign Strategies to Reduce Environmental Impact

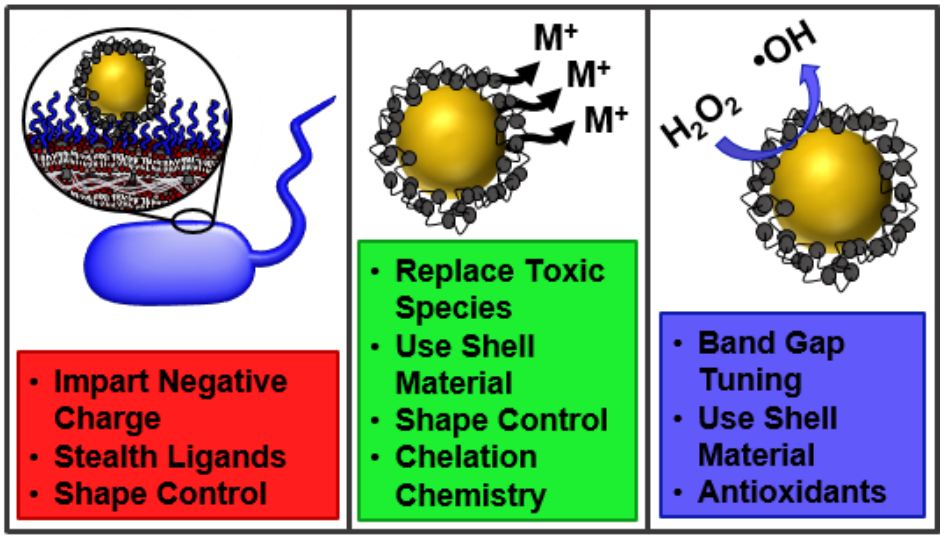

Reproduced in part from: Buchman, J.T.; Hudson-Smith, N.V.; Landy, K.M.; Haynes, C.L. Understanding nanoparticle toxicity mechanisms to inform redesign strategies to reduce environmental impact. *Acc. Chem. Res.*, *In Press*. Copyright 2019, with permission from the American Chemical Society.

1.1 Overview

There has been a surge of consumer products that incorporate nanoparticles, which are used because they can improve or impart new functionalities to the products based on their unique physicochemical properties. With such an increase in products containing nanomaterials, there is a need to understand their potential impacts on the environment. This is often done using various biological models that are abundant in the different environmental compartments where the nanomaterials may end up after use.

Beyond studying whether nanomaterials simply kill an organism, the molecular mechanisms by which nanoparticles exhibit toxicity has been extensively studied. Some of the main mechanisms include: 1) direct nanoparticle association with the cell surface of an organism, where the membrane can be damaged or initiate internal signalling pathways that damage the cell, 2) dissolution of the material, releasing toxic ions that impact the organism, generally through impairing important enzyme functions or through direct interaction with a cell's DNA, and 3) the generation of reactive oxygen species and subsequent oxidative stress on an organism, which can also damage important enzymes or an organism's genetic material. This chapter reviews these toxicity mechanisms, presenting examples for each with different types of nanomaterials.

Understanding the mechanism of nanoparticle toxicity will inform efforts to redesign nanoparticles with reduced environmental impact. The redesign strategies will need to be chosen based on the major mode of toxicity, but also considering what changes can be made to the nanomaterial that do not impact its ability to perform in its intended application. To reduce interactions with the cell surface, nanomaterials can be designed to have a negative surface charge, use ligands such as PEG that reduce protein binding, or have a morphology that discourages binding with a cell surface. To reduce the nanoparticle dissolution to toxic ions, the toxic species can be replaced with less toxic elements that have similar properties, the nanoparticle can be capped with a shell material, the morphology of the nanoparticle can be chosen to minimize surface area and thus minimize dissolution, or a chelating agent can be co-introduced or functionalized onto the surface of a nanomaterial. To reduce the production of reactive oxygen species, the band gap of the material can be tuned either by using different elements or by doping, a shell material can be utilized to inhibit direct contact with the core, or antioxidant molecules can be tethered to the nanoparticle surface. When redesigning nanoparticles, it will be important to test that the redesign strategy actually reduces its toxicity to organisms from relevant environmental compartments. It is also necessary to confirm that the nanomaterial still

demonstrates the critical physicochemical properties that inspired its inclusion in a product or device.

1.2 Introduction

Since being recognized as a particularly interesting size regime for materials, engineered nanoparticles (NPs) have seen an increase in their intentional design, manufacture, and incorporation into consumer products due to their novel physicochemical properties. It is currently estimated that nanoparticles are used in over 1800 commercial products, in applications ranging from cosmetics to energy storage.[1] At any stage in the lifetime of these nano-enhanced products, the nanoparticles they contain could be released into the environment. As with any traditional molecular species that may be discharged into the environment, efforts need to be taken to understand what impact nanomaterials will have on the environment.

In the few decades that environmental nanotoxicity has been studied, significant progress has been made in understanding ways nanoparticles may affect the environment. Initially, studies that were completed focused on the effects of simple nanomaterials on the viability of model organisms. More recently, there's been a push to understand the mechanisms of toxicity of nanoparticles to environmentally relevant organisms.[2] The mechanisms of nanotoxicity have been extensively reviewed,[3,4] and some known mechanisms include: distressing the cell or organism by binding to its exterior, releasing toxic ions, and inducing oxidative stress. These mechanisms will be discussed in detail in this chapter.

Scientists working in this field have reached a stage where knowledge of nanotoxicity mechanisms can be applied to drive the intentional redesign of nanomaterials to reduce their environmental impact. Strategies have been developed that can discourage the binding of nanoparticles to the cell surface, reduce the burden of dissolved toxic metal ions, or to tune the band gap of nanoparticles to mitigate oxidative stress. In this chapter, we review efforts in our group to redesign nanomaterials to reduce their overall toxicity, focusing mostly on metal/metal oxide nanoparticles. We place some emphasis on bacterial toxicity because bacteria are ubiquitous in the environment and have many important environmental roles, making them a good diagnostic of overall environmental health.[5,6] For a more holistic environmental perspective, examples of toxicity to other environmentally relevant organisms are also presented. The redesign strategies to mitigate nanoparticle toxicity that are discussed in this chapter are summarized in Figure 1.1.

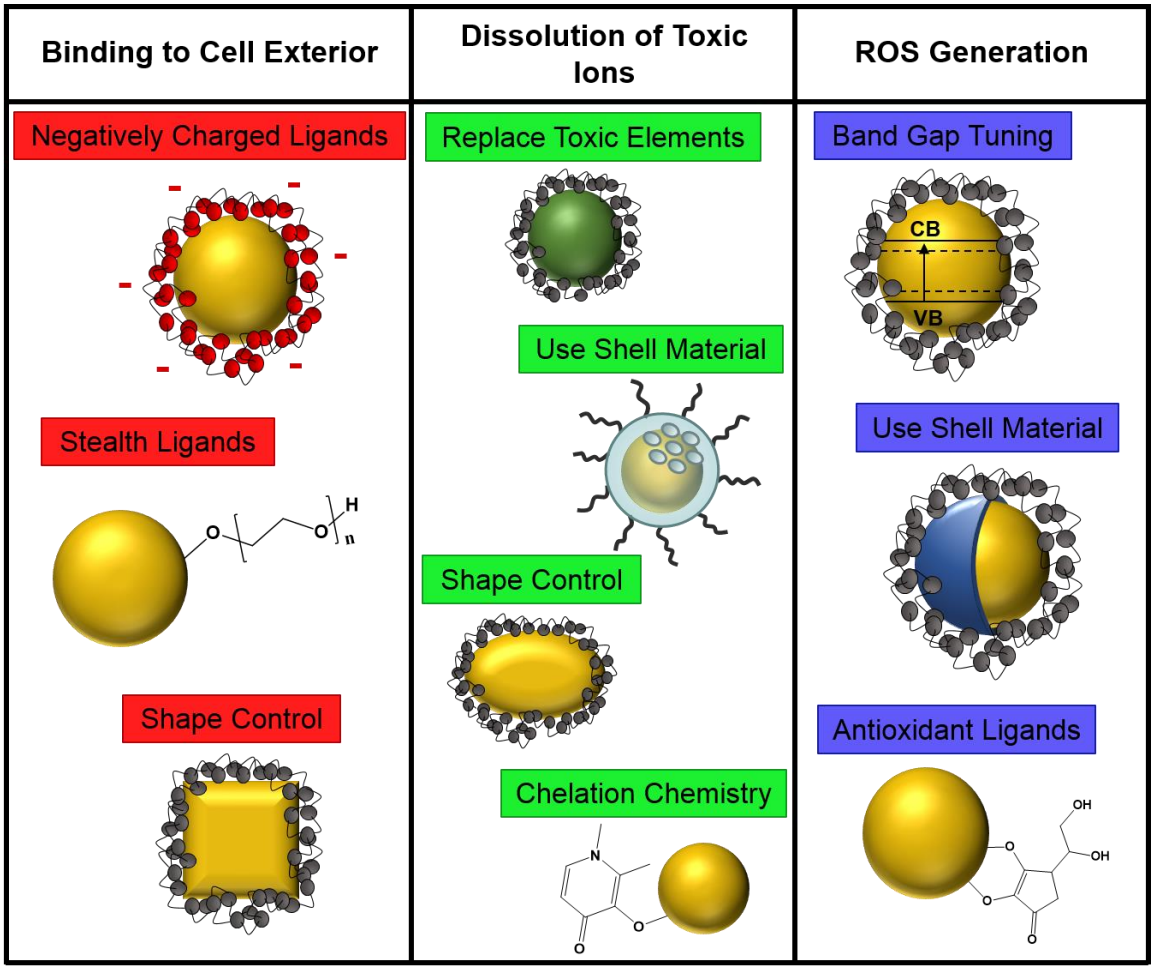

Figure 1.1. The various redesign strategies presented in this chapter organized by the major toxicity mechanism that the redesign is impacting.

1.3 Mechanisms of Nanoparticle Toxicity

In considering redesign of NPs to reduce their impact, it is important to first understand the main, though certainly not the only, mechanism(s) by which they are toxic. Here, we present some of the major mechanisms by which nanoparticles exhibit toxicity, namely, through direct association with the cell membrane, by dissolving to release ions that have toxic impacts on organisms, and oxidative stress. After presenting the toxicity mechanisms, we give strategies for how these mechanisms may be mitigated, thus reducing toxicity and promoting sustainable use of engineered nanomaterials.

1.3.1 Binding of Nanoparticles to Cell Exterior

One of the ways that nanoparticles elicit toxicity is through direct interaction with the cell surface. For multicellular organisms, this interaction can lead to the nanoparticles being taken up by a subset of cells, the consequences of which have been reviewed elsewhere.[7,8] For bacterial cells, the nanoparticles mostly stay on the cell surface, where

they can cause physical disruption by removing/destroying the lipid membrane,[9,10] induce internal signaling pathways that damage the cell,[11] dissolve to release cell-permeable toxic ions right at the bacterial surface,[12] as well as other toxic pathways.[13,14]

When in proximity with cells or organisms, nanoparticles can interact based on electrostatic attraction. Given that bacteria exhibit an overall negative surface charge,[15] it is generally expected that positively charged nanoparticles will associate with bacteria to a greater extent than negatively charged nanoparticles. In work by Feng et al., gold nanoparticles with ligands that gave them positive (via functionalization with mercaptopropylamine or polyallylamine hydrochloride, PAH) or negative (via functionalization with mercaptopropionic acid) charges were exposed to either a Gram-positive or Gram-negative bacterium (Figure 1.2).[16] They used biological transmission electron microscopy (TEM) to demonstrate that the gold nanoparticles were bound to the bacterial surfaces; in fact, in some images it is clear that intact lipid bilayers from the bacterial cell wall had been extracted by and were adhered to the gold nanoparticles. To quantify the amount of bacteria with bound gold *in situ*, they used flow cytometry, which revealed that there was minimal binding with the negatively charged gold nanoparticles to either bacteria, and that both bacteria exhibit significant association with the positively charged gold nanoparticles. The observed toxicity of each gold nanoparticle indicated that more nanoparticle binding led to increased nanoparticle toxicity for both the Gram-positive and Gram-negative bacterial species.

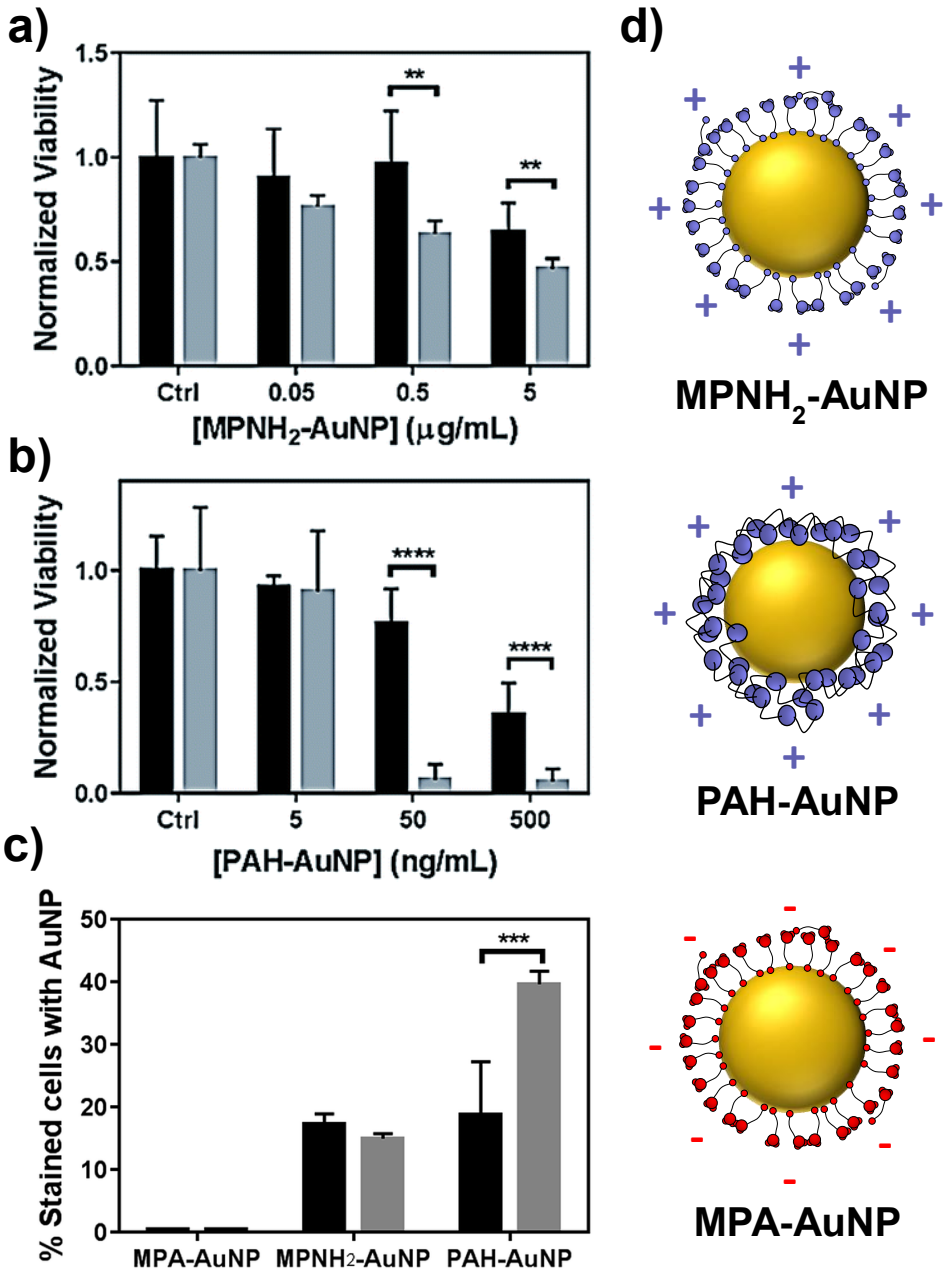

Figure 1.2. Gold nanoparticle toxicity to two bacterial models. The toxicity of a) mercaptopropylamine-functionalized gold nanoparticles ($MPNH_2$-AuNPs) and b) polyallylamine hydrochloride-functionalized gold nanoparticles (PAH-AuNPs) was determined for *S. oneidensis* MR-1 (black bars) and *B. subtilis* SB491 (gray bars). c) The amount of bacteria that had AuNPs bound to them (*S. oneidensis*: black bars, *B. subtilis*: gray bars) correlates with the observed toxicities (mercaptopropionic acid-functionalized gold nanoparticles is abbreviated MPA-AuNP). d) Cartoon representations of the nanoparticles used for this study. Figure adapted with permission from ref 16. Copyright 2015 Royal Society of Chemistry. **p<0.01, ***p<0.001, ****p<0.0001

Investigating how nanoparticles bind to bacteria, Jacobson et al. showed that the interaction with Gram-negative bacteria is dominated by binding to the lipopolysaccharides (LPS), a negatively charged moiety present on the surface.[17] In this work, the importance of LPS for nanoparticle binding was shown in both supported lipid bilayers (SLBs) with varying amounts of incorporated LPS as well as the bacterium, *Shewanella oneidensis* MR-1. Binding of positively charged and negatively charged AuNPs to SLBs was monitored with a quartz crystal microbalance in dissipation mode, which revealed that SLBs with LPS exhibited higher binding with cationic NPs than those without LPS, and that in an ionic strength of 25 mM, an increasing trend in binding amount was seen with amount of incorporated LPS into the bilayer. To assess association with *S. oneidensis*, flow cytometry, dark-field microscopy, and hyperspectral imaging were employed on bacteria with native LPS levels and depleted LPS levels. This showed that more bacteria were bound with cationic AuNPs when they had native LPS levels than the bacteria with reduced LPS; in fact, a 50% depletion in wild type LPS led to a ~70% decrease in bacteria-associated nanoparticles. Anionic gold nanoparticles were not found to appreciably bind to the SLBs or bacteria.

An analogous moiety for Gram-positive bacteria is under investigation with the hypothesis that teichoic acids may be the critical mediator for nanoparticle-bacteria interactions. Even though it is still unclear what molecule on the Gram-positive bacterial surface is the important site for NP binding, it is clear that NPs bind to their surface.[16,18]

Once bound to the bacterial surface, nanoparticles can disrupt and damage the cell membrane, potentially causing the organism to die. Studies completed with poly(diallyldimethylammonium chloride)-coated CdSe quantum dots (QDs) used atomic force microscopy and quartz crystal microbalance in dissipation mode to show that these QDs attach and embed themselves into a supported lipid bilayer.[19] Once attached, they disrupt the membrane by collapsing the liquid ordered domains of the bilayer; liquid ordered domains are important for signal transduction and membrane trafficking for both prokaryotic and eukaryotic cells.

In work by Lai et al., the association of QDs to *Escherichia coli* and model membranes was correlated with their toxicity and membrane damage.[20] Cysteamine-coated (positively charged) and mercaptopropionic acid-coated (negatively charged) QDs were used, with effects only being seen with the positively charged quantum dots. There was notable inhibition of *E. coli* upon exposure to cysteamine-coated QDs (CA-QDs) as well as increased attachment when investigated with TEM. Monitoring the lysis activity by sodium

dodecyl sulfate treatment revealed that there was increased membrane permeability for *E. coli* after exposure to CA-QDs. These whole organism studies were supported by model membrane studies, which showed an increase in membrane fluidity and increased liposome leakage after exposure to CA-QDs.

Similarly, in work by Williams et al., the toxicity of traditional cadmium-based quantum dots (CdSe and CdSe/ZnS core/shell structures) were evaluated in comparison with zinc-based quantum dots (ZnSe and ZnSe/ZnS).[21] All the quantum dots have the same uncharged polyethylene glycol ligands and therefore only differ in their core composition. Liposomes containing fluorescent dyes were used as a model membrane, with membrane damage being evident if the fluorescent dye leaked out of the liposome, and *S. oneidensis* MR-1 was used as a bacterial model to investigate the impacts of these quantum dots. The liposomes showed greater membrane disruption in the cadmium-containing QDs versus zinc-containing quantum dots; this was attributed to association of QDs to the liposomes since negligible cadmium and selenium dissolution was observed over the course of the experiment, and work with a 1,2-dioleoyl-*sn*-glycero-3-phosphoethanolamine-N-(7-nitro-2-1,3-benzoxadiazol-4-yl) dye indicated that ROS was not a major contributor to the liposome disruption. Association of the QDs led to a high local release of ions, especially zinc ions. The greatest zinc ion release was observed for CdSe/ZnS QDs, which also demonstrated the greatest liposome disruption. The crystal plane mismatch between the CdSe core and ZnS shell are likely why such high zinc ion release was observed, whereas minimal zinc ion release occurs for the cadmium-free QDs used in this study. The QD association seen with *S. oneidensis* corroborated the liposome results. In toxicity studies, both of the cadmium-free quantum dots exhibited negligible impact whereas the cadmium-containing quantum dots exhibited toxicity even at doses as low as 0.01 mg/L Se equivalents.

1.3.2 Dissolution to Toxic Ions

Whether through leaching ions directly at an organism's surface after NP binding or by releasing ions into the surrounding environment that then interact with an organism, the dissolution of toxic elements from nanoparticles is an important mechanism of nanotoxicity. There are several ways by which ion release can be toxic, which partially depend on the identity of the ion. Several ions are capable of binding to proteins and enzymes, thus critically compromising their role for the organism.[22,23] In this way, the presence of metal ions can inhibit important cellular functions. Metal ions can also directly

interact with an organism's phospholipid membrane or genetic material, with deleterious consequences.[24–26] Finally, metal ions can elicit oxidative stress in organisms.[27]

For silver nanoparticles, dissolution has been identified as a major cause of toxicity to organisms.[28–31] Work by Xiu et al. takes advantage of the fact that AgNPs do not dissolve to release Ag^+ ions under anaerobic conditions.[32] Exposing AgNPs to *E. coli* in both aerobic and anaerobic conditions, they found significant toxicity when oxygen was in the test atmosphere and no toxicity under anaerobic conditions. To test this further, they exposed AgNPs to aerobic conditions, measured the released Ag^+ ion concentration, and then moved the nanoparticles to anaerobic conditions to prevent further dissolution and compared the toxicity observed with toxicity from Ag^+ dosed via $AgNO_3$. They found indistinguishable toxicity between the AgNP doses and equivalent Ag^+ doses performed in this way, indicating the importance of Ag^+ release. Along these lines, XANES/EXAFS analysis has been used to show that the silver present inside of *Bacillus subtilis* after AgNP exposure was in the form Ag_2O, suggesting that Ag^+ ions penetrated the cell wall and were oxidized by internal cell machinery.[33]

For complex oxides such as lithium nickel manganese cobalt oxide (NMC), dissolution of the material was also revealed to be a major mode of its toxicity to the bacterium, *S. oneidensis* MR-1.[34] In this work, Hang et al. utilized optical density measurements to monitor bacterial growth and respirometry to monitor bacterial respiration, which gives insights into overall bacterial health and growth. These studies demonstrated that NMC dissolved to release ions of lithium, nickel, manganese, and cobalt, but that the toxicity observed from the NMC nanomaterial was recapitulated when the bacteria were dosed with the released ion concentrations from nickel and cobalt. To further demonstrate the importance of dissolution to NMC toxicity, equistoichiometric NMC was made to have three different morphologies, and toxicity was tested toward *S. oneidensis*.[35] These different morphologies were chosen so that they would present different crystal faces, as it was expected that the energetics of dissolution might vary with the different crystal faces that presented varied levels of transition metal coordination. The toxicity of the different morphologies was observed, showing that nanosheets were most toxic, followed by nanoblocks, and then a commercial, microscale NMC. Given that dissolution is related to the exposed surface area of a material, the NMC was also dosed by surface area rather than mass. In dosing with surface area, all morphologies exhibited the same toxicity, indicating that if there were differences in dissolution based on the presented crystal face, it was not significant enough to change the observed toxicity with *S. oneidensis*.

Mahendra et al. investigated the effects of weathering of CdSe-based QDs on three different bacteria.[36] They monitored bacterial growth by taking optical density measurements, and they noted that weathered CdSe-based QDs were toxic to three bacteria, while unweathered QDs were minimally toxic. They attribute the toxicity observed to the release of Cd^{2+} and SeO_3^{2-} ions by introducing the bacteria to Cd^{2+} or to Cd^{2+} and SeO_3^{2-} simultaneously. Only when both ions were dosed simultaneously did the observed toxicity match the QD toxicity. They also observed that addition of chelating agents such as oxalate or EDTA reduced the dissolution of both Cd^{2+} and SeO_3^{2-} ions. Consequently, bacteria that were exposed to these co-introduced QDs with chelating agents experienced decreased toxicity from the QDs. Similarly, work by Gallagher et al., demonstrated the toxicity of the weathered components of QDs embedded in poly(methyl methacrylate) (PMMA) to *S. oneidensis*.[37] Tracking the toxicity after various weathering times of the QD-PMMA nanocomposites (210.5, 336, and 504 hr) indicated that as weathering time increased, more toxicity was observed. This is likely because the polymer was degrading to small polymer fragments that contained QDs, and over time, these polymer fragments were being further degraded to smaller sizes. Since these smaller sizes are more likely to associate with the bacterial surface, they would likely release high local concentrations of toxic Cd^{2+} ions.

1.3.3 Oxidative Stress

The production of reactive oxygen species (ROS) and the accompanying oxidative stress as a mechanism for nanotoxicity has been extensively reviewed.[14,38,39] Lipid peroxidation is a commonly seen result of ROS generation.[40] ROS is also capable of targeting different enzymes that are important for cell functions, such as mononuclear iron proteins.[41–43] Furthermore, ROS can oxidize the bases and ribose of DNA, causing mutations and damage to the organism.[44,45] This is evident in work demonstrating that mutants lacking enzyme machinery to scavenge ROS from cells acquired more mutations when in an aerobic environment.[46]

Work is being done to correlate the electronic structures of various nanomaterials with their ROS production and with their toxicity. Li et al. used seven metal oxide nanoparticles with band edges near the redox potential of reactive redox couples, and demonstrated that the amount of abiotic ROS produced by the material correlated with its toxicity to *E. coli*. In another study, the toxicity for 24 metal oxide nanoparticles to *E. coli* was evaluated, finding seven of them to be toxic.[47] When assessing ROS generation in *E. coli* after nanoparticle exposure, it was observed that only the seven toxic nanoparticles

caused increased intracellular ROS and that five of the seven toxic particles also directly produced ROS even in the absence of bacteria. Using nano-structure activity relationship analysis, the toxicity of metal oxide nanoparticles was found to be related to the conduction band energy of the material as well as its ability to dissolve, as represented by its hydration enthalpy; if the conduction band energy overlapped with that of biomolecules and the material was more prone to dissolution, then the material was observed to be more toxic (Figure 1.3). These results allow for predictability of the toxicity of some nanomaterials, and can be useful for informing nanoparticle redesign to reduce the toxic impact.

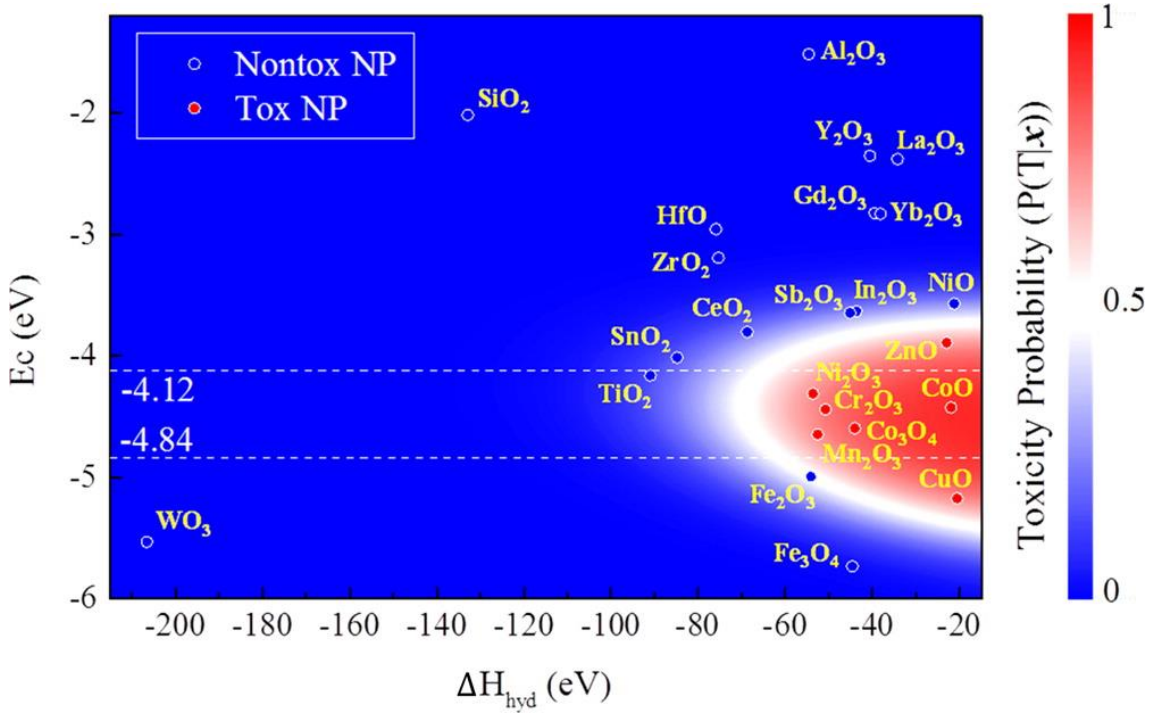

Figure 1.3. Nano-structure activity relationship predictions of nanoparticle toxicity. The probability that a given metal oxide nanoparticle is toxic from nano-structure activity relationship calculations is shown to be related to the hydration enthalpy and conduction band energy of the material. Figure used with permission from ref 47. Copyright 2015 American Chemical Society.

In work by Wang et al., the generation of ROS by different metal oxide species after photoillumination was investigated.[48] All nanoparticles tested generated superoxide radical, whereas hydroxyl radical and hydrogen peroxide were only detected from TiO_2 and ZnO NPs. The toxicity of the materials to *Photobacterium phosphoreum* matched the trend seen in superoxide production, with the materials generating more superoxide exhibiting the highest toxicity. To further implicate the importance of superoxide in the toxicity, superoxide dismutase was added to scavenge superoxide, resulting in reduced

toxicity. However, when isopropanol was added to scavenge hydroxyl radical or hydrogen peroxide was directly added, no change in toxicity was observed.

Beyond the production of ROS by nanomaterials themselves, the presence of nanomaterials can activate signaling pathways within organisms that causes oxidative stress. In work done by Domínguez et al.,[49] oxidative stress in the guts of *Daphnia magna* was evaluated after exposure to positively or negatively charged nanodiamond of two sizes (5 and 15 nm). This revealed that 15-nm-diameter nanodiamonds induced ROS generation in *D. magna* guts in a dose-dependent manner, while 5-nm-diameter nanodiamond showed much lower ROS production. In the latter exposure, the gut cells displayed increased expression of oxidative stress genes, like heat shock protein, demonstrating that the cells were working to combat ROS.

1.4 Redesign Strategies to Mitigate Environmental Impact

The knowledge of important toxicity mechanisms for a given NP can inform how that nanoparticle can be redesigned to reduce toxicity. To complicate matters, many NPs exhibit toxicity that can be attributed to more than one of these mechanisms;[50] in this case, mitigating one such mechanism will still lead to an overall reduction of NP toxicity. On the other hand, many of these toxicity mechanisms can themselves be linked to each other, such as ROS production that results from NP dissolution to ions.[51] Therefore, reducing one of the mechanisms of toxicity in a material may also reduce others. Another complication is that the toxicity of a material can be specific to given organisms, and therefore to evaluate the effectiveness of a redesign strategy, it would be beneficial to assess the toxicity to a range of organisms relevant to the environments where a nanomaterial is most likely to end up.

1.4.1 Binding of Nanoparticles to Cell Exterior

Since association of NPs to the exterior of an organism can lead to toxicity through several pathways, one way that NPs can be redesigned to reduce their impact is to reduce the binding affinity of a given NP for biological surfaces. One simple method to do so can be seen in Section 1.3.1, in which work that used NPs with different surface charges was introduced. Given that cells are commonly negatively charged, it is generally seen that negatively charged NPs have little to no association with organisms and therefore have reduced toxicity compared to positively charged analogues. Positively charged NPs show more association to organisms and generally have increased toxicity.[20,52,53] Therefore, if the NP application allows it, using negatively charged ligands is one way to redesign nanoparticles to reduce their toxicity to environmental organisms. Similarly, while the

mechanisms that cause PEG to be biocompatible are not fully understood,[54] coating a nanoparticle with PEG can lead to reduction in its toxicity by reducing NP association to organisms, by reducing nonspecific protein interactions. A PEG coating also often stabilizes the particles, meaning that this coating would increase the environmental persistence and therefore the time it is bioavailable to aquatic organisms.[55]

Given that nanoparticle association can cause membrane damage in organisms, studies will often look at the association and subsequent membrane damage to understand toxicity. As a Cd-containing QD alternative, silicon-based QDs have also been demonstrated to have reduced association with *S. oneidensis* MR-1 and *B. subtilis* SB491.[56] To both bacteria, high toxicity was observed after CdSe QD exposure, and CdSe/ZnS QDs were only toxic to *B. subtilis* at the highest concentration tested (200 mg/L). SiQDs exhibited no toxicity to either bacteria at the concentrations tested. While CdSe QDs showed bacterial membrane damage in TEM, there was no QD association or membrane damage present for bacteria that had been exposed to SiQDs; this was further corroborated by a LIVE/DEAD assay looking at membrane integrity, which also showed that there was no membrane damage for SiQDs. Though redesign of the CdSe QD was successful both by addition of a ZnS shell and by replacing the cadmium completely with silicon, the better redesign strategy was judged to be the latter, based on the earth abundance of silicon compared to cadmium and zinc. In a follow-up study investigating boron- and phosphorus-doped SiQDs,[57] it was shown that both dopants caused the otherwise nontoxic SiQDs to exhibit some toxicity to bacteria, with the most highly doped phosphorus-doped SiQDs being most toxic. This correlated with significantly increased ROS production by phosphorus-doped SiQDs and a slight increase in ROS production by boron-doped SiQDs. Interestingly, boron-doped SiQDs were observed to significantly bind to the surface of *S. oneidensis* yet showed less damage, revealing that not all toxicity mechanisms have the same level of bacterial impact (i.e. in this case, the ROS production effects outweigh the membrane association effects).

Another direct way to tune nanoparticle interactions with the cell membrane is by changing the morphology of the nanoparticles. The different morphologies of NPs can help to facilitate their interaction and potential internalization into cells. Theoretical calculations done by Li et al. demonstrate that at low ligand coverage for gold nanospheres, nanocubes, nanorods, and nanodisks, the biological membrane wrapping times, simulating endocytosis, around the nanoparticles increases in the order nanospheres < nanocubes < nanorods < nanodisks.[58] This trend mirrors the membrane bending energy

associated with each nanoparticle type. Experimental data with silver nanoplates, nanowires, and nanospheres of different diameters (10, 20, 40 nm) show that nanoplates exhibit the most toxicity to a fish gill cell line, followed by nanospheres (whose toxicity was related to their surface area) and then nanowires.[59] The nanoplate toxicity was due to its ability to cause oxidative stress, as demonstrated by Mitosox Red dye that showed superoxide radical production and that addition of N-acetylcysteine dramatically reduced toxicity. Even though silver nanoplates were the most toxic, they released the lowest amount of dissolved silver. It was demonstrated that direct cell contact was required for toxicity; thus, when the nanomaterials were physically separated from fish gill cells with a dialysis membrane, their toxicity was drastically reduced. When exposed to zebrafish embryos, nanoplates were again the most toxic material. When comparing the results of this study with the theoretical study by Li et al., it demonstrates the importance of determining the main mechanism of toxicity, since solely from a membrane interaction standpoint, the theoretical study shows that nanospheres should have the greatest membrane interaction. Despite their reduced membrane interactions, the nanoplates were significantly more redox active and were, therefore, the more toxic morphology.

1.4.2 Dissolution to Toxic Ions

It has been demonstrated that the dissolution of toxic ions from nanomaterials can impact organisms. Given that nanoparticles dissolve to release these ions, this could lead to a high localized concentration of ions that would impact the biota more than just a homogeneous solution of the ions, especially if the nanoparticles release these ions in an environment where the anions that normally sequester the ions by forming precipitates are not available. To combat this toxicity, there are several ways to reduce nanoparticle dissolution to toxic ions. One method is to simply replace the toxic species in the nanomaterial with something less toxic, though that will usually lead to significant changes in the nanomaterial properties that make them useful (e.g. decreasing catalytic activity or shifting a nanocathode material's redox potential). On the other hand, a more indirect method to reduce dissolution of toxic species is to stabilize the structure of the nanomaterial. This can be done by tuning the composition or doping in an extra component for improved stability, or by adding a shell to the nanomaterial in question. Given that different nanoparticle morphologies have different dissolution rates, controlling the morphology may be another way to reduce dissolution. Finally, addition of exogenous chelating agents may help to reduce the toxicity of dissolved ions.

1.4.2.1 Replace Toxic Elements with a More Benign Element

A direct way to reduce dissolution is to replace the toxic species with more benign elements. For example, in the complex oxide material, NMC, it was shown that the dissolution to produce nickel and cobalt ions dominated the toxicity to the bacterium, *S. oneidensis* MR-1 for an equistoichiometric NMC material, $Li_{0.33}Ni_{0.33}Mn_{0.33}Co_{0.33}O_2$. Reduction of the toxicity of NMC was achieved by changing the composition to have more manganese at the expense of nickel and cobalt, namely by making $Li_{0.68}Ni_{0.31}Mn_{0.39}Co_{0.30}O_2$, $Li_{0.61}Ni_{0.23}Mn_{0.55}Co_{0.22}O_2$, and $Li_{0.52}Ni_{0.14}Mn_{0.72}Co_{0.14}O_2$ nanosheets.[51] Using respirometry as a marker for bacterial health, a clear pattern emerged, showing that as the manganese content of NMC was increased, the nanomaterial's impact on the growth rate of bacteria was decreased (Figure 1.4). The respiration of bacteria exposed to Mn-enriched NMC recovered more quickly than those exposed to NMC containing less manganese. This work demonstrates that by replacing the toxic species in the material, the dissolution of toxic ions is reduced, which reduces the overall toxicity of the material. Since the composition of these transition metal oxide battery materials can often be tuned to change battery characteristics,[60,61] it is expected that the stoichiometries used in the Mn-enriched NMC would be functional cathode materials.

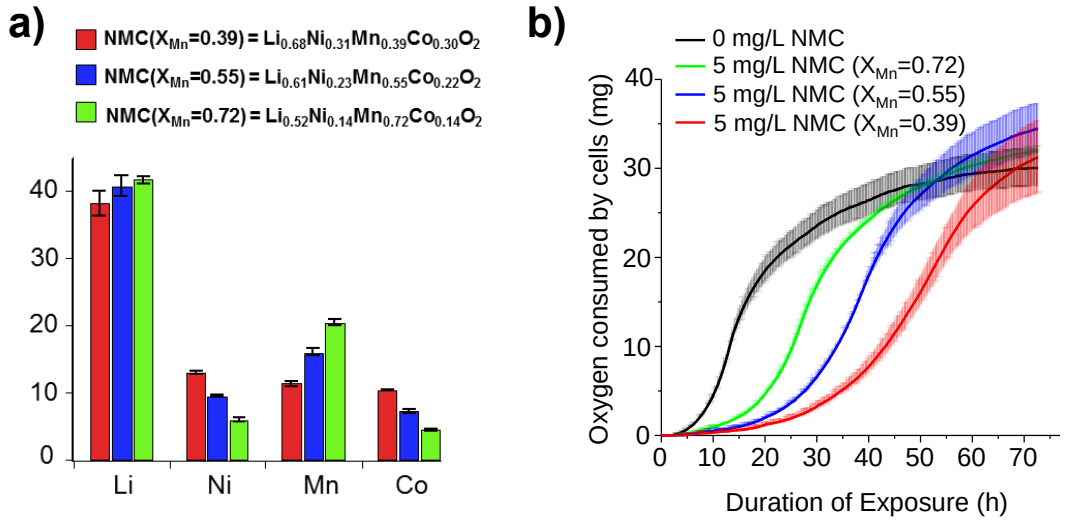

Figure 1.4. Mn-enriched NMC nanosheets demonstrated reduced toxicity to bacteria. As the manganese content in NMC nanosheets was increased, a) decreased amounts of nickel and cobalt were dissolved and subsequently, b) reduced toxicity to *S. oneidensis* MR-1 was observed with respirometry, indicated by the fact that the respiration in bacteria exposed to NMC with higher Mn content recovered to the same levels as the control more quickly. Figure adapted with permission from Ref 51. Copyright 2017 Royal Society of Chemistry.

1.4.2.2 Improve Nanoparticle Stability to Reduce Overall Dissolution

To see if the dissolution-dominated toxicity trend observed with manganese-enriched NMC would hold true for other formulations of NMC, other compositions with increased nickel content were synthesized. Given that nickel is one of the toxic components of NMC, it was expected that a Ni-enriched NMC would be more toxic than equistoichiometric NMC. When *S. oneidensis* MR-1 were exposed to NMC with increasing nickel content, however, the toxicity was observed to be the same between all the materials. This led to a computational investigation of NMC dissolution energies, which showed that additional nickel in Ni-enriched NMC had an oxidation state greater than +2, which has a less energetically favorable release since a redox reaction needs to be initiated to get it to the stable +2 oxidation state to dissolve. Theoretical calculations predict that metal release from equistoichiometric NMC and Ni-enriched NMC will be similar because of the enhanced stability of Ni-enriched NMC, which explains the similar toxicity to *S. oneidensis* exhibited by these materials. Ni-enriched NMC is discussed in more detail in Chapter 3.

Other work has taken advantage of increased nanoparticle stability to reduce NP toxicity. In work by Xia et al., the toxicity of ZnO nanoparticles to zebrafish, mice, and rats was noted to be due to the release of toxic Zn^{2+} ions.[62] Iron was doped into ZnO nanoparticles by mixing zinc naphthenate with iron naphthenate at desired weight percents and then synthesizing nanoparticles by flame spray pyrolysis. Zinc dissolution was reduced for nanoparticles with increasing iron content, and therefore the hatching rate of zebrafish was found to increase with increasing iron content of the nanoparticles. Increasing the iron content also benefitted the mice and rats, both of which showed reduced pulmonary inflammation.

1.4.2.3 Use of a Shell Material

Another way to reduce the dissolution of a material is to put a capping material over it, such as a polymer or silica shells.[63] The shell serves as a physical barrier that should minimize water interaction with the nanomaterial surface and the release of toxic ions from the core material to interact with organisms. It has been discussed in previous sections that for QDs, the addition of a ZnS shell can reduce toxicity by preventing dissolution of cadmium ions.[56] In work by Derfus et al., QDs were synthesized to have different coatings (ZnS and bovine serum albumin (BSA)).[64] Both coatings showed reduced cadmium dissolution from QDs, and therefore also demonstrated reduced toxicity to hepatocytes. In other work, the dissolution of QDs with PEG carboxylic acid, PEG amine, and PDDA surface coatings was investigated.[65] Both PEG-based shells exhibited similar dissolution

of cadmium and selenium, while the PDDA-coated QDs showed decreased dissolution. While toxicity was not evaluated in this work, it is likely that the reduced dissolution would cause reduced toxicity. It was suggested that the decreased dissolution seen with PDDA-coated QDs is because QDs demonstrate improved stability when coated with polymer shells that have longer chains, higher molecular weights, and greater structural complexity.

Similarly, a mesoporous silica shell presents itself as a good redesign strategy when aqueous infiltration to the core is required for nanoparticle performance, as the pores still allow access to the core by small molecules.[66] Mahoney et al. investigated the use of various silica coatings with <2-nm-diameter nickel nanoparticles: 1) NiNPs that were associated with the outside of a silica shell (Ni-SiO_2), 2) NiNPs in the pores of a nonhollow silica shell (hNi@SiO_2), and 3) NiNPs in the middle cavity of a porous hollow silica shell (nhNi@SiO_2).[67] While reduced Ni^{2+} dissolution was observed for NiNPs within silica shells compared to NiNPs on the exterior of a silica shell, there were no effects to survival of zebrafish embryos or noticeable larval deformations that formed. Differences in larval motor behavior were seen after exposure to hNi@SiO_2 and Ni-SiO_2. While bare NiNPs were not used in this study, they have been previously shown to be toxic,[68,69] partly due to nickel dissolution, and the lack of toxicity in this study indicates that a silica shell is mitigating NiNP toxicity. Use of a mesoporous silica shell to mitigate the effects of iron oxide nanoparticles on bacteria is further discussed in Chapter 4.

1.4.2.4 Nanoparticle Morphology

While nanoparticle morphology was addressed in Section 1.4.1, as morphology can impact the interaction of nanoparticles with cellular membranes, nanoparticle morphology can also be related to dissolution of the material.[70] When relating nanoparticle morphology to dissolution, two potentially important parameters are the different surface areas associated with each particle morphology and the different crystal planes that are revealed with varied particle morphology. As surface area increases, dissolution rate will also be expected to increase. The curvature of a particle is also important, as particles with a smaller curvature radius are less energetically favorable and consequently undergo more dissolution. Therefore, it would be expected that morphologies like nanorods would dissolve less than nanospheres, meaning nanorods would be a less toxic nanoparticle morphology. Indeed, in work done by Helmlinger et al. with silver nanospheres, nanoplatelets, nanorods, and nanocubes, it was found that the dissolution rates were nanoplatelets > nanospheres (avg diameter: 60 nm) > nanospheres (avg diameter:

150 nm) ≈ nanorods > nanocubes, which matches the trend for decreasing surface area of the material.[71] When the AgNPs were introduced to *Staphylococcus aureus*, toxicity was found to also match this trend, with nanoplatelets exhibiting the highest toxicity and nanocubes the lowest toxicity. The trends for dissolution with these morphologies is slightly different from the trend for nanoparticle binding to cell surfaces presented in Section 1.4.1, again illustrating the importance of determine the main toxicity mechanism to inform the redesign method chosen.

1.4.2.5 Chelating Agents

For nanoparticles that release toxic ions, a potential redesign strategy that would leave the nanomaterial of interest intact would be to synthesize the nanoparticles with a chelating agent for its ions as a ligand. Several instances of using chelating agents as nanoparticle ligands can be found in the literature, with applications ranging from removing metal ions during water treatment[72] to removing metal ions in the brains of patients with Alzheimer's disease.[73] In the field of environmental nanotoxicity, the use of chelating agents as ligands has the potential to reduce the impact of dissolved toxic ions, as they would complex with the chelating agent shortly after dissolution. There is precedent for co-exposing toxic nanoparticles and chelating agents to environmental organisms to reduce toxicity.[36] Also, as the chelating agents for cationic metal ions are generally negatively charged, using them as a nanoparticle ligand should further reduce toxicity by imparting a negative surface charge, which as discussed above, causes a reduction in NP toxicity. Directly attaching the chelating agent to the nanoparticle increases the likelihood that the chelating agent will end up in the same environmental site as the nanoparticle, as it would be impractical to add chelating agents to the environments that have unintentionally been exposed to nanoparticles. It is important to assess the efficacy of this redesign strategy, as the success of coexposure to toxic nanoparticles and chelating agents is dependent on the biological system and environmental matrix for the given nanoparticle type. Future active nanoparticle design could also include a slow release or delayed release of chelating agents to potentially increase the efficacy of this approach.

1.4.3 Generation of Reactive Oxygen Species

A major toxicity mechanism of QDs, and many other nanoparticles, to organisms is related to oxidative stress. A classical method that reduces the toxicity of cadmium-based QDs is to coat them with a passivating high energy band gap material like ZnS.[21] Although this is generally done to maintain core integrity and improve quantum yield of the QD, these coatings reduce the ability of the material to produce ROS, thus reducing toxicity.[64]

Other ways to mitigate ROS generation is to replace some of the metals with other materials that are less redox active, or to dope a material to change its electronic structure. Also, as was suggested with chelating agents above, addition of antioxidants to the nanoparticle surface can alleviate oxidative stress.

1.4.3.1 Use of Dopants and Other Materials to Tune Band Gap Properties

Beyond putting a coating onto cadmium-containing QDs to inhibit ROS production, Brunetti et al. demonstrated that changing the core material to be InP caused a reduction of oxidative stress in the environmental model, *Drosophila melanogaster*, when fed with QD-supplemented food.[74] Increased apoptosis of larval hemocytes was noted for CdSe, which correlated with increased expression of genes related to combating oxidative stress; InP/ZnS QDs caused minimal larval hemocyte death and no changes in oxidative stress gene expression. This suggests that the band gap energy of CdSe QDs favors the production of reactive oxygen species more than that of InP QDs. It is worth noting their observation that, when investigating human cell lines, both InP/ZnS and CdSe/ZnS QDs released similar amounts of indium and cadmium into the cell medium, respectively, but toxicity was only seen in CdSe/ZnS QDs and could be attributed to released Cd^{2+}. This suggests that InP/ZnS may be a good redesign strategy in aqueous environments by also reducing the amount of released cadmium.

Carbon dots are also being investigated as alternatives to cadmium-based quantum dots, as carbon dots are capable of luminescence. There are many types of carbon dots which are capable of luminescence,[75] and here we discuss the use of amorphous polymeric carbon dots as a cadmium-containing quantum dot alternative. Unlike quantum dots, of which one of the main mechanisms of toxicity is oxidative stress, carbon dots generally do not produce a substantial amount of ROS.[76] Zhi et al. recently demonstrated that both malic acid- and citric acid-based carbon dots, as well as their phosphorus-doped counterparts, are not toxic to *S. oneidensis* MR-1, and that they actually facilitate bacterial growth, even at very high concentrations (5 mg/mL). This suggests that *S. oneidensis* can use the carbon dots as a source of nutritional carbon. Therefore, unlike with cadmium-based carbon dots, not only does the band gap energy of carbon dots seem to not favor significant reactive oxygen species generation, the carbon dots themselves are also beneficial for sustaining bacterial growth.

Metal oxide nanoparticles also can be toxic due to the induction of oxidative stress. A way to combat this is to use dopants that tune the band gap of the material to reduce production of ROS. This has been demonstrated many times with materials that are used

in a human context,[77,78] although generally with the goal of increasing oxidative stress and toxicity to clinical models such as cancer cells.[79–81] However, while a number of doped systems have been studied, examples of demonstrating reduced nanoparticle toxicity to environmental organisms via reduced ROS production due to the use of dopants are challenging to find. Similarly, the band gap of quantum dots can be tuned, the strategies of which have been extensively reviewed.[82] These strategies should be employed for the redesign of nanoparticles to investigate their reduction in toxicity to environmentally relevant organisms such as bacteria or *D. magna*.

1.4.3.2 Antioxidant Addition

Given that the function of antioxidants is to combat oxidation, antioxidants can also be used to reduce toxicity of nanomaterials. In work by Posgai et al., in which the impact of feeding TiO_2 NPs and AgNPs to *D. melanogaster* was investigated, it was found that titania nanoparticles didn't impact survival or development of the organism, but did cause increased superoxide dismutase and glutathione activity. For fruit flies that consumed AgNPs, decreased survival and issues with development were noted, as well as increased superoxide dismutase and glutathione activity. When the food source was supplemented with the antioxidant, vitamin C, these negative effects were found to be at least partially alleviated. However, it is not practical to consider a separate addition of antioxidants to environmental compartments that have been exposed unintentionally to nanoparticles.

While some nanoparticles have been found to have intrinsic antioxidant behavior, such as ceria or yttria nanoparticles,[83] antioxidant molecules can also be tethered to nanoparticles that otherwise do not exhibit antioxidant activity. This will allow the nanoparticle itself to act as a scavenger for ROS. This has been demonstrated in work by Nie et al., where AuNPs are functionalized with a vitamin E analogue, Trolox.[84] In a system without any organisms, the effectiveness of the Trolox-AuNPs at reacting with 2,2-diphenyl-1-picrylhydrazyl (DPPH•) radical was compared to Trolox. This demonstrated that the reaction rate for Trolox-AuNPs with DPPH• was about eight times higher than for Trolox alone, indicating that functionalizing the antioxidant on this surface was improving its function. Other antioxidant-functionalized nanoparticles have been developed for clinical applications.[85–88] The strategies employed in synthesizing antioxidant-functionalized nanoparticles could also be applied to redesigning nanoparticles for non-biomedical applications with the goal of reducing environmental impact when the nanoparticles are ultimately released.

1.5 Conclusions

Herein, we describe several methods in which redesign of nanoparticles for reduced environmental impact may be possible, and we offer some redesign ideas that, to our knowledge, have not been investigated before with an environmental focus. With these methods, examples are given to demonstrate where they have been successfully implemented. Currently, there is a dearth of literature on redesigning nanoparticles to reduce their environmental impact, offering many opportunities to use some of the strategies outlined in this chapter, as well as working to add to our redesign arsenal. When redesigning nanoparticles, an important consideration is that the nanoparticles still work in their original application; it does no good to design an environmentally friendly nanoparticle that is no longer functional for the desired application or product. This chapter focuses on the properties of as-synthesized nanoparticles. Another aspect that is important to consider is how these materials will be transformed in the environmental compartments they end up in, such as interaction with natural organic matter,[10,29,30] but that is beyond the scope of this chapter.

Chapter 2

Using an Environmentally Relevant Panel of Gram-negative Bacteria to Assess the Toxicity of Polyallylamine Hydrochloride-wrapped Gold Nanoparticles

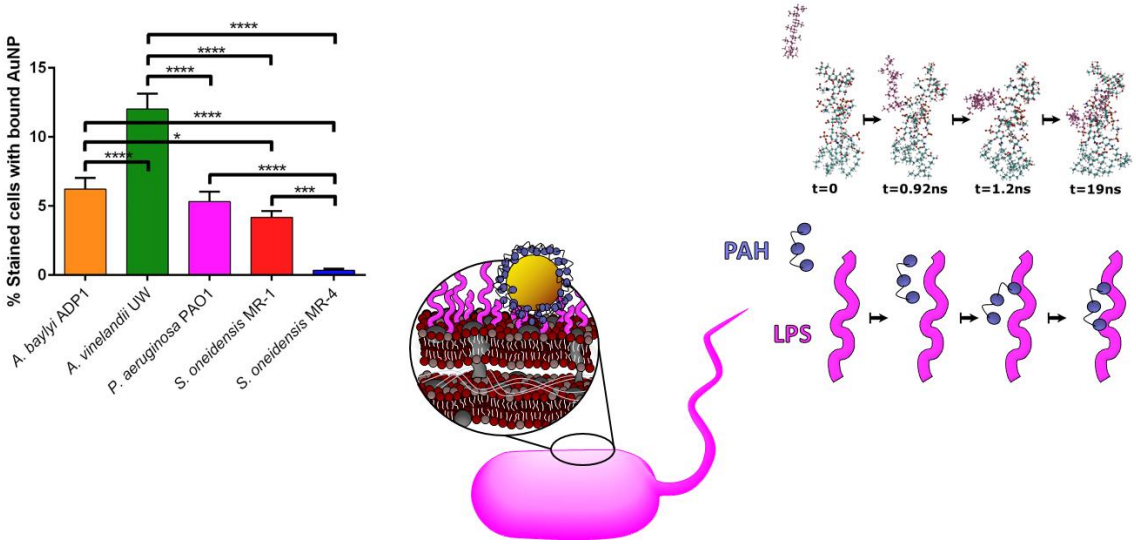

Reprinted in part from: Buchman, J.T.; Rahnamoun, A.; Landy, K.M.; Zhang, X.; Vartanian, A.M.; Jacob, L.M.; Murphy, C.J.; Hernandez, R.; Haynes, C.L. Using an environmentally-relevant panel of Gram-negative bacteria to assess the toxicity of polyallylamine hydrochloride-wrapped gold nanoparticles. *Environ. Sci.: Nano*, 5, 279-288. Copyright 2018, with permission from the Royal Society of Chemistry.

2.1 Overview

We aim to establish the effect of environmental diversity in evaluating nanotoxicity to bacteria. We assessed the toxicity of 4 nm polyallylamine hydrochloride-wrapped gold nanoparticles (PAH AuNPs) to a panel of bacteria from diverse environmental niches. The bacteria experienced a range of toxicities as evidenced by the different minimum bactericidal concentrations determined; the sensitivities of the bacteria was *A. vinelandii* = *P. aeruginosa* > *S. oneidensis* MR-4 > *A. baylyi* > *S. oneidensis* MR-1. Interactions between gold nanoparticles and molecular components of the cell wall were investigated by TEM, flow cytometry, and computational modeling. Binding results showed a general trend that bacteria with smooth LPS bind more PAH AuNPs than bacteria with rough LPS, however the observed toxicity is not directly related to the amount of nanoparticle binding. Computational models reveal that the PAH molecule that is wrapped on the NP surface migrates to phosphate groups in the core of the LPS structure. While a simplified model was used, the simulations also demonstrate that the PAH molecule interacts similarly with rough and smooth LPS structures. Overall, our results demonstrate that simple interactions between nanoparticles and the bacterial cell wall cannot fully account for observed trends in toxicity, which points to the importance of establishing more comprehensive approaches for modeling environmental nanotoxicity.

2.2 Introduction

One method to probe the potential environmental impact of nanoparticles is through the use of bacterial models, which, as decomposers, occupy an important trophic level; decomposers recycle nutrients that can be used by primary producers.[1] Therefore, any effects on bacteria may impact organisms in other trophic levels, making bacteria a good diagnostic for overall environmental health. Often, only one bacterial model is used in nanoparticle toxicity studies,[2–4] but this can lead to results that may not be generalizable across bacteria from different environments. Therefore, we have assembled a panel of Gram-negative bacteria with sequenced genomes that occupy different environmental niches for use in nanotoxicity studies.

When evaluating nanoparticle toxicity to bacteria, direct interactions of nanoparticles to the bacterial surface play a role in the toxicity, with several studies demonstrating a correlation between the amount of NPs bound to bacteria and observed toxicities.[5–8] It has been shown that bound NPs can rupture the bacterial cell membrane,[9,10] lead to alterations in the membrane potential,[11] release ions that are localized right at the bacterial surface,[12] and generate reactive oxygen species at the cell membrane.[13] In previous work, we have

shown that a main component of the Gram-negative bacterial surface, lipopolysaccharides, are important in facilitating the binding of nanoparticles with the surface of the model bacterium, *S. oneidensis* MR-1.[14] There are two broad classes of LPS, designated as either rough or smooth. Rough LPS have a lipid A region that anchors the LPS into the membrane and an oligosaccharide portion that is bound to the lipid A. In contrast, smooth LPS have both lipid A and core oligosaccharide regions, with the addition of an O-antigen, a polysaccharide domain bound to the core oligosaccharide, elongating the overall LPS structure. Based on the clear role of LPS in binding nanoparticles, it makes sense to generate a panel that focuses on variation in LPS structure. Such a panel would exclude Gram-positive bacteria, which are also important environmental organisms, but allows us to focus on specific surface chemistry differences between the bacteria used.

Table 2.1. Different characteristics of bacteria in the panel. The bacteria in the panel come from a range of habitats and have different respiration abilities. The panel includes bacteria with either rough or smooth LPS presented on their surface. Each bacterium in the panel has an important role in the environment.

Bacterial Strain	Habitat	Respiration	LPS type	Environmental Role
Azotobacter vinelandii UW	Soil[15]	Obligate aerobe[15]	Smooth[16]	Nitrogen cycle
Acinetobacter baylyi ADP1	Soil, sediment, aquatic[17]	Obligate aerobe[17]	Smooth[17]	Metabolize aromatic compounds
Shewanella oneidensis MR-1	Soil, marine[18]	Facultative anaerobe[18]	Rough[19]	Geochemical nutrient cycle
Shewanella oneidensis MR-4	Soil, marine[18]	Facultative anaerobe[18]	Rough[20]	Geochemical nutrient cycle
Pseudomonas aeruginosa PAO1	Ubiquitous[21]	Obligate aerobe[21]	Smooth[22]	Metabolic diversity

The five bacteria that make up the bacterial panel introduced in this chapter include *Azotobacter vinelandii* UW, *Acinetobacter baylyi* ADP1, *Shewanella oneidensis* MR-1, *Shewanella oneidensis* MR-4, and *Pseudomonas aeruginosa* PAO1. They are a mix of Gram-negative bacteria that have smooth or rough LPS on their surface. Differences between the bacteria in the panel are highlighted in Table 2.1. In the environment, *A. vinelandii* has an important role in the nitrogen cycle since it is capable of fixing nitrogen even in the presence of atmospheric oxygen.[23] The smooth LPS of *A. baylyi* likely has branched O-antigens since that is characteristic of the genus *Acinetobacter*;[17] this bacterium is capable of great metabolic diversity, notably in its ability to metabolize aromatic compounds that are often products of plant degradation.[24] *S. oneidensis* MR-1 has an important environmental role in geochemical nutrient cycling since it is capable of

reducing a wide variety of metals.[18] Similarly, *S. oneidensis* MR-4 is also capable of dissimilatory reduction of many different metals.[20] Finally, *P. aeruginosa* PAO1 is an obligate aerobe that can adapt to live in many different environments due to its metabolic diversity. *P. aeruginosa* is often used as a biofilm formation model; biofilms may serve as a sink for NPs entering the environment, making it likely that *P. aeruginosa* would encounter nanomaterials that are released into the environment.[25]

Since these bacteria occupy diverse environmental niches and have different surface compositions, we expect that they will be representative of bacteria in the environments that nanoparticles may end up in. These differences should also make them suitable for showing a range of responses to nanoparticle exposure so that a particular nanoparticle is not deemed non-toxic because a single bacterial species happens to be tolerant to it. The motivation for noting the different LPS structures on each bacterial species' cell surface is that the differences in LPS length and composition may impact their interaction with the NPs used in this study. The saccharide portions of the LPS structures of *P. aeruginosa*,[26,27] *S. oneidensis* MR-1,[19] and *S. oneidensis* MR-4[20] have been elucidated (Figure 2.1), but the LPS structures of the other bacteria in the panel are not as well characterized. The structures given for *P. aeruginosa*, *S. oneidensis* MR-1, and *S. oneidensis* MR-1 can be used to calculate the charges of their LPS. Indeed, the charges of these LPS structures as well as other LPS structures used in simulations in this chapter are available in Table 2.2.

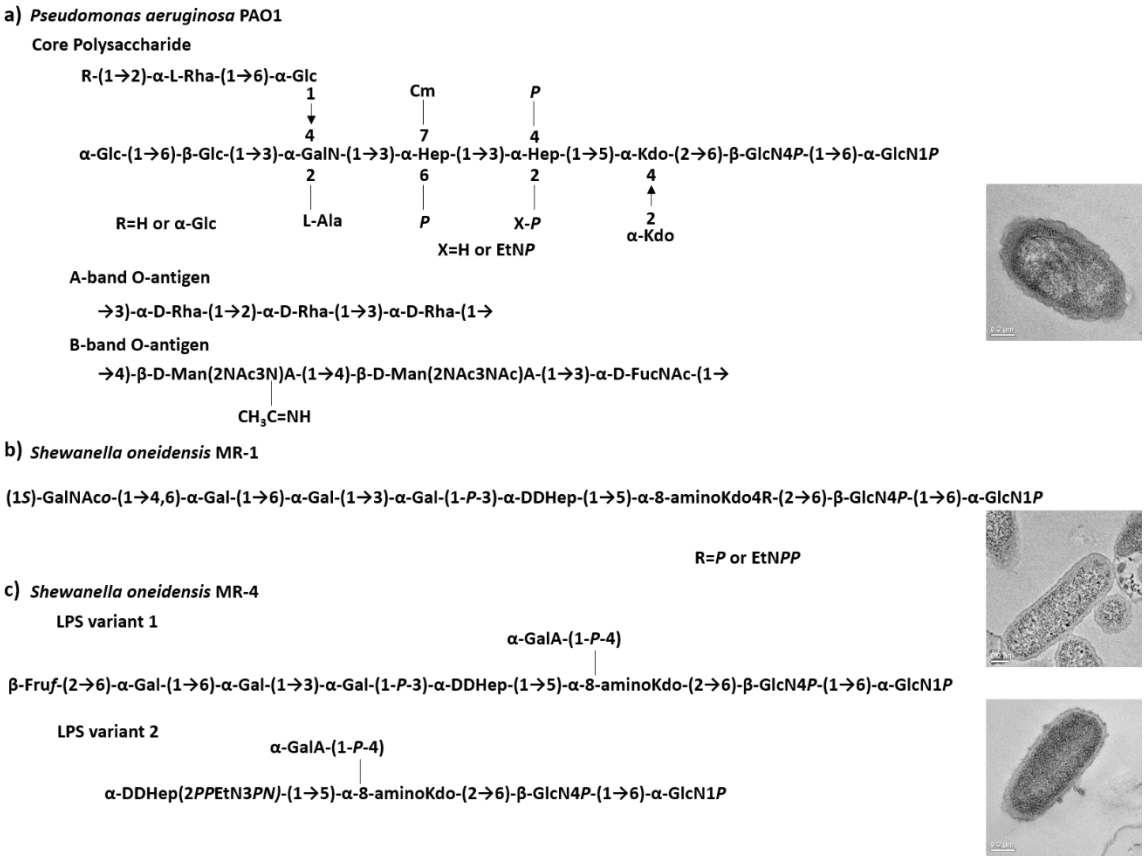

Figure 2.1. Known LPS structures for bacteria in the panel. The structure of the polysaccharide portion of the LPS and a representative TEM image of a) *P. aeruginosa*.[26] This bacterium creates two different O-antigens, namely the A-band and B-band; the A-band has about 23 repeats and the B-band has over 50 repeats.[27] The saccharide region and representative TEM images of b) *S. oneidensis* MR-1[19] and c) *S. oneidensis* MR-4. *S. oneidensis* MR-4 expresses two variants for its core polysaccharide structure.[20] These structures have been adapted from references.[19,20,26,27] The structures of the polysaccharide portion of LPS for *A. vinelandii* and *A. baylyi* are not as well characterized and are therefore not shown here.

Table 2.2. Important LPS characteristics for simulations. The number of phosphates and charge of the LPS core polysaccharide structure are provided for several bacterial strain variants (first three rows) and model structures (remaining four rows). O-antigens were entirely absent in all rough model structures and only two O-antigens are included in the "smoother" structure. Due to PAH wrapping around the NP, it is expected that the LPS would first interact with the surface PAH molecules. The PAH used in the simulations has a charge of +10 leading to the total charges listed in the final column, corresponding to the overall charge after the interaction of PAH with each LPS. Negative and positive charges were neutralized in the simulations using the corresponding number of sodium cations or chloride anions, respectively.

Bacterial Strain	Number of Phosphate Units	Charge of LPS	Charge of LPS + PAH
S. oneidensis MR-1	5	-7	+3
S. oneidensis MR-4 variant 1	4	-6	+4
S. oneidensis MR-4 variant 2	6	-5	+5
Rough *P. aeruginosa* PAO1 variant	6	-12	-2
"Smoother" *P. aeruginosa* PAO1 variant	6	-14	-4
Rough *S. typhimurium*	4	-10	0
Rough *E. coli*	5	-9	+1

To demonstrate the use of the bacterial panel in this chapter, each species was exposed to 4-nm-diameter polyallylamine hydrochloride-wrapped gold nanoparticles. AuNPs were used in this study due to their chemical inertness and ease of characterization.[28,29] Polyelectrolyte coating is an industrially-relevant modification of materials as these functionalized materials have many applications in diverse fields,[30–32] and this particular coating is known to interact with bacterial surfaces and cause membrane disruption as its toxicity mechanism.[5,33] While there is limited work studying PAH AuNPs with the bacteria in this panel,[34] in previous work, the toxicity of PAH AuNPs was investigated for *S. oneidensis* MR-1 using a colony counting method.[5] In this chapter, the effects of the PAH AuNPs to each bacterium are noted by determining the minimum bactericidal concentration (MBC). The MBC is defined as the lowest nanoparticle concentration that kills at least 99% of the bacteria. This is a facile method to demonstrate the different responses that each bacterium has to NP exposure. To test the hypothesis that extent of NP binding to the bacterial cell surface correlates with toxicity, transmission electron microscopy was used to visualize and flow cytometry was used to quantify PAH AuNP association with each species. In parallel, a molecular dynamics simulation was used to calculate relative association energies of the PAH that caps the nanoparticles with

different LPS structures to determine if the presentation of negatively charged phosphate groups facilitates the interaction of LPS with the amine groups of PAH. Taken together, the results demonstrate that a simple hypothesis related to the molecular character of the LPS is not sufficient to explain the nanoparticle association and toxicity results. This is a benefit to using such a panel, as it identifies instances where the biological complexity can mask simple, expected trends. Indeed, this panel does reveal which bacterial strains are most critical for follow-on work and facilitates the formulation of further hypotheses. While AuNPs are the focus of this work, this panel can be adapted for use with a range of nanomaterials.

2.3 Materials and Methods

2.3.1 Materials

Magnesium sulfate ($MgSO_4$), sucrose, sodium molybdate dihydrate ($Na_2MoO_4 \cdot 2H_2O$), 4-(2-hydroxyethyl)-1-piperazineethanesulfonic acid (HEPES), gold (III) chloride trihydrate ($HAuCl_4 \cdot 3H_2O$), sodium citrate tribasic dihydrate ($C_6H_5Na_3O_7 \cdot 2H_2O$), polyallylamine hydrochloride (PAH, MW 17.5 kDa), sodium borohydride ($NaBH_4$), and sodium chloride (NaCl) were purchased from Sigma-Aldrich (Milwaukee, WI). Potassium phosphate dibasic trihydrate ($K_2HPO_4 \cdot 3H_2O$) was purchased from Mallinckrodt (Phillipsburg, NJ). Potassium phosphate monobasic (KH_2PO_4) was obtained from J.T. Baker (Center Valley, PA). Dulbecco's phosphate-buffered saline was purchased from Corning (Aurora, CO) and LB broth and agar were obtained from BD Difco (Franklin Lakes, NJ). SYTO9 nucleic acid stain was obtained from Molecular Probes (Waltham, MA). Calcium chloride ($CaCl_2$) and ferrous sulfate ($FeSO_4$) were purchased from Fisher Scientific (Rockford, IL). Absolute anhydrous 99.5% ethanol was obtained from Pharmco-Aaper (Brookfield, CT). All chemicals were used as received. Deionized water (18.2 MΩ·cm) was purified using a Milli-Q Millipore water purification system (Billerica, MA).

Shewanella oneidensis MR-1 was obtained from Jeffrey Gralnick (Dept of Microbiology, University of Minnesota). *Shewanella oneidensis* MR-4 was obtained from Daad Saffarini (Dept of Biological Sciences, University of Wisconsin – Milwaukee). *Acinetobacter baylyi* (ATCC® 33305™), *Azotobacter vinelandii* (ATCC® 13705™), and *Pseudomonas aeruginosa* (ATCC® 47085™) were purchased from the American Type Culture Collection (Manassas, VA)

2.3.2 Polyallylamine Hydrochloride-wrapped Gold Nanoparticles

PAH AuNPs were synthesized by polyelectrolyte wrapping of as-synthesized citrate-capped AuNPs. 4-nm-diameter citrate-capped AuNPs were synthesized using a flow

reactor based on modified procedures that have been previously reported.[35,36] Briefly, 20 mL of 0.01 M $HAuCl_4$ was added to 1600 mL nanopure deionized water in a 2 L Erlenmeyer flask to make the gold precursor solution. At the same time, 10 mL of 0.1 M $NaBH_4$ was added to 1616 mL of chilled nanopure deionized water in another 2 L Erlenmeyer flask. 6 mL of 0.1 M sodium citrate was added to the gold precursor solution prior to the synthesis. Both the gold precursor solution and sodium borohydride solution were put through a flow reactor (peristaltic pump) at 40 mL/min into a 4 L jug with gentle stirring. Once the two solutions were combined in the reactor lines, the resulting solution became a light pink color, and was stirred for at least 1 h before using. The diameters of citrate-capped AuNPs were determined in suspension by UV−vis extinction spectroscopy (Figure 2.3a).[37]

To the approximately 3.2 L of as-synthesized citrate-capped AuNPs, 32.0 mL of 100 mM NaCl and 100.0 mL of a PAH solution (MW 17.5 kDa) (10 mg/mL in 1 mM NaCl) was added with vigorous stirring. The solution was stirred overnight and concentrated to around 30 mL by diafiltration cassettes (Tangential Flow Filtration Capsules, 50K MWCO, VWR). The concentrated PAH AuNPs were purified by centrifugation at 13,000×*g* for 55 min.

2.3.3 Gold Nanoparticle Characterization

PAH AuNPs were characterized post-synthesis by UV-vis extinction spectroscopy, TEM, and ζ-potential measurement. The size and ζ-potential for the PAH AuNPs were also characterized in the exposure medium using UV-vis extinction spectroscopy and ζ-potential measurement. UV-vis extinction spectra post-synthesis were obtained on a Cary 500 UV-vis-NIR spectrophotometer and the measurements taken in exposure medium were obtained on an Ocean Optics USB2000 spectrophotometer. For TEM studies, 5 µL of a dilute solution of PAH AuNPs was drop-cast onto a TEM grid (Ted Pella, Redding, CA), and the PAH AuNP sample images were taken with a JEOL 2100 TEM. ζ-potential measurements were obtained using a Brookhaven ZetaPALS instrument.

2.3.4 Quantification of Free Polyallylamine Hydrochloride

To wrap the AuNPs with PAH, a suspension containing excess PAH was mixed with the citrate-capped AuNPs. Purification via centrifugation was performed on the resulting PAH AuNP suspension, however, some excess PAH remained in the suspension as well. The amount of leftover free PAH in the AuNP suspension was quantified so that relevant free PAH controls could be completed in this study. The concentration of free PAH in the AuNP suspension was determined using a fluorescamine assay as described previously.[38]

Briefly, the samples were first centrifuged at 66,000×*g* for 45 min at 4 °C to remove all of the AuNPs. The supernatant was removed and concentrated using a Savant Speedvac concentrator. Then, 120 µL of the sample was mixed with 20 µL of sodium borate buffer (pH 8) and 60 µL of 0.1% (w/v) fluorescamine in acetonitrile in a 96 well plate. The reaction occurred at room temperature for 5 min before the fluorescence was detected using a plate reader that excited at 425 nm and quantified the emission at 480 nm. The fluorescence detected was converted to a PAH concentration with the use of a calibration curve. This information is critical for doing free PAH controls during toxicity experiments.

2.3.5 Bacterial Culture Conditions

Bacteria were stored at -80 °C until ready for use. For *S. oneidensis* MR-1*, S. oneidensis* MR-4*, A. baylyi,* and *P. aeruginosa,* the appropriate bacterial stock was plated on a sterilized Luria-Bertani (LB) agar plate and incubated at 30 °C. Two colonies were inoculated in 10 mL of LB broth and incubated overnight. For *A. vinelandii*, plates with Burk's medium adapted from Newton et al.[39] were used and two colonies were inoculated in 10 mL of Burk's medium. The bacteria at late log phase were centrifuged at 750×*g* for 10 min and washed with Dulbecco's phosphate-buffered saline (DPBS) before resuspension in HEPES buffer (2 mM HEPES, 25 mM NaCl, pH=7.4) to the appropriate cell density.

2.3.6 Minimum Bactericidal Concentration Determination

The cells were diluted in HEPES buffer to a cell density of 2×10^6 cells/mL. Cells were either exposed to PAH AuNPs (2.81, 0.28, or 0.028 ppm) or to free PAH (21.16, 2.116, or 0.2116 ppm) for 10 minutes by mixing 180 µL of bacterial suspension with 20 µL of PAH AuNP or free PAH suspension. Free PAH controls were performed since the PAH AuNP suspension contained free PAH that was left over from the wrapping process. The concentrations of free PAH present in the AuNP suspensions were determined using a fluorescamine assay and were used to distinguish the impact of free polyelectrolyte from polyelectrolyte presented on the AuNP surface. Following the 10-minute exposure, six 10 µL drops of each treatment were dropped onto a dried, UV-sterilized LB agar plate (Burk's medium plates were used for *A. vinelandii*). Once the drops absorbed into the agar, the plates were incubated upside-down in a 30 °C incubator overnight. The PAH AuNP and free PAH concentration that killed at least 99% of the bacteria were recorded.

2.3.7 Transmission Electron Microscopy Analysis

Before taking images of nanoparticle-exposed bacteria with the TEM, the samples had to be embedded in epoxy resin.[5,40] At an optical density of 0.8 in HEPES, the bacteria

were exposed to 0.281 ppm PAH AuNPs for 10 min and then washed three times in 0.1 M cacodylate buffer. The cells were fixed using 2.5% glutaraldehyde in 0.1 M cacodylate buffer. This step proceeds for 50 min, flipping the pellet after 25 min to ensure fixation. The pellet is then washed (without resuspension) three times in 0.1 M cacodylate buffer. To dehydrate the cells, they were washed for 5 min with increasing concentrations of ethanol in water (30%, 50%, 70%, 80%, 95%, and 100% ethanol). They were rinsed three times with propylene oxide before being incubated with a 2:1 propylene oxide:resin mix for 2 hours uncovered. Then they were incubated with 1:1 propylene oxide:resin overnight followed by 1:1 propylene oxide:resin for 4 hours and pure resin overnight. After replacement with fresh resin, the samples were incubated at 40 °C for 24 hours and then 60 °C for 48 hours. The samples were cut into ~70-nm-thick sections using a LEICA EM UC6 ultramicrotome and stained with uranyl acetate and lead citrate to improve image contrast. The sections were placed on 200 mesh copper grids that have Formvar and carbon supports, and images were taken using a FEI Tecnai T12 transmission electron microscope using an operating voltage of 120 kV.

2.3.8 Flow Cytometry Analysis

After the bacteria reached the late log phase, they were washed in DPBS and resuspended in HEPES buffer. Bacterial suspensions at 4 $\times 10^8$ cells/mL were exposed to 2.81 ppm PAH AuNPs for 10 min and then incubated with 3.34 mM SYTO9 dye at room temperature for 15 min. The samples were analyzed with a Becton Dickenson LSRII SORP flow cytometer with a 20 mW, 488 nm laser, using a control set of bacteria not exposed to NPs to draw the gates. SYTO9 fluorescence was used to distinguish bacteria from other debris in the sample, and light scattering was used to determine which bacteria had associated AuNPs. In total, each sample was done in triplicate, collecting 20,000 events in each run.

2.3.9 Computational Models and Simulation

The use of molecular dynamics simulations to characterize the large-scale association and relaxation of LPS with the PAH presented on the AuNP surface can yield insight into the underlying chemistry by resolving which sites, or sets of sites, induce interactions.[41,42] Representative model structures of the LPS molecules found on the surface of *P. aeruginosa*, *Salmonella typhimurium*, and *Escherichia coli* have been prepared. While these three structures are not perfect matches for the bacteria in this panel (largely because not all the LPS structures are well-known), they represent a range of LPS structures and should still yield insight about critical interaction features, since they exhibit

different overall charges and have differing numbers of phosphate units in their structure. Several force fields have been developed for prediction of interfacial properties of biological materials and their interactions with inorganic and organic nanostructures.[43–46] We employed the CHARMM36 force field because it is a transferable potential that has been widely used and benchmarked, and it presented no challenges to the numerical convergence in the current studies. These structures have been energy minimized and equilibrated in the presence of 13,000–25,000 explicit (TIP3P) water molecules (depending on the size of the system) through equations of motion driven by the CHARMM36 force field. The mixture of PAH, LPS molecules, and water is neutralized through the addition of counter-ions that corresponds to the number of sodium cations or chloride anions needed to neutralize the "charge of LPS + PAH" as listed in the corresponding column of Table 2.2. For simplicity, we use a 10-mer PAH construct as it provides a balance between the non-chain like monomer and computationally expensive long-chain polymers with hundreds or more monomeric units. The chemical and molecular structure of the selected LPS have been obtained from known properties of the LPS from the chosen bacteria listed above. Each trajectory was then propagated for 19-20 nanoseconds at a cost of 65-75 hours of computer time on the XSEDE Bridges regular memory nodes with 2.3 GHz Intel Xeon EP-Series CPUs and 128 GB memory per CPU. In all cases, the PAH approaches the LPS molecule, allowing us to consider the time to approach and the location of the approach as figures of merit (or observables).

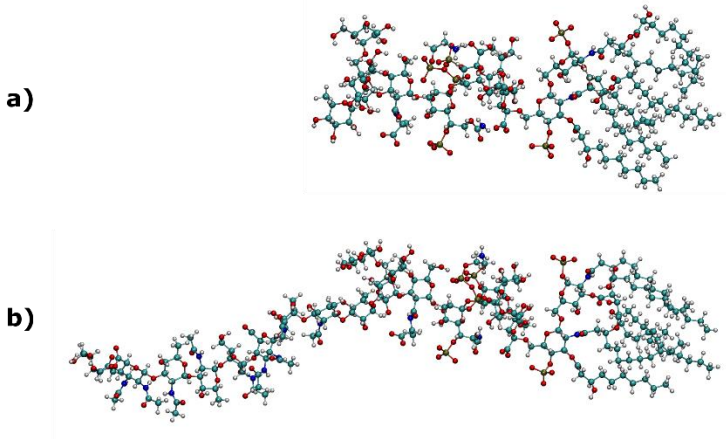

Figure 2.2. Rough and "Smoother" LPS models used in simulations. Ball-and-stick renderings of representative structures of a) rough LPS and b) rough LPS with two added O-antigen units onto the *P. aeruginosa* LPS structure.

A computational study was performed to investigate PAH binding using a rough LPS model and a LPS construct with "smoother" character. The LPS models used here vary

according to the corresponding incorporation of O-antigens. The addition of two O-antigen units to the rough *P. aeruginosa* LPS was constructed using the CHARMM-GUI[47] and models a smoother construct (Figure 2.2) useful for our systematic study. The interaction between PAH and the LPS of *P. aeruginosa*, *E. coli,* and *S. typhimurium* (structures shown in Figure 2.6), was observed through similar molecular dynamics trajectories.

The strength of the association of PAH to each LPS was evaluated from trajectory simulations to better understand specific interactions between the polyelectrolytes and LPS with different structures. Specifically, the changes in the interaction energies between the LPS and PAH are calculated after the complete simulation trajectories are obtained. The effects of the water molecules and ions on these energies are subtracted. Consequently, the reported energies include only the contributions from the interaction between the polyelectrolytes and LPS molecules.

2.4 Results and Discussion

2.4.1 Synthesis and Characterization of Gold Nanoparticles

We first verified the size of the citrate-capped AuNPs before and after functionalization with PAH using several methods. Citrate-capped AuNPs in solution were validated after synthesis by UV-vis spectroscopy[37] (Figure 2.3a), which demonstrated that the nanoparticle diameter was approximately 4 nm. After functionalization with PAH, TEM analysis indicated that the PAH AuNPs possessed a core diameter of 4.2 ± 1.2 nm (n>200), and a representative TEM image is shown (Figure 2.3b). The ζ-potential of the PAH AuNPs was 46.6 ± 2.6 mV. Taken together, these results demonstrate that positively charged PAH AuNPs were synthesized with uniform size distribution. In the exposure medium, the size of the PAH AuNPs were determined to be 12 ± 2 nm by UV-vis extinction spectroscopy, indicating there was some affiliation of the nanoparticles to each other during the exposure. The ζ-potential of the PAH AuNPs was 34 ± 2 mV, which shows a slight reduction in ζ-potential in HEPES buffer, but the magnitude is large enough for the particles to remain stable in suspension.

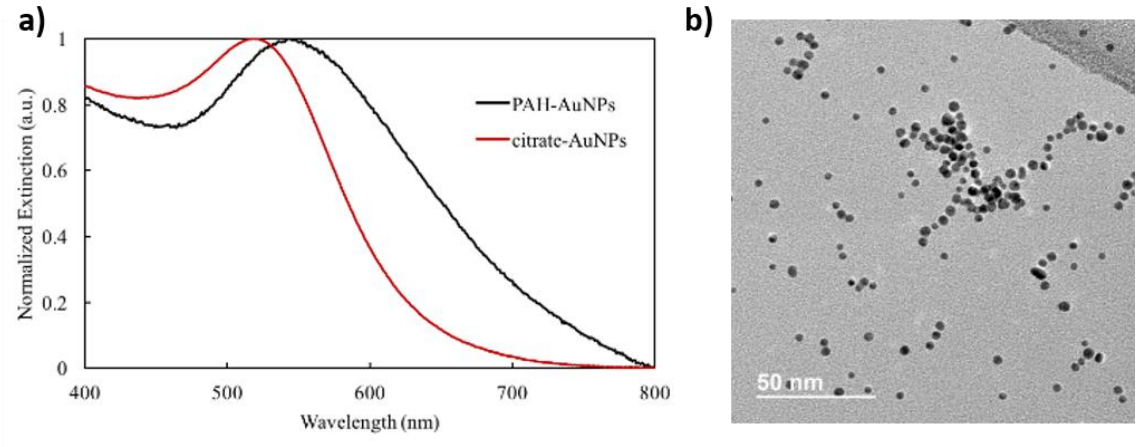

Figure 2.3. UV-vis spectra for citrate-capped AuNPs and PAH AuNPs and a representative TEM image of PAH AuNPs. a) UV-vis spectra reveal that citrate-capped AuNPs have a diameter of approximately 4 nm and b) from TEM images, a core diameter for PAH AuNPs was determined to be 4.2 ± 1.2 nm (n>200).

2.4.2 Minimum Bactericidal Concentration Determination

To test their toxicity, the MBCs were determined for PAH AuNPs and free PAH (Table 2.3). With the use of the fluorescamine assay, the concentration of free PAH in the AuNP suspension was determined to be 7.53 ± 0.20 mg/L of PAH per mg Au/L of AuNPs. Analyzing the minimum bactericidal concentrations showed that each of the bacteria had different sensitivities to the toxicants used in this study. The sensitivities of each bacterium to PAH AuNPs are *A. vinelandii* = *P. aeruginosa* > *S. oneidensis* MR-4 > *A. baylyi* > *S. oneidensis* MR-1, which was tolerant to all concentrations of PAH AuNPs used in this study. The trend identified by MBC shows that the toxicity cannot be as easily predicted simply based on the smooth or rough character of bacterial LPS as originally hypothesized, since the observed sensitivities do not follow a pattern correlated with LPS type. For three of the bacteria (*A. baylyi*, *S. oneidensis* MR-1, *S. oneidensis* MR-4), the toxicity of the PAH AuNPs is explained by the free PAH that is present in those suspensions, which is consistent with previous findings.[38] For *A. vinelandii* and *P. aeruginosa*, a nanospecific effect is seen for the PAH AuNPs since the concentration of free PAH required to kill 99% of these bacteria was higher than the concentration present in the toxic PAH AuNP suspensions. The wide range of sensitivities to both PAH AuNPs and PAH demonstrates the importance of using a bacterial panel when assessing nanoparticle properties that impact toxicity. From this experiment, the two bacteria exhibiting a nanoparticle effect have been identified to be used for follow-on work to study

the mechanism of toxicity for this nanoparticle type, whereas the other three bacteria were merely experiencing the toxicity of free PAH.

Table 2.3. Determination of minimum bactericidal concentrations for each bacterium. Minimum bactericidal concentration values observed for each bacterium after exposure to PAH AuNPs and to free PAH. The value in the column after the MBC for PAH AuNPs indicates the amount of free PAH present in that concentration of PAH AuNPs as determined by the fluorescamine assay.[38] (Ex: 0.281 ppm of PAH AuNPs contains a free PAH concentration of 2.12 ppm). The MBCs were determined in at least triplicate measurements.

Bacteria	$MBC_{PAH\ AuNPs}$ (ppm)	Free PAH present at PAH AuNP MBC concentration (ppm)	$MBC_{Free\ PAH}$ (ppm)
A. vinelandii UW	≤0.0281	≤0.212	2.12
P. aeruginosa PAO1	≤0.0281	≤0.212	>21.2
S. oneidensis MR-4	0.281	2.12	2.12
A. baylyi ADP1	2.09	15.8	14.8
S. oneidensis MR-1	≥2.81	≥21.2	≥21.2

2.4.3 Nanoparticle Association with Bacteria

Post-exposure to PAH AuNPs, the binding was visualized using TEM, with examples where binding is visible shown with a red arrow in the top images of Figure 2.4a-e. Dark-field TEM was utilized to confirm the presence of the diffracting AuNPs as the high crystallinity of AuNPs greatly improves their contrast in dark-field mode,[48] making them appear as bright spots amidst the bacterial matrix. The dark-field images are shown in the bottom images of Figure 2.4a-e and the bright spots (AuNPs) can be seen at the cell surfaces for each of the bacteria. The images show that bound PAH AuNPs cover just a small area of the bacterial cell envelope, with upwards of tens of nanoparticles bound to any particular bacterium. However, only a thin slice can be imaged with TEM, making it a more qualitative technique.

To quantify NP binding to bacteria, flow cytometry was used (Figure 2.4f-h). To draw the gates in flow cytometry to determine which bacterial population was bound by PAH AuNPs, a control sample of bacterial cells with SYTO9 stain that was not exposed to AuNPs was used. A representation of this data can be seen for *A. baylyi* in Figure 2.4f. The bacterial cells are first distinguished from other debris by the presence of SYTO9 stain (top plot). The gate was then drawn using the scattering of the cells (bottom plot), as AuNPs have efficient scattering properties, which means cells bound to AuNPs have a higher forward and side scattering than bare bacterial cells. Therefore, the gate was drawn

at the high edge of scattering for the bacterial cell controls for each species of bacteria. Based on flow cytometry data, at 2.81 ppm PAH AuNP, binding was seen for all bacteria except *S. oneidensis* MR-4, which showed minimal binding. The order of binding from greatest to least is *A. vinelandii* (12 ± 1%), *A. baylyi* (6.2 ± 0.8%), *P. aeruginosa* (5.3 ± 0.7%), *S. oneidensis* MR-1 (4.2 ± 0.5%), and *S. oneidensis* MR-4 (0.3 ± 0.1%). These data show that, in general, the bacteria with smooth LPS exhibit higher AuNP binding than those with rough LPS, although for *P. aeruginosa* and *S. oneidensis* MR-1, these binding amounts are very similar. We speculate that this is because the O-antigen of smooth LPS generally has a larger number of negatively charged sites for cationic nanoparticles to interact with than rough LPS.[49]

Comparing the binding data with toxicity data reveals some interesting observations. Namely, there are instances where there are similar binding amounts but different observed toxicities (i.e. *P. aeruginosa* and *S. oneidensis* MR-1) and where there is similar toxicity but a different amount of binding (*A. vinelandii* and *P. aeruginosa*). It is often assumed that direct nanoparticle interactions with the cell envelope drive toxicity, and these simple relationships between molecular components of the cell wall and nanoparticle properties can and have been identified.[5] Once you start incorporating a wider range of organisms, however, some of these simple relationships start to be masked by an increasing biological complexity. This indicates that there are more complex mechanisms involved in this interaction, and identifying these other mechanisms will be important for each nanoparticle/bacterial interaction and can lead to insight into that biological complexity.

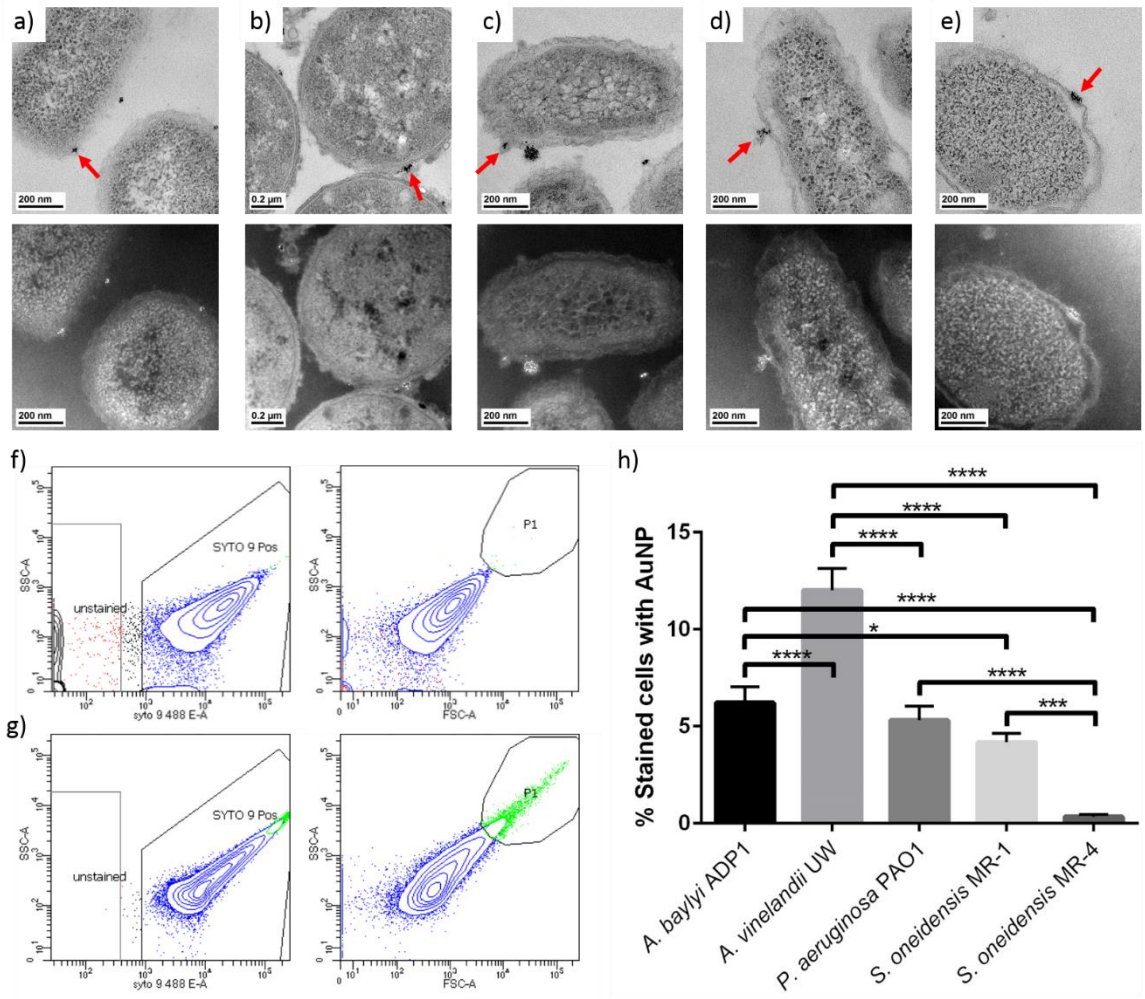

Figure 2.4. Association of PAH AuNPs to bacteria as assessed by transmission electron microscopy and flow cytometry. Transmission electron micrographs showing association of PAH AuNPs with a) *A. baylyi* ADP1, b) *A. vinelandii* UW, c) *P. aeruginosa* PAO1, d) *S. oneidensis* MR-1, and e) *S. oneidensis* MR-4 in bright-field (top images) with their corresponding dark-field images (bottom images). The red arrows show an example of PAH AuNP attachment to the bacterial cell wall. Representative data for f) *A. baylyi* is shown to demonstrate how the gate determining PAH AuNP binding was drawn. With a sample of cells stained with SYTO9 and no AuNPs, the left plot was used to determine what events were bacterial cells based on the presence of SYTO9 stain. The right plot shows only events that had SYTO9 stain present, and the gate for AuNP binding was drawn at the high scattering edge of the events from this control experiment lacking AuNPs. Representative flow cytometry data for g) *A. baylyi* exposed to 2.81 ppm PAH AuNPs. The left plot was used to identify cells based on the presence of SYTO9 stain, which is the boxed region of events labeled “SYTO 9 Pos”. The right plot contains only the cells present in the boxed region of the left plot, and the events with both high side scattering and forward scattering were the population of cells with bound AuNPs. This gate was drawn using the maximum scattering seen in

cells that were not exposed to PAH AuNPs. The blue dots correspond to cells stained with SYTO9 and the green events are stained bacterial cells that are bound to AuNPs. From flow cytometry, the h) percentage of cells that were bound to AuNPs are shown for the bacterial species after exposure to 2.81 ppm PAH AuNPs. *p<0.05, ***p<0.001, ****p<0.0001

2.4.4 Computational Model Results

While the experiments performed cannot be done at the same time-scale as the computational models, simulations are used here to derive some molecular-level insight about the interaction between the PAH on the nanoparticle surface (modeled as a 10-mer) and LPS. Representative snapshots of the motion of PAH toward LPS (from *P. aeruginosa*) are shown in

Figure **2.5**. The PAH molecule was seen to move towards phosphate units of the core region in the trajectory.

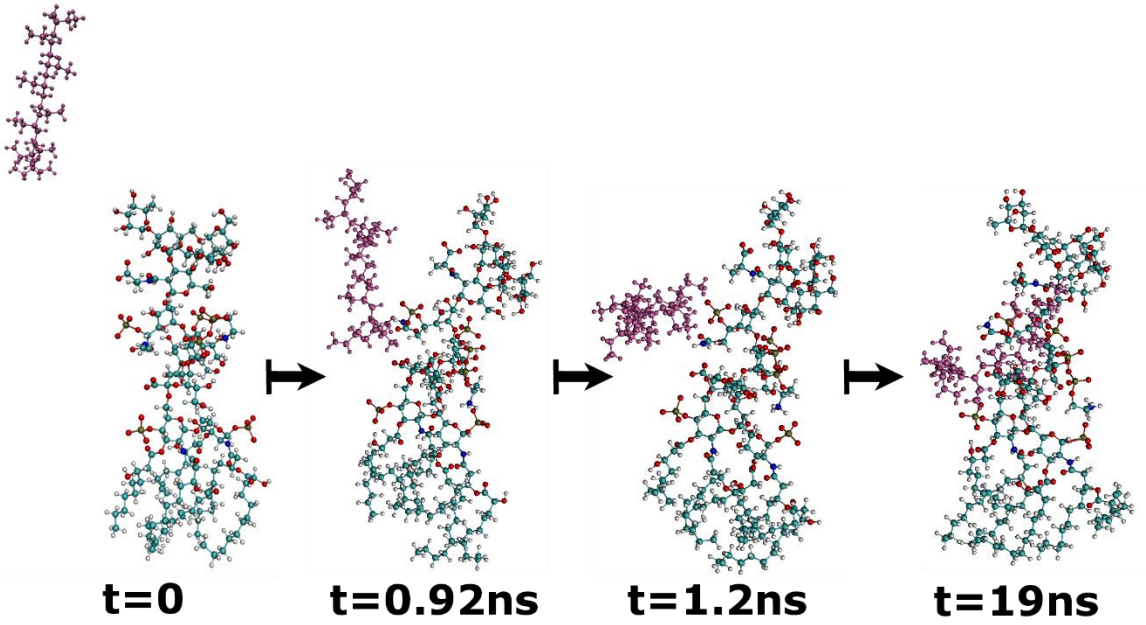

Figure 2.5. Computational simulation of the interaction of PAH with LPS. Snapshots of LPS from *P. aeruginosa* (in color-coded atoms) and PAH (with atoms in magenta) during a 19 ns simulation of the two molecules in explicit water (not shown). The PAH can be seen migrating toward the phosphate groups of the LPS.

Since the PAH molecules were seen to migrate to the phosphate units of LPS, the distance between phosphorus atoms in the *P. aeruginosa*, *E. coli*, and *S. typhimurium* LPS and the center of mass of the PAH molecule were monitored during the computational simulation. The configurations of the rough LPS structures for these three bacteria along with labeled positions for each phosphorus atom are shown in Figure 2.6. The distances between the PAH center of mass and each phosphorus atom throughout the 19 ns

simulations can also be seen in Figure 2.6. The PAH relaxes to equilibrium distances within the first 5 nanoseconds of the simulation. On average, P1 shows highest proximity to the PAH center of mass.

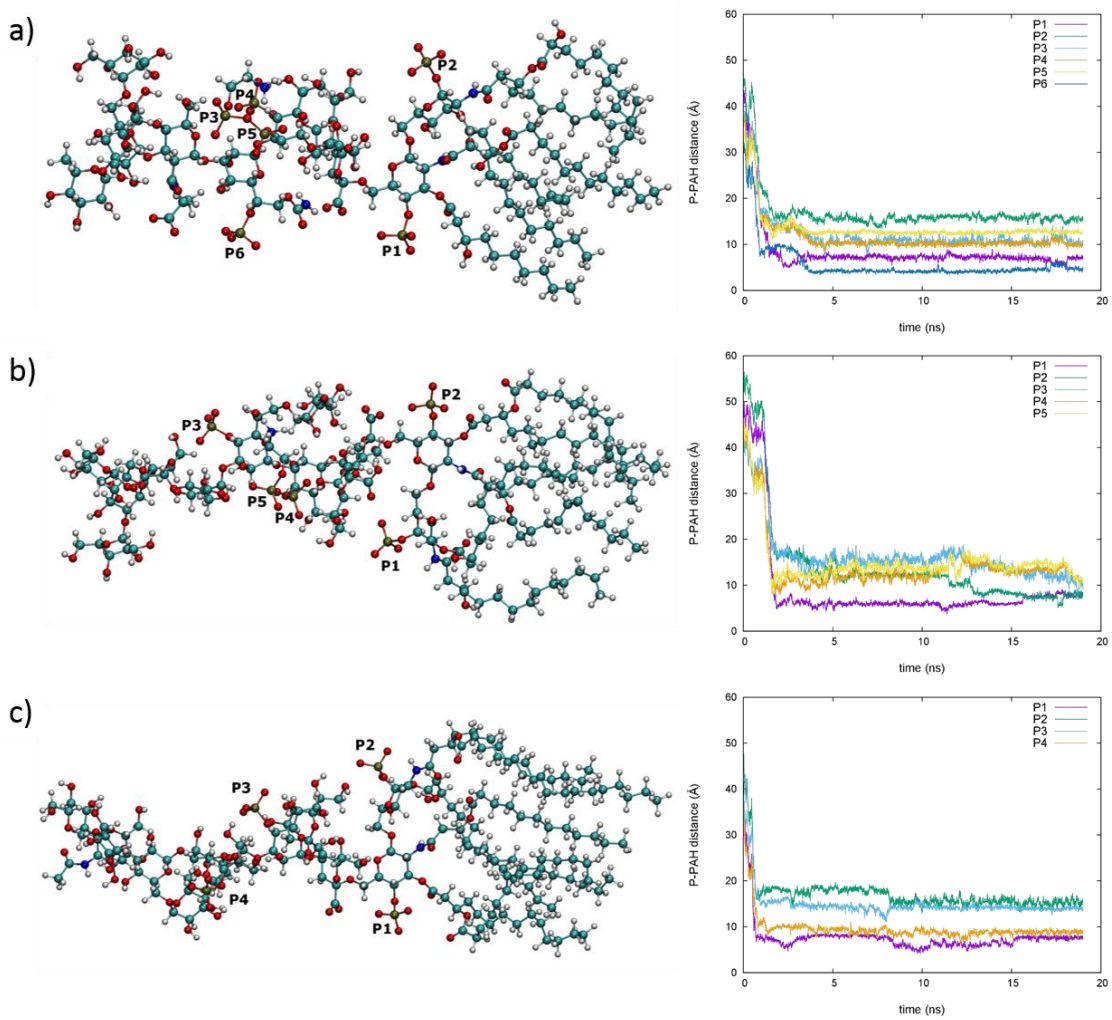

Figure 2.6. LPS structures used in simulations and distance between PAH and phosphorus atoms. Ball-and-stick renderings of representative structures (left structures) of rough LPS for a) *P. aeruginosa*, b) *E. coli*, and c) *S. typhimurium* with labeled phosphorus atoms. The distance between the PAH center of mass and the labeled phosphorus atoms in each LPS structure was monitored through 19 ns simulations (right graphs).

The electrostatic association energies of PAH with rough LPS extracted from *P. aeruginosa*, *S. typhimurium*, and *E. coli* were also monitored. The number of phosphates in the core region of the LPS from *S. typhimurium* is one unit less than that of *E. coli* and two units less than the *P. aeruginosa* LPS structure, allowing consideration of the impact of the core phosphate on association with PAH. Overall charge differences between the structures also allows for consideration of the impact of charge. The

electrostatic association energies are shown in Figure 2.7. These graphs suggest that the total charge of the LPS and the number of phosphate units are important parameters in determining PAH association. The *E. coli* LPS has one unit less total negative charge compared to that of *S. typhimurium* (Table 2.2). Consequently, we observe a slower association of PAH to *E. coli* LPS. However, the *E. coli* LPS has one phosphate unit more than the LPS of *S. typhimurium*. The combination of these two competing factors is one possible reason for the observation of nearly equal association energy values at the end of the simulations for *E. coli* and *S. typhimurium* LPS. On the other hand, the LPS of *P. aeruginosa* has a higher negative charge and more phosphate units, leading to a quicker association of PAH to LPS that is also stronger at the end of the simulation than the other two bacteria.

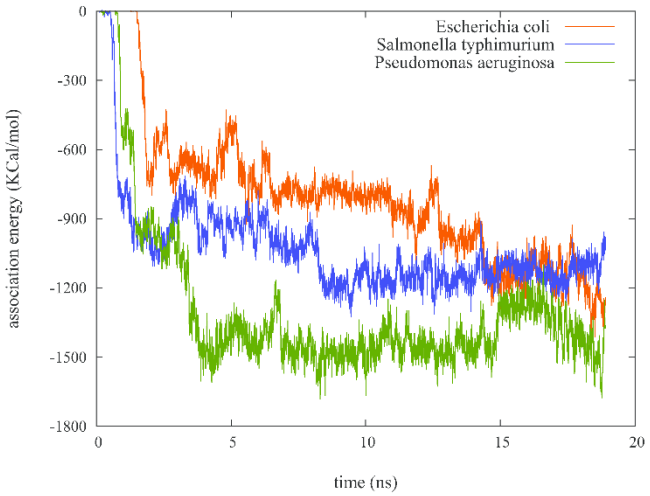

Figure 2.7. Electrostatic association energies during LPS/PAH interaction. Electrostatic energies of the LPS/PAH association during a 19 ns simulation of 10-mer PAH interacting with the rough LPS of *P. aeruginosa* (green), *E. coli* (red), and *S. typhimurium* (blue), whose structures are shown in Figure 2.6.

We also investigated the different electrostatic association energies of PAH with increasingly smooth LPS character. The degree of PAH association to the rough LPS-exhibiting *P. aeruginosa* was compared to that of a smoother construct of *P. aeruginosa* with two added O-antigen units and is shown in Figure 2.8. The LPS structure of *P. aeruginosa* with two added O-antigen units has a total charge of -14. The changes in the LPS/PAH electrostatic association energies and the distance between a selected phosphorus atom and the PAH center of mass are shown in Figure 2.8. The traces in Figure 2.8 suggest that PAH associates to the O-antigen sections of the smoother LPS molecule at early stages of the simulation and finally moves toward the phosphate units

in the core region. Moreover, the addition of two O-antigen units does not significantly slow down the overall movement of PAH towards the core region of LPS. Typically, smooth LPS has many more than the two repeats of O-antigen monomer used here. In the case of the B-band in *P. aeruginosa*, for example, there can be greater than 50 repeats. Future computational work will build toward this more complex LPS structure. Since the B-band LPS structure of *P. aeruginosa* PAO1 has many more negatively charged sites—because many of its sugars are amino-derivatized uronic acid or fucose moieties,[49]—this band is expected to offer more binding sites for cationic particles than the more hydrophobic A-band. Therefore, smooth LPS should have many more binding sites that extend further into solution than those of rough LPS. This is likely why we see more binding to the bacteria with smooth LPS in our experimental work.

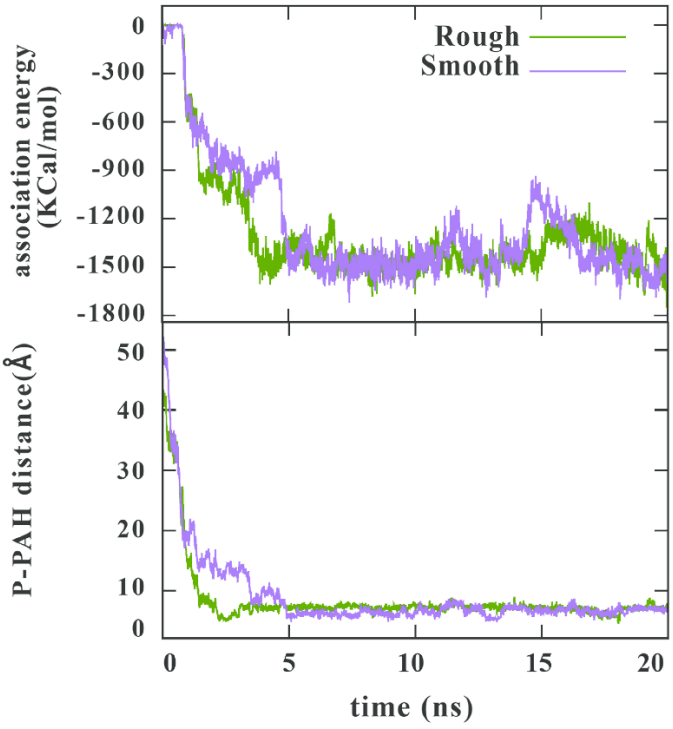

Figure 2.8. Electrostatic association energies and PAH/phosphorus distance for PAH with rough and "smoother" LPS. Electrostatic energies of the LPS/PAH association (top) and the distance between a selected phosphorus on LPS to the PAH center of mass (bottom) during a 20 ns simulation of 10-mer PAH interacting with the rough (green) and smoother (purple) LPS

constructs from *P. aeruginosa*, whose structures are shown in Figure 2.2. (Note that the electrostatic energy trace for rough LPS is recapitulated from Figure 2.7 to facilitate interpretation.)

2.5 Conclusions

This work exploits a set of bacteria that represent a diverse array of environments where nanoparticles may be released. These bacteria also have important ecological roles, making any effects felt by them impactful on overall environmental health. We demonstrated the use of this bacterial panel in monitoring the toxicity of a model nanoparticle, PAH AuNPs. While we observed increased PAH AuNP binding for bacteria with smooth LPS compared to those with rough LPS, the resulting toxicity did not follow this same trend. We expected that the toxicity observed would correlate with the binding of these NPs to the bacteria, a process mediated by the bacterium's LPS, which is the major surface structure, making up 75% of the Gram-negative bacterial surface for some bacteria.[50] In reality, the situation is more complex, which demonstrates the importance of using a bacterial panel for nanotoxicity studies. Regardless of the care in controlling for many variables, biology can introduce complexity to otherwise simple relationships.

The increased complexity of the biological panel presented here can be used for several applications. Due to the different LPS present on the surface of these bacteria, this panel is a good candidate for investigating bacterial surfaces. Indeed, the results obtained from the molecular dynamics simulation yield early insight into the interactions of polyelectrolyte-wrapped NPs with bacteria by taking the sugar sequences of the LPS into account. This panel is also good for an initial screen of nanoparticle toxicity; in using this bacterial panel, we can identify which bacteria are experiencing an effect specific to nanoparticles, which merit further investigation. While we would expect different results than those presented here if different NPs were used, this Gram-negative bacterial panel can be adapted for use with a range of nanomaterials.

Chapter 3

The Technologically Relevant Complex Oxide Battery Material, Ni-enriched NMC, has Differential Toxicity to *S. oneidensis* MR-1 and *D. magna*

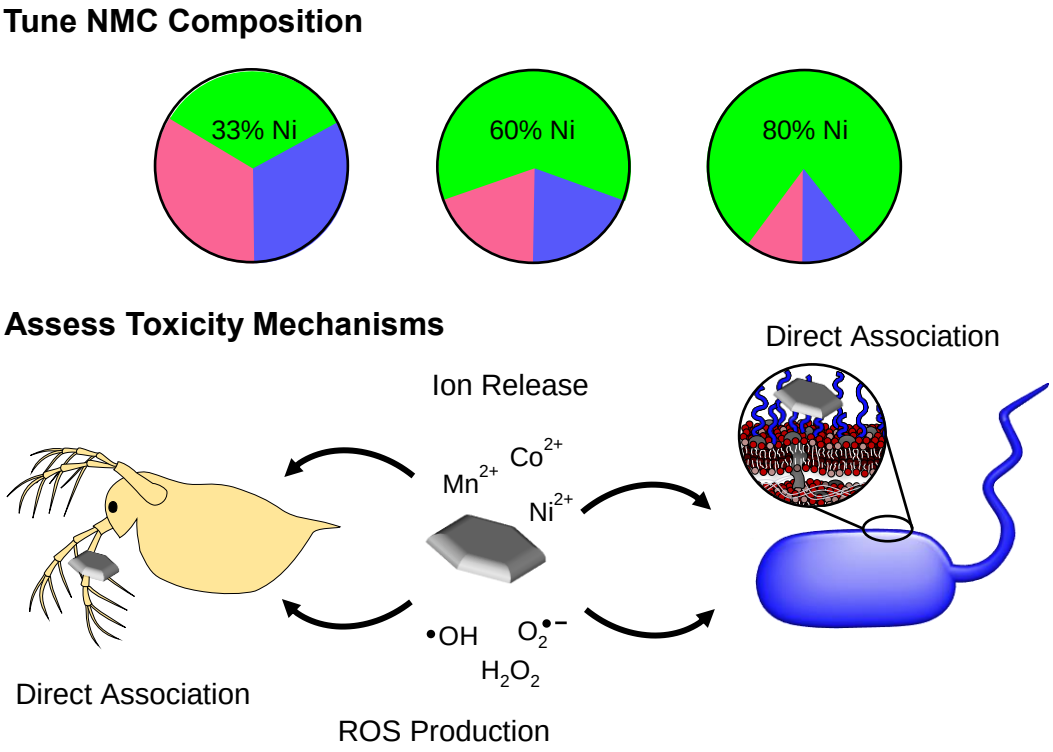

Adapted from: Buchman, J.T.; Bennett, E.A.; Bennett, J.W.; Wang, C.; Abbaspour Tamijani, A.; Hudson, B.G.; Clement, P.L.; Zhi, B.; Green, C.M.; Henke, A.H.; Laudadio, E.D.; Hamers, R.J.; Mason, S.E.; Klaper, R.D.; Haynes, C.L. The technologically relevant complex oxide battery material, Ni-enriched NMC, has differential toxicity to *S. oneidensis* MR-1 and *D. magna*. *In preparation.*

3.1 Overview

Lithium intercalation compounds, such as the complex metal oxide, lithium nickel manganese cobalt oxide, have demonstrated importance due to their utility as energy storage materials. In response to recent concerns about the global supply of cobalt, industrially-synthesized NMCs are shifting from using equal stoichiometries of nickel, manganese, and cobalt, to enriching the nickel content of these materials. However, nickel is one of the more toxic components of NMC materials, meriting investigation of the toxicity of these materials on environmentally-relevant organisms. Herein, the toxicity of both nanoscale and microscale Ni-enriched NMC to the bacterium, *Shewanella oneidensis* MR-1, and the zooplankton, *Daphnia magna*, was assessed. For the bacterium, all of these materials exhibited similar toxicity when exposed to equal surface area-based doses. Material dissolution to toxic species, namely nickel and cobalt ions, was modelled using density functional theory calculations, which showed an increase in material stability due to the Ni-enriched material containing nickel with an oxidation state >2. This increased stability means that similar dissolution is expected between Ni-enriched NMC and equistoichiometric NMC. In fact, similar dissolution to the toxic species was found in experiments, which correlates to the similar toxicity seen when *S. oneidensis* were exposed to these materials. For *D. magna*, nickel enrichment increased the observed toxicity for the nanoscale materials, while microscale materials indicated no toxicity. As in previous work, the bulk release of ions from NMC materials did not reduce the viability of *D. magna*. Different ROS profiles were noted for the materials in the bacterial and daphnid media. Nanoscale and microscale materials both associate with the surface of *S. oneidensis* whereas with *D. magna*, the nanoscale materials tended to adhere to the daphnid carapace and the microscale materials were largely ingested. This work demonstrates that for organisms where the major mode of toxicity is based on ion release, including more nickel in NMC does not impact toxicity due to increased particle stability; however, for organisms where the core composition dictates the toxicity, including more nickel in the redesign strategy may lead to greater toxicity due to NP-specific impacts on the organism.

3.2 Introduction

Complex metal oxides are used in a variety of applications, such as catalysts or as cathode materials for lithium ion batteries.[1,2] Layered lithium-intercalation compounds such as $LiCoO_2$ have long served as the primary cathode materials for lithium ion batteries.[3] In recent years, concerns about the potential global supply of cobalt has driven

increasing interest in exploring compositions that replace cobalt with nickel, manganese, and other more earth-abundant transition metals.[4] Therefore, materials of the general composition $LiNi_xMn_yCo_{1-x-y}O_2$, here referred to as "NMC," have been used because of the low cost of nickel and manganese compared with cobalt.

Increases in NMC commercialization lead to correspondingly larger manufacturing quantities and therefore increased potential for environmental release. Recent estimates predict that by 2025, worldwide manufacture of NMC materials will be between 136 kilotons/year and 330 kilotons/year, where the exact amount of nickel, manganese, and cobalt depends on the cathode stoichiometries used.[5] While many present-generation cathodes use particles with primary sizes in the micron size range, nanoscale materials have been shown to improve certain performance characteristics such as charge rate.[6–8] As a result, nanoparticulate materials are increasingly being used in both cathodes and anodes. Furthermore, even for large particles, weathering of electrodes during use leads to extensive fracturing and formation of much smaller particles, including those in the nanoparticle size regime.[9–11]

Within the family of NMC materials, the equistoichiometric composition, $LiNi_{1/3}Mn_{1/3}Co_{1/3}O_2$, sometimes referred to as "333 NMC,"[12,13] is the most stable as it perfectly balances the preferred oxidation state of all three metal ions: Ni^{2+}, Mn^{4+}, and Co^{3+}.[12,14,15] Yet, economic driving factors are leading to rapidly increased commercialization of Ni-enriched materials such as $LiNi_{0.6}Mn_{0.2}Co_{0.2}O_2$ (622 NMC) and $LiNi_{0.8}Mn_{0.1}Co_{0.1}O_2$ (811 NMC). In order to balance the oxidation states, increases in nickel concentration lead to some of the nickel being present in the 3+ and 4+ oxidation states, which are highly reactive. As a result, such Ni-enriched NMC materials are expected to show unusual reactivity when compared to 333 NMC, as high-valence cations tend to change the lattice stability.[16] If such ions are released into aqueous media, they are also able to induce reactions such as the oxidation of OH^- to $\cdot OH$, a highly potent oxidizing agent. Because of the significant changes in stability and reactivity, many studies have been devoted to understanding how these changes impact the utilization of Ni-enriched NMC materials for energy storage. However, no prior studies have investigated how such high nickel concentrations impact chemical transformations relevant to understanding the environmental impact of this class of materials.

Here, we report investigations of the impact of Ni-enriched NMC compositions on two model organisms relevant to understanding the potential environmental impact that could result from release of these materials into the environment. Both *Shewanella oneidensis*

MR-1 and *Daphnia magna* are aquatic organisms that represent different trophic levels. In this work, they are used as model organisms for assessing environmental impact, as they are ubiquitous in a range of aquatic environments, making them likely to be exposed to NMC in the event of aquatic introduction. *S. oneidensis* is capable of respiring many different metals in its environment,[17] and *D. magna* is an important component of the freshwater food web and is sensitive to many environmental pollutants.[18] Daphnids are a parthenogenetic organism and therefore maintain nearly identical genetic composition throughout a population, which makes them ideal for experimentation.

Our results show that at matching surface area-based doses, all of the NMC materials studied here had similar toxicity to our bacterial model, *S. oneidensis*. Dissolution analysis of the nanoscale materials reveals that the dissolution to ions toxic to *S. oneidensis*, namely nickel and cobalt, is similar between 333 and 622 NMC. In contrast, with *D. magna*, nickel-enriched NMC nanoparticles exhibited a higher toxicity than 333 NMC nanoparticles. This comparative work demonstrates the importance of using multiple organisms to assess environmental toxicity of a nanomaterial, and shows how the same strategy to redesign a nanomaterial can have different organismal impacts based on the nanomaterial toxicity mechanism.

3.3 Experimental

3.3.1 Materials

Nickel (II) chloride hexahydrate ($NiCl_2 \cdot 6H_2O$), magnesium chloride ($MgCl_2$), ammonium chloride (NH_4Cl), calcium chloride ($CaCl_2$), hydrogen peroxide (H_2O_2), 4′-aminophenyl fluorescein (APF), and 2′,7′-dichlorofluorescin diacetate (H_2DCF-DA) were purchased from Thermofisher Scientific (Waltham, MA). Sodium chloride (NaCl), sodium sulfate (Na_2SO_4), dibasic sodium phosphate (Na_2HPO_4), 4-(2-hydroxyethyl)-1-piperazineethanesulfonic acid (HEPES), dimethylsulfoxide (DMSO), manganese (II) nitrate tetrahydrate ($Mn(NO_3)_2 \cdot 4H_2O$), cobalt (II) nitrate hexahydrate ($Co(NO_3)_2 \cdot 6H_2O$), and lithium nitrate ($LiNO_3$) were obtained from Sigma-Aldrich (St. Louis, MO). Manganese (II) sulfate monohydrate ($MnSO_4 \cdot H_2O$), cobalt (II) chloride hexahydrate ($CoCl_2 \cdot 6H_2O$), and potassium chloride (KCl) were acquired from Mallinckrodt (St. Louis, MO). Propylene oxide and 10% glutaraldehyde in water were purchased from Electron Microscopy Sciences (Hatfield, PA). Poly/Bed® 812 resin kit was obtained from Polysciences, Inc. (Warrington, PA). A horseradish peroxidase (HRP) solution containing Triton-X and cholate, came from an amplex red kit that was acquired from Cayman Chemical (Ann Arbor, MI). Absolute ethanol was purchased from Pharmco-Aaper (Brookfield, CT).

Sodium lactate and nickel (II) nitrate hexahydrate ($Ni(NO_3)_2 \cdot 6H_2O$) were purchased from Alfa Aesar (Haverhill, MA). Lithium hydroxide monohydrate ($LiOH \cdot H_2O$) was obtained from VWR (Radnor, PA). Luria-Bertani broth and agar were purchased from BD Difco (Franklin Lakes, NJ). Commercial 333, 622, and 811 NMC (herein referred to as c333, c622, and c811 NMC) were acquired from Electrodes and More (Richardson, TX). Ultrapure water (18.2 MΩ·cm resistivity) was purified from a Milli-Q Millipore water purification system (Billerica, MA). *S. oneidensis* MR-1 BAA1096 was purchased from the American Type Culture Collection (Manassas, VA).

3.3.2 Synthesis of NMC Nanoparticles

333 NMC nanoparticles were synthesized using a two-step procedure. First, a nickel manganese cobalt hydroxide precursor was synthesized via a co-precipitation technique in which an aqueous mixture of 0.2 M $Ni(NO_3)_2 \cdot 6H_2O$, 0.2 M $Mn(NO_3)_2 \cdot 4H_2O$, and 0.2 M $Co(NO_3)_2 \cdot 6H_2O$ was added dropwise to 0.2 M LiOH under magnetic stirring. To make 622 NMC nanosheets, the following concentrations were instead used: 0.3 M $Ni(NO_3)_2 \cdot 6H_2O$, 0.1 M $Mn(NO_3)_2 \cdot 4H_2O$, and 0.1 M $Co(NO_3)_2 \cdot 6H_2O$. A dark brown precipitate of metal hydroxides was collected via repeated cycles of centrifugation (Thermo Scientific Sorvall Legend X1R centrifuge with Thermo TX-400 rotor, 4696×*g*) and resuspension in water (1×) and methanol (4×) followed by drying under vacuum at 30 °C. This metal hydroxide precursor (~500 mg) was then added to a 10 g molten flux containing 6:4 molar ratio of $LiNO_3$:LiOH at 230 °C in a high-alumina crucible. The reaction was quenched after 3 hours using ultrapure water, producing NMC with a nanosheet morphology. These nanosheets were isolated using repetitive cycles of centrifugation at 4696×*g* and resuspension in water (2×) and methanol (3×) and dried under vacuum at 30 °C. The collected pellets were ground into a fine powder using an agate mortar and pestle. These purified nanoparticles were characterized using powder X-ray diffraction (XRD), inductively coupled plasma optical emission spectrometry (ICP-OES) to determine NMC stoichiometry, scanning electron microscopy, and nitrogen physisorption prior to being used for ion release and toxicity studies.

3.3.3 Characterization of NMC Stoichiometry

To analyze the chemical composition of both synthesized 333 and 622 NMC nanosheets, a PerkinElmer 4300 Dual View inductively coupled plasma optical emission spectrometer was used. First, solid materials were completely dissolved in freshly made aqua regia (3:1 v/v mixture consisting of 37% v/v HCl and 70% v/v HNO_3; *caution: aqua regia is highly corrosive!*) through soaking overnight. Then the dissolved contents were

diluted with ultrapure water and analyzed. The standards were prepared using a certified reference solution and the blank was 2% aqua regia aqueous solution. The ion concentrations were measured using three analytical replicates.

3.3.4 Powder X-ray Diffraction (XRD)

To analyze the structure of NMC materials, a Bruker D8 Advance Powder X-ray diffractometer with a Cu Kα source was used. The NMC powder was deposited onto a SiO_2 zero diffraction plate (MTI Corporation, Richmond, CA) and smoothed out with a spatula before analysis.

3.3.5 TEM and EDS of NMC

To acquire TEM images of the samples, the stock NMC materials were suspended in ultrapure water at 500 ppm and sonicated for 10 min to ensure dispersal. Afterward, 2 µL drops were placed on a 200 mesh TEM grid made of copper with Formvar and carbon supports (Ted Pella, Inc., Redding, CA). The grids were allowed to dry overnight prior to using a FEI Tecnai T12 TEM to acquire images at an operating voltage of 120 kV.

To determine the ratio of transition metals in each NMC material, energy-dispersive X-ray spectroscopy (EDS) was used. EDS spectra for the materials were acquired with an Oxford INCAx-sight EDS that was paired with the T12 TEM. TEM was used to focus on the NMC material, and then EDS was acquired for 0-10 keV with an ultrathin window Si(Li) detector. The ratios of the transition metals in each material were determined using the atomic percentages reported by EDS.

3.3.6 Morphology Characterization using Scanning Electron Microscopy

To characterize the morphology of the 333 and 622 NMC nanosheets, a methanolic colloidal suspension of each NMC was made and drop-cast onto boron-doped Si wafers. For imaging, a Leo Supra55 VP scanning electron microscope (SEM) was used with a standard in-lens detector (3 kV incident electron energy).

3.3.7 Surface Area Measurements

The Brunauer-Emmett-Teller (BET) specific surface areas of 333 and 622 NMC nanosheets were determined using N_2 adsorption/desorption isotherms obtained from a Micromeritics Gemini VII 2390 surface area analyzer. Each sample holder (Micromeritics) was loaded with ~70 mg of powder (~100 mg were used for commercial 622 and commercial 811 NMC samples) and outgassed at 120 °C under vacuum for 1 h using a Micromeritics VacPrep 061 sample degas system. The sample was subsequently introduced into the surface area analyzer and measured over the relative pressure range (P/P_0) of 0.05−0.3, where P_0 is the saturated pressure of N_2.

3.3.8 Zeta Potential of NMC in Exposure Media

To determine the ζ-potential of NMC in the exposure media, each NMC sample was suspended in either bacterial medium or moderately hard reconstituted water at a concentration of 25 ppm. ζ-potential measurements were acquired using a Brookhaven ZetaPALS instrument.

3.3.9 Bacterial Culture Conditions

S. oneidensis MR-1 BAA1096 was stored at -80 °C until needed. Then, the bacterial suspension was streaked onto a sterile LB agar plate and incubated overnight at 30 °C. Two colonies were inoculated in LB broth and incubated for ~16 hr (300 rpm, 30 °C). The bacteria in late log phase were centrifuged at 750×*g* for 10 min and resuspended in 0.85% NaCl. They were again centrifuged (10 min, 750×*g*) and resuspended in bacterial medium (composed of 11.6 mM NaCl, 4.0 mM KCl, 1.4 mM $MgCl_2$, 2.8 mM Na_2SO_4, 2.8 mM NH_4Cl, 88.1 µM Na_2HPO_4, 50.5 µM $CaCl_2$, 10 mM HEPES, and 100 mM sodium lactate). The OD_{600} was determined and adjusted as needed.

3.3.10 Bacterial Growth-based Viability Assays

To determine the toxicity of the NMC samples to *S. oneidensis*, a previously published growth-based viability assay protocol was adapted.[19] Briefly, the OD_{600} of *S. oneidensis* in bacterial medium was adjusted to 0.1 and then exposed to 333, 622, c622, and c811 NMC at surface area-based concentrations (determined based on BET analysis) ranging from 0.18-2.8 m^2/L in a 96-well plate for 3 hours with agitation. For ion controls, bacteria were exposed to a mixture of $LiOH \cdot H_2O$, $NiCl_2 \cdot 6H_2O$, $MnSO_4 \cdot H_2O$, and $CoCl_2 \cdot 6H_2O$ so that the concentrations of each metal matched the released concentration determined by ICP-MS for each nanoparticle exposure. In parallel, a calibration curve was set up using the stock bacterial suspension and diluting 1:1 with bacterial medium to get a range from 6.25-100% viable. After exposure, 5 µL of each suspension was diluted into 195 µL of fresh LB broth and OD_{600} was measured using a Biotek Synergy™ 2 multi-mode microplate reader, taking measurements every 20 min after 30 s shaking overnight. The resulting growth curves were analyzed using the R package provided by Qiu et al. to determine the bacterial viability post-exposure.[19]

3.3.11 *Daphnia magna* Culture Maintenance

D. magna were originally acquired from Aquatic Research Organisms (Hampton, NH) and were then maintained in the lab of Dr. Rebecca Klaper at the University of Wisconsin-Milwaukee School of Freshwater Sciences following guidelines described by the US EPA. *D. magna* were kept in moderately hard reconstituted water (daphnid medium), which was

produced at 2× concentrations and diluted to 96 mg/L $NaHCO_3$, 60 mg/L $CaSO_4$, 60 mg/L $MgSO_4$, 4 mg/L of KCl, and 0.02 ml/L of $Na_2SeO_3 \cdot 5H_2O$ (added using a 330 mg/L $Na_2SeO_3 \cdot 5H_2O$ solution). Media was aerated with an air stone for 48 hours before use. The cultures were kept at a population density of 20 adult daphnids/L in an incubator at 20 °C with a 16:8 light:dark cycle. The cultures were fed three times a week using 25 mL of algae (*Raphidocelis subcapitata*, 500,000 algal cells/mL) as well as 10 mL of alfalfa (*Medigo sativa*) supernatant (prepared by suspending 8 grams in 1 L of Milli-Q water and agitating the suspension for 20 min at 130 rpm on a Thermo Scientific MaxQ 4450 orbital shaker).

3.3.12 *Daphnia magna* Acute Toxicity Assays

D. magna were exposed to five different types of NMC materials: commercially produced microscale c333, c622, and c811 NMC, as well as 333 and 622 NMC materials synthesized in the lab. To test the toxicity of released ions, *D. magna* were also exposed to a mixture of $LiOH \cdot H_2O$, $NiCl_2 \cdot 6H_2O$, $MnSO_4 \cdot H_2O$, and $CoCl_2 \cdot 6H_2O$ at concentrations equivalent to those that were determined to be released by the nanoparticles. NMC stocks were prepared by adding 2.0 mg of NMC material to Milli-Q water (40 mL) to bring the concentration to 50 mg/L. The stock was sonicated for 10 minutes immediately prior to use. *D. magna* neonates (<24 hours old) from adults aged 14-28 days were placed in 10 mL solutions (comprised of 5 mL of 2× daphnid medium, and a combination of NMC stock for desired nanoparticle concentration, and Milli-Q water). The nanoscale NMC materials were tested at concentrations ranging from 0-2.8 m^2/L, and the commercially-available, microscale NMC materials were used at concentrations ranging from 0-0.024 m^2/L (corresponding to mass-based doses ranging from 0-10 mg/L). Exposures included 4 replicates per treatment with 5 neonates per replicate, and acute toxicity tests were conducted as per OECD guideline 202 with the assays being run for 48 hours with no food supplementation during this time. Survival was recorded after 24 and 48 hours.

Images of the *D. magna* were taken on an Evos XL Core Cell Imaging System to visualize the association of NMC with the daphnids. Live *D. magna* were photographed immediately following the 48-hour exposure to the various NMC materials. Images were processed for size analysis using ImageJ software.

3.3.13 Computational Modeling of Cation Release from Ni-enriched NMC

Density functional theory (DFT) calculations[20,21] of Ni-enriched NMC surface structures use the open source software package, Quantum Espresso.[22] All atoms are represented using ultrasoft GBRV-type pseudopotentials,[23,24] and all calculations employ a plane-wave

cutoff of 40 Ry for the wavefunction and 320 Ry for the charge density. All atoms are allowed to relax during structural optimizations, and the convergence criteria for all self-consistent relaxations was a maximum residual force of 5 meV/Å per atom. Calculations are performed at the DFT-GGA level using the PBE-GGA exchange correlation functional.[25]

Ni-enriched NMC surface slabs used here include four total O-*TM*-O layers, like the NMC surfaces modeled in previous work.[26,27] In this surface slab, the two interior (bulk-like) and two exterior layers (surface) are related by inversion symmetry. The surface cells are based on a $\left[\sqrt{3} \times \sqrt{3}\right]$R30° rotated modification of the lithium cobalt oxide primitive unit cell. In order to model step-wise cation release, both Li- and H-terminated surfaces are modeled (Figure 3.1), as detailed in previous work.[26,27] In all NMC structures investigated here, surface Li are above a 3-fold hollow site and H are above an O, forming an OH bond. Each supercell surface slab has in-plane lattice dimensions of either $2\sqrt{3}\mathrm{a} \times \sqrt{3}a$ or $3\sqrt{3}\mathrm{a} \times \sqrt{3}a$, where a=2.883 Å and cells have at least 15 Å of vacuum between surface slabs. Surface relaxations employ either a 3×6×1 *k* or 2×6×1 *k*-point grid[28] for the $2\sqrt{3}\mathrm{a} \times \sqrt{3}a$ or $3\sqrt{3}\mathrm{a} \times \sqrt{3}a$ slabs, respectively. For the $2\sqrt{3}\mathrm{a} \times \sqrt{3}a$ cells, we investigate two Ni-enriched NMC compositions: $Li_xNi_{2/6}Mn_{2/6}Co_{2/6}O_2$ (33% Ni, 33% Mn, 33% Co) denoted as 333 NMC, and $Li_xNi_{4/6}Mn_{1/6}Co_{1/6}O_2$ (66% Ni, 17% Mn, 17% Co) which will be denoted as 622 NMC. Note that this is not exactly the same stoichiometry as the 622 NMC used in the exposure experiments, but since each of these has six total transition metal sites, it simplifies the calculations to list the stoichiometry based on six atoms. Because there are six total transition metal sites, release of one transition metal from the surface results in a vacancy density of 1/6 or 16.67%. For the $3\sqrt{3}\mathrm{a} \times \sqrt{3}a$ cells, we investigated two Ni-enriched NMC compositions: $Ni_{3/9}Mn_{3/9}Co_{3/9}$ (33% Ni, 33% Mn, 33% Co) denoted as 333 NMC, and $Ni_{7/9}Mn_{1/9}Co_{1/9}$ (78% Ni, 11% Mn, 11% Co) denoted as 811 NMC. Each of these has nine total transition metal sites, so release of one transition metal from the surface results in a vacancy density of 1/9 or 11.11%.

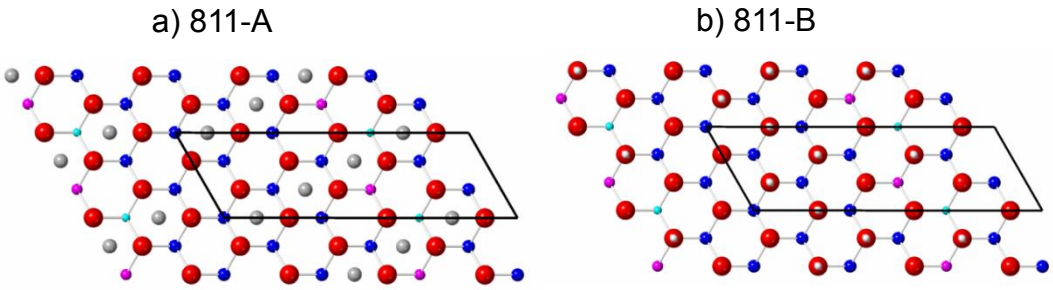

Figure 3.1. Computational models of Ni-enriched NMC surfaces with different terminations. Top-down views of representative a) Li-terminated and b) H-terminated Ni-enriched NMC surfaces. Lithium (gray) is found above a 3-fold hollow surface site and hydrogen (white) is located directly above an oxygen in the surface layer, forming an OH bond. Oxygen is red and the transition metals in the subsurface layer are depicted as follows: nickel is dark blue, manganese is magenta, and cobalt is cyan.

For the 622 NMC with six transition metal sites (622-A) and 333 NMC compositions, we investigate one distinct arrangement, and for the 811 NMC compositions, we investigate two distinct arrangements which are labeled A and B. These surfaces are shown in Figure 3.2 and form a representative set in which the oxidation state and coordination environment (via atomistic interactions such as neighboring atoms and surface terminations) can be compared. Each transition metal removed will have a subscript with the number of nickel nearest neighbors and a superscript with the number of manganese and/or cobalt nearest neighbors.

For example, removing the cobalt from 811-A with 4 nickel and 2 manganese neighbors (depicted in Figure 3.2) would be referred to as removing 811-A-$\mathrm{Co}_{4\mathrm{Ni}}^{2\mathrm{Mn}}$, and this structure is distinct from one when removing the cobalt from 811-B with 6 nickel neighbors (depicted in Figure 3.2), which would be referred to as 811-B-$\mathrm{Co}_{6\mathrm{Ni}}^{0\mathrm{Mn}}$. It should be noted that not every transition metal is removed from each Ni-enriched surface, but only a small set to map out the breadth of metal release from a complex metal oxide. The initial steps of dissolution are modeled as surface metal release by releasing a transition metal, oxygen, and hydrogen from the surface. Furthermore, it is assumed that release of any surface metal results in a change of oxidation state (caused by a delocalization of electrons) within the O-*TM*-O layer. This is because operation of Li-ion batteries relies upon oxidation/reduction response of redox active transition metals in the cathode.

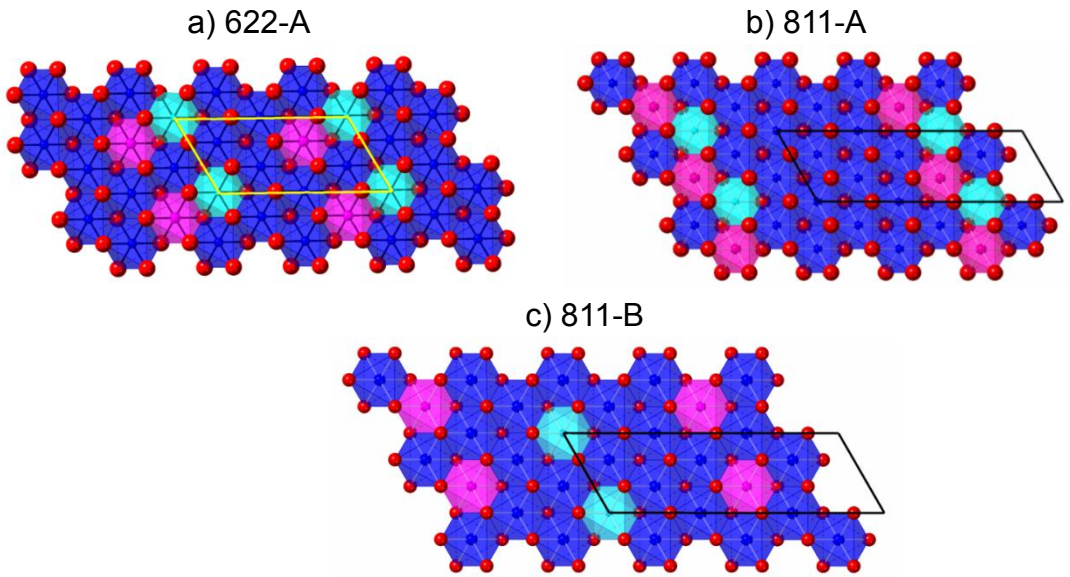

Figure 3.2. Computational models of Ni-enriched NMC surfaces with different stoichiometries. Top-down views of the a) 622 and b, c) 811 Ni-enriched NMC surfaces. The supercell slab repeat units are highlighted with yellow and black lines for the 622 and 811 compositions, respectively, to show the different size repeat units. For the 811 Ni-enriched NMC surfaces, the distance between manganese (magenta) and cobalt (cyan) octahedra is changed from b) nearest neighbor to c) manganese and cobalt separated by two nickel atoms.

To compute the thermodynamics of metal release, the change in free energy of dissolution, ΔG_{diss}, was computed using methodology that combines first-principles DFT and thermodynamics. This DFT + solvent ion method[29,30] is based on Hess's Law, where ΔG_{diss} is partitioned between the DFT-computed total energies of the reactants and products (used as ΔG_1) and experimental data (used as ΔG_2). Zero-point energy (ZPE) correction terms are added to the DFT total energies of Ni-enriched NMC slabs to obtain $\Delta G_1 = E_{products} - E_{reactants} + ZPE$, as described in the literature.[26,27] The total energies of lithium, transition metal, oxygen, and hydrogen released from the surface are for the atoms in their standard state, which implies that ΔG_1 can be used to gauge relative lattice stabilities for the overall release of a *TM*-OH unit.

The second term in the model, ΔG_2, is based on the Nernst equation, $\Delta G_2 = \Delta G^0_{SHE} - n_e e U_{SHE} - 2.303 n_{H^+} kT\, pH + kT \ln a\left(H_x AO_y^{z-}\right)$, where ΔG^0_{SHE} is the change in free energy of the aqueous cation/anion relative to the standard state, and these values are referenced to the standard hydrogen electrode (SHE). eU_{SHE} is the applied potential, relative to the SHE, and it is assumed that no external potential is applied ($eU_{SHE} = 0$). $H_x AO_y^{z-}$ are the concentrations of the released aqueous ions, and that these concentrations are 1×10^{-6} M;

this is the order of magnitude in line with measurements of released cations reported in experiment.[31,32] The n_e and n_{H^+} terms denote the number of electrons and protons involved in the chemical reactions required for surface release. The pH-independent species are Li^+, Ni^{2+}, Mn^{2+}, and Co^{2+}, and the pH-dependent species are $HCoO_2^-$, and oxygen and hydrogen, as H_2O, in the range of pH 1-9 investigated here.

The values of ΔG_{SHE}^0 used here are obtained from literature[33] and are found in Table 3.1. At conditions of $eU_{SHE} = 0$ and $a = 1 \times 10^{-6}\ M$, DFT-calculable Pourbaix diagrams[34] show that $Ni^{2+}_{(aq)}$ will be the preferred aqueous cation of nickel until ~pH 9.5 when $NiO_{(s)}$ will precipitate, $Mn^{2+}_{(aq)}$ will be dominant until ~pH 10, when $Mn_2O_{3(s)}$ or $Mn_3O_{4(s)}$ will precipitate, and $Co^{2+}_{(aq)}$ will be dominant until pH 7, where $Co^{2+}_{(aq)}$ reacts further with H_2O to produce $HCoO_2^-{}_{(aq)}$. $HCoO_2^-{}_{(aq)}$ becomes the preferred aqueous ion of cobalt at pH 7, and the dramatic change in thermodynamics of cobalt speciation, $Co^{2+}_{(aq)}$ $\left(\Delta G_{SHE}^0 = -0.563\right)$ vs. $HCoO_2^-{}_{(aq)}$ $\left(\Delta G_{SHE}^0 = -4.223\right)$, will be present as a discontinuity at pH 7.

One of the main objectives of this work is to investigate the release of metals from Ni-enriched NMC materials for a range of environmentally relevant conditions. Choosing a wide pH range allows for release comparisons of divalent transition metal cation species Ni^{2+}, Mn^{2+}, and Co^{2+} in many diverse aquatic environments. Example calculations of ΔG_{diss} from NMC materials are presented in the supplemental materials of previous work.[26,27]

Table 3.1. ΔG_2 for each aqueous species used in the surface metal release of Ni-enriched NMC. The values of ΔG_{SHE}^0 are taken from previous work[33] and converted to eV. For all calculations presented in this chapter, U_{SHE} is 0 and the concentration of each species, $a_{H_xAO_y^{z-}}$, is assumed to be 1×10^{-6} M.

Element	Aqueous Species	$\Delta G_{SHE}^0\ (eV)$	$\Delta G_2\ (eV)$
Li	Li^+	-3.039	$-1eU_{SHE} + 0.0257lna_{Li^+} - 3.039$
Ni	Ni^{2+}	-0.472	$-2eU_{SHE} + 0.0257lna_{Ni^{2+}} - 0.472$
Mn	Mn^{2+}	-2.363	$-2eU_{SHE} + 0.0257lna_{Mn^{2+}} - 2.363$
Co	Co^{2+}	-0.563	$-2eU_{SHE} + 0.0257lna_{Co^{2+}} - 0.563$
Co	$HCoO_2^-$	-4.223	$-2eU_{SHE} - 0.177pH + 0.0257lna_{HCoO_2^-} - 4.223$
O	H_2O	0	$2eU_{SHE} + 0.118pH$
H	H_2O	0	$-0.059pH$

3.3.14 Ion Dissolution from NMC in Exposure Medium

To empirically measure dissolution from the NMC materials in bacterial medium, the NPs were suspended in bacterial medium so that their surface area-based concentrations

ranged from 0.18-2.8 m^2/L and were agitated over the course of 3 hours. For measurements in daphnid medium, the NPs were suspended in glass vials (concentrations ranging from 0.11-2.8 m^2/L), and kept at 20 °C for 48 hours. After the exposure times for each media, the majority of the materials were removed by centrifugation at 4696×*g* for 30 min using a Beckman Coulter Allegra® X-15R centrifuge. The supernatant was then transferred to an ultracentrifuge tube and centrifuged at 286,000×*g* for one hour in an SW 55 Ti rotor on a Beckman Coulter Optima™ L-100K Ultracentrifuge. To verify that the NMC material had sedimented, and was therefore not present in the supernatant, dynamic light scattering (Brookhaven Instruments ZetaPALS zeta potential analyzer) was used. The bacterial medium supernatants were then diluted 10-fold and analyzed with a Thermo Scientific Xseries-2 ICP-MS. The supernatants from the daphnid medium were analyzed with a Thermo Scientific Element XR ICP-MS without dilution.

3.3.15 Abiotic ROS Determination for 333 and 622 NMC Nanosheets

To measure abiotic production of reactive oxygen species from 333 and 622 NMC in both bacterial medium and daphnid medium, a previously published method was utilized.[35,36] In this procedure, two fluorescent probes were employed: 3′-aminophenyl fluorescein (APF), which measures hydroxyl radical generation, and 2′,7′-dichlorofluorescin diacetate (H_2DCF-DA), which measures overall ROS production. The dyes have excitation and emission wavelengths of 495 nm/525 nm and 500 nm/530 nm, respectively. To first deacetylate the H_2DCF-DA prior to exposing to NMC, it was diluted by mixing 20 mM of H_2DCF-DA in anhydrous DMSO in a 1:1 ratio with 0.1 M NaOH in appropriate media and letting it sit in the dark for 30 minutes. To prepare working solutions of the dyes, APF (at 5 mM in DMF) and the base-treated H_2DCF-DA were diluted 50-fold and 100-fold, respectively, to achieve 100 µM solutions in media. Horseradish peroxidase (HRP) was prepared by doing a 100-fold dilution of the 1300 U/mL HRP stock into medium. An 88 µM stock of H_2O_2 in medium was also prepared beforehand. To their respective wells, combinations of the following were added, in this order, to give 100 µL per exposure: appropriate medium, 10 µL of dye working solution, 10 µL of 2.8 m^2/L 333 or 622 NMC suspension, 10 µL of HRP solution, and 10 µL of H_2O_2 solution. The combinations were as follows: i. negative control (dye, medium); ii. positive control (dye, HRP, H_2O_2, medium); iii. partial positive control #1 (dye, HRP, medium); iv. partial positive control #2 (dye, H_2O_2, medium); v. NMC exposure (dye, NMC, medium); and vi. NMC positive control interference check (dye, NMC, HRP, H_2O_2, medium). The exposures were done for

3 hours prior to reading optical density at 600 nm and fluorescence at the appropriate excitation/emission wavelengths.

3.3.16 NMC Association to *S. oneidensis* MR-1 using TEM and Hyperspectral Imaging

To take TEM images of the bacteria that had been exposed to NMC, the NMC-exposed bacterial samples were embedded in an epoxy resin using an adapted method.[32,37] Briefly, the bacteria were adjusted to an optical density of 0.8 in bacterial media and then exposed to 333, 622, c622, and c811 NMC at 12.5 ppm for 60 minutes on a nutating mixer. The cells were then washed in 0.1 M cacodylate buffer three times prior to being fixed for 50 minutes in 2.5% glutaraldehyde in 0.1 M cacodylate buffer; the pellet was flipped after 25 min to ensure complete fixation. Afterward, the pellet was again washed three times (without resuspension) in 0.1 M cacodylate buffer.

The bacteria were then dehydrated, washing for 5 min each with ethanol at increasing % v/v (30%, 50%, 70%, 80%, 95%, and 100% ethanol in water). Propylene oxide was used to rinse three times, and then the pellet was incubated uncovered at room temperature for 2 hours with a 2:1 propylene oxide:resin mix (samples were covered for subsequent incubations). Incubation with a 1:1 propylene oxide:resin mixture was then performed overnight, which was replaced with fresh 1:1 propylene oxide:resin for 4 hours. The pellet was then incubated with pure resin overnight. This was then replaced with fresh resin and then the samples were incubated at 40 °C for 24 hours followed by incubation at 60 °C for 48 hours. A LEICA EM UC6 ultramicrotome was used to cut the samples into ~70-nm-thick sections, which were then stained with uranyl acetate and lead citrate for improved contrast. The sections were placed on 200 mesh copper grids that have Formvar and carbon supports (TedPella Inc, Redding, CA); images were acquired with a Tecnai T12 transmission electron microscope at an operating voltage of 120 kV.

The association between *Shewanella oneidensis* MR-1 and various NMC battery materials was also analyzed using CytoViva enhanced dark-field microscopy and hyperspectral microscopy (CytoViva Inc., Auburn, AL). The entire system is composed of an upright optical microscope (Olympus BX43), a visible-near infrared CytoViva hyperspectral imaging system, and a halogen light source. Reference samples are a bacterial culture suspension in bacterial medium (OD_{600}=0.60) and NMC suspensions in water (25 mg/L 333 NMC, 25 mg/L 622 NMC, 2.6 mg/mL c622 NMC, and 1.5 mg/mL c811 NMC), which were used for spectral library construction. Samples that were subject to hyperspectral mapping were bacterial suspensions that had been exposed for 1 h to

different NMC materials. To mount the specimen, live bacterial exposure suspensions were drop-cast (~3 µL) onto a glass slide and then sealed with a coverslip. Slides were examined under 100x magnification in dark-field mode and subsequent line-by-line hyperspectral scanning (ENVI 4.8 software) was performed using 60-80% light source intensity and 0.25 s exposure time per line (696 lines in total for a typical full scan). Each pixel of the hyperspectral image (i.e., 3D datacube) contains its spatial information (x and y) and corresponding reflectance spectral data (z). Analysis of hyperspectral data (mapping) was performed using Spectral Angle Mapper Classification (SAM), which automatically compared the hyperspectral data of NMC-exposed bacteria to the reference libraries and identified different components. Pixels in the images that matched the reference libraries were pseudo-colored in red (*S. oneidensis*) and green (NMC materials).

3.4 Results and Discussion

3.4.1 Synthesis and Characterization of NMC Materials

After synthesis of the NMC nanoparticles, their stoichiometry was measured by dissolving the nanoparticles and quantifying the amount of each element using ICP-OES. This showed the composition of the 333 NMC nanoparticles to be $Li_{0.63}Ni_{0.34}Mn_{0.33}Co_{0.33}O_2$ and the 622 NMC nanoparticles to be $Li_{0.31}Ni_{0.60}Mn_{0.20}Co_{0.20}O_2$, which meets the expected transition metal stoichiometries for these materials. EDS corroborates the stoichiometries observed for the nanoparticles and shows the expected stoichiometries for the commercial samples as well. From EDS, we see the following stoichiometries for 333 NMC, 622 NMC, c622 NMC, and c811 NMC: $Li_xNi_{0.29}Mn_{0.37}Co_{0.34}O_2$, $Li_xNi_{0.59}Mn_{0.21}Co_{0.20}O_2$, $Li_xNi_{0.57}Mn_{0.19}Co_{0.23}O_2$, and $Li_xNi_{0.78}Mn_{0.12}Co_{0.10}O_2$, respectively; note that lithium was not quantified due to limitations of EDS.[18] Both TEM and SEM images of the nanosheets depict the sheet-like morphology of these materials and that there is a range of sizes present in each sample. From TEM of the commercial NMC materials, it can be seen that the size of the particles is on the microscale. The surface areas of the nanoparticles were determined to be very similar, with 333 NMC and 622 NMC having surface areas of 114.0 m^2/g and 107.3 m^2/g, respectively. Being microscale materials, the commercial NMC samples had much lower surface areas, with c622 NMC being 0.536 m^2/g and c811 NMC at 0.956 m^2/g. These surface areas were used to inform the surface-area based dosing of NMC to *S. oneidensis* MR-1 and *D. magna*. ζ-potential measurements revealed that the nanoscale materials exhibited a less negative surface charge in both bacterial medium and in daphnid medium (Table 3.2) than the microscale materials.

Table 3.2. Zeta potential measured for the different NMC compositions in bacterial medium and daphnid medium.

	Zeta Potential (mV)			
NMC Type	**333**	**622**	**c622**	**c811**
Bacterial medium	-13 ± 3	-12 ± 1	-21 ± 3	-23 ± 1
Daphnid medium	0 ± 5	-1 ± 3	-14 ± 6	-15 ± 2

3.4.2 Toxicity of NMC Materials to *S. oneidensis* MR-1

To analyze the toxicity of NMC to *S. oneidensis*, the bacteria were exposed to the material for 3 h, and then viability was measured using a growth-based viability assay. Throughout the exposure, the samples were shaken to keep the nanoparticles and bacteria in suspension, but no effort was made to control the aggregation state of the NMC, as aggregation is expected in environmental settings. Unexpectedly, both the nanomaterials and microscale materials demonstrated similar toxicity to *S. oneidensis*, regardless of nickel content (Figure 3.3). It was expected that, since nickel and cobalt are the main contributors of NMC toxicity to these bacteria, there would be more nickel available from the Ni-enriched NMC materials and they would therefore exhibit an increased toxicity. These results prompted further investigation of the dissolution behaviors of NMC of different compositions.

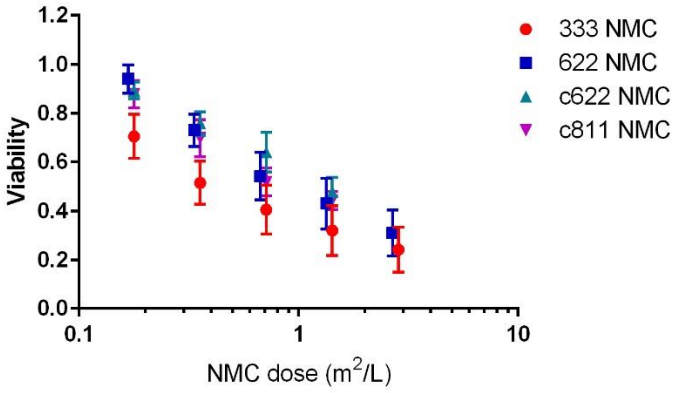

Figure 3.3. Toxicity of NMC to *S. oneidensis*. Surface area-based dosing of NMC materials to *S. oneidensis* demonstrates that toxicity of equistoichiometric and Ni-enriched NMC materials is similar. The error bars represent the standard error of seven replicates (nanoscale materials) or three replicates (microscale materials). To test for statistical significance, a one-way ANOVA with Tukey's multiple comparisons test was used on calculated LD50 values for each material.

3.4.3 Toxicity of NMC Materials to *D. magna*

Where the major toxicity mechanism of NMC to *S. oneidensis* is in its release of toxic ions, toxicity in *D. magna* has been shown to be nanoparticle-specific. To test the acute

toxicity of Ni-enriched NMC, daphnids were exposed for 48 hours, and survival at 0, 24, and 48 hours was assessed (Figure 3.4). For the nanoscale materials, it can be seen that daphnid survival is significantly reduced for 333 NMC at 1.1 and 2.8 m^2/L and for 622 NMC at 0.11, 1.1, and 2.7 m^2/L. Given that a lower dose of 622 NMC is required to exhibit toxicity, these results indicate that the 622 NMC is more toxic than 333 NMC to *D. magna*.

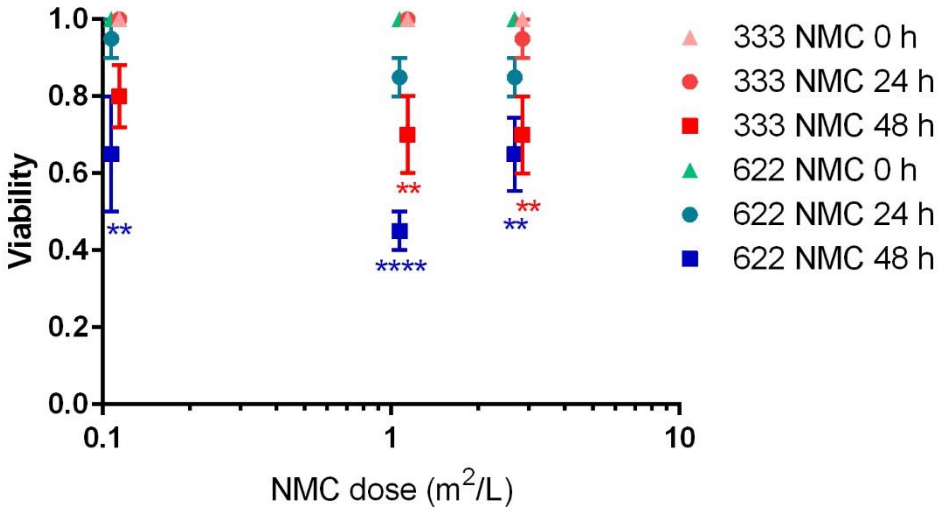

Figure 3.4. Ni-enriched NMC displays a higher toxicity to *D. magna*. Assessment of daphnid survival after 0, 24, and 48 hours of exposure to 333 NMC and 622 NMC. The error bars in these graphs represent the standard error from four exposure replicates. The error bars are not visible for the data points where all daphnids survived exposure. Two-way ANOVA was used to assess the statistical significance between each treatment and the negative control. **p<0.01, ****p<0.0001

Practical limitations precluded the use of commercial, microscale materials at matching surface area doses to daphnids because the low surface area would require large masses of commercial NMC to be suspended in solution, therefore these materials were used at matching mass-based doses to the nanoscale materials. At equivalent mass-based doses, there was no toxicity observed from any of the commercially available, microscale materials (Figure 3.5). In previous work, it was noted that the actual NPs have an impact on daphnids rather than the ion dissolution from the NPs, which explains why even though these materials have similar dissolution profiles, 622 NMC is exhibiting higher toxicity to *D. magna*. Furthermore, *D. magna* is more sensitive to nickel and cobalt than to manganese,[38] and it therefore makes sense that Ni-enriched NMC would be more toxic.

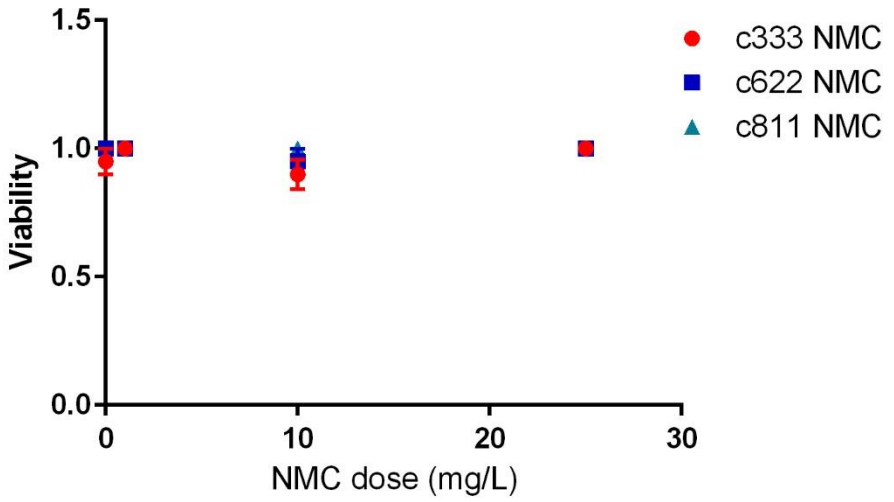

Figure 3.5. Toxicity of commercial NMC materials to *D. magna*. Assessment of daphnid survival after 48 hours of exposure to commercial 333 NMC, commercial 622 NMC, and commercial 811 NMC. None of the commercial NMC materials were found to be toxic to the daphnids with a two-way ANOVA. The error bars in these graphs represent the standard error from four exposure replicates. The error bars are not visible for some data points due to all of the daphnids surviving the exposure.

3.4.4 Cation Release from Ni-enriched NMC

Here we discuss computationally predicted metal release trends from the surface, using the ΔG_{diss} values in Table 3.3. In general, the metal release rates observed experimentally correlate to the trends in ΔG_{diss}, where the order is Ni>Co>Mn. Also, ΔG_{diss} increases (toward positive values) as the percent of released metal increases from 11.11 to 16.67%. This indicates that the surface release may not be energetically favorable above a certain *TM*-OH vacancy threshold. The data in Table 3.3 show that for nickel, cobalt, and manganese, release of 11.11% of the surface metal at pH 6 is thermodynamically favored, but at 16.67%, only nickel is predicted to be released.

Table 3.3. ΔG_{diss} at pH 6 for nickel, cobalt, and manganese at different surface vacancy concentrations.

Cation	% Vacancy	ΔG (eV)
811-A-$Ni_{6Ni}^{0Mn-0Co}$	11.11	-2.97
811-B-$Ni_{4Ni}^{2Mn-0Co}$	11.11	-2.82
811-A-$Ni_{3Ni}^{2Mn-1Co}$	11.11	-2.64
811-B-$Ni_{5Ni}^{0Mn-1Co}$	11.11	-2.47
333-A-$Ni_{0Ni}^{3Mn-3Co}$	11.11	-2.11
622-A-$Ni_{4Ni}^{1Mn-1Co}$	16.67	-1.32
333-A-$Ni_{0Ni}^{3Mn-3Co}$	16.67	-1.24
622-A-$Ni_{4Ni}^{2Mn-0Co}$	16.67	-0.88
622-A-$Ni_{2Ni}^{2Mn-2Co}$	16.67	-0.04
811-A-Co_{4Ni}^{2Mn}	11.11	-2.19
811-B-Co_{6Ni}^{0Mn}	11.11	-1.51
333-A-Co_{3Ni}^{3Mn}	11.11	-1.39
622-A-Co_{5Ni}^{1Mn}	16.67	0.10
333-A-Co_{3Ni}^{3Mn}	16.67	-0.16
811-A-Mn_{4Ni}^{2Co}	11.11	-1.46
811-B-Mn_{6Ni}^{0Co}	11.11	-1.43
333-A-Mn_{3Ni}^{3Co}	11.11	-0.57
622-A-Mn_{5Ni}^{1Co}	16.67	0.46
333-A-Mn_{3Ni}^{3Co}	16.67	0.97

Turning our attention to metal specific trends, we find that nickel release (at 11.11% surface vacancy) tracks as a function of the number of cobalt neighbors across both the 811 and 333 surfaces. The more cobalt neighbors about nickel, the more tightly they hold onto nickel. At 16.67%, both nickel release values are still negative, but smaller in size, and within 0.1 eV of each other. This indicates that at the higher surface vacancy concentration, compositions with 33-66% nickel may exhibit similar nickel release. To illustrate this, we calculate the maximum differences in ΔG_{diss} for each surface vacancy concentration. For 11.11% nickel surface vacancies, for compositions that started with 78 or 33% nickel, this number is 0.80 eV. At 16.67% nickel surface vacancy density, for

compositions with 66 or 33% nickel, it is 0.08 eV, or one-tenth the value at lower vacancy density. For cobalt and manganese release at 11.11% surface vacancy density, these numbers are 0.80 and 0.89 eV, respectively, and release at 16.67% is predicted to be thermodynamically unfavorable. The variation in ΔG_{diss} across all compositions at 11.11% surface vacancy density is similar, meaning that the Ni>Co>Mn trend in release is upheld at lower surface vacancy densities, but as the metals are released, only nickel is predicted to continue release beyond 16.67%. The thermodynamics of metal release follow the previously observed incongruent dissolution.[31,32]

While the two media used in this study have different compositions, they both have similar, slightly alkaline pHs. However, the pH-dependent release of transition metals from NMC was investigated to provide insight about how aqueous conditions affect cation release. In general, we find that for the nickel, manganese, and cobalt pH-dependent release profiles in Figure 3.6, ΔG_{diss} values track as Ni>Co>Mn, and that ΔG_{diss} of 1/9 transition metal release (11.11% surface vacancy density) is more negative than for 1/6 transition metal release (16.67%). In these plots, the dotted black line indicates $\Delta G_{diss}=0$, as release is predicted to be thermodynamically unfavorable for $\Delta G>0$. We compute that for almost all removed transition metals, ΔG_{diss} of the Ni-enriched NMC are lower than for equistoichiometric NMC, which are shown as the dashed lines in Figure 3.6. This is caused by increasing the amount of nickel from 33 to 66 or 78%, relative to the amount of manganese and cobalt; in Ni-enriched NMC configurations, there is an interruption of the cation identity and oxidation states that are found in the perfectly alternating 333 NMC configurations. The perturbations to chemical environment, via changing the identity of the neighboring cations, is most evident for ΔG_{diss} values corresponding to 1/9 transition metal release. All solid lines (corresponding to 1/9 transition metal release) in Figure 3.6 are lower than the dashed lines for 333 NMC. In these plots, nickel and cobalt display large variations in ΔG_{diss}, pointing towards a dependence of chemical environment on metal release, while manganese seems insensitive. The ΔG_{diss} vs. pH plot for manganese shows two lines that almost overlap, while for nickel and cobalt, there are multiple solid lines with different ΔG_{diss} at the same pH.

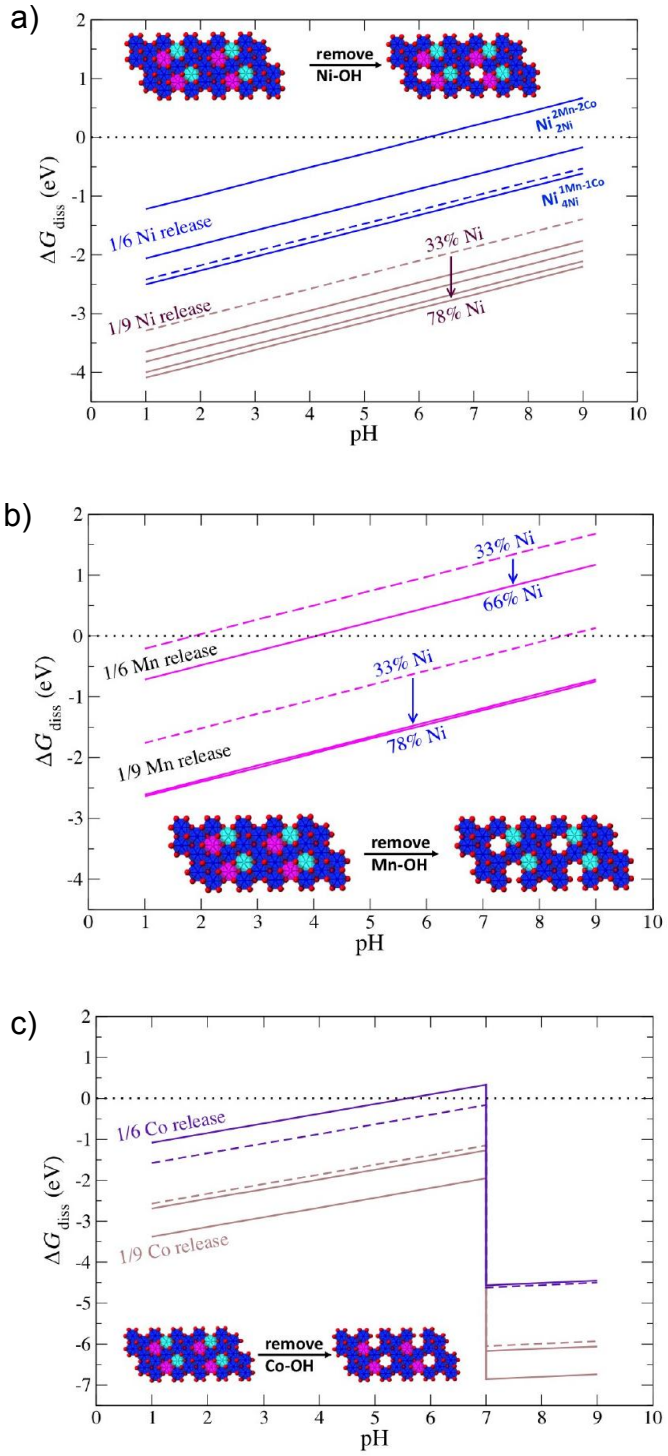

Figure 3.6. Theoretical calculations compute the release of ions from NMC. pH-dependent release profiles of a) nickel, b) manganese, and c) cobalt from NMC supercell surface slabs. Dashed lines refer to cation release from 333 NMC and solid lines refer to cation release from Ni-enriched NMC compositions. The dotted black line indicates ΔG_{diss}=0.

There are three exceptions to ΔG_{diss} of the Ni-enriched NMC being lower than for equistoichiometric NMC, and they all occur for 1/6 transition metal release. The specific cations are 622-A-$\mathrm{Ni}_{2\mathrm{Ni}}^{2\mathrm{Mn}-2\mathrm{Co}}$, 622-A-$\mathrm{Ni}_{4\mathrm{Ni}}^{1\mathrm{Mn}-1\mathrm{Co}}$, and 622-A-$\mathrm{Co}_{5\mathrm{Ni}}^{1\mathrm{Mn}}$, which have at least 1/3 nickel neighbors. One reason for the switch in transition metal release trend for these cations could be that before removal, the nickel behaves more like a Ni^{4+} than Ni^{2+}, and that 622-A-$\mathrm{Co}_{5\mathrm{Ni}}^{1\mathrm{Mn}}$ is one of its neighbors. Release of any transition metal with a 4+ oxidation state will be less energetically favorable than for a transition metal in the 2+ oxidation state, because the aqueous stable transition metal species are all 2+, and higher oxidation states (3+, 4+) will require a reduction step to be released in solution as aqueous cations.

The DFT total charge density is decomposed into atomic contributions using a projected density of states (PDOS) analysis. The PDOS of the 622-A surface slab shows that nickel exists in a range of oxidation states, and we find that the range of oxidation states can be correlated to the ease of metal release. Figure 3.7 is the PDOS of surface nickel and can be used as a guide to determine the redox properties of specific nickel. For all four surface nickel PDOS, the spin-up peaks, shown as green curves both above and below the Fermi level (E_F, dashed line) remain almost constant. The spin-down peaks, blue curves, evolve as a function of oxidation state. On the far right, they are found only below E_F, consistent with a $3d^8$ Ni^{2+} cation. As one goes from right to left, the blue peaks cross E_F, indicating an increase in oxidation state as nickel loses electrons in the filled spin-down state. The crystal field split diagrams at the bottom of Figure 3.7 are color coded to illustrate the differences in spin population of surface nickel in Ni-enriched NMC for Ni^{2+} and Ni^{3+}. The highest oxidation state observed is on the far left, where nickel is oxidizing further and is more like a Ni^{4+}. A consequence of the range of oxidation states found in Ni-enriched NMC is that the surface states will be metallic.

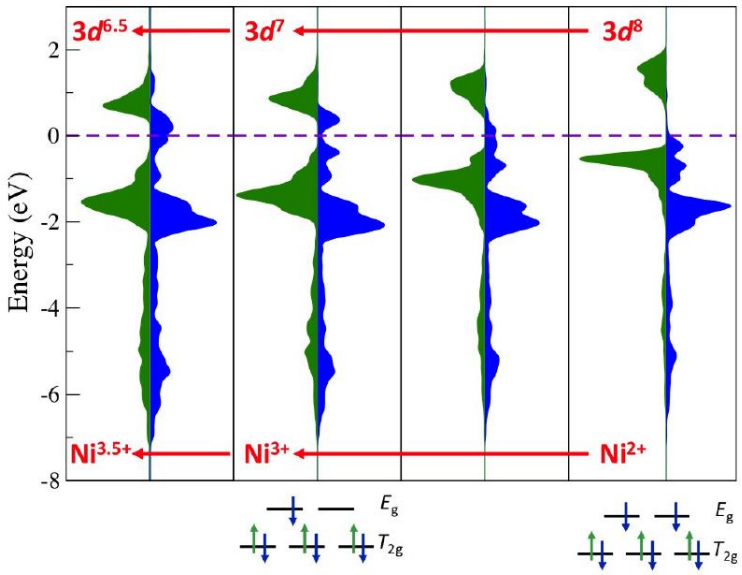

Figure 3.7. PDOS of surface nickel in the 622-A supercell surface slabs shows distinct nickel oxidation states. Nickel species are, from left to right, $Ni_{2Ni}^{2Mn-2Co}$, $Ni_{4Ni}^{2Mn-0Co}$, $Ni_{4Ni}^{2Mn-0Co}$, and $Ni_{4Ni}^{1Mn-1Co}$. Spin-up electrons are green, spin-down electrons are blue, and the Fermi level (E_F) is a dashed purple line set to 0 eV. Crystal field split diagrams are used to illustrate how the PDOS can be used to assign nickel oxidation states.

These theoretical insights correlate well with what is seen in our experimental dissolution studies. Ion dissolution was measured in bacterial medium after 3 hours by removing NMC and then running ICP-MS analysis on the supernatant. As predicted by the calculations of ΔG_{diss}, these materials exhibited a transition metal release rate trend of Ni>Co>Mn (Table 3.4). Even though 622 NMC has double the nickel content of 333 NMC, only a slightly higher nickel release by 622 NMC (44.3 µM vs. 37 µM for the highest NMC dose) is observed, likely due to the increased stability imparted by nickel being in a higher oxidation state in Ni-enriched NMC, as was determined by theoretical calculations. A reduction in cobalt release was observed in 622 NMC (11.02 µM vs. 19.1 µM for the highest NMC dose) compared to 333 NMC. Given that nickel and cobalt have been identified as major players in NMC toxicity,[31] it is worth noting that the sum of released nickel and cobalt is essentially the same for 333 and 622 NMC. Both 333 and 622 NMC released similar concentrations of manganese after 3 h, which for the highest NMC dose were 8.5 µM and 6.52 µM manganese, respectively. While overall dissolution is much lower in daphnid medium, these trends mostly hold true in this medium as well. For the highest dose of NMC used, the sum of nickel and cobalt dissolution is higher for 622 NMC than for 333 NMC (Table 3.5).

Table 3.4. Release of ionic species from NMC nanoparticles into bacterial medium as revealed by ICP-MS. ICP-MS analysis reveals the release of lithium, nickel, manganese, and cobalt from 333 and 622 NMC nanosheets after 3 hours in bacterial medium. The error represents the standard deviations from three analytical replicates collected for each condition.

	NMC type							
	333				622			
[NMC] (m^2/L)	Li (μM)	Mn (μM)	Co (μM)	Ni (μM)	Li (μM)	Mn (μM)	Co (μM)	Ni (μM)
2.8	100 ± 3	8.5 ± 0.4	19.1 ± 0.7	37 ± 2	57 ± 2	6.52 ± 0.03	11.02 ± 0.05	44.3 ± 0.3
1.4	50 ± 2	5.4 ± 0.1	10.7 ± 0.2	19.9 ± 0.1	29 ± 1	5 ± 1	6.1 ± 0.2	24.0 ± 0.9
0.71	25 ± 3	3.1 ± 0.2	5.6 ± 0.2	10 ± 1	14.4 ± 0.8	2.2 ± 0.1	3.2 ± 0.2	12 ± 1
0.36	12.7 ± 0.7	1.74 ± 0.09	3.0 ± 0.2	5.2 ± 0.5	7.9 ± 0.9	1.2 ± 0.3	1.5 ± 0.3	6 ± 1
0.18	6.5 ± 0.7	0.99 ± 0.04	1.59 ± 0.09	2.7 ± 0.2	4.43 ± 0.07	0.7 ± 0.2	0.8 ± 0.2	4 ± 2

Table 3.5. Release of ionic species from NMC NPs into daphnid medium. This shows the order of release from the transition metals is Ni>Co>Mn. The error arises from standard deviations of three analytical replicates.

	NMC type							
	333				622			
[NMC] (m^2/L)	Li (μM)	Mn (μM)	Co (μM)	Ni (μM)	Li (μM)	Mn (μM)	Co (μM)	Ni (μM)
2.8	115 ± 3	0.03 ± 0.03	0.10 ± 0.03	1.7 ± 0.3	34 ± 2	-0.003 ± 0.001	0.007 ± 0.004	2.3 ± 0.4
1.1	44 ± 3	0.000 ± 0.002	0.17 ± 0.01	1.4 ± 0.1	13.0 ± 0.5	0.000 ± 0.006	0.016 ± 0.007	1.7 ± 0.2
0.11	4.2 ± 0.8	0.003 ± 0.002	0.101 ± 0.008	0.29 ± 0.04	1.258 ± 0.008	-0.001 ± 0.004	0.023 ± 0.002	0.31 ± 0.02

3.4.5 Toxicity of Released Ions from NMC Nanomaterials

To assess the toxicity of the ions that are released over the course of bacterial exposure to NMC, the bacteria were exposed to the same concentration of ions as determined by ICP-MS for 3 h, and viability was again measured using a growth-based viability assay. Toxicity of ions to *D. magna* was evaluated using ICP-MS data for the 48-hour exposure period in daphnid medium. Toxicity from the released ions recapitulated the toxicity observed with the nanomaterials themselves for the bacteria (Figure 3.8). This implicates the ions as a major source of toxicity of the nanomaterials to bacterial species, which is consistent with previous work.[31] Given that the total concentration of nickel and cobalt released from 333 and 622 NMC was similar, this also suggests that the two ions have an equal role in the toxicity of the material to *S. oneidensis*. Nickel and cobalt toxicity to organisms is mainly due to their ability to either generate reactive oxygen species or to

interfere with important enzymes via several mechanisms,[39,40] and both of these could be contributing factors to the observed toxicity.

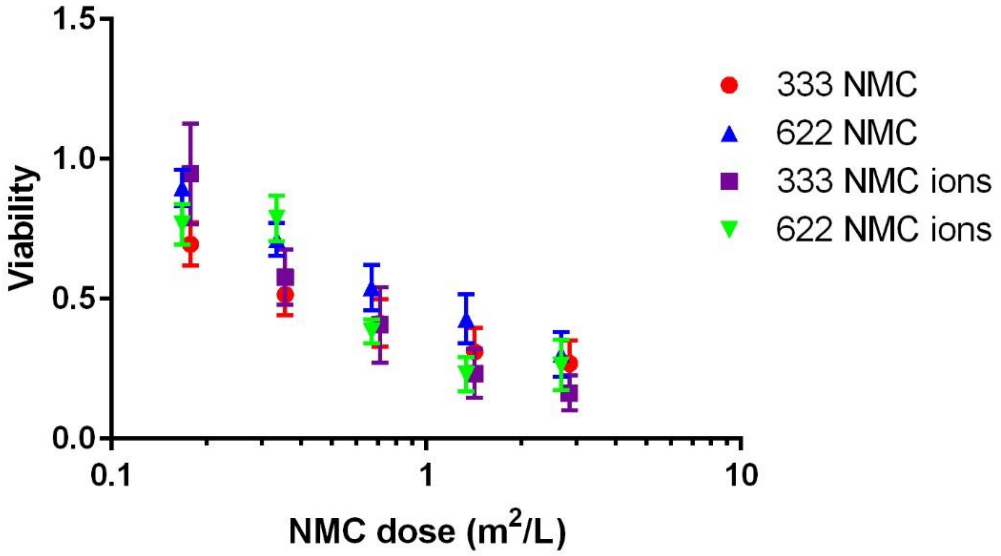

Figure 3.8. The toxicity from the ions that are released from NMC recapitulate the toxicity observed for the respective nanomaterial for *S. oneidensis*. Please note that the toxicity data for 333 NMC and 622 NMC here is the same as from Figure 3.3 and is included to facilitate interpretation. The error bars indicate the standard error from seven replicates for the NMC materials and four replicates for the ion controls.

To assess the toxicity of the ions released in daphnid medium over the 48-hour exposure, daphnids were exposed to the ions at the measured release concentration for 48 hours. We observe higher concentrations of released ions in the bacterial medium than the daphnid medium, as previously reported.[31,41] The enhanced dissolution may be due to the high concentration of lactate (100 mM) in the bacterial medium. Small organic acids have been shown to enhance dissolution of NMC materials, a phenomenon which is being harnessed by the recycling community.[42–44] As in previous work,[41] daphnids were unaffected by the bulk release of ions from the NMC nanomaterials used in this study (Figure 3.9), suggesting again that daphnids experience a NP-specific toxicity from NMC.

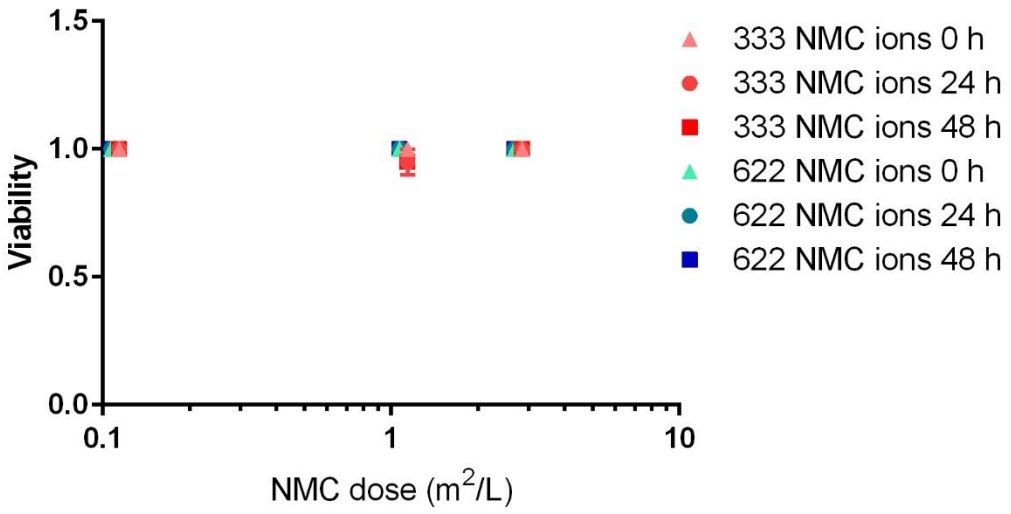

Figure 3.9. The toxicity of released ions from NMC nanomaterials to *D. magna* show that daphnids are tolerant of the ions released from both 333 NMC and 622 NMC over a 48-hour exposure. Since all of the daphnids survived the ion exposures (with the exception of the 1.1 m^2/L ion equivalents from 333 NMC), all of the points are overlaid on each other at 100% daphnid survival. The error bars are from the standard error of triplicate exposures to sets of five animals. Some error bars are not visible due to all of the daphnids surviving the exposure.

3.4.6 Abiotic ROS Production from NMC Nanomaterials

To investigate the contribution of NMC-induced ROS to the toxicity profiles observed, different dyes were used as reporters of ROS levels after a 3-hour exposure. To detect overall ROS levels, H_2DCF-DA was used, and to detect hydroxyl radical specifically, APF was used. The level of ROS production from the commercial materials could not be determined since at matching surface area doses, the concentrations were so high that fluorescence from the dyes would be masked by the turbidity of the suspensions.

From the nanomaterials, it is seen that 622 NMC generates more hydroxyl radical in both the bacterial medium and daphnid medium. Significant hydroxyl radical generation does not occur from 333 NMC in either medium (Figure 3.10). Given that a majority of the added nickel in Ni-enriched NMC was in an oxidation state higher than +2 and that dissolution of the transition metals from NMC that are not already at their lowest oxidation state (Ni^{2+}, Mn^{2+}, and Co^{2+}) need to initiate an oxidative reaction that produces ROS to dissolve,[26,32] it was expected that Ni-enriched NMC would produce more hydroxyl radicals. In both media, the overall production of ROS by 333 and 622 NMC is at significant levels compared to a NP-free control. While identifying the ROS species being generated by these materials is outside the scope of this work, this will be the focus of future studies. In

bacterial medium, 333 NMC is producing more ROS than 622 NMC (normalized fluorescence of 0.90 vs 0.83, respectively). The opposite is true in daphnid medium, in which 622 NMC is producing more ROS than 333 NMC (normalized fluorescence of 0.73 vs 0.52, respectively). ROS induces toxicity to organisms in a variety of ways,[45–47] and these data suggest that ROS is contributing to the toxicity seen from these materials to *S. oneidensis* and *D. magna*. While overall production of ROS by 333 NMC is greater in bacterial medium, it is noted that there is significantly greater generation of hydroxyl radicals, a very highly reactive ROS with a half-life on the order of 10^{-9} s,[48] by 622 NMC. The interplay of the different ROS generated from these materials could be contributing to the equal toxicity seen by 333 and 622 NMC to *S. oneidensis*. In daphnid medium, the overall ROS production by 622 NMC is higher than with 333 NMC, correlating with the increased toxicity seen by 622 NMC to *D. magna*.

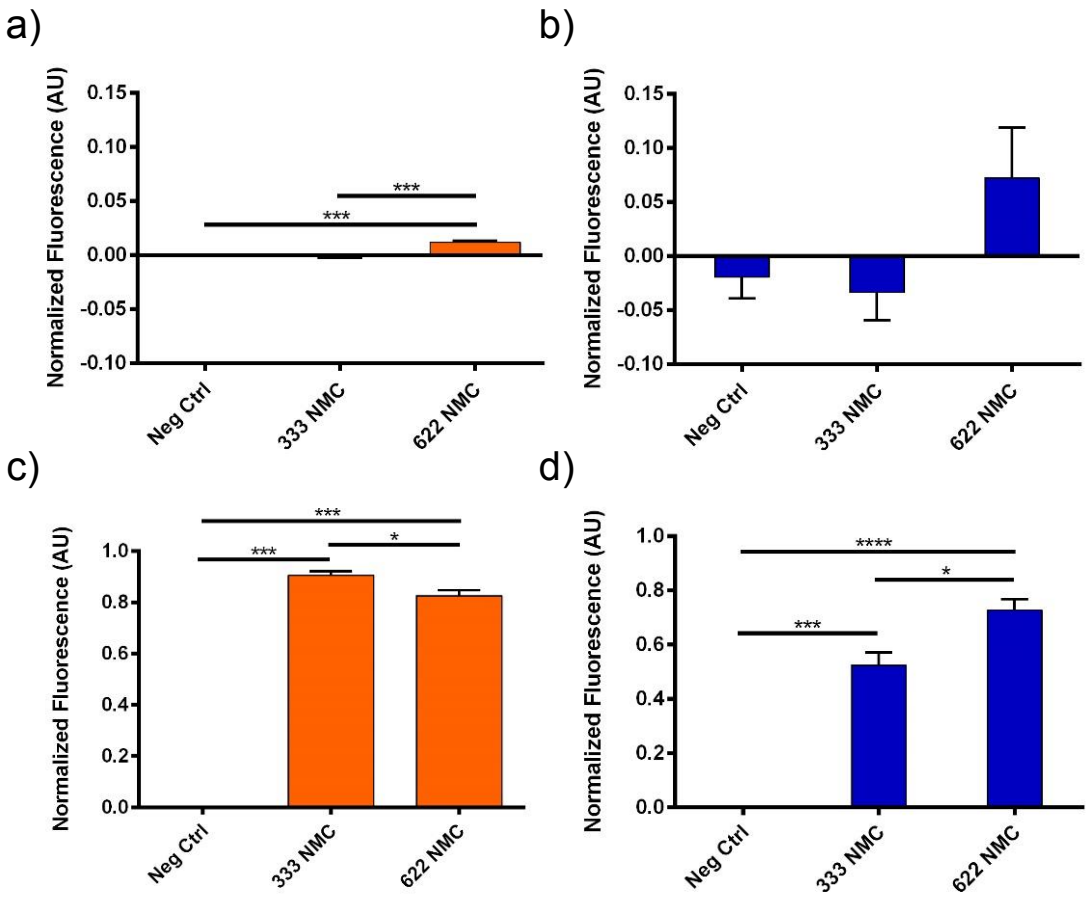

Figure 3.10. Abiotic ROS generation from NMC nanomaterials in bacterial and daphnid media. Fluorescent dyes were used to assess the production of hydroxyl radicals from NMC nanomaterials, which shows a trend that in a) bacterial medium and b) daphnid medium, 622 NMC produces more ·OH than 333 NMC. Monitoring general production of ROS in c) bacterial medium reveals that 333 NMC is producing more ROS than 622 NMC, whereas in d) daphnid medium, 622 NMC is producing greater quantities of total ROS than 333 NMC. The fluorescence intensities were background subtracted and normalized to the positive control; statistical analysis was done with a one-way ANOVA. *p<0.05, **p<0.01, ***p<0.001, ****p<0.0001

3.4.7 NMC Association to *S. oneidensis* and *D. magna*

To see if there is any direct interaction of NMC materials with the organisms, different microscopy techniques were used. For *S. oneidensis*, following NMC exposure, TEM micrographs and hyperspectral images were acquired to give visual evidence of material association (Figure 3.11). From the TEM images, instances of binding of the nanomaterials (333 and 622 NMC) to *S. oneidensis* MR-1 can be seen, but it is not very frequent. For the microscale materials (c622 and c811 NMC), very little if any binding is observed in the TEM images acquired; this does not preclude the fact that there may be

binding, it merely suggests that it is very rare. Analysis of the hyperspectral images, however, shows more instances of binding of the nanomaterials to bacteria than the TEM images. A spectral library was created for the bacteria and all of the NMC materials; in the hyperspectral images, pixels where the signal for bacteria or NMC were identified are falsely colored as red or green, respectively. It is apparent that there is significant binding observed for these materials as colocalization of these colors can be seen for both the nanoscale materials as well as the commercial, microscale materials. With the microscale materials, it appears as though the bacteria swarm the larger chunks, while small chunks are bound to their surface similarly to the nanoscale chunks of 333 and 622 NMC. This is the first instance showing significant binding between NMC materials and *S. oneidensis*. Given that minimal binding is seen in the TEM images, this suggests that the interaction between *S. oneidensis* and NMC is a weak binding interaction, as the centrifugation steps for biological TEM prep are likely removing the nanoparticles from the bacterial surface, which is why these interactions have not previously been observed. Binding of nanomaterials to bacterial surfaces can help to facilitate toxicity by disrupting the cell wall,[49–51] initiating internal pathways within the cell,[52] by dissolving toxic ions right at the cell surface,[53] or by generating ROS near the bacterial surface.[45] Given that it is known that ion dissolution is a major pathway for toxicity of these materials, NMC binding to the bacterial surface will facilitate the dissolution of ions near the bacteria. However, since the toxicity of ions alone recapitulates the toxicity of the nanomaterials, if there is any enhancement in toxicity due to nanoparticle binding to bacteria in this case, it is minute.

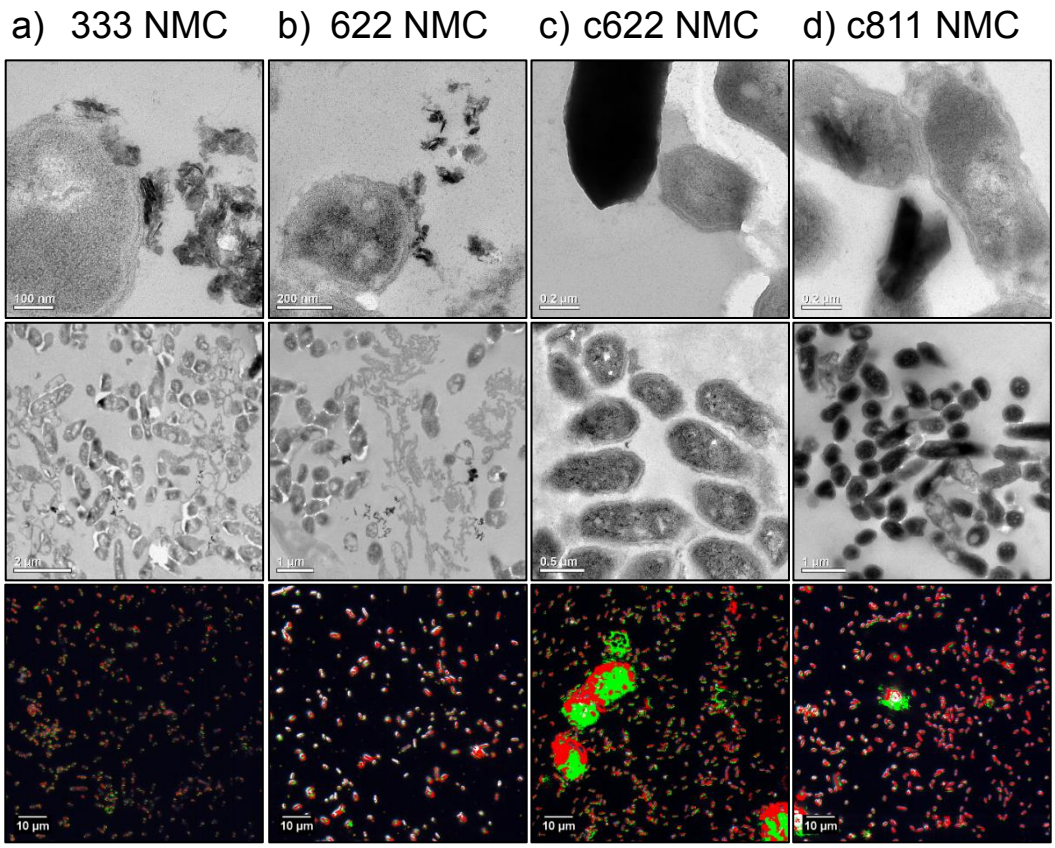

Figure 3.11. NMC association with *S. oneidensis*. The attachment of a) 333 NMC, b) 622 NMC, c) c622 NMC, and d) c811 NMC to *S. oneidensis* was assessed using two imaging techniques. (Top row) Zoomed in TEM images showing interacting particles or those in close proximity to the cell surface, (middle row) zoomed out image showing the frequency of interaction, and (bottom row) hyperspectral image that has been falsely colored to show the colocalization of signals from bacteria (red) and NMC (green).

To observe direct interaction with *D. magna*, bright-field microscopy was used. From the images collected, interaction of *D. magna* with all of the NMC materials can be seen (Figure 3.12). These images also demonstrate a different interaction between the daphnids and nanoscale and microscale NMC materials; for the nanoscale NMC (Figure 3.12a-c), they are mostly adhered to the bodies of the organism, whereas for the microscale NMC (Figure 3.12d-f), they have been ingested and are seen mainly in the daphnid gut. There is likely an interplay between the surface charge and size of the nanomaterials. It has previously been shown that positively charged NPs are more toxic than negatively charged NPs to daphnids,[54] in part due to the higher affinity of positively charged particles for the negatively charged surface of the cell membrane. The nanoscale materials used here exhibited a neutral ζ-potential in daphnid medium whereas the

microscale materials had a negative surface charge, which could explain the observed association patterns. The size differences also likely play a role here, since it was observed that the larger particles settled to the bottom of the beaker more quickly than the nanoscale materials. Daphnids are also capable of more efficiently ingesting larger particles,[55] consistent with what is observed here. It is worth noting that association of 622 NMC to *D. magna* was consistently more prevalent than 333 NMC, and there are also some of both NMC nanomaterials visible in the daphnid gut. This could negatively impact the daphnids by disrupting the membrane or being taken up intracellularly via different processes, releasing ions right at the daphnid surface, or by causing the daphnids to molt more frequently (a defense mechanism for daphnids to remove metal pollutants[56]) and thus use more energy. Given the overall greater production of ROS by 622 NMC in daphnid medium, ROS generation at the surface of the animal may also be contributing to the toxicity, which would be enhanced by the greater binding observed by 622 NMC than 333 NMC.

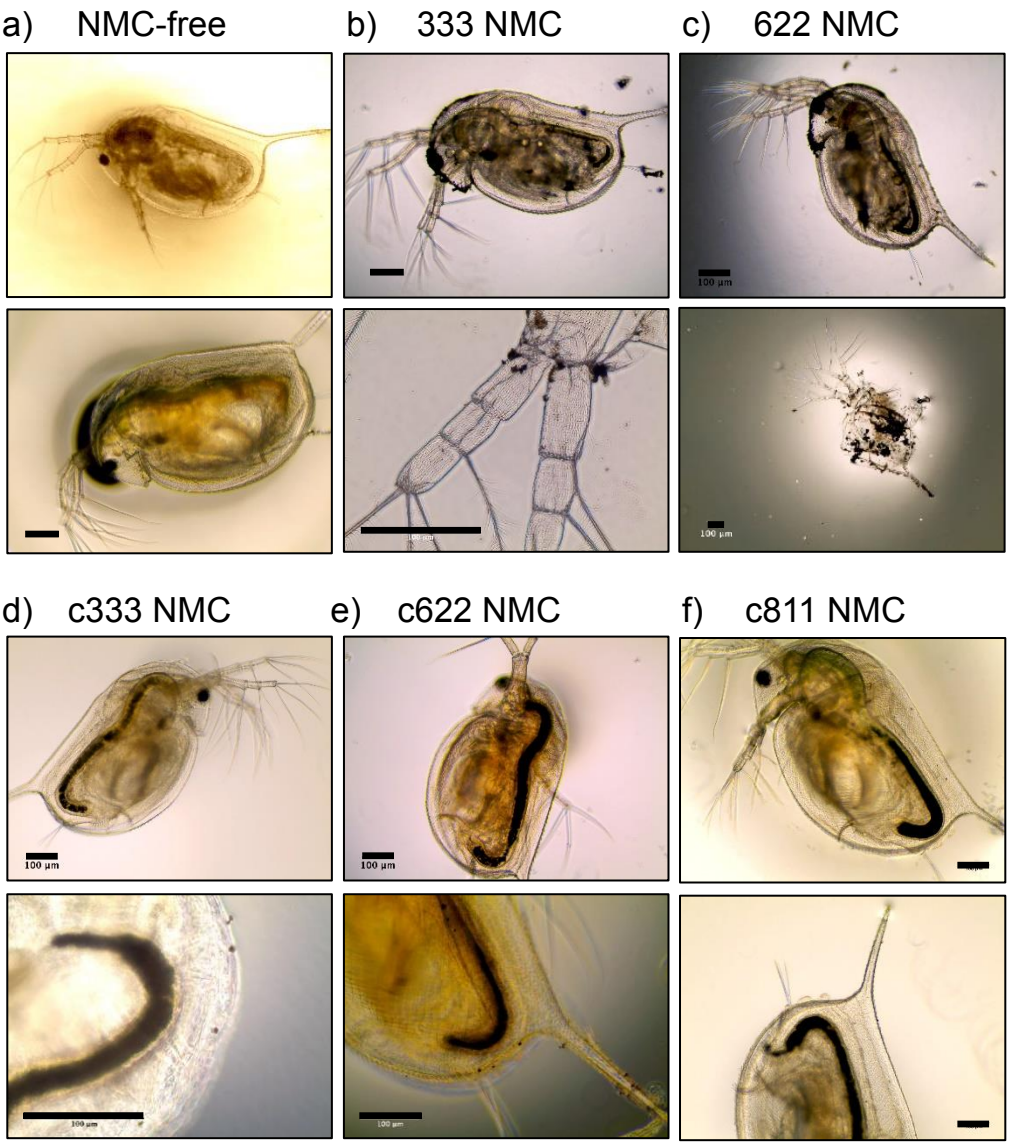

Figure 3.12. NMC association with *D. magna*. Microscope images of *D. magna* after a 48-hour exposure to NMC or to a) no NMC materials. Images of live daphnids after exposure to b) 333 NMC nanosheets and c) 622 NMC nanosheets shows NMC association both with the exterior of the animal, which can be seen in the zoomed in images (bottom row) and in the gut, while images with d) commercial 333 NMC, e) commercial 622 NMC, and f) commercial 811 NMC demonstrates that the majority of the NMC ends up in the daphnid gut. Zoomed in images (bottom row) highlight the darkened gut of the animal, indicating that the NMC had been ingested. All of the scale bars indicate 100 µm.

3.5 Conclusions

Taken together, these data demonstrate that redesign of NMC to the higher nickel form has differential impacts on bacteria and daphnids and this could be due to different mechanisms at work. The materials 622, c622, and c811 NMC have the same impact on

our bacterial model as equistoichiometric NMC when exposed at matching surface areas, due to equivalent ion dissolution from the materials. Given that nickel is a toxic component of the material, this was a surprising result. However, computational work demonstrated that there was increased stability of the NMC material against dissolution due to the oxidation states of the additional nickel in Ni-enriched NMC. These calculations indicated that this increased stability meant that similar dissolution of toxic ions would be noted for both 333 and 622 NMC. Indeed, similar dissolution profiles between 333 and 622 NMC were obtained in experiments, and since *S. oneidensis* is known to be sensitive to ion release, this explains the similar toxicity results obtained. For the invertebrate, *D. magna,* 622 NMC was found to be more toxic than equistoichiometric NMC and no impact was found related to ion dissolution from the materials. The pattern of ROS production by NMC mirrored the toxicity seen in the two media, suggesting that ROS production may be contributing to the overall toxicity of the material. Some of the nanoscale materials adhered to the carapace of the animal, likely due to differences in surface charge, but for microscale NMC, they were mostly ingested. For *D. magna*, the toxicity is dictated by the core composition of the material, and since nickel is more toxic than manganese to these organisms, doping in extra nickel at the expense of manganese leads to a negative impact. This is a significant observation, and reveals the importance of determining the molecular mechanisms of toxicity to organisms to inform redesign efforts.

Chapter 4

Coating Iron Oxide Nanoparticles with Mesoporous Silica Reduces their Interaction and Impact on *S. oneidensis* MR-1

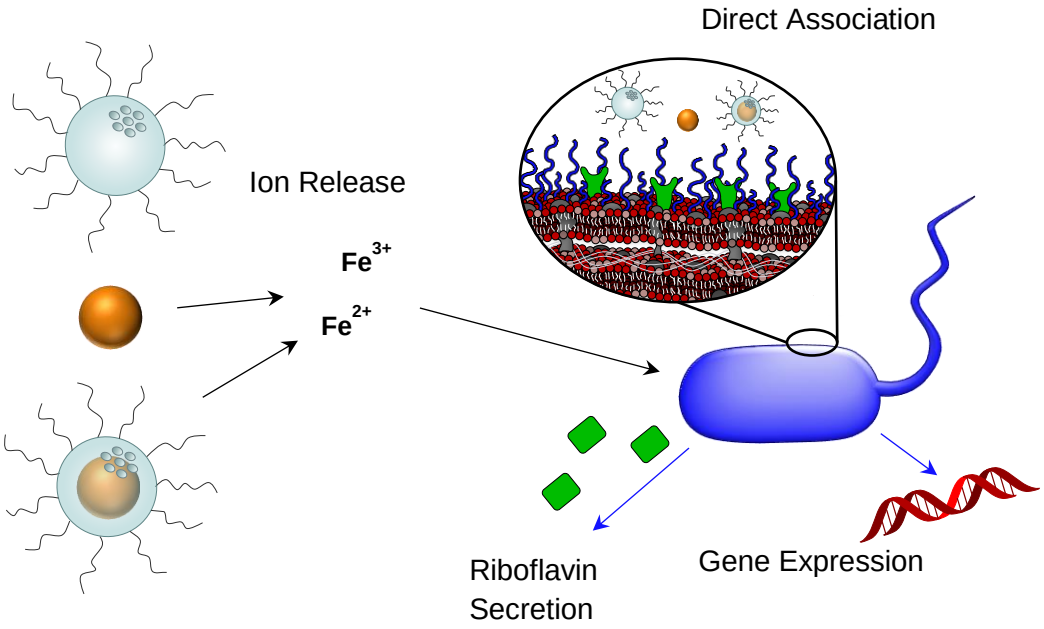

Adapted from: Buchman, J.T.; Pho, T.; Rodriguez, R.S.; Feng, Z.V.; Haynes, C.L. Coating iron oxide nanoparticles with mesoporous silica reduces their interaction and impact on *S. oneidensis* MR-1. *Submitted*.

4.1 Overview

Here, we investigate the impact of iron oxide nanoparticles (IONPs) and mesoporous silica-coated iron oxide nanoparticles (msIONPs) on *S. oneidensis* in an aerobic environment, which is likely the main environment where such nanoparticles will end up after use in consumer products or biomedical applications. Monitoring the viability of *S. oneidensis*, a model environmental organism, after exposure to the nanoparticles reveals that IONPs promote bacterial survival, while msIONPs do not impact survival. These apparent impacts are correlated with association of the nanoparticles with the bacterial membrane, as revealed via TEM and ICP-MS studies, and upregulation of membrane-associated genes. However, similar survival in bacteria was observed when exposed to equivalent concentrations of released ions from each nanomaterial, indicating that aqueous nanoparticle transformations are responsible for the observed changes in bacterial viability. Therefore, this work demonstrates that a simple mesoporous silica coating can control the dissolution of the IONP core by greatly reducing the amount of released iron ions, making msIONPs a more sustainable option to reduce perturbations to the environment upon release of nanoparticles into the environment.

4.2 Introduction

The applications of magnetic iron oxide nanoparticles can range from data storage[1] to biomedical imaging and therapies.[2,3] With such widespread use of these inexpensive and easy-to-synthesize nanomaterials, it is inevitable that some of the nanomaterials will end up in the environment. Therefore, it is critical to understand the potential environmental impact of these nanomaterials after their release, especially into aquatic environments.

Given that iron oxide nanoparticles (IONPs) are often susceptible to aggregation when in suspension with complex biological milieu, a silica shell is commonly added to the iron oxide nanoparticle core to improve their stability in complex matrices,[4,5] expanding the range of their utility for different applications. Since a mesoporous silica coating has pores in its structure, this method of capping nanoparticles still allows access by water to the core material, an attribute that is critical for performance in a variety of biomedical applications.[6] For example, literature has shown, when using iron oxide nanoparticles to image tumors in mice, that use of the mesoporous silica shell is required to stabilize the iron oxide nanoparticles so their magnetic properties facilitate the acquisition of images.[7] With the relevance of this particular platform (mesoporous silica-coated iron oxide nanoparticles) in mind, as well as the general concept of pursuing nanoparticle design motifs that control a nanoparticle's effect on our ecosystem, this work explores the impact

of iron oxide and mesoporous silica-coated iron oxide nanoparticles on a model bacterium, *Shewanella oneidensis* MR-1.

Bacteria are used as a surrogate for environmental health due to their important role as decomposers to recycle nutrients for use by other organisms. Therefore, any impacts on bacteria due to nanoparticle interaction could also ultimately affect other environmental organisms. *S. oneidensis* MR-1, specifically, is commonly considered for bioremediation since it is capable of respiring many different metals and is therefore an important part of the geochemical nutrient cycle.[8] *S. oneidensis* has three main mechanisms through which it respires metals (like the constituents of the iron oxide nanoparticles under consideration here): direct interactions with cytochromes on the bacterial surface, the secretion of flavins for extracellular reduction, and growth of electrically conductive pili capable of metal reduction. *S. oneidensis* synthesizes many different cytochromes, including cytochrome *c*,[9] and these cytochromes can be found associated with the bacteria's outer membrane, periplasmic space, and inner membrane. The system of cytochromes is capable of reducing metals when they come into direct contact with the outer membrane-associated cytochromes.[10,11] *S. oneidensis* also secretes flavins, which are capable of extracellular electron transfer at distances greater than 50 μm from the cell surface.[12] The flavin system is intimately linked with the outer membrane-associated cytochromes since they shuttle electrons from the cytochromes to the extracellular metals.[13] The third mechanism for *S. oneidensis* to reduce extracellular metals is through direct contact with electrically conductive pili, which can grow to be longer than 10 μm.[14] However, it has been demonstrated that the electrical pili are only present in significant quantities on *S. oneidensis* when grown under O_2-limited conditions,[14] and therefore are not relevant in the conditions considered herein.

Iron oxides are among the materials that *S. oneidensis* is capable of reducing.[9,15,16] Often, under anaerobic conditions, *S. oneidensis* reduces iron oxides to synthesize extracellular magnetite.[17–19] For example, when direct contact is made with hematite NPs, *S. oneidensis* reduces them to form magnetite nanoparticles.[20,21] *S. oneidensis* has also demonstrated an ability to dissolve and reduce magnetite.[22,23] While many of these studies are performed anaerobically, a related species of *S. oneidensis, S. putrefaciens* 200R, has been shown to attach to magnetite at similar levels under both aerobic and anaerobic conditions.[24] There is also evidence that some reduction machinery is upregulated in *S. oneidensis* MR-1 under aerobic conditions.[25] While there are many studies exploring the relationships between *S. oneidensis* and bulk iron oxides, there is a dearth of literature

looking at the interactions of nanoscale magnetite with *S. oneidensis*. Given that nanoparticles have a much higher surface area-to-volume ratio than their bulk counterparts, which imparts unique physicochemical properties to particles at the nanoscale, simply extrapolating the interactions of *S. oneidensis* with bulk iron oxide to nanoscale iron oxide may not wholly account for these increased complexities.

Herein, we report the interactions between *S. oneidensis* and iron oxide nanoparticles, and then detail our use of a mesoporous silica coating around the IONPs to mitigate their impact. The studies presented here investigate the impact of nanoscale magnetite under aerobic conditions, as those are likely to be the prevailing conditions in aquatic environments where nanoparticles are released. Colony counting was utilized to investigate the impact on bacterial survival after nanoparticle exposure. To understand the differential survival, the binding of the nanoparticles was investigated with TEM and ICP-MS. The contribution of ion release by the nanoparticles was assessed, and any impact on the production of riboflavin was investigated with HPLC. To probe these differences even further, changes in gene expression in *S. oneidensis* was analyzed using quantitative reverse transcription polymerase chain reaction (RT-qPCR). These studies showed that IONPs promote bacterial survival through the release of iron ions, and that, by reducing ion dissolution, the addition of a mesoporous silica coating mitigates that impact.

4.3 Experimental

4.3.1 Materials

Sodium chloride (NaCl), 4-(2-hydroxyethyl)-1-piperazineethanesulfonic acid (HEPES), polyvinylpyrrolidone (PVP-10, average molecular weight 10,000), n-cetyltrimethylammonium bromide (CTAB), tetraethylorthosilicate (TEOS), citric acid, methanol, and iron (III) chloride hexahydrate ($FeCl_3 \cdot 6H_2O$) were purchased from Sigma-Aldrich (St. Louis, MO). Ammonium hydroxide (NH_4OH, 28-30% as NH_3) was acquired from Avantor Performance Materials (Center Valley, PA). Chloro-trimethyl silane was obtained from Fluka and 2-[methoxy(polyethyleneoxy)$_{9\text{-}12}$propyl]-trimethoxysilane, tech 90 (PEG-silane, molecular weight 591-723 g/mol, 9-12 EO) was purchased from Gelest, Inc. (Morrisville, PA). EMG 308 Ferrofluid was acquired from Ferrotec (Santa Clara, CA). Ammonium nitrate (NH_4NO_3) was obtained from Mallinckrodt (St. Louis, MO). RNAzol® RT was acquired from Molecular Research Center, Inc. (Cincinnati, OH) and iTaq™ Universal SYBR® Green Supermix was obtained from Bio-Rad Laboratories, Inc. (Hercules, CA). Deoxyribonucleotides, random primers, SuperScript III reverse transcriptase, and RNaseOUT™ recombinant ribonuclease inhibitors were acquired from Invitrogen

(Carlsbad, CA). Primers for specific genes for *S. oneidensis* were purchased from Integrated DNA Technologies (Skokie, IL). Propylene oxide and 10% glutaraldehyde aqueous solution were obtained from Electron Microscopy Sciences (Hatfield, PA). Poly/Bed® 812 resin kit was acquired from Polysciences, Inc. (Warrington, PA). Absolute ethanol was purchased from Pharmco-Aaper (Brookfield, CT) and absolute ethanol (molecular biology grade) was acquired from Thermofisher Scientific (Waltham, MA). Luria-Bertani broth and agar were purchased from BD Difco (Franklin Lakes, NJ). Ultrapure water (18.2 MΩ·cm resistivity) was purified from a Milli-Q Millipore water purification system (Billerica, MA). *Shewanella oneidensis* MR-1 was graciously provided by Dr. Jeffrey Gralnick (Dept of Microbiology, University of Minnesota).

4.3.2 Synthesis of MSNs and msIONPs

To synthesize mesoporous silica nanoparticles (MSNs), a previously published protocol was adapted and used.[26] Briefly, cetyltrimethylammonium bromide (0.29 g) was mixed with 150 mL of 0.36 M NH_4OH [*caution: concentrated NH_4OH is both toxic and corrosive!*] and stirred (1 hr, 300 rpm, 50 °C). Then, 2.5 mL of 0.88 M tetraethylorthosilicate in ethanol was added dropwise and stirred (1 hr, 600 rpm, 50 °C), followed by slow addition of 450 µL of 2-[methoxy(polyethyleneoxy)9-12propyl]-trimethoxysilane and stirring (30 min, 600 rpm, 50 °C). Finally, 68 µL of chlorotrimethylsilane were added and stirred (30 min, 600 rpm, 50 °C) with the beaker covered.

A previously published method was used to prepare msIONPs.[7] Since the purchased IONPs have an anionic, proprietary ligand on their surface, they were first overcoated with PVP-10, a hydrophobic coating that will allow for favorable interactions with the hydrophobic tails of CTAB, used later in the synthesis. To make the EMG 308/surfactant suspension, the following materials were added sequentially into 5 mL of ultrapure water while sonicating, with 1 hr sonication steps between each addition: 0.6 g PVP-10, 400 µL EMG 308 suspension, and 0.29 g CTAB. To an Erlenmeyer flask, 145 mL of ultrapure water was added. While sonicating, the EMG 308/surfactant suspension was added dropwise; sonication continued for another hour to ensure dispersity. The temperature was increased to 50 °C, and the suspension was stirred (15 min, 300 rpm). Then, 2.5 mL of 28% NH_4OH was added and stirred (15 min, 300 rpm, 50 °C), followed by dropwise addition of 2.5 mL of 0.88 M ethanolic tetraethylorthosilicate with stirring (1 hr, 700 rpm, 50 °C). Slowly, 450 µL of 2-[methoxy(polyethyleneoxy)$_{9\text{-}12}$propyl]-trimethoxysilane was added and then stirred (30 min, 700 rpm, 50 °C) and lastly, 68 µL of chlorotrimethylsilane was added and stirred (30 min, 700 rpm, 50 °C) with the flask covered by a glass Petri

dish. The suspension was then transferred to a clean 250 mL Erlenmeyer flask without a stir bar.

For gentle evaporation, both MSNs and msIONPs were then aged at 50 °C for ~20 hours (care was taken to ensure that not all the solvent evaporates), followed by hydrothermal treatment at 90 °C for 24 hr to improve particle stability. Oxygen was removed from msIONPs prior to hydrothermal treatment by purging the reaction vessel and sparging with nitrogen gas to reduce oxidation of the cores at the higher temperatures of hydrothermal treatment. The NPs were purified by ultracentrifugation (30 min, 61,579×*g*) and resuspension in 50 mL of 6 g/L NH_4NO_3 for reflux (1 hr, 300 rpm, 60 °C). The suspension was then ultracentrifuged (all subsequent ultracentrifugation steps were done for 20 min at 61,579×*g*) and resuspended in 95% ethanol. This was ultracentrifuged and resuspended in 6 g/L NH_4NO_3 to reflux again (1 hr, 300 rpm, 60 °C). The suspension was ultracentrifuged three more times and resuspended in the following order: 95% ethanol, 99% ethanol, 99% ethanol. The final suspension was filtered through a 0.2 µm GHP syringe filter.

4.3.3 Transmission Electron Microscopy

To prepare the nanoparticles for imaging by transmission electron microscopy, they were first diluted to a suspension of approximately 0.5 mg/mL (IONPs were used at ~2 mg/mL) and sonicated for 10 min to ensure dispersal. Then, for MSNs and msIONPs, a 200 mesh copper grid with Formvar and carbon supports (Ted Pella, Inc., Redding, CA) was briefly dipped into the suspension. For IONPs, a 3 µL drop of the suspension was placed onto the grid surface. All grids were dried near an open 65 °C oven prior to imaging with a FEI Tecnai T12 transmission electron microscope. To acquire the images, the microscope was used at an operating voltage of 120 kV. Size analysis was performed on the images using ImageJ,[27] with size determined by drawing a line across the diameter of at least 500 randomly chosen nanoparticles.

4.3.4 Hydrodynamic Diameter and Zeta Potential Measurements

To determine the hydrodynamic diameter and zeta potential of the nanoparticles used in this study, the nanoparticles were first suspended in water at a concentration of 0.5 mg/mL. The hydrodynamic diameters and ζ-potentials were then analyzed using a Brookhaven ZetaPALS instrument. The stability of the nanoparticles in the exposure medium (HEPES buffer) was also assessed by suspending the nanoparticles (300 µg/mL) in HEPES buffer and checking their hydrodynamic diameter after 30, 60, and 120 min.

4.3.5 Bacterial Culture Conditions

S. oneidensis MR-1 was stored at -80 °C until ready for use, when it was then plated on a sterilized Luria-Bertani (LB) agar plate and incubated overnight at 30 °C. From the plate, two colonies were inoculated in 10 mL of LB broth overnight to reach the late log phase (OD_{600} =0.6-1.0). The bacteria were washed by centrifuging (10 min, 750×*g*), resuspended in DPBS, and incubated at room temperature on a nutating mixer for 10 min. The bacteria were centrifuged again (10 min, 750×*g*), and resuspended in HEPES buffer (2 mM HEPES, 25 mM NaCl, pH 7.4) to the appropriate OD_{600}.

4.3.6 Nanoparticle Dissolution in Bacterial Medium

To measure how much iron dissolves in the HEPES buffer after one hour, suspensions in HEPES buffer were made by mixing 450 µL of nanoparticle stock with 5.55 mL of HEPES buffer to a final concentration of 300 µg/mL of iron oxide. These were left at room temperature for one hour before being centrifuged at 4700×*g* for 30 min, followed by centrifuging the supernatant twice at 286,000×*g* for two hours. Removal of nanoparticles was confirmed with DLS, and the iron content of the supernatants was measured with a Thermo Scientific XSERIES 2 ICP-MS.

4.3.7 Drop Plate Colony Counting Assays for Viability

To assess the viability of *S. oneidensis* MR-1 after exposure to the NPs, the bacterial OD_{600} in HEPES buffer was adjusted to 0.2 (which corresponds to ~2×10^8 cells/mL) and then diluted 1000-fold. To a suspension of bacteria (925 µL), NP treatments were added (75 µL), and exposures lasted 1 hr. Both iron-containing nanoparticles were used at iron concentrations of 300 µg/mL (as a control nanoparticle, the MSNs were used so that the silica mass matched that of the silica in msIONPs (4.7 mg/mL)). Six 10 µL drops of each suspension were dropped onto dried, UV-resterilized LB agar plates and incubated for ~17 hr at 30 °C. In separate experiments assessing the viability of bacteria after exposure to iron ions, iron (III) chloride hexahydrate was used for exposure concentrations of 7.6 and 1.0 ppb, to recreate the iron ion concentration determined to be released from IONPs and msIONPs, respectively. The number of colonies that grew in each treatment were counted and recorded. These colony counts were normalized by dividing by the number of colonies that grew in the negative control samples to facilitate comparison between trials.

4.3.8 MINTEQ Evaluation of Dissolved Iron Species

To understand the oxidation state of the dissolved iron species determined in ICP-MS, Visual MINTEQ 3.1 software was used. The components of the exposure were input into

the software ([HEPES]: 2 mmolal, [Na^+]: 25 mmolal, [Cl^-]: 25 mmolal, magnetite as a finite solid: 1.296 mmolal), and the pH was fixed at 7.4 because the suspension is buffered. The redox couple of Fe^{2+}/Fe^{3+} was enabled for these calculations. The mass distribution was analyzed to determine the likely oxidation state of the dissolved iron in the experimental conditions used.

4.3.9 Nanoparticle Association with Transmission Electron Microscopy

To visualize the binding of nanoparticles to *S. oneidensis*, the bacterial OD_{600} was adjusted to 0.8 (which corresponds to ~8×10^8 cells/mL) before mixing the bacterial suspension (925 µL) with nanoparticles (75 µL). The nanoparticles were used at the same concentrations as for colony counting experiments. After a one-hour exposure, the samples were centrifuged at 800×*g* for 5 min and the supernatant discarded.

The bacterial samples were prepared for TEM by adapting previously reported methods.[28,29] The samples were washed thrice without resuspension using 0.1 M cacodylate buffer, centrifuging at 500×*g* for 2 min between each wash step. To fix the sample, the pellet was resuspended in 2.5% glutaraldehyde in 0.1 M cacodylate buffer for 50 min, followed by centrifuging at 800×*g* for 5 min. The pellet was again washed three times with 0.1 M cacodylate buffer without resuspension. To dehydrate the samples, a series of ethanol washes was done at increasing ethanol concentrations in water, using each concentration twice (30%, 50%, 70%, 80%, 95%, and 100% ethanol). The samples were then washed three times with propylene oxide prior to using a 2:1 propylene oxide:resin mix for two hours, uncovered. This 2:1 mixture was replaced with 1:1 propylene oxide:resin to soak overnight, after which it was replaced with fresh 1:1 propylene oxide:resin for four hours. The samples were then incubated in pure resin overnight, which was replaced with fresh resin the next day. To cure the resin, the samples were put in a 40 °C oven for 24 hours and then a 60 °C oven for 48 hours. The samples were sliced into ~70 nm thick sections using a LEICA EM UC6 ultramicrotome, which were stained with uranyl acetate and lead citrate. The slices were placed on 200 mesh copper grids with carbon and Formvar supports (Ted Pella, Inc., Redding, CA). Images of the samples were acquired using a FEI T12 transmission electron microscope at an operating voltage of 120 kV.

4.3.10 Nanoparticle Association using ICP-MS

To measure the amount of iron oxide nanoparticles and mesoporous silica-coated iron oxide nanoparticles that bind to *S. oneidensis*, the OD_{600} of bacteria was adjusted to be 0.2 (~2×10^8 cells/mL) and then exposed to nanoparticles by mixing 925 µL of bacterial

suspension with 75 µL of nanoparticles to achieve final concentrations of 300 µg/mL of iron oxide. Control experiments were set up simultaneously that mixed HEPES buffer with nanoparticles. After the one-hour exposure, the samples were centrifuged twice at 800×*g*, discarding all but 50 µL of the supernatant since the pellet is easily disturbed. After the first centrifugation, the pellet was resuspended carefully in 1 mL HEPES buffer, and after the second centrifugation, the pellet was resuspended in 150 µL of HEPES buffer. The resuspended pellet (125 µL) was diluted with 375 µL of concentrated nitric acid [*Caution: use care when handling corrosive acids*] and the sample was digested at 60 °C overnight. The samples were then diluted 14-fold and centrifuged at 17,000×*g* for 20 min to remove cell debris. The samples were analyzed using a Thermo Scientific XSERIES 2 ICP-MS. To determine the amount of iron associated with the bacteria, the iron concentration detected in the respective control and the iron contribution by the bacteria were subtracted from the iron concentration in the experimental/bacterial samples, and then the dilutions were taken into account.

4.3.11 Riboflavin Secretion Measurements

A previous method was adapted to determine the amount of riboflavin secreted by bacteria after nanoparticle exposure.[30] To begin, the OD_{600} in HEPES buffer was adjusted to 0.2. The bacteria were then exposed to NPs for 1 hr and then centrifuged at 17,000×*g* for 20 min to pellet both the bacteria and NPs. The supernatant was collected, and 200 µL was transferred to an HPLC vial with 250 µL glass insert. The supernatant was analyzed using an Agilent 1200 HPLC fitted with a Zorbax Eclipse XDB-C_{18} analytical column (4.6 x 150 mm, 5 µm packing material) and an Eclipse XDB-C_{18} analytical guard column (4.6 x 12.5 mm, 5 µm packing material) ahead of the fluorescence detector. Isocratic HPLC was performed with a mobile phase composed of 70/30 20 mM citric acid buffer (pH 3.3)/methanol with an injection volume of 30 µL, flow rate of 1 mL/min, and run time of 8 min. Excitation and emissions wavelengths of 450 and 530 nm, respectively, were used to detect riboflavin.

4.3.12 Extracting RNA from *S. oneidensis* after Nanoparticle Exposure

The RNA extraction was performed using a Zymo Research Direct-zol™ RNA MiniPrep Plus kit. To do the one-hour nanoparticle exposure prior to RNA extraction, the bacterial OD_{600} in HEPES buffer was adjusted to 1.0 (corresponding to ~1×10^9 cells/mL), and 1.85 mL of bacterial suspension was mixed with 150 µL of nanoparticle suspension (or water as a negative control), using nanoparticle concentrations that matched the colony counting experiments. Afterward, the suspensions were centrifuged at 2000×*g* for

10 min and the pellet was resuspended in 200 µL of RNAzol RT. Centrifugation at 16,000×*g* for 1 min removed particulate debris, and 200 µL of 200 proof molecular biology grade ethanol was added to the supernatant and mixed. This mixture was added to a Zymo-Spin IIC column in a collection tube and centrifuged at 16,000×*g* for 30 sec, discarding the flow through. To the column, 400 µL of RNA wash buffer was added and centrifuged at 16,000×*g* for 30 sec. To do a DNase I treatment, 5 µL of DNase I and 75 µL of DNA digestion buffer were mixed separately and then transferred to the column surface, incubating at room temperature for 15 min to digest DNA. Then, the column was washed twice by sequential additions of 400 µL of Direct-zol RNA PreWash and centrifuging at 16,000×*g* for 30 sec, discarding the flow through. 700 µL of RNA wash buffer was added to the column and centrifuged at 16,000×*g* for 2 min. The column was transferred to a clean, RNase-free Eppendorf tube where 80 µL of DNase/RNase-free water was added and centrifuged at 16,000×*g* for 30 sec to collect the RNA product. The concentration and quality of the RNA was measured using a Thermo Scientific NanoDrop™ One^{C}.

4.3.13 Monitoring Gene Expression Changes in *S. oneidensis* after Nanoparticle Exposure

Total purified RNA was reverse transcribed into complementary deoxyribonucleic acid (cDNA) as previously described.[31] cDNA was synthesized using 100 ng of total RNA template and was incubated with an aliquot of deoxyribonucleotides and random primers at 65 °C for 5 min followed by chilling on ice for 1 min. SuperScript III reverse transcriptase, dithiothreitol, and RNaseOUT™ recombinant ribonuclease inhibitors were added into the mixture after the incubation following the temperature program of 25 °C for 5 minutes, 50 °C for 60 minutes, and 70 °C for 15 minutes for primer extension. Synthesized cDNA was then stored at -20 °C.

Table 4.1. List of genes and primers used for gene expression analysis with qPCR.

Target Gene	Forward Primer (5'-3')	Reverse Primer (5'-3')	Protein Product	Function	Accession Number	Gene ID
exbB	GCT TGG TCT GGC GAT GAA TA	CGC CCA GAT CCC GAA TAA AT	TonB1 energy transduction system for heme uptake inner membrane component ExbB	Iron uptake	NP_719212	1171327
tonB	ACG TGT TAC CTT AAA CCC TGT TA	CAA TGA TGC GTG ATG GGA TTG	TonB1 energy transduction system for heme uptake energy transducer component TonB	Iron uptake	NP_719211	1171326
ftn	TCA CCT ATG TGA GCG AAA CC	CGA ATA AGG CCA GCA GAG AA	Ferritin	Sequestration of iron	NP_715781	1168033
bfd	ACG AGT CTT GCT GAC GTT AAA	CAA TTT CCA GTT GAT TCT GGA TGA T	Bacterioferritin-associated ferredoxin Bfd	Utilization of sequestered iron	NP_716218	1168450
pubA	CGG CAC TGT GTG AAC CTA TTA	TCG GCC ATA GTG ACC AAA TC	Putrescine monooxygenase PubA	Ferric ion usage	NP_718598	1170715
feoA	CGA TTA GAT CTG CCG CAA AC	TAT CCA GCT CTA AAC CTG AGC	Ferrous iron transport protein A FeoA	Ferrous ion transport	NP_717392	1169557
mtrC	GGT CTA TAT TCT ACG CCG ATC AC	CAT CAA CAA CTG CAC CGA AAG	Extracellular iron oxide respiratory system surface decaheme cytochrome *c* component MtrC	Iron oxide respiration	NP_717387	1169552
omcA	TGT TGA GTT GTA TGC TGG TGT A	GGA TGT AAG CGT AGC GAG TAT C	Extracellular iron oxide respiratory system surface decaheme cytochrome *c* component OmcA	Iron oxide respiration	NP_717388	1169553
ribBA	GGC CCT GAT TGA ATA CCG TAA TA	ACC ATA TCG AAC TCA CCG AAA C	3,4-Dihydroxy-2-butanone-4-phosphate synthase	Riboflavin biosynthesis	NP_719016	1171143
radA	GTT CGG TGA GGT AGG GTT ATC	GAG GCA CTA TCG CTC GTT TA	ATP-dependent protease	DNA repair	NP_716849	1169052
gyrB	GCA ACG TTA TCC AAC GCA TAT C	AGG CGT CGA TCC ATT CTT TC	DNA gyrase B subunit GyrB	Catalyzes negative super-coiling of DNA	NP_715653	1167909

Quantitative reverse transcription PCR was run to determine the expression levels of several genes involved in iron acquisition, storage, and utilization for *S. oneidensis*, with *radA* and *gyrB* genes serving as housekeeping genes for analysis (Table 4.1). An iQ5 real-time PCR detection system (Bio-Rad Laboratories) using SYBR Green for the fluorescent intercalating dye (iTaq™ Universal SYBR® Green Supermix) was used for this process. Each of the qPCR reactions containing cDNA (1 µL) mixed with primers (1 µL) with fluorescent dye (10 µL) and nuclease-free water (8 µL) was carried out in 96-well PCR plates, centrifuging the plates at 1000×*g* for 10 min at 4 °C prior to running the qPCR. The polymerase chain reactions started at 95 °C for 10 minutes for DNA denaturing, then underwent 40 real-time PCR amplification cycles (15 s at 95 °C, followed by 30 s at 60 °C).

Fluorescence of the SYBR Green was then detected at the end of each PCR cycle. All samples were analyzed with technical duplicates.

4.4 Results and Discussion

4.4.1 Characterization of MSNs, IONPs, and msIONPs

The nanomaterials used in this study were characterized by a variety of methods. Using TEM, the morphology and size distribution of the materials could be determined (Figure 4.1). The mesoporous silica nanoparticles were found to have a diameter of 60 ± 15 nm (n=632), similar to the diameter of 57 ± 10 nm (n=521) found for mesoporous silica-coated iron oxide nanoparticles. The purchased iron oxide nanoparticles were smaller, with a diameter of 12 ± 5 nm (n=557).

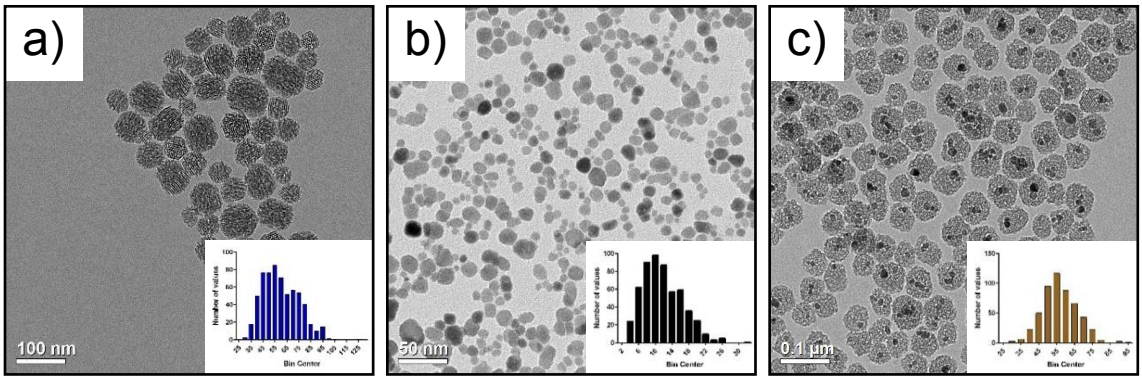

Figure 4.1. Size distribution of nanoparticles. Transmission electron microscope images reveal the size and dispersity of a) mesoporous silica nanoparticles, b) iron oxide nanoparticles, and c) mesoporous silica-coated iron oxide nanoparticles. An inset in each image shows the size histogram determined for each nanoparticle type. Note that the scale bar for image (b) is half the size of that for the other two images.

The hydrodynamic diameters of the material were also determined for MSNs (86 ± 21 nm), msIONPs (90 ± 6 nm), and IONPs (55 ± 6 nm), reflecting the trend seen by TEM size analysis. The ζ-potential for msIONPs (-39 ± 12 mV) was more negative than that for MSNs (-18 ± 9 mV) or IONPs (-23 ± 15 mV); these values suggest that all three nanoparticle formulations should be relatively colloidally stable. In fact, throughout the course of the exposure experiment, all three nanoparticles were stable, as indicated by their unchanging hydrodynamic diameter in HEPES buffer over 2 h (Figure 4.2).

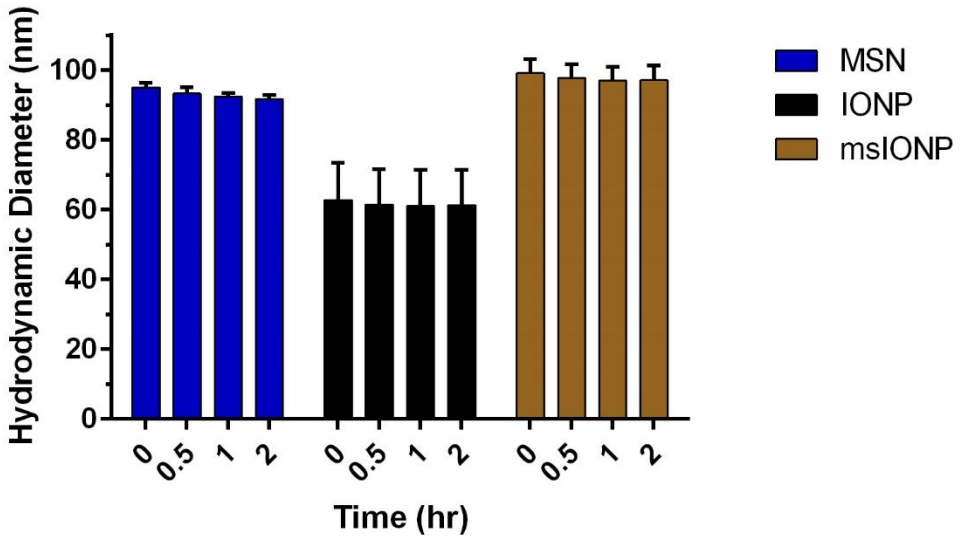

Figure 4.2. Stability of MSNs, IONPs, and msIONPs in HEPES buffer. The hydrodynamic diameters of MSNs, IONPs, and msIONPs do not change over the course of the bacterial exposure time, indicating their stability. Error bars show the standard deviations of triplicate measurements.

4.4.2 Impact of Nanoparticles on *S. oneidensis*

After a one-hour exposure to the different nanoparticles, the impact to *S. oneidensis* was assessed using a colony counting assay (Figure 4.3). The results demonstrate that while mesoporous silica-coated iron oxide nanoparticles and mesoporous silica nanoparticles have no impact on bacterial survival compared to the control, the iron oxide nanoparticles enhance the growth of the bacteria in HEPES buffer and therefore have an enhanced survival rate. Iron is an essential nutrient for bacteria,[32] thus it is reasonable that the presence of exogenous iron could enhance their growth. Specifically for *S. oneidensis* MR-1, iron oxide is a metal that they are capable of respiring anaerobically as a means of obtaining energy;[9] alternately, dissolution product iron ions may contribute to bacterial sustenance. To probe the mechanism by which iron helps sustain bacteria in HEPES buffer, the contributions of the various means by which *S. oneidensis* can respire iron oxide were determined, as well as any impact of iron dissolution from the iron oxide nanoparticles. To evaluate how the mesoporous silica coating mitigates the impact by IONPs, effects on these endpoints by IONPs and msIONPs were compared.

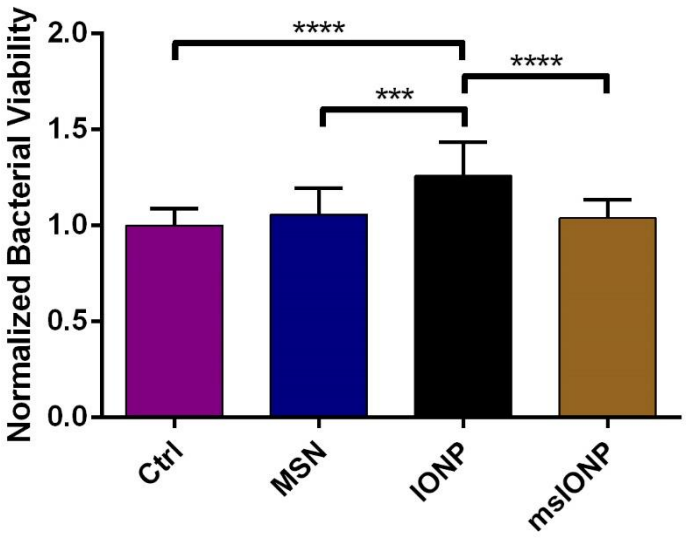

Figure 4.3. Impact of MSN, IONP, and msIONP exposure on *S. oneidensis*. The colony counts determined from each nanoparticle type after being normalized to the control indicates that mesoporous silica and mesoporous silica-coated iron oxide nanoparticles have no impact on survival while the iron oxide nanoparticles enhance bacterial survival compared to a negative control. The error bars represent standard deviations from sixteen replicates. Statistical significance was evaluated using a one-way ANOVA with Tukey's multiple comparisons post-hoc test. ***p<0.001, ****p<0.0001

4.4.3 Differential Ion Release is Observed for Nanoparticles

To determine the concentrations of iron that were released from IONPs and msIONPs during their one-hour exposure to bacteria in HEPES buffer, ICP-MS was used to measure iron concentrations from an abiotic supernatant after removing the NPs from suspension. Results showed that IONPs released significantly more iron (7.6 ± 0.2 ppb) compared to msIONPs (1.0 ± 0.4 ppb) after an hour in HEPES buffer ($p<0.0001$). This observation suggests that a silica coating mitigates dissolution of the nanoparticle core.[33] While these results indicate the iron concentrations released from the nanoparticles, they do not specify the oxidation states of the dissolved iron. MINTEQ modeling was used to show that at equilibrium, Fe^{3+} is the dominant oxidation state for the dissolved iron (Table 4.2), prompting the use of iron (III) chloride hexahydrate for the ion control studies performed.

Table 4.2. MINTEQ determination of oxidation state of dissolved iron species. MINTEQ output showing the total dissolved concentration of Fe^{3+} (1.64×10^{-14} molal) was more than the total dissolved concentration of Fe^{2+} (2.48×10^{-18} molal) in the conditions of this study.

Component	Total dissolved (molal)	% dissolved	Total sorbed (molal)	% sorbed	Total precipitated (molal)	% precipitated
Cl^-	0.025	100	0	0	0	0
Fe^{2+}	2.48E-18	100	0	0	0	0
Fe^{3+}	1.64E-14	0	0	0	0.0039	100
H^+	0.0011	100	0	0	0	0
$HEPES^-$	0.002	100	0	0	0	0
Na^+	0.025	100	0	0	0	0

4.4.4 Iron Ion Exposure Recapitulates Effect Seen by Nanoparticles

S. oneidensis were exposed to the concentrations of iron ions released during nanoparticle exposure, and their viability was assessed using the colony counting assay. From this assay, it was seen that the iron ion exposure recapitulates the results of nanoparticle exposure, with the iron ion concentrations equivalent to the release from the control and msIONP trials both showing a similar viability around 1.0, and the iron ion concentrations equivalent to release from IONPs showing an increased bacterial survival (Figure 4.4). The bacterial viability after exposure to the ion concentration representing IONP exposure was 1.24 ± 0.27, which is not statistically distinct from the 1.26 ± 0.18 viability seen after exposure to IONPs. These comparisons demonstrate that the dissolved ion constituents of these nanoparticles are dominating the observed effect of the nanoparticles on *S. oneidensis*. In addition, these results show that, since the presence of a mesoporous silica coating reduces dissolution to levels that do not impact *S. oneidensis*, this reduced dissolution is the major contributor to the mechanism by which the mesoporous silica coating mitigates IONP impact.

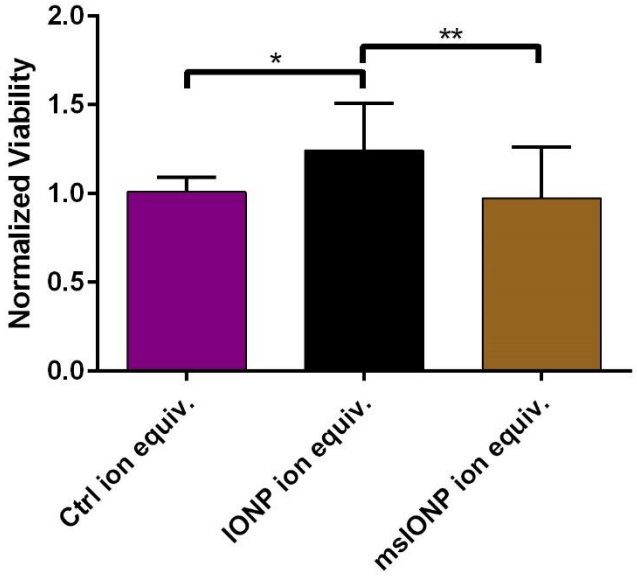

Figure 4.4. Bacterial exposure to released iron concentrations recapitulate the effect seen by nanoparticle exposure. At Fe^{3+} ion concentrations that match those released during nanoparticle exposure, it can be seen that 7.6 ppb iron ions (equivalent to the released concentration from IONPs) are enhancing bacterial survival to the same extent as observed with IONP exposure, while at 1.0 ppb (equivalent to the released concentration from msIONPs), no impact on growth is observed. These data demonstrate that the impact from the iron ions is recapitulating the impact observed from the nanoparticle exposures, and therefore ion dissolution is the main contributor to the nanoparticles' effects. The error bars represent the standard deviations from fifteen replicate trials. One-way ANOVA with Tukey's multiple comparisons test was used to evaluate statistical significance. *$p<0.05$, **$p<0.01$

4.4.5 IONPs Display Significant Binding to the Bacterial Surface

While the ion studies indicate that ion release is the major contributor to the impacts of the nanoparticles, the other mechanisms by which *S. oneidensis* can interact with iron oxide nanoparticles were assessed as well. Some of these mechanisms involve direct binding with the cell wall, thus, the interactions of the NPs with bacteria were visualized by first fixing the samples and embedding them in resin. Images of the resin-embedded samples were then acquired with TEM. For samples containing IONPs and msIONPs, the TEM was performed in dark-field mode to verify that nanoparticles were observed by taking advantage of the scattering efficiency of crystalline iron oxide nanoparticles.[34] These images clearly show that the IONPs are binding to *S. oneidensis* to a greater extent than MSNs or msIONPs (Figure 4.5). Given that all three nanoparticles used in this study have a negative surface charge, which often leads to electrostatic repulsion from the net-

negative charge of the bacterial membrane, it is not surprising that there is no interaction between the membrane and MSNs or msIONPs. However, it is interesting that there is such prevalent binding of IONPs, which implies specific interactions by the bacteria with this material.

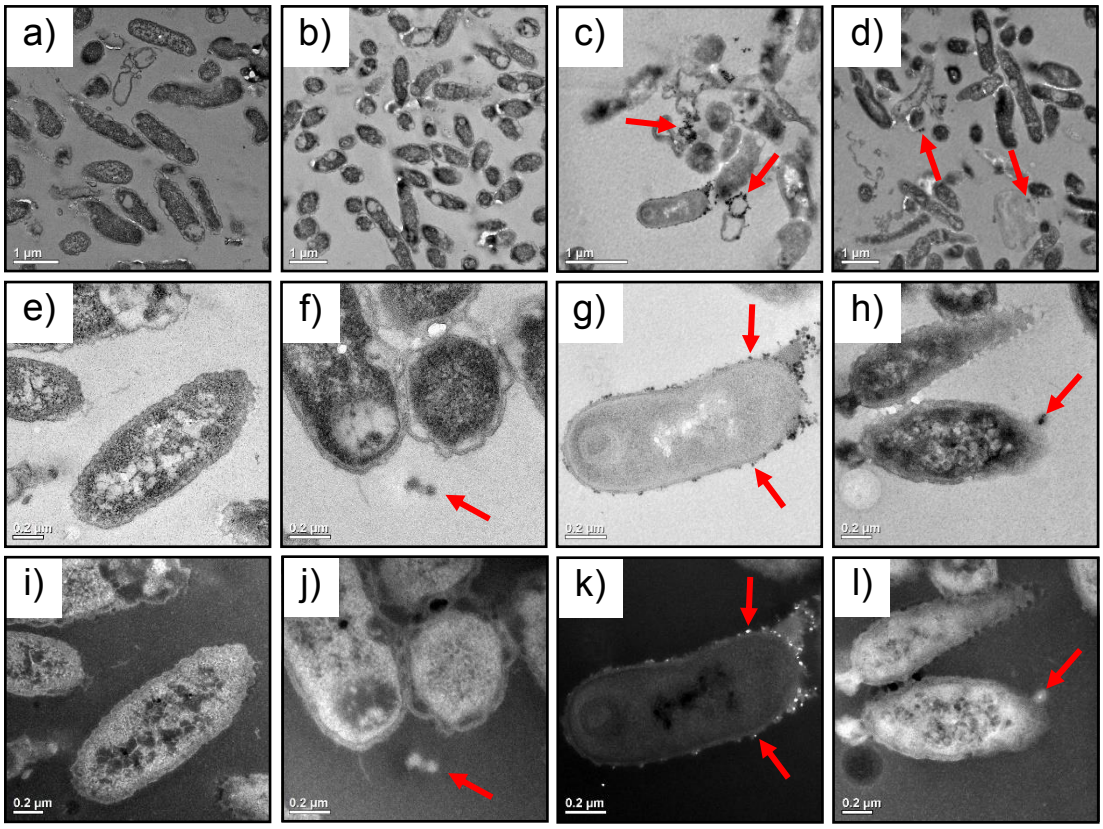

Figure 4.5. Association of MSNs, IONPs, and msIONPs with *S. oneidensis*. A low magnification view of bacteria after exposure to a) nanoparticle-free suspension, b) MSNs, c) IONPs, and d) msIONPs as well as a high magnification view of e) NP-free suspension, as well as bacteria exposed to f) MSNs, g) IONPs, and h) msIONPs reveal that there is more binding with IONPs than the other two nanomaterials. No instance of direct binding by MSNs could be found, which indicates that if they do occur, they are a rare occurrence. Where present, instances of nanoparticles in each image are highlighted with red arrows. Dark-field images of i) NP-free bacteria are included as a comparison to bacteria exposed to j) MSNs, k) IONPs, and l) msIONPs. The bright points are due to the high scattering efficiency of IONPs in both images and are not seen in the control image. Mesoporous silica nanoparticles do not exhibit the same scattering intensity in dark-field mode due to their noncrystalline nature.

Beyond the visual evidence from TEM, quantitative evidence of increased IONP binding was acquired by exposing the bacteria to nanoparticles, pelleting the bacteria, and digesting them to quantify the amount of iron material that was associated with the bacteria

(likely the surface, based on TEM data). Since iron quantitation was the endpoint, this does not reveal anything about the binding of MSNs to the bacterial surface. Corroborating the TEM images, a significant increase in iron content from bacteria that were exposed to IONPs was found compared to those that were exposed to msIONPs (Figure 4.6). In fact, msIONPs displayed bacterial association that was not statistically different from the negative control. These quantitative data demonstrate that *S. oneidensis* is bound to 0.9% of the available NPs when exposed to IONPs and to 0.01% of the available msIONPs in that exposure. This was calculated by dividing the bound iron mass by the total iron content present in each exposure.

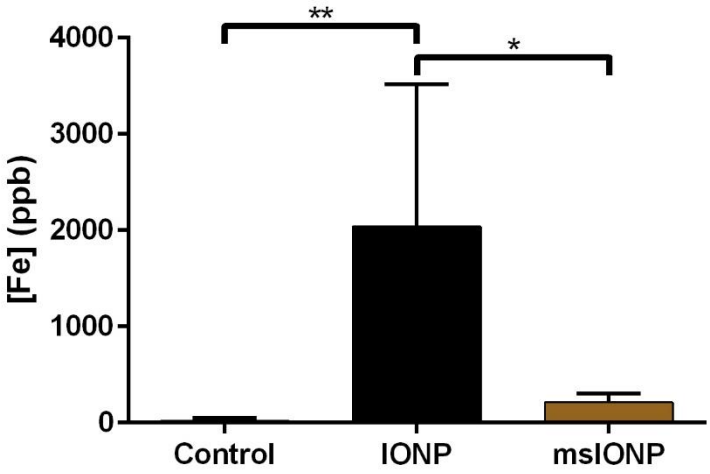

Figure 4.6. Quantitative iron association with *S. oneidensis*. The iron content determined from bacteria that had been exposed to IONPs and msIONPs shows that there is significant iron bound to the surface of IONP-exposed bacteria. Statistical testing was performed with a one-way ANOVA of at least three replicates, using Tukey's multiple comparisons test to compare the effects of each treatment. *p<0.05, **p<0.01

Taken together, these data show that there is significantly more binding of IONPs to the bacterial surface than MSNs or msIONPs. While this observation is important, it was shown in Section 4.4.4 that the bacterial viability after exposure to nanoparticles was recapitulated by the released iron ions, demonstrating that this increased association has negligible contributions to the effects of IONPs to bacterial survival. Therefore, while coating the IONPs with a mesoporous silica shell does reduce the association, this reduced physical association does not contribute to the mitigation of the impact of IONPs on bacterial viability.

4.4.6 Riboflavin Production is Unchanged by Nanoparticle Exposure

Riboflavin secretion is one method by which *S. oneidensis* is capable of respiring extracellular iron oxide. To assess the mechanism that extracellular electron shuttling via riboflavin secretion is contributing to the beneficial impacts seen with IONP exposure, the production of riboflavin in bacteria was monitored via HPLC. Secreted riboflavin, which elutes around 6.3 min with the separation method used, was measured from all of the samples; however, it is noted that the secretion of riboflavin from *S. oneidensis* is not changed by the presence of any of the nanomaterials (Figure 4.7). Given that riboflavin is secreted by bacteria to perform extracellular electron transfers to respire metals, these findings indicate that this extracellular respiration is not a major contributor to the beneficial impact seen with IONPs.

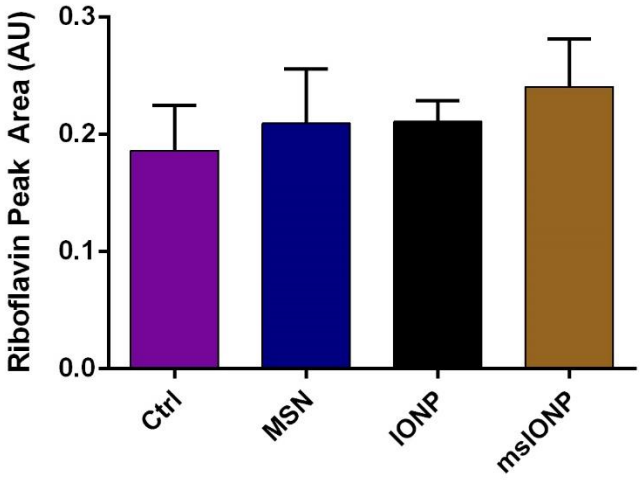

Figure 4.7. Impact of MSNs, IONPs, and msIONPs on riboflavin secretion. The secretion of riboflavin by *S. oneidensis* is not impacted by exposure to any of the nanomaterials used in this study. The error bars represent the standard deviations from six replicates. One-way ANOVA with Tukey's multiple comparisons test was used to determine statistical significance between the treatments.

4.4.7 Changes in Gene Expression are Nanoparticle-Specific

Since it is clear that *S. oneidensis* is using the iron oxide nanoparticles, it was expected that there would be changes in gene expression of bacterial genes relating to the transport, storage, and utilization of iron after exposure to IONPs and their released ion equivalents. To probe this, changes in gene expression after exposure to nanoparticles or to the released iron ion equivalents were monitored using RT-qPCR (Figure 4.8). There was no noted change in the expression of *ribBA*, whose function is in the synthesis of riboflavin. This corroborates the lack of increased production of riboflavin after NP

exposure in the HPLC analysis shown in Figure 4.7, and verifies that this mechanism is not contributing significantly to the impact of IONPs on *S. oneidensis*. Most of the genes that code for proteins that are associated with the membrane of the bacteria, *exbB*, *tonB*, *feoA,* have been upregulated by IONPs and msIONPs, except for *pubA*. The gene, *pubA,* codes for a siderophore that complexes with ferric iron and shuttles it back to the cell for storage via a TonB-dependent siderophore, which suggests it is still related to processes at the bacterial surface.[35] Given that *exbB* and *tonB* both have functions related to the intracellular uptake of iron,[36] it is clear that *S. oneidensis* is working to sequester at least some of the extra iron that it is encountering in the presence of the IONPs or msIONPs; however, the increased bacterial association seen with IONPs helps to facilitate this process better than with msIONPs. For the gene, *ftn*, which corresponds with iron sequestration, there is no change in expression noted, which makes sense given that in an iron-rich environment, the bacterium would not need to store it for later use. Conversely, for *bfd*, a gene that codes for a protein that initiates use of sequestered iron, upregulation is observed. An interesting observation is that there is increased expression of *feoA*, which is specific for ferrous ion transport into the cell.[37] Since our MINTEQ calculations showed that the oxidation state of the majority of released iron would be Fe^{3+}, the increased *feoA* expression suggests that *S. oneidensis* may be processing the nanoparticles to make ferrous ion, which is then transported into the cell for use. The fact that gene expression changes after exposure to IONPs and msIONPs appear to be very similar, and yet only IONP exposure is aiding bacterial survival, indicates that while genes for iron uptake and usage are being upregulated in both exposures, there is more iron present in the IONP exposures for the bacteria to actually use. This highlights the fact that gene expression changes are more sensitive to environmental changes than more macro-level endpoints such as overall bacterial survival.

These observed gene expression changes appear to be nanoparticle-specific, as treatment with equivalent doses of released ions did not induce the same changes. In fact, exposure to ions caused very few gene expression changes, with just a few genes being downregulated upon exposure to 1 ppb Fe^{3+}. We speculate that the observed association of the nanoparticles to the bacteria may be initiating these gene expression changes by dissolving to form a higher localized concentration of iron ions right at the cell surface, especially if the bacteria are also assisting in the dissolution by processing the nanoparticles to generate ferrous ion, as suggested by the upregulation of *feoA*.

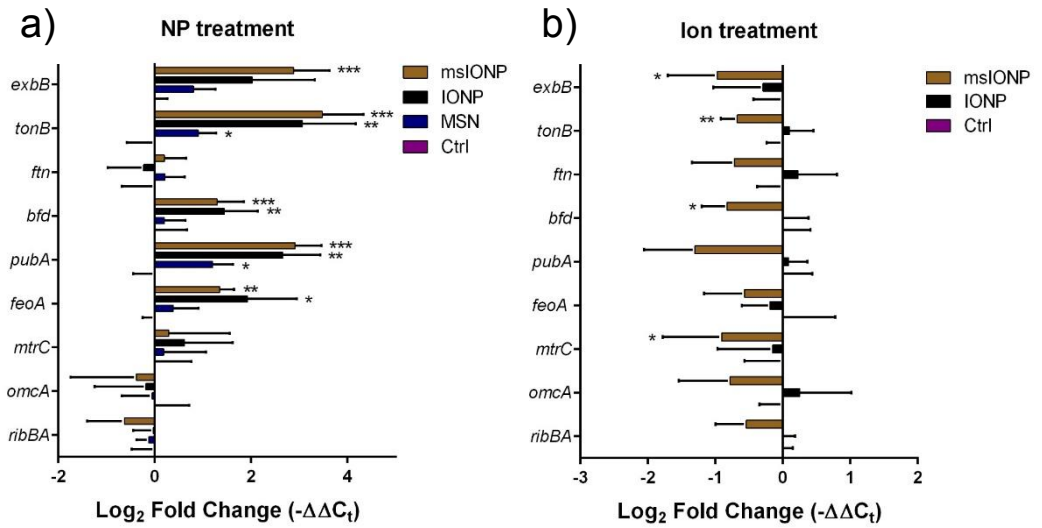

Figure 4.8. Nanoparticle and ion induction of gene expression changes. Gene expression changes in *S. oneidensis* after exposure to a) nanoparticles and b) equivalent released ion concentrations. The error bars represent standard deviations from five replicates. One-way ANOVA with a Dunnett's multiple comparisons test was used to determine statistical significance between the different treatments and the control. *p<0.05, **p<0.01, ***p<0.001

4.5 Conclusions

The work presented herein investigates the impact of IONPs and their mesoporous silica-coated counterparts on *S. oneidensis.* After exposure to the nanoparticles, colony counting reveals that IONPs promote bacterial survival. Exposing *S. oneidensis* to ferric ion at a dose equivalent to released iron from IONPs and msIONPs recapitulates the viability seen with nanoparticle exposure, indicating that ion release is the major contributor to the bacterial impact of IONPs. As expected, the presence of a mesoporous silica shell on IONPs reduced the iron dissolution observed, which explains the mitigated impact of msIONPs on the bacteria. Association between the nanoparticles and *S. oneidensis* shows that there is the greatest bacterial association with IONPs, with minimal association by msIONPs or MSNs. Interestingly, while the ions account for the enhanced bacterial survival after exposure to the nanoparticles, at the genetic level, a nanoparticle-specific effect is observed since the ion controls did not induce the same gene expression changes. Given that the genes impacted upon nanoparticle exposure mostly code for membrane-associated proteins, we speculate that the observed association of nanoparticles with the bacterial membrane may be causing upregulation of these genes. This could be due to a higher localized concentration of iron released near the bacterial surface or simply due to the direct interaction between the nanoparticles and bacterial

membrane. Since perturbations to the environment, whether by increasing or decreasing survival for select organisms, can be detrimental in some situations, the mesoporous silica-coated iron oxide nanoparticles are deemed here to be a better option for sustainability. Given that a mesoporous silica shell should reduce dissolution for other core materials, this strategy could also be applied to more toxic NPs whose major toxicity mechanism is related to dissolution of ions, where it would similarly be expected to reduce harmful impacts to organisms.

Chapter 5

Optimizing the Impact of Mesoporous Silica Nanoparticles on Watermelon Plant Defenses and Growth

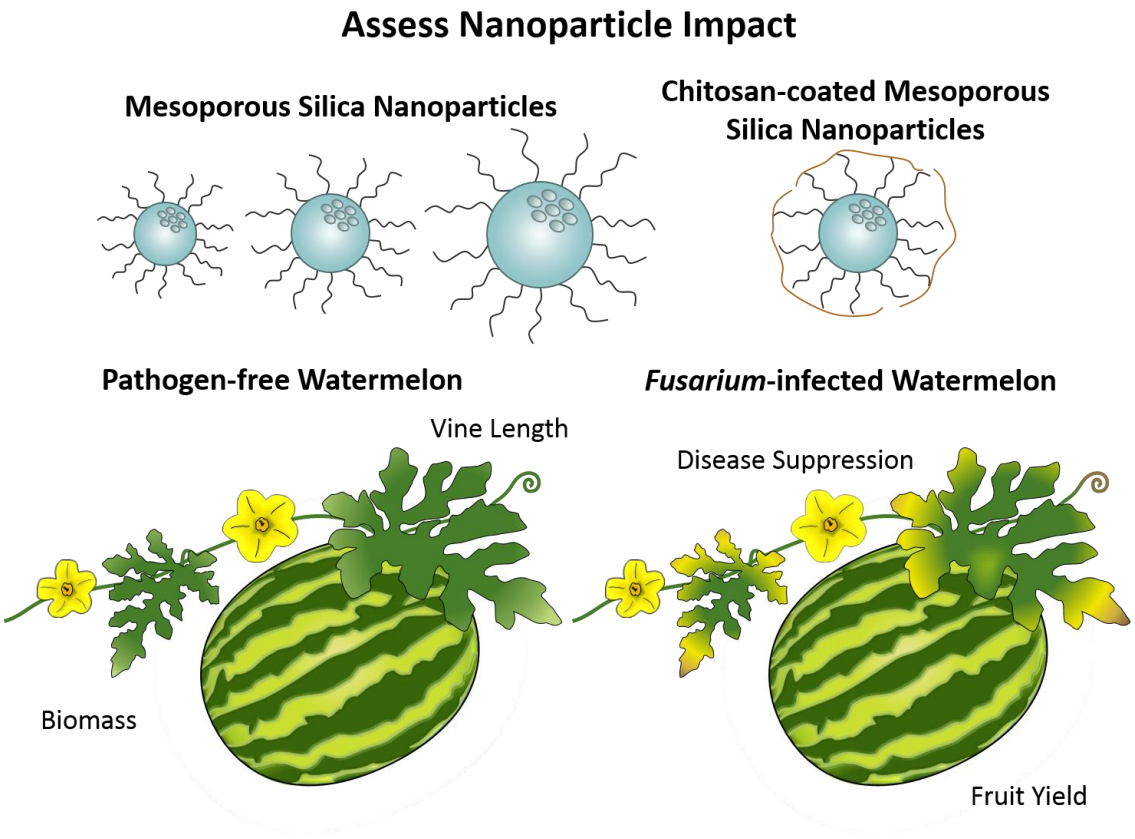

Adapted in part from: Buchman, J.T.; Ma, C.; Landy, K.M.; Hudson-Smith, N.V.; Kang, H.; Elmer, W.; White, J.C.; Haynes, C.L. Tuning mesoporous silica nanoparticle size to optimize impact on watermelon plant health. *In preparation*.

Also adapted in part from: Buchman, J.T.; Elmer, W.; Ma, C.; Landy, K.M.; White, J.C.; Haynes, C.L. Coating mesoporous silica nanoparticles with chitosan improves watermelon plant defenses and growth. *In preparation.*

5.1 Overview

This chapter assesses the impact of micronutrient delivery by mesoporous silica nanoparticles and chitosan-coated mesoporous silica nanoparticles to improve disease suppression in watermelon plants infected with *Fusarium* wilt. The utility of these materials to improve overall plant health was assessed by monitoring the plant biomass, vine length, and fruit production in both healthy and pathogen-infected plants after a single nanoparticle application. In greenhouse studies, mesoporous silica nanoparticles showed no appreciable change in disease severity to *Fusarium*-infected watermelon. However, a nanoparticle size-dependent benefit was seen to overall plant health in pathogen-free plants, as application of smaller mesoporous silica nanoparticles caused improved biomass and vine length at lower doses compared to larger mesoporous silica nanoparticles used in this study. In field studies, both mesoporous silica nanoparticles and chitosan-coated mesoporous silica nanoparticles aided the natural defense mechanisms of watermelon to minimize disease severity as measured by the area under a disease progress curve. In healthy plants, a single application of chitosan-coated mesoporous silica nanoparticles had a significant impact on the fruit yield, leading to an increased mass of produced watermelon. These benefits demonstrate the utility of a single application of mesoporous silica nanoparticles and chitosan-coated mesoporous silica nanoparticles to watermelon at the start of the growing season and represent an excellent opportunity for nanomaterials to promote sustainability in the context of the global food supply.

5.2 Introduction

Every year, 20-40% of crop plants are lost as a result of infection by various diseases.[1] This is a major contributor to the global food shortage currently being experienced. Some diseases are caused by fungal pathogens, such as *Fusarium* wilt caused by *Fusarium oxysporum*.[2] This soilborne pathogen infects the root system of several plants, such as the watermelon plant (*Citrullus lanatus*), which is part of the cucurbit family. After infecting the roots, this fungus is capable of disrupting water transport within the plant's vascular system, causing them to wilt, ultimately killing the plant.[3] For watermelon plants, *Fusarium* wilt is one of the major factors limiting global fruit production.[4] This hardy fungus is capable of surviving six years in soil without the presence of a host,[5] contributing to the challenge of controlling its effects. Given the importance of watermelon as a foodsource, which is grown on 7% of the global land dedicated to vegetable production,[6] understanding ways to mitigate crop loss due to *Fusarium* wilt is necessary. Given that incidence of *Fusarium* wilt to many different plants is on the rise due, in part, to a reduction in agricultural use of

methyl bromide, and management is difficult due to its ability to persist in soil even without the presence of its host,[7] finding methods to manage the impacts of *Fusarium oxysporum* is important.

Micronutrients, such as silicon, play important roles in initiating the defense response of plants against pathogens like *Fusarium*. While silicon accumulation is more prevalent for monocotyledons, the family, *Cucurbitaceae*, are one of a few dicotyledons that uptake and accumulate silicon.[8] This silicon is often acquired as silica, which can transform to release silicic acid and other bioavailable forms of silicon. When taken up by the plant, silicon will often polymerize in the cell walls, forming silica phytoliths that fortify the plant's cell walls.[9] This makes it more challenging for pathogens to penetrate the tissues to infect the plants. Silicon is also capable of stimulating plant defense mechanisms against disease.[10] While micronutrients are beneficial, they are often present in low amounts in soil due to the alkaline conditions or because complexation with organic matter limits their bioavailability.[11,12] As such, exogenous delivery of these nutrients to plants is often necessary. One method with great potential for the efficient delivery of micronutrients, that also conserves raw materials, is the use of slow-dissolving nanoparticles for nutrient delivery.[13] Furthermore, while nutrients such as silicon cannot be translocated basipetally, NPs have a demonstrated ability to efficiently translocate from shoots to roots.[14] The uptake and distribution of mesoporous silica nanoparticles in wheat, lupin, and *Arabidopsis* has been monitored,[15] and silica nanoparticles have demonstrated the ability to improve plant defenses against fungal pathogens.[16]

Other compounds, such as chitosan, are also important in plant disease resistance. While there is some evidence of antifungal behavior from chitosan,[17] its greatest impact is to initiate a signaling cascade within plants to bolster their natural defense mechanisms.[18,19] In fact, chitosan has been applied as a treatment for suppressing plant disease.[20,21] Other benefits of a chitosan treatment for plants include increased plant growth and overall yield of fruit.[22,23] Due to their different pathways to promote disease resistance, chitosan can be combined and co-treated with silica, and together, they have been shown to enhance disease suppression.[24,25]

In this work, the impact of size on nanoscale mesoporous silica's ability to promote watermelon defense was evaluated, as well as the presence of a chitosan coat on the silica surface. Both silicon and chitosan are earth abundant materials; silicon is the second most abundant element in Earth's crust and chitin (the precursor of chitosan) is the second most abundant renewable carbon source,[22] making use of these materials in agriculture

very sustainable. Mesoporous silica nanoparticles were employed because of their increased surface area, which could facilitate faster degradation to monosilicic acid than nonporous silica, and for their ability to load various cargo (i.e. nutrients or pesticides) for a synergistic delivery platform in the future.[26] The size dependence of MSN's benefits to plants was evaluated by assessing the disease suppression of *Fusarium* wilt in infected plants, as well as monitoring their impact on the biomass of vine length of *Fusarium*-infected plants and pathogen-free plants. To assess the impact of chitosan-coated mesoporous silica nanoparticles (CTS-MSNs), the suppression of *Fusarium* wilt, as well as a common foliar disease, powdery mildew, was assessed in plants, while also monitoring changes to the fruit yield of the plants. While some benefit was found in disease reduction for MSNs and CTS-MSNs for infected plants, a majority of the benefit of these nanoparticles was in their application to pathogen-free plants, where an overall increase in biomass, vine length, and fruit production was observed.

5.3 Experimental

5.3.1 Materials

Tetraethylorthosilicate, n-cetyltrimethylammonium bromide, and chitosan (50-190 kDa) were obtained from Sigma-Aldrich (St. Louis, MO). Ammonium hydroxide (NH_4OH, 28-30% as NH_3) was purchased from Avantor Performance Materials (Center Valley, PA). Chlorotrimethyl silane was purchased from Fluka and 2-[methoxy(polyethyleneoxy)$_{9\text{-}12}$propyl]-trimethoxysilane, tech 90 (PEG-silane, molecular weight 591-723 g/mol, 9-12 EO) was obtained from Gelest, Inc. (Morrisville, PA). Ammonium nitrate was purchased from Mallinckrodt (St. Louis, MO). Absolute ethanol was acquired from Pharmco-Aaper (Brookfield, CT). Ultrapure water (18.2 MΩ·cm resistivity) was purified from a Milli-Q Millipore water purification system (Billerica, MA).

5.3.2 Synthesis of Mesoporous Silica Nanoparticles

MSNs were synthesized with a range of sizes (29, 34, 43, and 67 nm) by adapting an established protocol.[27] Briefly, 0.29 g of n-cetyltrimethylammonium bromide was mixed with 150 mL of NH_4OH and stirred (1 hr, 300 rpm, 50 °C). The concentration of NH_4OH [*caution: concentrated NH_4OH is both toxic and corrosive!*] was varied to change the nanoparticle size, using 0.146, 0.212, 0.256, and 0.471 M to make 29, 34, 43, and 69 nm diameter MSNs, respectively. Tetraethylorthosilicate (2.5 mL, 0.88 M) in ethanol was then added dropwise and stirred (1 hr, 600 rpm, 50 °C). Then, 2-[methoxy(polyethyleneoxy)$_{9\text{-}12}$propyl]-trimethoxysilane (450 µL) was added slowly and stirred (30 min, 600 rpm, 50 °C), followed by addition of chlorotrimethylsilane (68 µL). The beaker was immediately covered

and then the mixture was stirred (30 min, 600 rpm, 50 °C). Afterward, the cover was removed and the MSNs were aged at 50 °C for ~20 hours.

To purify the MSNs, they were first ultracentrifuged (30 min, 61,579×*g*) and resuspended in 50 mL of 6 g/L NH_4NO_3 and refluxed (1 hr, 300 rpm, 60 °C). The suspension was again ultracentrifuged (all further ultracentrifugation steps were done for 20 min at 61,579×*g*) and resuspended in 95% ethanol. To complete another reflux (1 hr, 300 rpm, 60 °C), the suspension was ultracentrifuged and resuspended again in 6 g/L NH_4NO_3. To finish purification, the suspension was ultracentrifuged three more times with resuspension in between in the following order: 95% ethanol, 99% ethanol, 99% ethanol. After the final wash step, the MSNs were dried using a rotary evaporator.

5.3.3 Coating MSNs with Chitosan

To coat the 43-nm-diameter MSNs with chitosan, a procedure from Chen et al. was adapted.[28] The chitosan coat adheres to the silica due to hydrogen bonding between the surface silanol groups of MSNs and amine groups on chitosan. A 0.6% w/v solution of chitosan was prepared in 10% v/v aqueous acetic acid. The pH was then adjusted to 6.0 using 1 M NaOH. Dried MSNs were added to the chitosan solution with magnetic stirring to prepare a 0.5% w/v suspension, typically with 100 mg of MSNs added to 20 mL chitosan solution. The suspension was then stirred at room temperature for 48 hours. Excess chitosan was removed via ultracentrifugation at 6842×*g* for 15 minutes. CTS-MSNs were then redispersed in water and collected via rotary evaporation. To characterize the chitosan coating, TEM imaging was used, as well as determination of the hydrodynamic diameter and zeta potential. Changes in the porosity and surface area of the material was monitored with nitrogen physisorption, and the amount of coated chitosan was quantified using thermogravimetric analysis (TGA).

5.3.4 Transmission Electron Microscopy

To prepare the MSNs for imaging with TEM, they were diluted to 0.5 mg/mL in ethanol and sonicated for 10 min to ensure dispersity. Afterward, 200 mesh copper grids with Formvar and carbon supports (Ted Pella, Inc., Redding, CA) were dipped in the suspension and allowed to air dry for 10 min. For the CTS-MSNs, they were first diluted to 0.5 mg/mL in water and sonicated for 10 min. Then, 3 µL of the suspensions were drop-cast onto TEM grids which were allowed to air dry overnight. Images were acquired using a FEI Tecnai T12 transmission electron microscope at a 120 kV operating voltage. To determine the size of the MSNs, the images were analyzed using ImageJ[29] to draw a line

across the diameter of at least 500 randomly selected nanoparticles from each synthetic condition.

5.3.5 Hydrodynamic Diameter and Zeta Potential Measurements

After synthesis of the MSNs and coating of CTS-MSNs, the nanoparticles were suspended in water at 0.5 mg/mL. The nanoparticles were sonicated for 10 min to ensure that they were well-dispersed. The hydrodynamic diameters and ζ-potentials were then determined using a Brookhaven ZetaPALS instrument (Holtsville, NY).

5.3.6 Nitrogen Physisorption

The surface area of the nanoparticles was determined with nitrogen physisorption in order to inform the surface area-based dosing to plants. Surface area-based dosing was used because previous studies, with other organisms and cells, have demonstrated that nanoparticle impacts track with surface area rather than mass.[30] This technique was also used to confirm loading of chitosan onto the MSN surface. To the sample holder, approximately 15 mg of MSNs were added (for CTS-MSNs, >60 mg were required). The samples were degassed prior to analysis with a Micromeritics ASAP™ 2020 (Norcross, GA). The surface area was determined using the BET method.

5.3.7 Thermogravimetric Analysis

To assess the amount of chitosan on the MSN surface, thermogravimetric analysis was used. MSNs and CTS-MSNs were first thoroughly dried using a rotary evaporator overnight. Then, ~10 mg of material were weighed onto an aluminum pan and placed onto a platinum tray. This was analyzed using a TA Instruments Q500 TGA (New Castle, DE) operated at a temperature range from 25-550 °C (ramp rate: 10 °C/min) using 100 mL/min nitrogen gas (40 mL/min for balance, 60 mL/min for sample).

5.3.8 Preparation of Millet Inoculum

To assess the impact of mesoporous silica nanoparticles on the resistance of watermelon to *Fusarium* wilt caused by *Fusarium oxysporum* f. sp. *niveum,* inoculum was increased on Japanese millet using a previously published protocol.[31] The isolate used here was from a colony stored at 4 °C that had originated from a single spore obtained from infected watermelon seeds from CT in 2014. This millet inoculum is used to infest potting soil planted with watermelon to test nanoparticle impact on the plant's ability to resist disease.

5.3.9 Nanoparticle Application to Plants

Prior to nanoparticle administration, watermelon seeds (*Citrullus lanatus* Thunb. cv Sugar Baby, Harris Seed Co., Rochester, NY) were germinated in ProMix BX potting mix

(Premier Hort Tech, Quakertown, PA). Three weeks later, they were fertilized with Peter's soluble 20-10-20 N-P-K fertilizer (40 mL, R. J. Peter's Inc., Allentown, PA). One week after application of fertilizer, the watermelon plants were inverted and dipped in nanoparticle suspensions (containing nanoparticles in water amended with a nonionic surfactant) for approximately 5 sec, keeping the root unexposed. Plants were allowed to drain and dry upside down to minimize root contact with the nanoparticle amendments used for subsequent greenhouse (different sized MSNs) and field experiments (chitosan-coated MSN treatments).

5.3.9.1 Greenhouse Experiments

Suspensions of different sized MSNs were prepared by suspending them in water at surface area-based doses of 338 m^2/L and 85 m^2/L (which correspond to ~400 and 100 mg/L, respectively). One to two drops of Regulaid nonionic surfactant (1 mL/L) was added to each suspension prior to sonication with a probe sonicator for 2 min. The watermelon plants were dipped in these suspensions as noted above and were then transplanted into pots. Separate replicate plants were dipped into a suspension of Regulaid and water without MSNs as controls. There were 16 plants used for each treatment, with eight being transplanted into pathogen-free ProMix BX potting mix and eight transplanted into potting mix containing the prepared millet inoculum (0.75 g/L potting mix). Peter's soluble 20-20-20 N, P, K fertilizer (50 mL) was applied once per month, and a single application of imidacloprid was made for insect control.

Disease progress in the infected watermelon was monitored by determining disease severity after 7, 9, 11, and 13 days, using a 1 to 5 scale (1 = no disease symptoms, 2 = slightly stunted, 3 = stunted and/or partially wilted, 4 = completely wilted, and 5 = dead). The cumulative severity ratings on the plants were plotted as a function of time, and disease progress is represented by the area under the disease progress curve (AUDPC); a higher AUDPC indicates more severe disease progress. The trapezoid rule was used to calculate the AUDPC (Equation 1), following a previously published procedure.[32]

$$\boldsymbol{AUDPC} = \sum \left[\boldsymbol{Y_i} + \boldsymbol{Y_{(i+1)}}\right]/\mathbf{2} \times \left(\boldsymbol{t_{(i+1)}} - \boldsymbol{t_i}\right) \quad (1)$$

In this equation, Y_i is the disease severity rating at time t_i. At the end of the experiments, the vine lengths for the uninfected plants were measured and recorded. Finally, the plants were harvested, and their overall fresh mass was determined, followed by separate determination of their shoot and root mass.

5.3.9.2 Field Experiments

Suspensions of CTS-MSNs and MSNs were prepared at 500 mg/L by suspending them into water. Suspensions of bulk silica and chitosan were prepared by mixing silica (500 mg/L, Strem Chemicals, Inc., Newburyport, MA) and chitosan (500 mg/L) followed by addition of one to two drops of Regulaid nonionic surfactant (1 mL/L). The suspensions were then probe sonicated for 2 min. Watermelon plants were dipped into these suspensions as noted above prior to transplanting into two field locations (Griswold, CT and Hamden, CT). Millet inoculum (~2 g) had been hand mixed into the planting holes (approximately 2 liter volume of soil) for the *Fusarium*-infested treatment groups. There were twelve replicate plants of each treatment, with six plants being exposed to the pathogen, *F. oxysporum*, and six plants being pathogen-free.

After 31, 61, and 95 days post-planting, the watermelon plants at Griswold, CT were assessed for the severity of *Fusarium* wilt as described above to generate an AUDPC measurement for each treatment. After 65 and 100 days in the field, the fruit of the watermelon plants were harvested and the overall mass yielded from each plant was measured. Since it was determined that a foliar application of chitosan-based MSNs could also show improvement in common leaf pathogens, after 89 days in the field, these plants were also evaluated for disease severity of powdery mildew, a disease caused by the fungal pathogen, *Podosphaera xanthi*, which infects the leaves and stems of plants. To measure the severity of powdery mildew, plants were rated on a scale from 1 to 10 (1 = no powdery mildew symptoms, 10 = 100% of plant foliage is affected by powdery mildew).

5.4 Results and Discussion

5.4.1 Greenhouse Experiments

5.4.1.1 Characterization of Different Sized MSNs

To characterize the MSNs of different sizes used in this study, several techniques were used. Transmission electron microscopy was used to visualize nanoparticle morphology and size (Figure 5.1). The varying sized nanoparticles were determined to have the following diameters: 29 ± 5, 34 ± 6, 43 ± 9, and 67 ± 17 nm. These sizes were chosen because nanoparticles may be taken up by porosity in the cell wall of plant cells, and these pores can be as large as 50 nm.[33] Analysis of the ζ-potentials for the different sized MSNs revealed that the surface charge of the 29, 34, 43, and 67 nm MSNs were -15.6 ± 0.2, -26.9 ± 0.5, -15.4 ± 0.4, and -17.3 ± 5.7 mV, respectively. Using nitrogen physisorption, the surface areas of each nanoparticle (in ascending diameter order) were measured to be 845.4, 1036.4, 960.3, and 1025.7 m^2/g with the following pore sizes: 4.5, 3.4, 9.3, and

7.0 nm, respectively. As in previous work, it was noted that there is not much variability to surface area when changing nanoparticle size within this size range.[34] These surface areas were used to inform the surface area-based dosing of NPs to watermelon plants in this study.

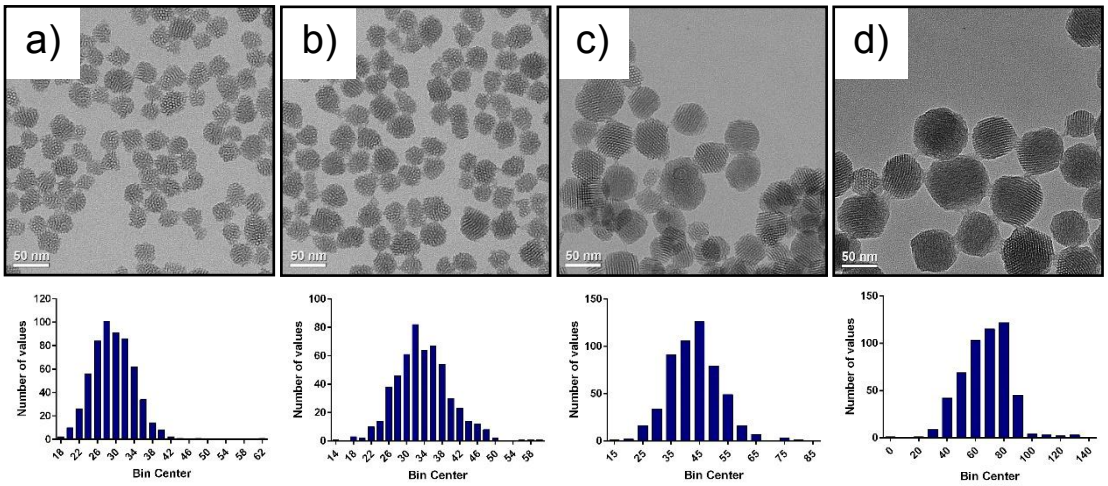

Figure 5.1. Size distribution of MSNs. The size and dispersity of the mesoporous silica nanoparticles were revealed by TEM to be a) 29 ± 5, b) 34 ± 6, c) 43 ± 9, and d) 67 ± 17 nm. Below each TEM image is a histogram depicting the size distribution for each nanoparticle where n > 500. The mesoporous nature of these silica nanoparticles is evident by the lower contrast holes and stripes between the darker contrast silica nanoparticle portions.

5.4.1.2 Role in *Fusarium* Wilt Suppression

Since the size of MSNs will influence both their uptake and dissolution characteristics, thus changing the availability of micronutrients and therefore impact on plants, the ability of MSNs to stimulate watermelon defense mechanisms against *F. oxysporum* in the greenhouse was assessed by calculating the area under the disease progress curve generated from disease severity ratings taken on four different days (Figure 5.2). From these data, it can be seen that, at the concentrations used here, MSNs are not helping watermelon reduce their symptoms from *Fusarium* wilt. Given data that is presented in future sections, it is probable that there was not enough silica in these treatments to elicit an impact to *Fusarium* wilt. The impact of MSNs on other plant attributes were investigated to determine if MSNs were being utilized by the plants.

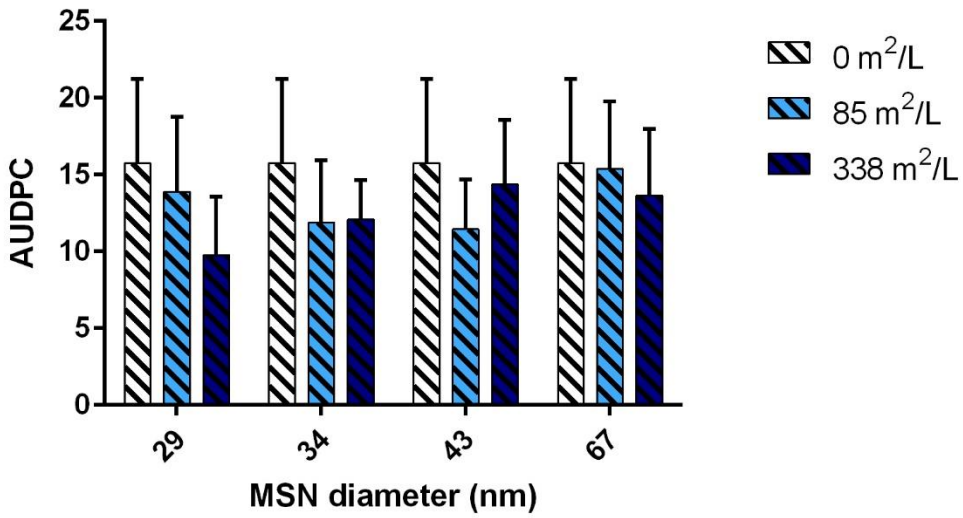

Figure 5.2. MSN impact on disease suppression in watermelon. The area under the disease progress curve was calculated for *F. oxysporum*-infected watermelon plants that had received each treatment as a single high and low surface area-based dose. The error bars represent the standard deviations from eight different plants in each treatment. Note that the 0 m^2/L is from the same control data set that is shown for each MSN diameter to facilitate interpretation. Statistical analysis was performed using a two-way ANOVA with Sidak's multiple comparisons test to compare the different doses to each other within each size regime.

5.4.1.3 Changes in Biomass are Sensitive to MSN Diameter

Another method to assess the health of a plant is by monitoring its biomass. In this work, the overall mass of each plant was determined at the end of the experiment, followed by separate determinations of the root and shoot masses (Figure 5.3). When looking at plants that had not been infected with *Fusarium* wilt, it is clear that there is an increase in biomass after exposure to MSNs. The greatest impact is seen with the 29, 34, and 43-nm-diameter MSNs, which show increased biomasses in plants when dosed at either 85 or 338 m^2/L. An increase in plant biomass is only seen for 67-nm-diameter MSNs at the highest dose tested, which also demonstrates that the NPs do not need to be taken up by the plant to have an impact, since particles of this size are not expected to enter the plant tissues. The benefits of MSNs to watermelon plant growth is observed to be size dependent, with MSNs of smaller diameter having a greater impact. Breakdown of the increased overall growth shows that the mass of aboveground tissues are being increased, while there is minimal increase in root mass seen here. Given that silicon is an important nutrient for the growth of cucurbits, it makes sense that the presence of silica nanoparticles would improve the biomass. A similar size regime for gold nanoparticles has

been reported to be bioavailable for plants, with a reduced accumulation of 50 nm tannate-coated AuNPs compared to 30- and 10-nm AuNPs.[33] Given the foliar application, it also follows that the shoots would benefit more than the plant roots. Assessment of the biomass of *Fusarium*-infected plants shows that there is no change in the mass after dosing with MSNs of any size. Further analysis of the root and shoot masses shows that there are also no significant changes on either part. Given that the MSNs did not have any impact on the progress of *Fusarium* wilt in these plants, it follows that there would be no impact on biomass either.

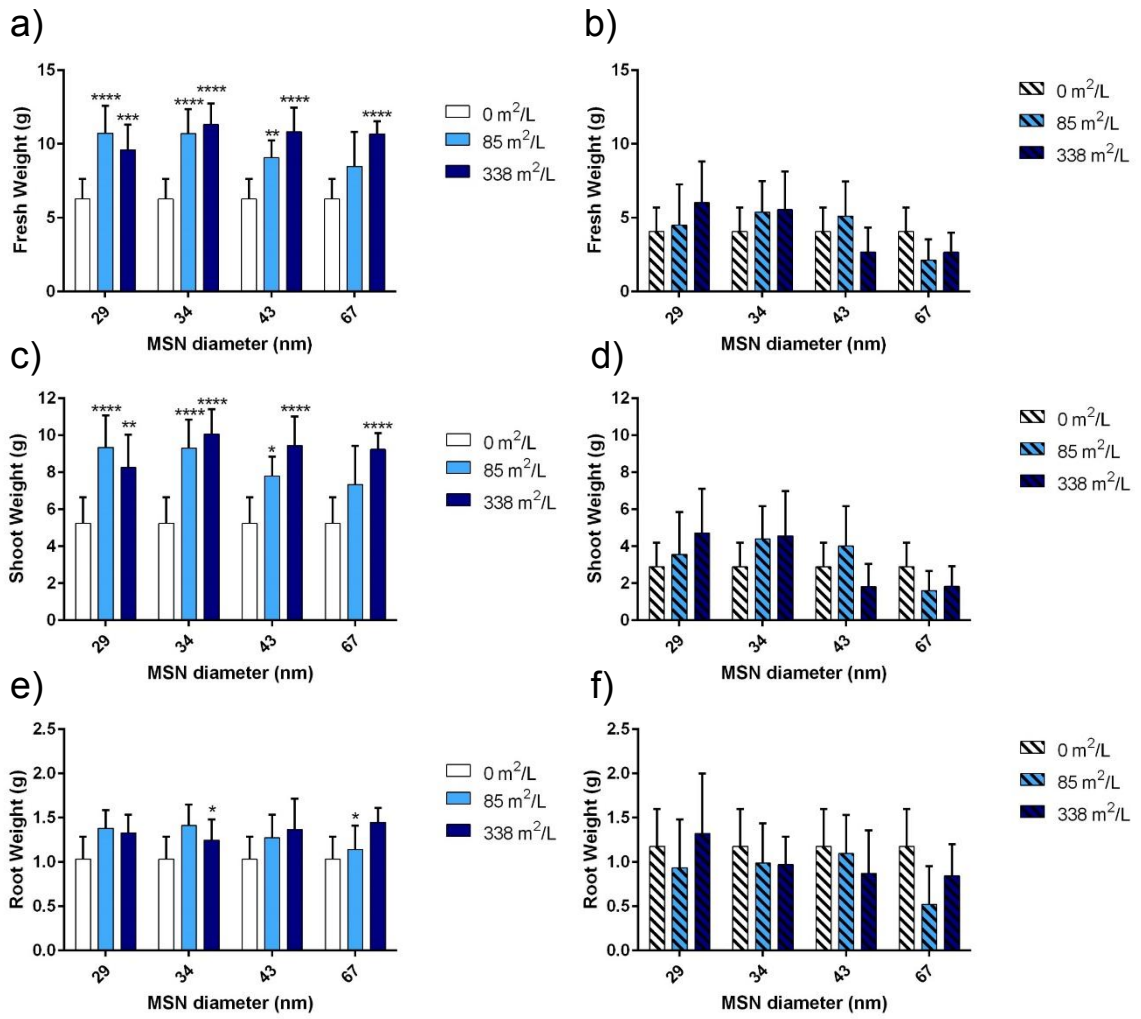

Figure 5.3. Influence of MSN application on plant biomass. Changes in the overall fresh weight of *Citrullus lanatus* are noted in a size-dependent manner for a) pathogen-free plants, whereas no change in overall biomass is observed in b) *Fusarium*-infected watermelon. In c) healthy plants, increases in shoot weight are noted, again in a size-dependent manner, and for d) infected plants, there is no change to shoot weight from any MSNs used in this study. Root weight is largely unchanged in either e) healthy watermelon or f) *Fusarium*-infected plants, with a few significant differences noted in the healthy watermelon. Note that the graphs with angled lines in the bars indicate *Fusarium*-infected watermelon plants. The error bars in these graphs represent the standard deviations from eight plants used in the different treatments. Note that the 0 m^2/L is from the same control data set that is shown for each MSN diameter to facilitate interpretation. Statistical testing was done using a two-way ANOVA with Sidak's multiple comparisons test to compare effects of the different concentrations within each MSN diameter. *p<0.05, **p<0.01, ***p<0.001, ****p<0.0001

5.4.1.4 MSNs Influence Vine Length in a Size-dependent Manner

For plants with running stems, the vine length is another parameter that illustrates overall plant health. Here, the vine length for *Fusarium*-free watermelon plants were determined at the end of the exposure (Figure 5.4); the vine lengths were not determined for *Fusarium*-infected plants due to the lack of change in biomass. It is clear that there is a dependence on overall plant health based on the size of the applied MSNs. For both 29- and 34-nm-diameter MSNs, an increased vine length compared to the control was seen at both concentrations tested. For 43- and 67-nm-diameter-MSNs, a beneficial impact was not observed unless a higher dose (338 m^2/L) was applied to the plants. This is likely because smaller particles can be more efficiently taken up by the plants and translocated through their tissues. Taken together with the biomass data, this demonstrates that, for otherwise healthy plants, application of mesoporous silica nanoparticles can improve the overall health of the plant, with smaller diameter MSNs exhibiting stronger impact on plant health. From a sustainability perspective, these are exciting results, as there is less material with the smaller nanoparticles, meaning that resources are being conserved.

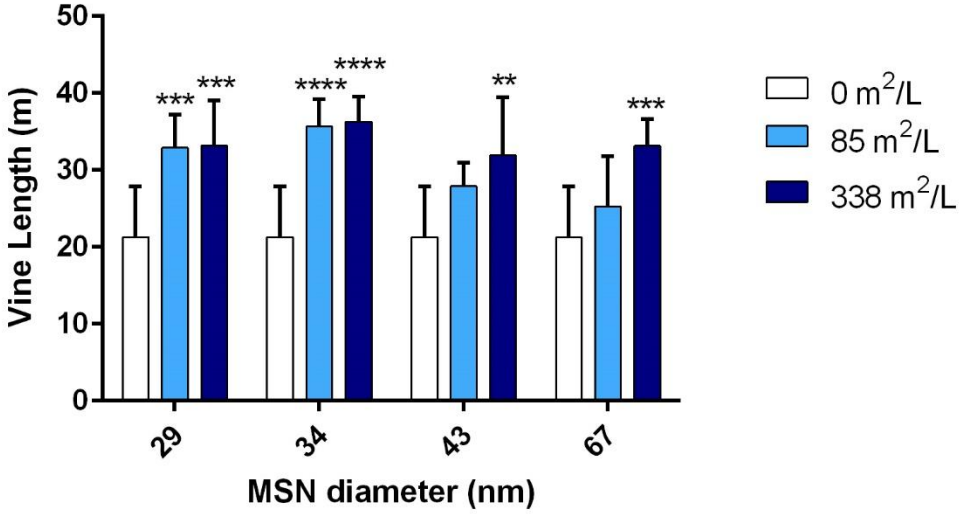

Figure 5.4. MSN application causes increased vine lengths of healthy plants. The vine lengths measured from healthy plants show that the smaller diameter MSNs increase vine length at both concentrations studied, and larger MSNs increase vine length when dosed to the plants at the highest concentration. Note that the 0 m^2/L is from the same control data set that is shown for each MSN diameter to facilitate interpretation. The error bars here are from the standard deviations of measurements from eight different plants, and two-way ANOVA with a Sidak's multiple comparisons test was used to determine significance between the different concentrations within each MSN diameter. **p<0.01, ***p<0.001, ****p<0.0001

5.4.2 Field Experiments

5.4.2.1 Characterization of Chitosan-coated MSNs

When moving from greenhouse studies to field studies, we decided to add chitosan, which also can induce plant defenses, to the mesoporous silica nanoparticles. To characterize the mesoporous silica nanoparticles and their chitosan-coated counterparts, TEM was used to measure the size of the nanoparticles. Three batches of MSNs were coated with chitosan, which had diameters of 36 ± 7, 35 ± 7, and 39 ± 6 nm, as measured from TEM images. Representative TEM images of MSNs before and after coating can be seen in Figure 5.5. Since chitosan is made up of carbon, it is expected that its presence would not be apparent in these images, which is what was observed.

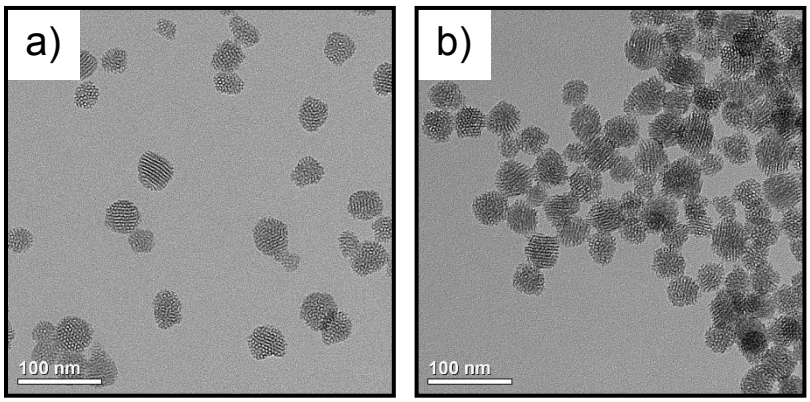

Figure 5.5. Visualization of MSNs and CTS-MSNs. Representative TEM images of a) mesoporous silica nanoparticles without a chitosan coating and after they have been b) coated with chitosan.

The hydrodynamic diameters were measured before and after the chitosan coating, and the ζ-potential measurement was used to confirm the presence of the chitosan coat (Figure 5.6a, b). Results from the hydrodynamic diameter measurements suggest that the particles may be experiencing slight aggregation after being coated with chitosan. Chitosan is a positively charged polysaccharide; therefore, evidence of its successful coating on MSNs is shown by the zeta potential measurements. Uncoated MSNs have a negative zeta potential (-39 ± 3 mV) while chitosan-coated MSNs have a positive zeta potential (24 ± 2 mV). Nitrogen physisorption was employed to observe the surface area and pore volume change that arose from applying the chitosan coating (Figure 5.6c, d). A decrease in both surface area and pore volume indicate that the pores of the MSNs are being coated by the chitosan, decreasing the effective internal surface area of the nanoparticles as well as the pore volume. Also, thermogravimetric analysis was used to determine the mass contribution of chitosan to the chitosan-coated MSNs. From four

replicates of chitosan-coated MSNs, it was found that 22 ± 7% of the mass of the CTS-MSNs was from chitosan.

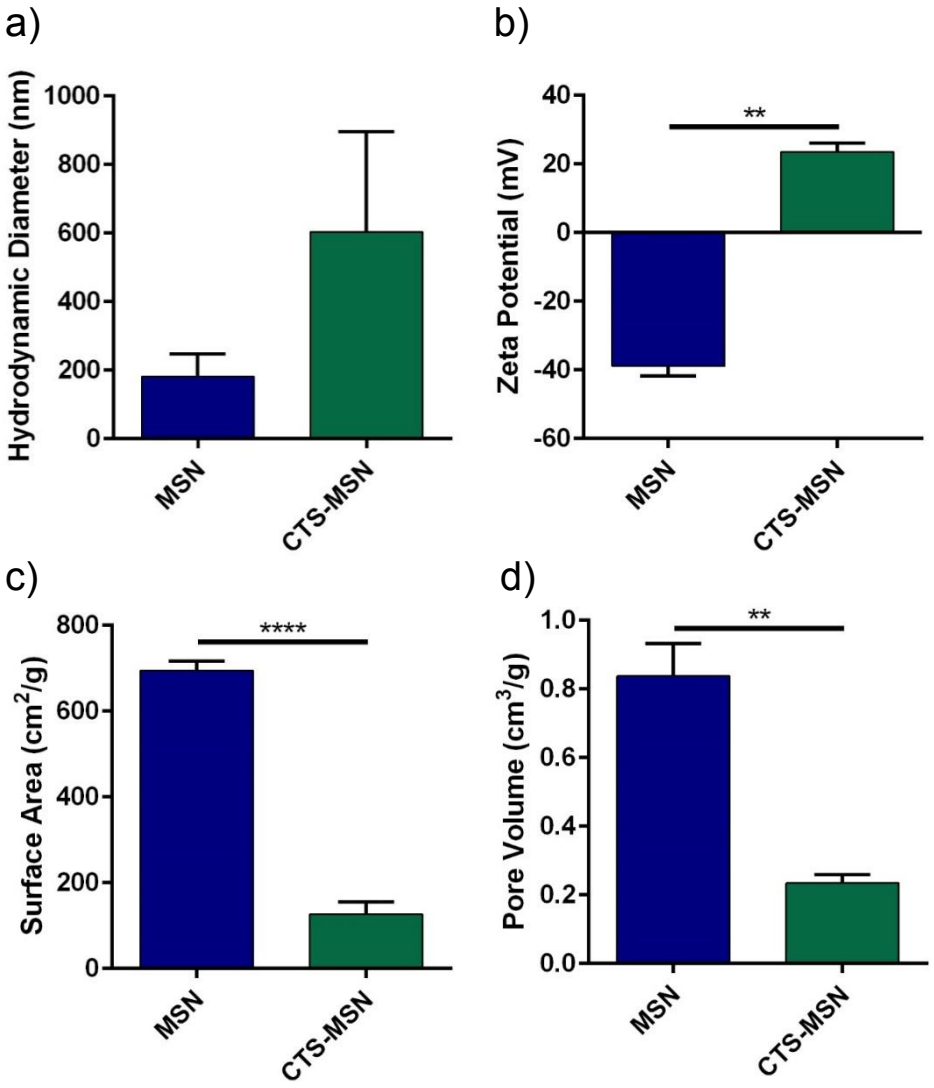

Figure 5.6. Chitosan coating induces changes in MSN characteristics. The a) hydrodynamic diameters were determined before and after application of a chitosan coat. Evidence of the successful chitosan coating can be seen in the zeta potential measurement, which shows that before coating, the MSNs had a negative surface charge and after coating, the surface charge was positive. A c) decrease in the surface area of the particles indicates that the pores were covered with chitosan, blocking the interior surface area of the particles, and d) the pore volume decreased, again due to coverage of the pores by chitosan. The error bars represent the standard deviations from triplicate measurements, and paired t-tests were used to determine statistical significance between the uncoated and coated MSNs. **p<0.01, ****p<0.0001

5.4.2.2 Role in Disease Suppression

While greenhouse experiments allow for better control of environmental conditions, doing experiments in the field present more realistic conditions that will be experienced during the agricultural use of these nanoparticles. In the field experiments, the role of CTS-MSNs in suppressing *Fusarium* wilt was evaluated by determining the area under the disease progress curve as outlined in Section 5.3.9.1. This was used to see if the materials were helping the defense of the plant against the disease (Figure 5.7a, b). In healthy plants, there is no change to the AUDPC, which makes sense, given that they were not infected with *F. oxysporum* and therefore should not be displaying symptoms of *Fusarium* wilt. With infected plants, however, it can be seen that both MSNs and CTS-MSNs improved the plant's ability to defend itself against the disease. Since both MSNs and CTS-MSNs have beneficial impacts, it is clear that the delivery of silica to the plant is helping them resist disease. For the CTS-MSNs, it is also possible that the presence of chitosan is helping to stimulate the immune system of the plants to fight *Fusarium* wilt, although given the lack of response in the chitosan control, it is possible that the MSNs are transporting the chitosan to a location in the plant that is more sensitive to chitosan presence. Interestingly, in the greenhouse experiments presented earlier, MSNs were not enough to aid the infected plants in disease suppression. However, in these field studies, MSNs contributed to disease resistance. In the field studies, MSNs were used at a higher concentration (500 mg/L) than in the greenhouse experiments (~400 mg/L). Therefore, these experiments may be revealing the minimum MSN dose required to help plants suppress *Fusarium* wilt infection.

Since a foliar application was used to treat plants with the different materials used here, the ability of the plants to fight off powdery mildew, a common disease affecting foliage that is caused by *P. xanthi*, was evaluated by assessing symptoms on a 1-10 scale. In the healthy plants and pathogen-infected plants, there does not appear to be any difference in symptoms of powdery mildew with any of the treatments (Figure 5.7c, d). This can indicate that these treatments are ineffective at aiding the plant in defense against powdery mildew.

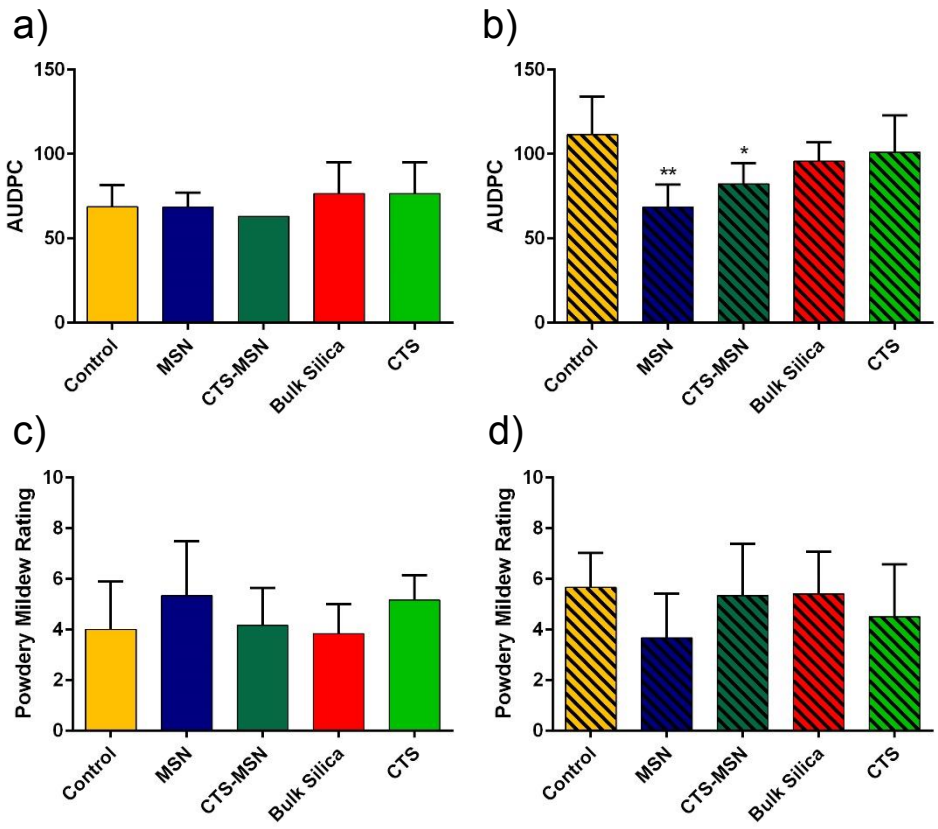

Figure 5.7. The effect of MSN and CTS-MSN applications on disease suppression. In a) healthy plants, there is no difference in the determined AUDPC, demonstrating the minimum value for this quantitative technique in these studies for plants that are not infected with *Fusarium* wilt. In b) *Fusarium*-infected watermelon, both 43 nm MSNs and CTS-MSNs are helping watermelon resist *Fusarium* wilt. As for *P. xanthi* symptoms, there was no change in powdery mildew rating in c) *Fusarium*-free plants or d) *Fusarium*-infected plants. The error bars represent the standard deviations from six plants, with statistical significance testing done using a one-way ANOVA with Dunnett's multiple comparisons test to compare effects of the different treatments to the control. *p<0.05, **p<0.01

5.4.2.3 Impact of Chitosan-coated MSNs on Fruit Yield

An aspect of plant health that is of practical interest is the fruit yield from watermelon plants. Since health benefits were seen with mesoporous silica application to healthy plants in the size-dependent studies, it was hypothesized that these particles and their chitosan-coated counterparts may improve the overall watermelon yield. Watermelon were harvested from the plants 65 and 100 days post-planting, and the cumulative watermelon yield is shown (Figure 5.8). A single application of 500 mg/L CTS-MSNs to healthy plants led to a significantly increased watermelon yield, whereas none of the treatments applied to plants infected with *Fusarium* wilt caused any appreciable change

in fruit production. Since the number of fruits produced was relatively unchanged between treatments, this indicates that CTS-MSNs are encouraging the growth of fruit that is ~50% larger in pathogen-free watermelon plants. These findings also demonstrate a potential economic incentive for applying these nanoparticles to watermelon crops regardless of the presence of *Fusarium oxysporum*.

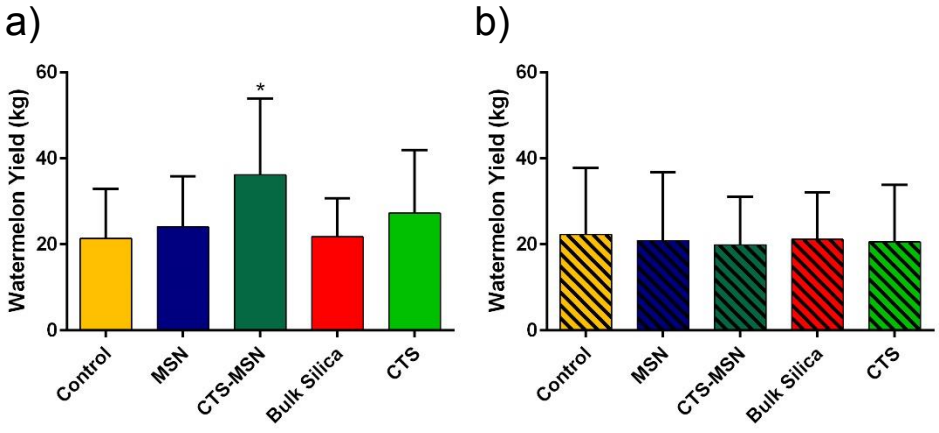

Figure 5.8. Changes in fruit yield after exposure to nanoparticles. When applied to a) pathogen-free watermelon plants, CTS-MSNs are showing a significant increase in the watermelon yield that is not seen from any of the other treatments. For b) *Fusarium*-infected watermelon plants, no change in yield of fruit is seen for any of the nanoparticle treatments used. The error bars are from the standard deviations of twelve replicates. Statistical testing was performed with a one-way ANOVA with Dunnett's multiple comparisons test to compare the treatment effects to the control plants. *p<0.05

5.5 Conclusions

The original inspiration for this work was to synthesize a nanoparticle system that helps watermelon plants defend against *F. oxysporum*, however, a common motif seen throughout this work is that, while there may be some benefit to watermelon plants infected with *Fusarium* wilt, application of MSNs and CTS-MSNs to pathogen-free watermelon appears to have important benefits to overall plant health and fruit yield of pathogen-free plants. Due to the overall improvement of plant health, as measured by an increase in biomass and vine length, it is clear that the watermelon plants are utilizing both MSNs and CTS-MSNs as a source of nutritional silicon. A size-dependence to the improved plant health emerged as the smallest MSNs in this work increased biomass and vine length at the lowest dose used in this study, while the larger MSNs required higher doses to see these improvements. The approximately 50% increase in fruit yield from healthy plants after a single application of CTS-MSNs demonstrates the utility of these materials to

contribute to increased food production from plants, suggesting that there may be economic incentive to dosing watermelon plants with these particles at the start of the season. In future work, the ability for plants to take up and transport mesoporous silica nanoparticles will be investigated using fluorescent mesoporous silica nanoparticles, which will allow for exploration of the mechanism of action.

Bibliography

Chapter 1

(1) Woodrow Wilson International Center for Scholars. Project on Emerging Nanotechnologies: Consumer Products Inventory http://www.nanotechproject.org/cpi/ (accessed Aug 9, 2018).

(2) Qiu, T. A.; Clement, P. L.; Haynes, C. L. Linking Nanomaterial Properties to Biological Outcomes: Analytical Chemistry Challenges in Nanotoxicology for the next Decade. *Chem. Commun.* **2018**, *54*, 12787–12803.

(3) Nel, A.; Xia, T.; Mädler, L.; Li, N. Toxic Potential of Materials at the Nanolevel. *Science.* **2006**, *311*, 622–627.

(4) Djurišić, A. B.; Leung, Y. H.; Ng, A. M. C.; Xu, X. Y.; Lee, P. K. H.; Degger, N.; Wu, R. S. S. Toxicity of Metal Oxide Nanoparticles: Mechanisms, Characterization, and Avoiding Experimental Artefacts. *Small* **2015**, *11*, 26–44.

(5) Caruso, G.; Azzaro, M.; Caroppo, C.; Decembrini, F.; Monticelli, L. S.; Leonardi, M.; Maimone, G.; Zaccone, R.; La Ferla, R. Microbial Community and Its Potential as Descriptor of Environmental Status. *ICES J. Mar. Sci.* **2016**, *73*, 2174–2177.

(6) Hermans, S. M.; Buckley, H. L.; Case, B. S.; Curran-Cournane, F.; Taylor, M.; Lear, G. Bacteria as Emerging Indicators of Soil Condition. *Appl. Environ. Microbiol.* **2017**, *83*, e02826-16.

(7) Moore, M. N. Do Nanoparticles Present Ecotoxicological Risks for the Health of the Aquatic Environment? *Environ. Int.* **2006**, *32*, 967–976.

(8) Fabrega, J.; Luoma, S. N.; Tyler, C. R.; Galloway, T. S.; Lead, J. R. Silver Nanoparticles: Behaviour and Effects in the Aquatic Environment. *Environ. Int.* **2011**, *37*, 517–531.

(9) Tu, Y.; Lv, M.; Xiu, P.; Huynh, T.; Zhang, M.; Castelli, M.; Zengrong, L.; Huang, Q.; Fan, C.; Fang, H.; Zhou, R. Destructive Extraction of Phospholipids from *Escherichia coli* Membranes by Graphene Nanosheets. *Nat. Nanotechnol.* **2013**, *8*, 594–601.

(10) Mensch, A. C.; Hernandez, R. T.; Kuether, J. E.; Torelli, M. D.; Feng, Z. V.; Hamers, R. J.; Pedersen, J. A. Natural Organic Matter Concentration Impacts the Interaction of Functionalized Diamond Nanoparticles with Model and Actual Bacterial Membranes. *Environ. Sci. Technol.* **2017**, *51*, 11075–11084.

(11) Hussain, S.; Garantziotis, S.; Rodrigues-Lima, F.; Dupret, J.-M.; Baeza-Squiban, A.; Boland, S. Intracellular Signal Modulation by Nanomaterials. *Adv. Exp. Med. Biol.* **2014**, *811*, 111–134.

(12) Bondarenko, O.; Ivask, A.; Käkinen, A.; Kurvet, I.; Kahru, A. Particle-Cell Contact Enhances Antibacterial Activity of Silver Nanoparticles. *PLoS One* **2013**, *8*, e64060.

(13) Petersen, E. J.; Nelson, B. C. Mechanisms and Measurements of Nanomaterial-Induced Oxidative Damage to DNA. *Anal. Bioanal. Chem.* **2010**, *398*, 613–650.

(14) Von Moos, N.; Slaveykova, V. I. Oxidative Stress Induced by Inorganic Nanoparticles in Bacteria and Aquatic Microalgae - State of the Art and Knowledge Gaps. *Nanotoxicology* **2014**, *8*, 605–630.

(15) Dickson, J. S.; Koohmaraie, M. Cell Surface Charge Characteristics and Their Relationship to Bacterial Attachment to Meat Surfaces. *Appl. Environ. Microbiol.* **1989**, *55*, 832–836.

(16) Feng, Z. V.; Gunsolus, I. L.; Qiu, T. A.; Hurley, K. R.; Nyberg, L. H.; Frew, H.; Johnson, K. P.; Vartanian, A. M.; Jacob, L. M.; Lohse, S. E.; Torelli, M. D.; Hamers, R. J.; Murphy, C. J.; Haynes, C. L. Impacts of Gold Nanoparticle Charge and Ligand Type on Surface Binding and Toxicity to Gram-Negative and Gram-Positive Bacteria. *Chem. Sci.* **2015**, *6*, 5186–5196.

(17) Jacobson, K. H.; Gunsolus, I. L.; Kuech, T. R.; Troiano, J. M.; Melby, E. S.; Lohse, S. E.; Hu, D.; Chrisler, W. B.; Murphy, C. J.; Orr, G.; Geiger, F. M.; Haynes, C. L.; Pedersen, J. A. Lipopolysaccharide Density and Structure Govern the Extent and Distance of Nanoparticle Interaction with Actual and Model Bacterial Outer Membranes. *Environ. Sci. Technol.* **2015**, *49*, 10642–10650.

(18) Beranová, J.; Seydlová, G.; Kozak, H.; Benada, O.; Fišer, R.; Artemenko, A.; Konopásek, I.; Kromka, A. Sensitivity of Bacteria to Diamond Nanoparticles of Various Size Differs in Gram-Positive and Gram-Negative Cells. *FEMS Microbiol. Lett.* **2014**, *351*, 179–186.

(19) Mensch, A. C.; Buchman, J. T.; Haynes, C. L.; Pedersen, J. A.; Hamers, R. J. Quaternary Amine-Terminated Quantum Dots Induce Structural Changes to Supported Lipid Bilayers. *Langmuir* **2018**, *34*, 12369–12378.

(20) Lai, L.; Li, S.-J.; Feng, J.; Mei, P.; Ren, Z. H.; Chang, Y.-L.; Liu, Y. Effects of Surface Charges on the Bactericide Activity of CdTe/ZnS Quantum Dots: A Cell Membrane Disruption Perspective. *Langmuir* **2017**, *33*, 2378–2386.

(21) Williams, D. N.; Pramanik, S.; Brown, R. P.; Zhi, B.; McIntire, E.; Hudson-Smith, N.

V.; Haynes, C. L.; Rosenzweig, Z. Adverse Interactions of Luminescent Semiconductor Quantum Dots with Liposomes and *Shewanella oneidensis*. *ACS Appl. Nano Mater.* **2018**, *1*, 4788–4800.

(22) Barras, F.; Fontecave, M. Cobalt Stress in *Escherichia coli* and *Salmonella enterica*: Molecular Bases for Toxicity and Resistance. *Metallomics* **2011**, *3*, 1130–1134.

(23) Macomber, L.; Hausinger, R. P. Mechanisms of Nickel Toxicity in Microorganisms. *Metallomics* **2011**, *3*, 1153–1162.

(24) Dupont, C. L.; Grass, G.; Rensing, C. Copper Toxicity and the Origin of Bacterial Resistance - New Insights and Applications. *Metallomics* **2011**, *3*, 1109–1118.

(25) Stohs, S. J.; Bagchi, D. Oxidative Mechanisms in the Toxicity of Metal Ions. *Free Radic. Biol. Med.* **1995**, *18*, 321–336.

(26) Hoshino, N.; Kimura, T.; Yamaji, A.; Ando, T. Damage to the Cytoplasmic Membrane of *Escherichia coli* by Catechin-Copper (II) Complexes. *Free Radic. Biol. Med.* **1999**, *27*, 1245–1250.

(27) Winterbourn, C. C. Toxicity of Iron and Hydrogen Peroxide: The Fenton Reaction. *Toxicol. Lett.* **1995**, *82–83*, 969–974.

(28) Durán, N.; Durán, M.; de Jesus, M. B.; Seabra, A. B.; Fávaro, W. J.; Nakazato, G. Silver Nanoparticles: A New View on Mechanistic Aspects on Antimicrobial Activity. *Nanomedicine Nanotechnology, Biol. Med.* **2016**, *12*, 789–799.

(29) Gunsolus, I. L.; Mousavi, M. P. S.; Hussein, K.; Bühlmann, P.; Haynes, C. L. Effects of Humic and Fulvic Acids on Silver Nanoparticle Stability, Dissolution, and Toxicity. *Environ. Sci. Technol.* **2015**, *49*, 8078–8086.

(30) Mousavi, M. P. S.; Gunsolus, I. L.; Pérez De Jesús, C. E.; Lancaster, M.; Hussein, K.; Haynes, C. L.; Bühlmann, P. Dynamic Silver Speciation as Studied with Fluorous-Phase Ion-Selective Electrodes: Effect of Natural Organic Matter on the Toxicity and Speciation of Silver. *Sci. Total Environ.* **2015**, *537*, 453–461.

(31) Hudson-Smith, N. V.; Clement, P. L.; Brown, R. P.; Krause, M. O. P.; Pedersen, J. A.; Haynes, C. L. Research Highlights: Speciation and Transformations of Silver Released from Ag NPs in Three Species. *Environ. Sci. Nano* **2016**, *3*, 1236–1240.

(32) Xiu, Z.; Zhang, Q.; Puppala, H. L.; Colvin, V. L.; Alvarez, P. J. J. Negligible Particle-Specific Antibacterial Activity of Silver Nanoparticles. *Nano Lett.* **2012**, *12*, 4271–4275.

(33) Hsueh, Y.-H.; Lin, K.-S.; Ke, W.-J.; Hsieh, C.-T.; Chiang, C.-L.; Tzou, D.-Y.; Liu, S.-T. The Antimicrobial Properties of Silver Nanoparticles in *Bacillus subtilis* Are

Mediated by Released Ag^+ Ions. *PLoS One* **2015**, *10*, e0144306.

(34) Hang, M. N.; Gunsolus, I. L.; Wayland, H.; Melby, E. S.; Mensch, A. C.; Hurley, K. R.; Pedersen, J. A.; Haynes, C. L.; Hamers, R. J. Impact of Nanoscale Lithium Nickel Manganese Cobalt Oxide (NMC) on the Bacterium *Shewanella oneidensis* MR-1. *Chem. Mater.* **2016**, *28*, 1092–1100.

(35) Hang, M. N.; Hudson-Smith, N. V.; Clement, P. L.; Zhang, Y.; Wang, C.; Haynes, C. L.; Hamers, R. J. Influence of Nanoparticle Morphology on Ion Release and Biological Impact of Nickel Manganese Cobalt Oxide (NMC) Complex Oxide Nanomaterials. *ACS Appl. Nano Mater.* **2018**, *1*, 1721–1730.

(36) Mahendra, S.; Zhu, H.; Colvin, V. L.; Alvarez, P. J. Quantum Dot Weathering Results in Microbial Toxicity. *Environ. Sci. Technol.* **2008**, *42*, 9424–9430.

(37) Gallagher, M. J.; Buchman, J. T.; Qiu, T. A.; Zhi, B.; Lyons, T. Y.; Landy, K. M.; Rosenzweig, Z.; Haynes, C. L.; Fairbrother, D. H. Release, Detection and Toxicity of Fragments Generated during Artificial Accelerated Weathering of CdSe/ZnS and CdSe Quantum Dot Polymer Composites. *Environ. Sci. Nano* **2018**, *5*, 1694–1710.

(38) Imlay, J. A. The Molecular Mechanisms and Physiological Consequences of Oxidative Stress: Lessons from a Model Bacterium. *Nat. Rev. Microbiol.* **2013**, *11*, 443–454.

(39) Jiang, Y.; Dong, Y.; Luo, Q.; Li, N.; Wu, G.; Gao, H. Protection from Oxidative Stress Relies Mainly on Derepression of OxyR-Dependent KatB and Dps in *Shewanella oneidensis*. *J. Bacteriol.* **2014**, *196*, 445–458.

(40) Smeets, K.; Cuypers, A.; Lambrechts, A.; Semane, B.; Hoet, P.; Van Laere, A.; Vangronsveld, J. Induction of Oxidative Stress and Antioxidative Mechanisms in *Phaseolus vulgaris* after Cd Application. *Plant Physiol. Biochem.* **2005**, *43*, 437–444.

(41) Sobota, J. M.; Imlay, J. A. Iron Enzyme Ribulose-5-Phosphate 3-Epimerase in *Escherichia coli* Is Rapidly Damaged by Hydrogen Peroxide but Can Be Protected by Manganese. *Proc. Natl. Acad. Sci.* **2011**, *108*, 5402–5407.

(42) Anjem, A.; Imlay, J. A. Mononuclear Iron Enzymes Are Primary Targets of Hydrogen Peroxide Stress. *J. Biol. Chem.* **2012**, *287*, 15544–15556.

(43) Kuo, C. F.; Mashino, T.; Fridovich, I. α,β-Dihydroxyisovalerate Dehydratase. A Superoxide-Sensitive Enzyme. *J. Biol. Chem.* **1987**, *262*, 4724–4727.

(44) Galhardo, R. S.; Almeida, C. E. B.; Leitão, A. C.; Cabral-Neto, J. B. Repair of DNA Lesions Induced by Hydrogen Peroxide in the Presence of Iron Chelators in

Escherichia coli: Participation of Endonuclease IV and Fpg. *J. Bacteriol.* **2000**, *182*, 1964–1968.

(45) Imlay, J. A. Cellular Defenses against Superoxide and Hydrogen Peroxide. *Annu. Rev. Biochem.* **2008**, *77*, 755–776.

(46) Park, S.; You, X.; Imlay, J. A. Substantial DNA Damage from Submicromolar Intracellular Hydrogen Peroxide Detected in Hpx$^-$ Mutants of *Escherichia coli*. *Proc. Natl. Acad. Sci.* **2005**, *102*, 9317–9322.

(47) Kaweeteerawat, C.; Ivask, A.; Liu, R.; Zhang, H.; Chang, C. H.; Low-Kam, C.; Fischer, H.; Ji, Z.; Pokhrel, S.; Cohen, Y.; Telesca, D.; Zink, J.; Mädler, L.; Holden, P. A.; Nel, A.; Godwin, H. Toxicity of Metal Oxide Nanoparticles in *Escherichia coli* Correlates with Conduction Band and Hydration Energies. *Environ. Sci. Technol.* **2015**, *49*, 1105–1112.

(48) Wang, D.; Zhao, L.; Ma, H.; Zhang, H.; Guo, L.-H. Quantitative Analysis of Reactive Oxygen Species Photogenerated on Metal Oxide Nanoparticles and Their Bacteria Toxicity: The Role of Superoxide Radicals. *Environ. Sci. Technol.* **2017**, *51*, 10137–10145.

(49) Domínguez, G. A.; Torelli, M. D.; Buchman, J. T.; Haynes, C. L.; Hamers, R. J.; Klaper, R. D. Size Dependent Oxidative Stress Response of the Gut of *Daphnia magna* to Functionalized Nanodiamond Particles. *Environ. Res.* **2018**, *167*, 267–275.

(50) Joshi, N.; Ngwenya, B. T.; Butler, I. B.; French, C. E. Use of Bioreporters and Deletion Mutants Reveals Ionic Silver and ROS to Be Equally Important in Silver Nanotoxicity. *J. Hazard. Mater.* **2015**, *287*, 51–58.

(51) Gunsolus, I. L.; Hang, M. N.; Hudson-Smith, N. V; Buchman, J. T.; Bennett, J. W.; Conroy, D.; Mason, S. E.; Hamers, R. J.; Haynes, C. L. Influence of Nickel Manganese Cobalt Oxide Nanoparticle Composition on Toxicity toward *Shewanella oneidensis* MR-1: Redesigning for Reduced Biological Impact. *Environ. Sci. Nano* **2017**, *4*, 636–646.

(52) Arakha, M.; Saleem, M.; Mallick, B. C.; Jha, S. The Effects of Interfacial Potential on Antimicrobial Propensity of ZnO Nanoparticle. *Sci. Rep.* **2015**, *5*, 9578.

(53) El Badawy, A. M.; Silva, R. G.; Morris, B.; Scheckel, K. G.; Suidan, M. T.; Tolaymat, T. M. Surface Charge-Dependent Toxicity of Silver Nanoparticles. *Environ. Sci. Technol.* **2011**, *45*, 283–287.

(54) Xu, L.; Yang, J.; Xue, B.; Zhang, C.; Shi, L.; Wu, C.; Su, Y.; Jin, X.; Liu, Y.; Zhu, X.

Molecular Insights for the Biological Interactions between Polyethylene Glycol and Cells. *Biomaterials* **2017**, *147*, 1–13.

(55) Tejamaya, M.; Römer, I.; Merrifield, R. C.; Lead, J. R. Stability of Citrate, PVP, and PEG Coated Silver Nanoparticles in Ecotoxicology Media. *Environ. Sci. Technol.* **2012**, *46*, 7011–7017.

(56) Pramanik, S.; Hill, S. K. E.; Zhi, B.; Hudson-Smith, N. V.; Wu, J. J.; White, J. N.; McIntire, E. A.; Kondeti, V. S. S. K.; Lee, A. L.; Bruggeman, P. J.; Kortshagen, U. R.; Haynes, C. L. Comparative Toxicity Assessment of Novel Si Quantum Dots and Their Traditional Cd-Based Counterparts Using Bacteria Models *Shewanella oneidensis* and *Bacillus subtilis*. *Environ. Sci. Nano* **2018**, *5*, 1890–1901.

(57) Zhi, B.; Mishra, S.; Hudson-Smith, N. V.; Kortshagen, U. R.; Haynes, C. L. Toxicity Evaluation of Boron- and Phosphorous-Doped Silicon Nanocrystals towards *Shewanella oneidensis* MR-1. *ACS Appl. Nano Mater.* **2018**, *1*, 4884–4893.

(58) Li, Y.; Kröger, M.; Liu, W. K. Shape Effect in Cellular Uptake of PEGylated Nanoparticles: Comparison between Sphere, Rod, Cube and Disk. *Nanoscale* **2015**, *7*, 16631–16646.

(59) George, S.; Lin, S.; Ji, Z.; Thomas, C. R.; Li, L.; Mecklenburg, M.; Meng, H.; Wang, X.; Zhang, H.; Xia, T.; Hohman, J. N.; Lin, S.; Zink, J. I.; Weiss, P. S.; Nel, A. E. Surface Defects on Plate-Shaped Silver Nanoparticles Contribute to Its Hazard Potential in a Fish Gill Cell Line and Zebrafish Embryos. *ACS Nano* **2012**, *6*, 3745–3759.

(60) Manthiram, A. An Outlook on Lithium Ion Battery Technology. *ACS Cent. Sci.* **2017**, *3*, 1063–1069.

(61) Nitta, N.; Wu, F.; Lee, J. T.; Yushin, G. Li-Ion Battery Materials: Present and Future. *Mater. Today* **2015**, *18*, 252–264.

(62) Xia, T.; Zhao, Y.; Sager, T.; George, S.; Pokhrel, S.; Li, N.; Schoenfeld, D.; Meng, H.; Lin, S.; Wang, X.; Wang, M.; Ji, Z.; Zink, J. I.; Mädler, L.; Castranova, V.; Lin, S.; Nel, A. E. Decreased Dissolution of ZnO by Iron Doping Yields Nanoparticles with Reduced Toxicity in the Rodent Lung and Zebrafish Embryos. *ACS Nano* **2011**, *5*, 1223–1235.

(63) Wu, F.; Harper, B. J.; Harper, S. L. Differential Dissolution and Toxicity of Surface Functionalized Silver Nanoparticles in Small-Scale Microcosms: Impacts of Community Complexity. *Environ. Sci. Nano* **2017**, *4*, 359–372.

(64) Derfus, A. M.; Chan, W. C. W.; Bhatia, S. N. Probing the Cytotoxicity of

Semiconductor Quantum Dots. *Nano Lett.* **2004**, *4*, 11–18.

(65) Li, Y.; Zhang, W.; Li, K.; Yao, Y.; Niu, J.; Chen, Y. Oxidative Dissolution of Polymer-Coated CdSe/ZnS Quantum Dots under UV Irradiation: Mechanisms and Kinetics. *Environ. Pollut.* **2012**, *164*, 259–266.

(66) Gao, Z.; Burrows, N. D.; Valley, N. A.; Schatz, G. C.; Murphy, C. J.; Haynes, C. L. In Solution SERS Sensing Using Mesoporous Silica-Coated Gold Nanorods. *Analyst* **2016**, *141*, 5088–5095.

(67) Mahoney, S.; Najera, M.; Bai, Q.; Burton, E. A.; Veser, G. The Developmental Toxicity of Complex Silica-Embedded Nickel Nanoparticles Is Determined by Their Physicochemical Properties. *PLoS One* **2016**, *11*, e0152010.

(68) Boran, H.; Şaffak, S. Comparison of Dissolved Nickel and Nickel Nanoparticles Toxicity in Larval Zebrafish in Terms of Gene Expression and DNA Damage. *Arch. Environ. Contam. Toxicol.* **2018**, *74*, 193–202.

(69) Ispas, C.; Andreescu, D.; Patel, A.; Goia, D. V; Wallace, K. N. Toxicity and Developmental Defects of Different Sizes and Shape Nickel Nanoparticles in Zebrafish. *Environ. Sci. Technol.* **2009**, *43*, 6349–6356.

(70) Misra, S. K.; Dybowska, A.; Berhanu, D.; Luoma, S. N.; Valsami-Jones, E. The Complexity of Nanoparticle Dissolution and Its Importance in Nanotoxicological Studies. *Sci. Total Environ.* **2012**, *438*, 225–232.

(71) Helmlinger, J.; Sengstock, C.; Groß-Heitfeld, C.; Mayer, C.; Schildhauer, T. A.; Köller, M.; Epple, M. Silver Nanoparticles with Different Size and Shape: Equal Cytotoxicity, but Different Antibacterial Effects. *RSC Adv.* **2016**, *6*, 18490–18501.

(72) Huang, Y.; Keller, A. A. EDTA Functionalized Magnetic Nanoparticle Sorbents for Cadmium and Lead Contaminated Water Treatment. *Water Res.* **2015**, *80*, 159–168.

(73) Liu, G.; Men, P.; Perry, G.; Smith, M. A. Nanoparticle and Iron Chelators as a Potential Novel Alzheimer Therapy. *Methods Mol. Biol.* **2010**, *610*, 123–144.

(74) Brunetti, V.; Chibli, H.; Fiammengo, R.; Galeone, A.; Malvindi, M. A.; Vecchio, G.; Cingolani, R.; Nadeau, J. L.; Pompa, P. P. InP/ZnS as a Safer Alternative to CdSe/ZnS Core/Shell Quantum Dots: In Vitro and in Vivo Toxicity Assessment. *Nanoscale* **2013**, *5*, 307–317.

(75) Zhu, S.; Song, Y.; Zhao, X.; Shao, J.; Zhang, J.; Yang, B. The Photoluminescence Mechanism in Carbon Dots (Graphene Quantum Dots, Carbon Nanodots, and Polymer Dots): Current State and Future Perspective. *Nano Res.* **2015**, *8*, 355–

381.

(76) Zhi, B.; Gallagher, M. J.; Frank, B. P.; Lyons, T. Y.; Qiu, T. A.; Da, J.; Mensch, A. C.; Hamers, R. J.; Rosenzweig, Z.; Fairbrother, D. H.; Haynes, C. L. Investigation of Phosphorous Doping Effects on Polymeric Carbon Dots: Fluorescence, Photostability, and Environmental Impact. *Carbon N. Y.* **2018**, *129*, 438–449.

(77) Xie, X.; Mao, C.; Liu, X.; Tan, L.; Cui, Z.; Yang, X.; Zhu, S.; Li, Z.; Yuan, X.; Zheng, Y.; Yeung, K. W. K.; Chu, P. K.; Wu, S. Tuning the Bandgap of Photo-Sensitive Polydopamine/Ag_3PO_4/Graphene Oxide Coating for Rapid, Noninvasive Disinfection of Implants. *ACS Cent. Sci.* **2018**, *4*, 724–738.

(78) George, S.; Pokhrel, S.; Ji, Z.; Henderson, B. L.; Xia, T.; Li, L.; Zing, J. I.; Nel, A. E.; Mädler, L. Role of Fe Doping in Tuning the Band Gap of TiO_2 for Photooxidation Induced Cytotoxicity Paradigm. *J. Am. Chem. Soc.* **2011**, *133*, 11270–11278.

(79) Ahamed, M.; Khan, M. A. M.; Akhtar, M. J.; Alhadlaq, H. A.; Alshamsan, A. Role of Zn Doping in Oxidative Stress Mediated Cytotoxicity of TiO_2 Nanoparticles in Human Breast Cancer MCF-7 Cells. *Sci. Rep.* **2016**, *6*, 30196.

(80) Akhtar, M. J.; Alhadlaq, H. A.; Alshamsan, A.; Khan, M. A. M.; Ahamed, M. Aluminum Doping Tunes Band Gap Energy Level as Well as Oxidative Stress-Mediated Cytotoxicity of ZnO Nanoparticles in MCF-7 Cells. *Sci. Rep.* **2015**, *5*, 13876.

(81) Zhang, H.; Pokhrel, S.; Ji, Z.; Meng, H.; Wang, X.; Lin, S.; Chang, C. H.; Li, L.; Li, R.; Sun, B.; Wang, M.; Liao, Y.-P.; Liu, R.; Xia, T.; Mädler, L.; Nel, A. E. PdO Doping Tunes Band-Gap Energy Levels as Well as Oxidative Stress Responses to a Co_3O_4 p-Type Semiconductor in Cells and the Lung. *J. Am. Chem. Soc.* **2014**, *136*, 6406–6420.

(82) Smith, A. M.; Nie, S. Semiconductor Nanocrystals: Structure, Properties, and Band Gap Engineering. *Acc. Chem. Res.* **2010**, *43*, 190–200.

(83) Sharpe, E.; Andreescu, D.; Andreescu, S. Artificial Nanoparticle Antioxidants. In *Oxidative Stress: Diagnostics, Prevention, and Therapy*; American Chemical Society: Washington, DC, USA, 2011; Vol. 1083, pp 235–253.

(84) Nie, Z.; Liu, K. J.; Zhong, C.-J.; Wang, L.-F.; Yang, Y.; Tian, Q.; Liu, Y. Enhanced Radical Scavenging Activity by Antioxidant-Functionalized Gold Nanoparticles: A Novel Inspiration for Development of New Artificial Antioxidants. *Free Radic. Biol. Med.* **2007**, *43*, 1243–1254.

(85) Leu, J.-G.; Chen, S.-A.; Chen, H.-M.; Wu, W.-M.; Hung, C.-F.; Yao, Y.-D.; Tu, C.-

S.; Liang, Y.-J. The Effects of Gold Nanoparticles in Wound Healing with Antioxidant Epigallocatechin Gallate and α-Lipoic Acid. *Nanomedicine Nanotechnology, Biol. Med.* **2012**, *8*, 767–775.

(86) Du, L.; Suo, S.; Wang, G.; Jia, H.; Liu, K. J.; Zhao, B.; Liu, Y. Mechanism and Cellular Kinetic Studies of the Enhancement of Antioxidant Activity by Using Surface-Functionalized Gold Nanoparticles. *Chem. - A Eur. J.* **2013**, *19*, 1281–1287.

(87) Sistanipour, E.; Meshkini, A.; Oveisi, H. Catechin-Conjugated Mesoporous Hydroxyapatite Nanoparticle: A Novel Nano-Antioxidant with Enhanced Osteogenic Property. *Colloids Surfaces B Biointerfaces* **2018**, *169*, 329–339.

(88) Viglianisi, C.; Di Pilla, V.; Menichetti, S.; Rotello, V. M.; Candiani, G.; Malloggi, C.; Amorati, R. Linking an α-Tocopherol Derivative to Cobalt(0) Nanomagnets: Magnetically Responsive Antioxidants with Superior Radical Trapping Activity and Reduced Cytotoxicity. *Chem. - A Eur. J.* **2014**, *20*, 6857–6860.

Chapter 2

(1) Naeem, S.; Hahn, D. R.; Schuurman, G. Producer–decomposer Co-dependency Influences Biodiversity Effects. *Nature* **2000**, *403*, 762–764.

(2) Borcherding, J.; Baltrusaitis, J.; Chen, H.; Stebounova, L.; Wu, C.-M.; Rubasinghege, G.; Mudunkotuwa, I. A.; Caraballo, J. C.; Zabner, J.; Grassian, V. H.; Comellas, A. P. Iron Oxide Nanoparticles Induce *Pseudomonas aeruginosa* Growth, Induce Biofilm Formation, and Inhibit Antimicrobial Peptide Function. *Environ. Sci. Nano* **2014**, *1*, 123–132.

(3) Ostermeyer, A.-K.; Mumuper, C. K.; Semprini, L.; Radniecki, T. Influence of Bovine Serum Albumin and Alginate on Silver Nanoparticle Dissolution and Toxicity to *Nitrosomonas europaea*. *Environ. Sci. Technol.* **2013**, *47*, 14403–14410.

(4) Gunsolus, I. L.; Hang, M. N.; Hudson-Smith, N. V; Buchman, J. T.; Bennett, J. W.; Conroy, D.; Mason, S. E.; Hamers, R. J.; Haynes, C. L. Influence of Nickel Manganese Cobalt Oxide Nanoparticle Composition on Toxicity toward *Shewanella oneidensis* MR-1: Redesigning for Reduced Biological Impact. *Environ. Sci. Nano* **2017**, *4*, 636–646.

(5) Feng, Z. V.; Gunsolus, I. L.; Qiu, T. A.; Hurley, K. R.; Nyberg, L. H.; Frew, H.; Johnson, K. P.; Vartanian, A. M.; Jacob, L. M.; Lohse, S. E.; Torelli, M. D.; Hamers, R. J.; Murphy, C. J.; Haynes, C. L. Impacts of Gold Nanoparticle Charge and Ligand

Type on Surface Binding and Toxicity to Gram-Negative and Gram-Positive Bacteria. *Chem. Sci.* **2015**, *6*, 5186–5196.

(6) Liu, L.; Yang, J.; Xie, J.; Luo, Z.; Jiang, J.; Yang, Y. Y.; Liu, S. The Potent Antimicrobial Properties of Cell Penetrating Peptide-Conjugated Silver Nanoparticles with Excellent Selectivity for Gram-Positive Bacteria over Erythrocytes. *Nanoscale* **2013**, *5*, 3834–3840.

(7) Li, Z.; Greden, K.; Alvarez, P. J. J.; Gregory, K. B.; Lowry, G. V. Adsorbed Polymer and NOM Limits Adhesion and Toxicity of Nano Scale Zerovalent Iron to *E. coli*. *Environ. Sci. Technol.* **2010**, *44*, 3462–3467.

(8) Zhao, Y.; Chen, Z.; Chen, Y.; Xu, J.; Li, J.; Jiang, X. Synergy of Non-Antibiotic Drugs and Pyrimidinethiol on Gold Nanoparticles against Superbugs. *J. Am. Chem. Soc.* **2013**, *135*, 12940–12943.

(9) Goodman, C. M.; McCusker, C. D.; Yilmaz, T.; Rotello, V. M. Toxicity of Gold Nanoparticles Functionalized with Cationic and Anionic Side Chains. *Bioconjug. Chem.* **2004**, *15*, 897–900.

(10) Tu, Y.; Lv, M.; Xiu, P.; Huynh, T.; Zhang, M.; Castelli, M.; Zengrong, L.; Huang, Q.; Fan, C.; Fang, H.; Zhou, R. Destructive Extraction of Phospholipids from *Escherichia coli* Membranes by Graphene Nanosheets. *Nat. Nanotechnol.* **2013**, *8*, 594–601.

(11) Pelgrift, R. Y.; Friedman, A. J. Nanotechnology as a Therapeutic Tool to Combat Microbial Resistance. *Adv. Drug Deliv. Rev.* **2013**, *65*, 1803–1815.

(12) Bondarenko, O.; Ivask, A.; Käkinen, A.; Kurvet, I.; Kahru, A. Particle-Cell Contact Enhances Antibacterial Activity of Silver Nanoparticles. *PLoS One* **2013**, *8*, e64060.

(13) Foster, H. A.; Ditta, I. B.; Varghese, S. Photocatalytic Disinfection Using Titanium Dioxide: Spectrum and Mechanism of Antimicrobial Activity. *Appl. Microbiol. Biotechnol.* **2011**, *90*, 1847–1868.

(14) Jacobson, K. H.; Gunsolus, I. L.; Kuech, T. R.; Troiano, J. M.; Melby, E. S.; Lohse, S. E.; Hu, D.; Chrisler, W. B.; Murphy, C. J.; Orr, G.; Geiger, F. M.; Haynes, C. L.; Pedersen, J. A. Lipopolysaccharide Density and Structure Govern the Extent and Distance of Nanoparticle Interaction with Actual and Model Bacterial Outer Membranes. *Environ. Sci. Technol.* **2015**, *49*, 10642–10650.

(15) Rediers, H.; Vanderleyden, J.; De Mot, R. *Azotobacter vinelandii*: A *Pseudomonas* in Disguise? *Microbiology* **2004**, *150*, 1117–1119.

(16) Gaona, G.; Nuñez, C.; Goldberg, J. B.; Linford, A. S.; Nájera, R.; Castañeda, M.;

Guzmán, J.; Espín, G.; Soberón-Chávez, G. Characterization of the *Azotobacter vinelandii algC* Gene Involved in Alginate and Lipopolysaccharide Production. *FEMS Microbiol. Lett.* **2004**, *238*, 199–206.

(17) Dijkshoorn, L.; Nemec, A.; Vaneechoutte, M.; De Baere, T.; Pantophlet, R. A.; Williams, P. A.; Kay, C. M.; Averhoff, B.; Graf, I.; Ornston, L. N.; Schlimpert, S.; Buchan, A.; Parke, D.; Craven, S. H.; Ezezika, O. C.; Momany, C.; Neidle, E. L.; Gerischer, U.; Jerg, B.; Fischer, R.; Gutnick, D. L.; Bach, H.; Tomaras, A. P.; Dorsey, C. W.; McQueary, C.; Actis, L. A.; Seifert, H.; Wisplinghoff, H.; Towner, K. J. *Acinetobacter* Molecular Microbiology; Gerischer, U., Ed.; Caister Academic Press: Norfolk, UK, 2008.

(18) Hau, H. H.; Gralnick, J. A. Ecology and Biotechnology of the Genus *Shewanella*. *Annu. Rev. Microbiol.* **2007**, *61*, 237–258.

(19) Vinogradov, E.; Korenevsky, A.; Beveridge, T. J. The Structure of the Rough-Type Lipopolysaccharide from *Shewanella oneidensis* MR-1, Containing 8-Amino-8-Deoxy-Kdo and an Open-Chain Form of 2-Acetamido-2-Deoxy-D-Galactose. *Carbohydr. Res.* **2003**, *338*, 1991–1997.

(20) Vinogradov, E.; Kubler-Kielb, J.; Korenevsky, A. The Structure of the Carbohydrate Backbone of the LPS from *Shewanella* spp. MR-4. *Carbohydr. Res.* **2008**, *343*, 2701–2705.

(21) Stover, C. K.; Pham, X. Q.; Erwin, A. L.; Mizoguchi, S. D.; Warrener, P.; Hickey, M. J.; Brinkman, F. S. L.; Hufnagle, W. O.; Kowalik, D. J.; Lagrou, M.; Garber, R. L.; Goltry, L.; Tolentino, E.; Westbrock-Wadman, S.; Yuan, Y.; Brody, L. L.; Coulter, S. N.; Folger, K. R.; Kas, A.; Larbig, K.; Lim, R.; Smith, K.; Spencer, D.; Wong, G. K.-S.; Wu, Z.; Paulsen, I. T.; Reizer, J.; Saier, M. H.; Hancock, R. E. W.; Lory, S.; Olson, M. V. Complete Genome Sequence of *Pseudomonas aeruginosa* PAO1, an Opportunistic Pathogen. *Nature* **2000**, *406*, 959–964.

(22) Hong, C. S.; Shitashiro, M.; Kuroda, A.; Ikeda, T.; Takiguchi, N.; Ohtake, H.; Kato, J. Chemotaxis Proteins and Transducers for Aerotaxis in *Pseudomonas aeruginosa*. *FEMS Microbiol. Lett.* **2004**, *231*, 247–252.

(23) Setubal, J. C.; dos Santos, P.; Goldman, B. S.; Ertesvåg, H.; Espin, G.; Rubio, L. M.; Valla, S.; Almeida, N. F.; Balasubramanian, D.; Cromes, L.; Curatti, L.; Du, Z.; Godsy, E.; Goodner, B.; Hellner-Burris, K.; Hernandez, J. A.; Houmiel, K.; Imperial, J.; Kennedy, C.; Larson, T. J.; Latreille, P.; Ligon, L. S.; Lu, J.; Maerk, M.; Miller, N. M.; Norton, S.; O'Carroll, I. P.; Paulsen, I.; Raulfs, E. C.; Roemer, R.; Rosser, J.;

Segura, D.; Slater, S.; Stricklin, S. L.; Studholme, D. J.; Sun, J.; Viana, C. J.; Wallin, E.; Wang, B.; Wheeler, C.; Zhu, H.; Dean, D. R.; Dixon, R.; Wood, D. Genome Sequence of *Azotobacter vinelandii*, an Obligate Aerobe Specialized to Support Diverse Anaerobic Metabolic Processes. *J. Bacteriol.* **2009**, *191*, 4534–4545.

(24) de Berardinis, V.; Durot, M.; Weissenbach, J.; Salanoubat, M. *Acinetobacter baylyi* ADP1 as a Model for Metabolic System Biology. *Curr. Opin. Microbiol.* **2009**, *12*, 568–576.

(25) Morrow, J. B.; Arango Pinedo, C.; Holbrook, R. D. Association of Quantum Dot Nanoparticles with *Pseudomonas aeruginosa* Biofilm. *J. Environ. Qual.* **2010**, *39*, 1934–1941.

(26) Pier, G. B. *Pseudomonas aeruginosa* Lipopolysaccharide: A Major Virulence Factor, Initiator of Inflammation and Target for Effective Immunity. *Int. J. Med. Microbiol.* **2007**, *297*, 277–295.

(27) Rocchetta, H. L.; Burrows, L. L.; Lam, J. S. Genetics of O-Antigen Biosynthesis in *Pseudomonas aeruginosa*. *Microbiol. Mol. Biol. Rev.* **1999**, *63*, 523–553.

(28) Zhao, P.; Li, N.; Astruc, D. State of the Art in Gold Nanoparticle Synthesis. *Coord. Chem. Rev.* **2013**, *257*, 638–665.

(29) Giljohann, D. A.; Seferos, D. S.; Daniel, W. L.; Massich, M. D.; Patel, P. C.; Mirkin, C. A. Gold Nanoparticles for Biology and Medicine. *Angew. Chemie Int. Ed. Engl.* **2010**, *49*, 3280–3294.

(30) Gole, A.; Murphy, C. J. Polyelectrolyte-Coated Gold Nanorods: Synthesis, Characterization and Immobilization. *Chem. Mater.* **2005**, *17*, 1325–1330.

(31) Richardson, J. J.; Cui, J.; Björnmalm, M.; Braunger, J. A.; Ejima, H.; Caruso, F. Innovation in Layer-by-Layer Assembly. *Chem. Rev.* **2016**, *116*, 14828–14867.

(32) Gentile, P.; Carmagnola, I.; Nardo, T.; Chiono, V. Layer-by-Layer Assembly for Biomedical Applications in the Last Decade. *Nanotechnology* **2015**, *26*, 422001.

(33) Zhou, Y.; Kong, Y.; Kundu, S.; Cirillo, J. D.; Liang, H. Antibacterial Activities of Gold and Silver Nanoparticles against *Escherichia coli* and *Bacillus* Calmette-Guérin. *J. Nanobiotechnology* **2012**, *10*, 19.

(34) Qiu, T. A.; Bozich, J. S.; Lohse, S. E.; Vartanian, A. M.; Jacob, L. M.; Meyer, B. M.; Gunsolus, I. L.; Niemuth, N. J.; Murphy, C. J.; Haynes, C. L.; Klaper, R. D. Gene Expression as an Indicator of the Molecular Response and Toxicity in the Bacterium *Shewanella oneidensis* and the Water Flea *Daphnia magna* Exposed to Functionalized Gold Nanoparticles. *Environ. Sci. Nano* **2015**, *2*, 615–629.

(35) Gole, A.; Murphy, C. J. Seed-Mediated Synthesis of Gold Nanorods: Role of the Size and Nature of the Seed. *Chem. Mater.* **2004**, *16*, 3633–3640.

(36) Lohse, S. E.; Eller, J. R.; Sivapalan, S. T.; Plews, M. R.; Murphy, C. J. A Simple Millifluidic Benchtop Reactor System for the High-Throughput Synthesis and Functionalization of Gold Nanoparticles with Different Sizes and Shapes. *ACS Nano* **2013**, *7*, 4135–4150.

(37) Haiss, W.; Thanh, N. T. K.; Aveyard, J.; Fernig, D. G. Determination of Size and Concentration of Gold Nanoparticles from UV-vis Spectra. *Anal. Chem.* **2007**, *79*, 4215–4221.

(38) Qiu, T. A.; Torelli, M. D.; Vartanian, A. M.; Rackstraw, N. B.; Buchman, J. T.; Jacob, L. M.; Murphy, C. J.; Hamers, R. J.; Haynes, C. L. Quantification of Free Polyelectrolytes Present in Colloidal Suspension, Revealing a Source of Toxic Responses for Polyelectrolyte-Wrapped Gold Nanoparticles. *Anal. Chem.* **2017**, *89*, 1823–1830.

(39) Newton, J. W.; Wilson, P. W.; Burris, R. H. Direct Demonstration of Ammonia as an Intermediate in Nitrogen Fixation by *Azotobacter*. *J. Biol. Chem.* **1953**, *204*, 445–451.

(40) Schrand, A. M.; Schlager, J. J.; Dai, L.; Hussain, S. M. Preparation of Cells for Assessing Ultrastructural Localization of Nanoparticles with Transmission Electron Microscopy. *Nat. Protoc.* **2010**, *5*, 744–757.

(41) Cui, Q.; Hernandez, R.; Mason, S. E.; Frauenheim, T.; Pedersen, J. A.; Geiger, F. Sustainable Nanotechnology: Opportunities and Challenges for Theoretical/Computational Studies. *J. Phys. Chem. B* **2016**, *120*, 7297–7306.

(42) Wu, E. L.; Engström, O.; Jo, S.; Stuhlsatz, D.; Yeom, M. S.; Klauda, J. B.; Widmalm, G.; Im, W. Molecular Dynamics and NMR Spectroscopy Studies of *E. coli* Lipopolysaccharide Structure and Dynamics. *Biophys. J.* **2013**, *105*, 1444–1455.

(43) Cournia, Z.; Smith, J. C.; Ullmann, G. M. A Molecular Mechanics Force Field for Biologically Important Sterols. *J. Comput. Chem.* **2005**, *26*, 1383–1399.

(44) Emami, F. S.; Puddu, V.; Berry, R. J.; Varshney, V.; Patwardhan, S. V; Perry, C. C.; Heinz, H. Force Field and a Surface Model Database for Silica to Simulate Interfacial Properties in Atomic Resolution. *Chem. Mater.* **2014**, *26*, 2647–2658.

(45) Heinz, H.; Lin, T.-J.; Mishra, R. K.; Emami, F. S. Thermodynamically Consistent Force Fields for the Assembly of Inorganic, Organic, and Biological Nanostructures: The INTERFACE Force Field. *Langmuir* **2013**, *29*, 1754–1765.

(46) Lin, T.-J.; Heinz, H. Accurate Force Field Parameters and pH Resolved Surface Models for Hydroxyapatite to Understand Structure, Mechanics, Hydration, and Biological Interfaces. *J. Phys. Chem. C* **2016**, *120*, 4975–4992.

(47) Jo, S.; Cheng, X.; Lee, J.; Kim, S.; Park, S.-J.; Patel, D. S.; Beaven, A. H.; Lee, K. Il; Rui, H.; Park, S.; Lee, H. S.; Roux, B.; Mackerell Jr, A. D.; Klauda, J. B.; Qi, Y.; Im, W. CHARMM-GUI 10 Years for Biomolecular Modeling and Simulation. *J. Comput. Chem.* **2017**, *38*, 1114–1124.

(48) Klein, N. D.; Hurley, K. R.; Feng, Z. V.; Haynes, C. L. Dark Field Transmission Electron Microscopy as a Tool for Identifying Inorganic Nanoparticles in Biological Matrices. *Anal. Chem.* **2015**, *87*, 4356–4362.

(49) Lam, J. S.; Graham, L. L.; Lightfoot, J.; Dasgupta, T.; Beveridge, T. J. Ultrastructural Examination of the Lipopolysaccharides of *Pseudomonas aeruginosa* Strains and Their Isogenic Rough Mutants by Freeze-Substitution. *J. Bacteriol.* **1992**, *174*, 7159–7167.

(50) Le Brun, A. P.; Clifton, L. A.; Halbert, C. E.; Lin, B.; Meron, M.; Holden, P. J.; Lakey, J. H.; Holt, S. A. Structural Characterization of a Model Gram-Negative Bacterial Surface Using Lipopolysaccharides from Rough Strains of *Escherichia coli*. *Biomacromolecules* **2013**, *14*, 2014–2022.

Chapter 3

(1) Tarascon, J.-M.; Armand, M. Issues and Challenges Facing Rechargeable Lithium Batteries. *Nature* **2001**, *414*, 359–367.

(2) Whittingham, M. S. Lithium Batteries and Cathode Materials. *Chem. Rev.* **2004**, *104*, 4271–4301.

(3) Mizushima, K.; Jones, P. C.; Wiseman, P. J.; Goodenough, J. B. Li_xCoO_2 ($0<x\leq1$): A New Cathode Material for Batteries of High Energy Density. *Mater. Res. Bull.* **1980**, *15*, 783–789.

(4) Nitta, N.; Wu, F.; Lee, J. T.; Yushin, G. Li-Ion Battery Materials: Present and Future. *Mater. Today* **2015**, *18*, 252–264.

(5) Olivetti, E. A.; Ceder, G.; Gaustad, G. G.; Fu, X. Lithium-Ion Battery Supply Chain Considerations: Analysis of Potential Bottlenecks in Critical Metals. *Joule* **2017**, *1*, 229–243.

(6) Okubo, M.; Hosono, E.; Kim, J.; Enomoto, M.; Kojima, N.; Kudo, T.; Zhou, H.; Honma, I. Nanosize Effect on High-Rate Li-Ion Intercalation in $LiCoO_2$ Electrode. *J.*

Am. Chem. Soc. **2007**, *129*, 7444–7452.

(7) Poizot, P.; Laruelle, S.; Grugeon, S.; Dupont, L.; Tarascon, J.-M. Nano-Sized Transition-Metal Oxides as Negative-Electrode Materials for Lithium-Ion Batteries. *Nature* **2000**, *407*, 496–499.

(8) Jo, M.; Hong, Y.-S.; Choo, J.; Cho, J. Effect of $LiCoO_2$ Cathode Nanoparticle Size on High Rate Performance for Li-Ion Batteries. *J. Electrochem. Soc.* **2009**, *156*, A430–A434.

(9) Xu, R.; de Vasconcelos, L. S.; Shi, J.; Li, J.; Zhao, K. Disintegration of Meatball Electrodes for $LiNi_xMn_yCo_zO_2$ Cathode Materials. *Exp. Mech.* **2018**, *58*, 549–559.

(10) Pavoni, F. H.; Sita, L. E.; dos Santos, C. S.; da Silva, S. P.; da Silva, P. R. C.; Scarminio, J. $LiCoO_2$ Particle Size Distribution as a Function of the State of Health of Discarded Cell Phone Batteries. *Powder Technol.* **2018**, *326*, 78–83.

(11) Watanabe, S.; Kinoshita, M.; Hosokawa, T.; Morigaki, K.; Nakura, K. Capacity Fading of $LiAl_yNi_{1-x-y}Co_xO_2$ Cathode for Lithium-Ion Batteries during Accelerated Calendar and Cycle Life Tests (Effect of Depth of Discharge in Charge-Discharge Cycling on the Suppression of the Micro-Crack Generation of $LiAl_yNi_{1-x-y}Co_xO_2$ Particle). *J. Power Sources* **2014**, *260*, 50–56.

(12) Belharouak, I.; Sun, Y.-K.; Liu, J.; Amine, K. $Li(Ni_{1/3}Co_{1/3}Mn_{1/3})O_2$ as a Suitable Cathode for High Power Applications. *J. Power Sources* **2003**, *123*, 247–252.

(13) Johnson, C. S.; Li, N.; Lefief, C.; Vaughey, J. T.; Thackeray, M. M. Synthesis, Characterization and Electrochemistry of Lithium Battery Electrodes: $x Li_2MnO_3 \cdot (1-x) LiMn_{0.333}Ni_{0.333}Co_{0.333}O_2$ ($0 \le x \le 0.7$). *Chem. Mater.* **2008**, *20*, 6095–6106.

(14) Goodenough, J. B.; Kim, Y. Challenges for Rechargeable Li Batteries. *Chem. Mater.* **2010**, *22*, 587–603.

(15) Martha, S. K.; Sclar, H.; Framowitz, Z. S.; Kovacheva, D.; Saliyski, N.; Gofer, Y.; Sharon, P.; Golik, E.; Markovsky, B.; Aurbach, D. A Comparative Study of Electrodes Comprising Nanometric and Submicron Particles of $LiNi_{0.50}Mn_{0.50}O_2$, $LiNi_{0.33}Mn_{0.33}Co_{0.33}O_2$, and $LiNi_{0.40}Mn_{0.40}Co_{0.20}O_2$ Layered Compounds. *J. Power Sources* **2009**, *189*, 248–255.

(16) Liu, W.; Oh, P.; Liu, X.; Lee, M.-J.; Cho, W.; Chae, S.; Kim, Y.; Cho, J. Nickel-Rich Layered Lithium Transition-Metal Oxide for High-Energy Lithium-Ion Batteries. *Angew. Chemie Int. Ed.* **2015**, *54*, 4440–4457.

(17) Hau, H. H.; Gralnick, J. A. Ecology and Biotechnology of the Genus *Shewanella*. *Annu. Rev. Microbiol.* **2007**, *61*, 237–258.

(18) Gulati, R. D. The Ecology of Common Planktonic Crustacea of the Freshwaters in the Netherlands. *Hydrobiologia* **1978**, *59*, 101–112.

(19) Qiu, T. A.; Nguyen, T. H. T.; Hudson-Smith, N. V.; Clement, P. L.; Forester, D.-C.; Frew, H.; Hang, M. N.; Murphy, C. J.; Hamers, R. J.; Feng, Z. V.; Haynes, C. L. Growth-Based Bacterial Viability Assay for Interference-Free and High-Throughput Toxicity Screening of Nanomaterials. *Anal. Chem.* **2017**, *89*, 2057–2064.

(20) Hohenberg, P.; Kohn, W. Inhomogeneous Electron Gas. *Phys. Rev.* **1964**, *136*, B864–B871.

(21) Kohn, W.; Sham, L. J. Self-Consistent Equations Including Exchange and Correlation Effects. *Phys. Rev.* **1965**, *140*, A1133–A1138.

(22) Giannozzi, P.; Baroni, S.; Bonini, N.; Calandra, M.; Car, R.; Cavazzoni, C.; Ceresoli, D.; Chiarotti, G. L.; Cococcioni, M.; Dabo, I.; Dal Corso, A.; de Gironcoli, S.; Fabris, S.; Fratesi, G.; Gebauer, R.; Gerstmann, U.; Gougoussis, C.; Kokalj, A.; Lazzeri, M.; Martin-Samos, L.; Marzari, N.; Mauri, F.; Mazzarello, R.; Paolini, S.; Pasquarello, A.; Paulatto, L.; Sbraccia, C.; Scandolo, S.; Sclauzero, G.; Seitsonen, A. P.; Smogunov, A.; Umari, P.; Wentzcovitch, R. M. QUANTUM ESPRESSO: A Modular and Open-Source Software Project for Quantum Simulations of Materials. *J. Phys. Condens. Matter* **2009**, *21*, 395502.

(23) Vanderbilt, D. Soft Self-Consistent Pseudopotentials in a Generalized Eigenvalue Formalism. *Phys. Rev. B* **1990**, *41*, 7892–7895.

(24) Garrity, K. F.; Bennett, J. W.; Rabe, K. M.; Vanderbilt, D. Pseudopotentials for High-Throughput DFT Calculations. *Comput. Mater. Sci.* **2014**, *81*, 446–452.

(25) Perdew, J. P.; Burke, K.; Ernzerhof, M. Generalized Gradient Approximation Made Simple. *Phys. Rev. Lett.* **1996**, *77*, 3865–3868.

(26) Bennett, J. W.; Jones, D.; Huang, X.; Hamers, R. J.; Mason, S. E. Dissolution of Complex Metal Oxides from First-Principles and Thermodynamics: Cation Removal from the (001) Surface of $Li(Ni_{1/3}Mn_{1/3}Co_{1/3})O_2$. *Environ. Sci. Technol.* **2018**, *52*, 5792–5802.

(27) Bennett, J. W.; Jones, D. T.; Hamers, R. J.; Mason, S. E. First-Principles and Thermodynamics Study of Compositionally Tuned Complex Metal Oxides: Cation Release from the (001) Surface of Mn-Rich Lithium Nickel Manganese Cobalt Oxide. *Inorg. Chem.* **2018**, *57*, 13300–13311.

(28) Monkhorst, H. J.; Pack, J. D. Special Points for Brillouin-Zone Integrations. *Phys. Rev. B* **1976**, *13*, 5188–5192.

(29) Rong, X.; Kolpak, A. M. Ab Initio Approach for Prediction of Oxide Surface Structure, Stoichiometry, and Electrocatalytic Activity in Aqueous Solution. *J. Phys. Chem. Lett.* **2015**, *6*, 1785–1789.

(30) Rong, X.; Parolin, J.; Kolpak, A. M. A Fundamental Relationship between Reaction Mechanism and Stability in Metal Oxide Catalysts for Oxygen Evolution. *ACS Catal.* **2016**, *6*, 1153–1158.

(31) Hang, M. N.; Gunsolus, I. L.; Wayland, H.; Melby, E. S.; Mensch, A. C.; Hurley, K. R.; Pedersen, J. A.; Haynes, C. L.; Hamers, R. J. Impact of Nanoscale Lithium Nickel Manganese Cobalt Oxide (NMC) on the Bacterium *Shewanella oneidensis* MR-1. *Chem. Mater.* **2016**, *28*, 1092–1100.

(32) Gunsolus, I. L.; Hang, M. N.; Hudson-Smith, N. V.; Buchman, J. T.; Bennett, J. W.; Conroy, D.; Mason, S. E.; Hamers, R. J.; Haynes, C. L. Influence of Nickel Manganese Cobalt Oxide Nanoparticle Composition on Toxicity toward *Shewanella oneidensis* MR-1: Redesigning for Reduced Biological Impact. *Environ. Sci. Nano* **2017**, *4*, 636–646.

(33) Wagman, D. D. E.; Halow, I.; Parker, V. B.; Bailey, S. M.; Schumm, R. H. Selected Values of Chemical Thermodynamic Properties. *Natl. Bur. Stand.* **1971**.

(34) Persson, K. A.; Waldwick, B.; Lazic, P.; Ceder, G. Prediction of Solid-Aqueous Equilibria: Scheme to Combine First-Principles Calculations of Solids with Experimental Aqueous States. *Phys. Rev. B* **2012**, *85*, 235438.

(35) Cohn, C. A.; Pedigo, C. E.; Hylton, S. N.; Simon, S. R.; Schoonen, M. A. A. Evaluating the Use of 3′-(*p*-Aminophenyl) Fluorescein for Determining the Formation of Highly Reactive Oxygen Species in Particle Suspensions. *Geochem. Trans.* **2009**, *10*, doi: 10.1186/1467-4866-10-8.

(36) Cohn, C. A.; Simon, S. R.; Schoonen, M. A. A. Comparison of Fluorescence-Based Techniques for the Quantification of Particle-Induced Hydroxyl Radicals. *Part. Fibre Toxicol.* **2008**, *5*, doi: 10.1186/1743-8977-5-2.

(37) Schrand, A. M.; Schlager, J. J.; Dai, L.; Hussain, S. M. Preparation of Cells for Assessing Ultrastructural Localization of Nanoparticles with Transmission Electron Microscopy. *Nat. Protoc.* **2010**, *5*, 744–757.

(38) Okamoto, A.; Yamamuro, M.; Tatarazako, N. Acute Toxicity of 50 Metals to *Daphnia magna*. *J. Appl. Toxicol.* **2015**, *35*, 824–830.

(39) Macomber, L.; Hausinger, R. P. Mechanisms of Nickel Toxicity in Microorganisms. *Metallomics* **2011**, *3*, 1153–1162.

(40) Barras, F.; Fontecave, M. Cobalt Stress in *Escherichia coli* and *Salmonella enterica*: Molecular Bases for Toxicity and Resistance. *Metallomics* **2011**, *3*, 1130–1134.

(41) Bozich, J.; Hang, M.; Hamers, R.; Klaper, R. Core Chemistry Influences the Toxicity of Multicomponent Metal Oxide Nanomaterials, Lithium Nickel Manganese Cobalt Oxide, and Lithium Cobalt Oxide to *Daphnia magna*. *Environ. Toxicol. Chem.* **2017**, *36*, 2493–2502.

(42) Li, L.; Lu, J.; Ren, Y.; Zhang, X. X.; Chen, R. J.; Wu, F.; Amine, K. Ascorbic-Acid-Assisted Recovery of Cobalt and Lithium from Spent Li-Ion Batteries. *J. Power Sources* **2012**, *218*, 21–27.

(43) Li, L.; Ge, J.; Chen, R.; Wu, F.; Chen, S.; Zhang, X. Environmental Friendly Leaching Reagent for Cobalt and Lithium Recovery from Spent Lithium-Ion Batteries. *Waste Manag.* **2010**, *30*, 2615–2621.

(44) Billy, E.; Joulié, M.; Laucournet, R.; Boulineau, A.; De Vito, E.; Meyer, D. Dissolution Mechanisms of $LiNi_{1/3}Mn_{1/3}Co_{1/3}O_2$ Positive Electrode Material from Lithium-Ion Batteries in Acid Solution. *ACS Appl. Mater. Interfaces* **2018**, *10*, 16424–16435.

(45) Von Moos, N.; Slaveykova, V. I. Oxidative Stress Induced by Inorganic Nanoparticles in Bacteria and Aquatic Microalgae - State of the Art and Knowledge Gaps. *Nanotoxicology* **2014**, *8*, 605–630.

(46) Imlay, J. A. The Molecular Mechanisms and Physiological Consequences of Oxidative Stress: Lessons from a Model Bacterium. *Nat. Rev. Microbiol.* **2013**, *11*, 443–454.

(47) Jiang, Y.; Dong, Y.; Luo, Q.; Li, N.; Wu, G.; Gao, H. Protection from Oxidative Stress Relies Mainly on Derepression of OxyR-Dependent KatB and Dps in *Shewanella oneidensis*. *J. Bacteriol.* **2014**, *196*, 445–458.

(48) Sies, H. Strategies of Antioxidant Defense. *Eur. J. Biochem.* **1993**, *215*, 213–219.

(49) Mensch, A. C.; Hernandez, R. T.; Kuether, J. E.; Torelli, M. D.; Feng, Z. V.; Hamers, R. J.; Pedersen, J. A. Natural Organic Matter Concentration Impacts the Interaction of Functionalized Diamond Nanoparticles with Model and Actual Bacterial Membranes. *Environ. Sci. Technol.* **2017**, *51*, 11075–11084.

(50) Tu, Y.; Lv, M.; Xiu, P.; Huynh, T.; Zhang, M.; Castelli, M.; Zengrong, L.; Huang, Q.; Fan, C.; Fang, H.; Zhou, R. Destructive Extraction of Phospholipids from *Escherichia coli* Membranes by Graphene Nanosheets. *Nat. Nanotechnol.* **2013**, *8*, 594–601.

(51) Xing, X.; Ma, W.; Zhao, X.; Wang, J.; Yao, L.; Jiang, X.; Wu, Z. Interaction between

Surface Charge-Modified Gold Nanoparticles and Phospholipid Membranes. *Langmuir* **2018**, *34*, 12583–12589.

(52) Hussain, S.; Garantziotis, S.; Rodrigues-Lima, F.; Dupret, J.-M.; Baeza-Squiban, A.; Boland, S. Intracellular Signal Modulation by Nanomaterials. *Adv. Exp. Med. Biol.* **2014**, *811*, 111–134.

(53) Bondarenko, O.; Ivask, A.; Käkinen, A.; Kurvet, I.; Kahru, A. Particle-Cell Contact Enhances Antibacterial Activity of Silver Nanoparticles. *PLoS One* **2013**, *8*, e64060.

(54) Bozich, J. S.; Lohse, S. E.; Torelli, M. D.; Murphy, C. J.; Hamers, R. J.; Klaper, R. D. Surface Chemistry, Charge and Ligand Type Impact the Toxicity of Gold Nanoparticles to *Daphnia magna*. *Environ. Sci. Nano* **2014**, *1*, 260–270.

(55) Rist, S.; Baun, A.; Hartmann, N. B. Ingestion of Micro- and Nanoplastics in *Daphnia magna* – Quantification of Body Burdens and Assessment of Feeding Rates and Reproduction. *Environ. Pollut.* **2017**, *228*, 398–407.

(56) Lee, B.-T.; Ranville, J. F. The Effect of Hardness on the Stability of Citrate-Stabilized Gold Nanoparticles and Their Uptake by *Daphnia magna*. *J. Hazard. Mater.* **2012**, *213*, 434–439.

Chapter 4

(1) Teja, A. S.; Koh, P. Y. Synthesis, Properties, and Applications of Magnetic Iron Oxide Nanoparticles. *Prog. Cryst. Growth Charact. Mater.* **2009**, *55*, 22–45.

(2) Alcantara, D.; Lopez, S.; García-Martin, M. L.; Pozo, D. Iron Oxide Nanoparticles as Magnetic Relaxation Switching (MRSw) Sensors: Current Applications in Nanomedicine. *Nanomedicine Nanotechnology, Biol. Med.* **2016**, *12*, 1253–1262.

(3) Liu, H.; Zhang, J.; Chen, X.; Du, X.-S.; Zhang, J.-L.; Liu, G.; Zhang, W.-G. Application of Iron Oxide Nanoparticles in Glioma Imaging and Therapy: From Bench to Bedside. *Nanoscale* **2016**, *8*, 7808–7826.

(4) Hurley, K. R.; Lin, Y.-S.; Zhang, J.; Egger, S. M.; Haynes, C. L. Effects of Mesoporous Silica Coating and Postsynthetic Treatment on the Transverse Relaxivity of Iron Oxide Nanoparticles. *Chem. Mater.* **2013**, *25*, 1968–1978.

(5) Jeon, S.; Oberreit, D. R.; Van Schooneveld, G.; Gao, Z.; Bischof, J. C.; Haynes, C. L.; Hogan, C. J. Ion-Mobility-Based Quantification of Surface-Coating-Dependent Binding of Serum Albumin to Superparamagnetic Iron Oxide Nanoparticles. *ACS Appl. Mater. Interfaces* **2016**, *8*, 24482–24490.

(6) Gao, Z.; Burrows, N. D.; Valley, N. A.; Schatz, G. C.; Murphy, C. J.; Haynes, C. L.

In Solution SERS Sensing Using Mesoporous Silica-Coated Gold Nanorods. *Analyst* **2016**, *141*, 5088–5095.

(7) Hurley, K. R.; Ring, H. L.; Etheridge, M.; Zhang, J.; Gao, Z.; Shao, Q.; Klein, N. D.; Szlag, V. M.; Chung, C.; Reineke, T. M.; Garwood, M.; Bischof, J. C.; Haynes, C. L. Predictable Heating and Positive MRI Contrast from a Mesoporous Silica-Coated Iron Oxide Nanoparticle. *Mol. Pharm.* **2016**, *13*, 2172–2183.

(8) Hau, H. H.; Gralnick, J. A. Ecology and Biotechnology of the Genus *Shewanella*. *Annu. Rev. Microbiol.* **2007**, *61*, 237–258.

(9) Xiong, Y.; Shi, L.; Chen, B.; Mayer, M. U.; Lower, B. H.; Londer, Y.; Bose, S.; Hochella, M. F.; Fredrickson, J. K.; Squier, T. C. High-Affinity Binding and Direct Electron Transfer to Solid Metals by the *Shewanella oneidensis* MR-1 Outer Membrane *c*-Type Cytochrome OmcA. *J. Am. Chem. Soc.* **2006**, *128*, 13978–13979.

(10) Myers, J. M.; Myers, C. R. Role for Outer Membrane Cytochromes OmcA and OmcB of *Shewanella putrefaciens* MR-1 in Reduction of Manganese Dioxide. *Appl. Environ. Microbiol.* **2001**, *67*, 260–269.

(11) Shi, L.; Richardson, D. J.; Wang, Z.; Kerisit, S. N.; Rosso, K. M.; Zachara, J. M.; Fredrickson, J. K. The Roles of Outer Membrane Cytochromes of *Shewanella* and *Geobacter* in Extracellular Electron Transfer. *Environ. Microbiol. Rep.* **2009**, *1*, 220–227.

(12) Marsili, E.; Baron, D. B.; Shikhare, I. D.; Coursolle, D.; Gralnick, J. A.; Bond, D. R. *Shewanella* Secretes Flavins That Mediate Extracellular Electron Transfer. *Proc. Natl. Acad. Sci.* **2008**, *105*, 3968–3973.

(13) Fredrickson, J. K.; Romine, M. F.; Beliaev, A. S.; Auchtung, J. M.; Driscoll, M. E.; Gardner, T. S.; Nealson, K. H.; Osterman, A. L.; Pinchuk, G.; Reed, J. L.; Rodionov, D. A.; Rodrigues, J. L. M.; Saffarini, D. A.; Serres, M. H.; Spormann, A. M.; Zhulin, I. B.; Tiedje, J. M. Towards Environmental Systems Biology of *Shewanella*. *Nat. Rev. Microbiol.* **2008**, *6*, 592–603.

(14) Gorby, Y. A.; Yanina, S.; McLean, J. S.; Rosso, K. M.; Moyles, D.; Dohnalkova, A.; Beveridge, T. J.; Chang, I. S.; Kim, B. H.; Kim, K. S.; Culley, D. E.; Reed, S. B.; Romine, M. F.; Saffarini, D. A.; Hill, E. A.; Shi, L.; Elias, D. A.; Kennedy, D. W.; Pinchuk, G.; Watanabe, K.; Ishii, S.; Logan, B.; Nealson, K. H.; Fredrickson, J. K. Electrically Conductive Bacterial Nanowires Produced by *Shewanella oneidensis* Strain MR-1 and Other Microorganisms. *Proc. Natl. Acad. Sci.* **2006**, *103*, 113358–

11363.

(15) Bretschger, O.; Obraztsova, A.; Sturm, C. A.; Chang, I. S.; Gorby, Y. A.; Reed, S. B.; Culley, D. E.; Reardon, C. L.; Barua, S.; Romine, M. F.; Zhou, J.; Beliaev, A. S.; Bouhenni, R.; Saffarini, D.; Mansfeld, F.; Kim, B.-H.; Fredrickson, J. K.; Nealson, K. H. Current Production and Metal Oxide Reduction by *Shewanella oneidensis* MR-1 Wild Type and Mutants. *Appl. Environ. Microbiol.* **2007**, *73*, 7003–7012.

(16) Fukushima, T.; Gupta, S.; Rad, B.; Cornejo, J. A.; Petzold, C. J.; Chan, L. J. G.; Mizrahi, R. A.; Ralston, C. Y.; Ajo-Franklin, C. M. The Molecular Basis for Binding of an Electron Transfer Protein to a Metal Oxide Surface. *J. Am. Chem. Soc.* **2017**, *139*, 12647–12654.

(17) Perez-Gonzalez, T.; Jimenez-Lopez, C.; Neal, A. L.; Rull-Perez, F.; Rodriguez-Navarro, A.; Fernandez-Vivas, A.; Iañez-Pareja, E. Magnetite Biomineralization Induced by *Shewanella oneidensis*. *Geochim. Cosmochim. Acta* **2010**, *74*, 967–979.

(18) Perez-Gonzalez, T.; Valverde-Tercedor, C.; Yebra-Rodriguez, A.; Prozorov, T.; Gonzalez-Muñoz, M. T.; Arias-Peñalver, J. M.; Jimenez-Lopez, C. Chemical Purity of *Shewanella oneidensis*-Induced Magnetites. *Geomicrobiol. J.* **2013**, *30*, 731–748.

(19) Coker, V. S.; Pearce, C. I.; Pattrick, R. A. D.; Van Der Laan, G.; Telling, N. D.; Charnock, J. M.; Arenholz, E.; LLoyd, J. R. Probing the Site Occupancies of Co-, Ni-, and Mn-Substituted Biogenic Magnetite Using XAS and XMCD. *Am. Mineral.* **2008**, *93*, 1119–1132.

(20) Luo, H.-W.; Zhang, X.; Chen, J.-J.; Yu, H.-Q.; Sheng, G.-P. Probing the Biotransformation of Hematite Nanoparticles and Magnetite Formation Mediated by *Shewanella oneidensis* MR-1 at the Molecular Scale. *Environ. Sci. Nano* **2017**, *4*, 2395–2404.

(21) Liu, J.; Pearce, C. I.; Shi, L.; Wang, Z.; Shi, Z.; Arenholz, E.; Rosso, K. M. Particle Size Effect and the Mechanism of Hematite Reduction by the Outer Membrane Cytochrome OmcA of *Shewanella oneidensis* MR-1. *Geochim. Cosmochim. Acta* **2016**, *193*, 160–175.

(22) Kostka, J. E.; Nealson, K. H. Dissolution and Reduction of Magnetite by Bacteria. *Environ. Sci. Technol.* **1995**, *29*, 2535–2540.

(23) Venkateswaran, K.; Moser, D. P.; Dollhopf, M. E.; Lies, D. P.; Saffarini, D. A.; MacGregor, B. J.; Ringelberg, D. B.; White, D. C.; Nishijima, M.; Sano, H.;

Burghardt, J.; Stackebrandt, E.; Nealson, K. H. Polyphasic Taxonomy of the Genus *Shewanella* and Description of *Shewanella oneidensis* sp. nov. *Int. J. Syst. Bacteriol.* **1999**, *49*, 705–724.

(24) Roberts, J. A.; Fowle, D. A.; Hughes, B. T.; Kulczycki, E. Attachment Behavior of *Shewanella putrefaciens* onto Magnetite under Aerobic and Anaerobic Conditions. *Geomicrobiol. J.* **2006**, *23*, 631–640.

(25) Kasai, T.; Kouzuma, A.; Nojiri, H.; Watanabe, K. Transcriptional Mechanisms for Differential Expression of Outer Membrane Cytochrome Genes *omcA* and *mtrC* in *Shewanella oneidensis* MR-1. *BMC Microbiol.* **2015**, *15*, 68.

(26) Lin, Y.-S.; Abadeer, N.; Hurley, K. R.; Haynes, C. L. Ultrastable, Redispersible, Small, and Highly Organomodified Mesoporous Silica Nanotherapeutics. *J. Am. Chem. Soc.* **2011**, *133*, 20444–20457.

(27) Schneider, C. A.; Rasband, W. S.; Eliceiri, K. W. NIH Image to ImageJ: 25 Years of Image Analysis. *Nat. Methods* **2012**, *9*, 671–675.

(28) Schrand, A. M.; Schlager, J. J.; Dai, L.; Hussain, S. M. Preparation of Cells for Assessing Ultrastructural Localization of Nanoparticles with Transmission Electron Microscopy. *Nat. Protoc.* **2010**, *5*, 744–757.

(29) Buchman, J. T.; Rahnamoun, A.; Landy, K. M.; Vartanian, A. M.; Jacob, L. M.; Murphy, C. J.; Hernandez, R.; Haynes, C. L. Using an Environmentally-Relevant Panel of Gram-Negative Bacteria to Assess the Toxicity of Polyallylamine Hydrochloride-Wrapped Gold Nanoparticles. *Environ. Sci. Nano* **2018**, *5*, 279–288.

(30) Maurer-Jones, M. A.; Gunsolus, I. L.; Meyer, B. M.; Christenson, C. J.; Haynes, C. L. Impact of TiO_2 Nanoparticles on Growth, Biofilm Formation, and Flavin Secretion in *Shewanella oneidensis*. *Anal. Chem.* **2013**, *85*, 5810–5818.

(31) Qiu, T. A.; Bozich, J. S.; Lohse, S. E.; Vartanian, A. M.; Jacob, L. M.; Meyer, B. M.; Gunsolus, I. L.; Niemuth, N. J.; Murphy, C. J.; Haynes, C. L.; Klaper, R. D. Gene Expression as an Indicator of the Molecular Response and Toxicity in the Bacterium *Shewanella oneidensis* and the Water Flea *Daphnia magna* Exposed to Functionalized Gold Nanoparticles. *Environ. Sci. Nano* **2015**, *2*, 615–629.

(32) Andrews, S. C. Iron Storage in Bacteria. In *Advances in Microbial Physiology*; 1998; Vol. 40, pp 281–351.

(33) Mahoney, S.; Najera, M.; Bai, Q.; Burton, E. A.; Veser, G. The Developmental Toxicity of Complex Silica-Embedded Nickel Nanoparticles Is Determined by Their Physicochemical Properties. *PLoS One* **2016**, *11*, e0152010.

(34) Klein, N. D.; Hurley, K. R.; Feng, Z. V.; Haynes, C. L. Dark Field Transmission Electron Microscopy as a Tool for Identifying Inorganic Nanoparticles in Biological Matrices. *Anal. Chem.* **2015**, *87*, 4356–4362.

(35) Liu, L.; Li, S.; Wang, S.; Dong, Z.; Gao, H. Complex Iron Uptake by the Putrebactin-Mediated and Feo Systems in *Shewanella oneidensis*. *Appl. Environ. Microbiol.* **2018**, *84*, e01752-18.

(36) Noinaj, N.; Guillier, M.; Barnard, T. J.; Buchanan, S. K. TonB-Dependent Transporters: Regulation, Structure, and Function. *Annu. Rev. Biochem.* **2010**, *64*, 43–60.

(37) Lau, C. K. Y.; Krewulak, K. D.; Vogel, H. J. Bacterial Ferrous Iron Transport: The Feo System. *FEMS Microbiol. Rev.* **2016**, *40*, 273–298.

Chapter 5

(1) Savary, S.; Ficke, A.; Aubertot, J.-N.; Hollier, C. Crop Losses Due to Diseases and Their Implications for Global Food Production Losses and Food Security. *Food Secur.* **2012**, *4*, 519–537.

(2) Martyn, R. D. *Fusarium* Wilt of Watermelon: 120 Years of Research. In *Horticultural Reviews*; Janick, J., Ed.; John Wiley & Sons, Inc.: Hoboken, NJ, 2014; Vol. 42, pp 349–442.

(3) Lü, G.; Guo, S.; Zhang, H.; Geng, L.; Song, F.; Fei, Z.; Xu, Y. Transcriptional Profiling of Watermelon during Its Incompatible Interaction with *Fusarium oxysporum* f. sp. *niveum*. *Eur. J. Plant Pathol.* **2011**, *131*, 585–601.

(4) Zhang, Z.; Zhang, J.; Wang, Y.; Zheng, X. Molecular Detection of *Fusarium oxysporum* f. sp. *niveum* and *Mycosphaerella melonis* in Infected Plant Tissues and Soil. *FEMS Microbiol. Lett.* **2005**, *249*, 39–47.

(5) Zhang, M.; Xu, J. H.; Liu, G.; Yao, X. F.; Li, P. F.; Yang, X. P. Characterization of the Watermelon Seedling Infection Process by *Fusarium oxysporum* f. sp. *niveum*. *Plant Pathol.* **2015**, *64*, 1076–1084.

(6) Guo, S.; Zhang, J.; Sun, H.; Salse, J.; Lucas, W. J.; Zhang, H.; Zheng, Y.; Mao, L.; Ren, Y.; Wang, Z.; Min, J.; Guo, X.; Murat, F.; Ham, B.-K.; Zhang, Z.; Gao, S.; Huang, M.; Xu, Y.; Zhong, S.; Bombarely, A.; Mueller, L. A.; Zhao, H.; He, H.; Zhang, Y.; Zhang, Z.; Huang, S.; Tan, T.; Pang, E.; Lin, K.; Hu, Q.; Kuang, H.; Ni, P.; Wang, B.; Liu, J.; Kou, Q.; Hou, W.; Zou, X.; Jiang, J.; Gong, G.; Klee, K.; Schoof, H.; Huang, Y.; Hu, X.; Dong, S.; Liang, D.; Wang, J.; Wu, K.; Xia, Y.; Zhao,

X.; Zheng, Z.; Xing, M.; Liang, X.; Huang, B.; Lv, T.; Wang, J.; Yin, Y.; Yi, H.; Li, R.; Wu, M.; Levi, A.; Zhang, X.; Giovannoni, J. J.; Wang, J.; Li, Y.; Fei, Z.; Xu, Y. The Draft Genome of Watermelon (*Citrullus lanatus*) and Resequencing of 20 Diverse Accessions. *Nat. Genet.* **2013**, *45*, 51–58.

(7) Everts, K. L.; Himmelstein, J. C. *Fusarium* Wilt of Watermelon: Towards Sustainable Management of a Re-Emerging Plant Disease. *Crop Prot.* **2015**, *73*, 93–99.

(8) Bozarth, S. R. Diagnostic Opal Phytoliths from Rinds of Selected Cucurbita Species. *Am. Antiq.* **1987**, *52*, 607–615.

(9) Currie, H. A.; Perry, C. C. Silica in Plants: Biological, Biochemical and Chemical Studies. *Ann. Bot.* **2007**, *100*, 1383–1389.

(10) Fawe, A.; Menzies, J. G.; Chérif, M.; Bélanger, R. R. Silicon and Disease Resistance in Dicotyledons. In *Silicon in Agriculture*; Datnoff, L. E., Snyder, G. H., Korndöfer, G. H., Eds.; Elsevier: Amsterdam, 2001; pp 159–170.

(11) Carlisle, E. M. Silicon. In *Handbook of Nutritionally Essential Mineral Elements*; O'Dell, B. L., Sunde, R. A., Eds.; Marcel Dekker: New York, 1997; pp 603–618.

(12) Nielsen, F. H. Ultratrace Elements in Nutrition: Current Knowledge and Speculation. *J. Trace Elem. Exp. Med.* **1998**, *11*, 251–274.

(13) Khan, M. R.; Rizvi, T. F. Nanotechnology: Scope and Application in Plant Disease Management. *Plant Pathol. J.* **2014**, *13*, 214–231.

(14) Servin, A.; Elmer, W.; Mukherjee, A.; De la Torre-Roche, R.; Hamdi, H.; White, J. C.; Bindraban, P.; Dimkpa, C. A Review of the Use of Engineered Nanomaterials to Suppress Plant Disease and Enhance Crop Yield. *J. Nanoparticle Res.* **2015**, *17*, 92.

(15) Hussain, H. I.; Yi, Z.; Rookes, J. E.; Kong, L. X.; Cahill, D. M. Mesoporous Silica Nanoparticles as a Biomolecule Delivery Vehicle in Plants. *J. Nanoparticle Res.* **2013**, *15*, 1676.

(16) Suriyaprabha, R.; Karunakaran, G.; Kavitha, K.; Yuvakkumar, R.; Rajendran, V.; Kannan, N. Application of Silica Nanoparticles in Maize to Enhance Fungal Resistance. *IET Nanobiotechnology* **2014**, *8*, 133–137.

(17) El Hassni, M.; El Hadrami, A.; Daayf, F.; Barka, E. A.; El Hadrami, I. Chitosan, Antifungal Product against *Fusarium oxysporum* f. sp. a*lbedinis* and Elicitor of Defence Reactions in Date Palm Roots. *Phytopathol. Mediterr.* **2004**, *43*, 195–204.

(18) Doares, S. H.; Syrovets, T.; Weiler, E. W.; Ryan, C. A. Oligogalacturonides and

Chitosan Activate Plant Defensive Genes through the Octadecanoid Pathway. *Proc. Natl. Acad. Sci.* **1995**, *92*, 4095–4098.

(19) El Hadrami, A.; Adam, L. R.; El Hadrami, I.; Daayf, F. Chitosan in Plant Protection. *Mar. Drugs* **2010**, *8*, 968–987.

(20) Rabea, E. I.; Badawy, M. E.-T.; Stevens, C. V.; Smagghe, G.; Steurbaut, W. Chitosan as Antimicrobial Agent: Applications and Mode of Action. *Biomacromolecules* **2003**, *4*, 1457–1465.

(21) Bell, A. A.; Hubbard, J. C.; Liu, L.; Davis, R. M.; Subbarao, K. V. Effects of Chitin and Chitosan on the Incidence and Severity of *Fusarium* Yellows of Celery. *Plant Dis.* **1998**, *82*, 322–328.

(22) Malerba, M.; Cerana, R. Recent Advances of Chitosan Applications in Plants. *Polymers (Basel).* **2018**, *10*, 118.

(23) Dzung, P. D.; Phu, D. Van; Du, B. D.; Ngoc, L. S.; Duy, N. N.; Hiet, H. D.; Nghia, D. H.; Thang, N. T.; Le, B. Van; Hien, N. Q. Effect of Foliar Application of Oligochitosan with Different Molecular Weight on Growth Promotion and Fruit Yield Enhancement of Chili Plant. *Plant Prod. Sci.* **2017**, *20*, 389–395.

(24) Nguyen, N. T.; Nguyen, D. H.; Pham, D. D.; Dang, V. P.; Nguyen, Q. H.; Hoang, D. Q. New Oligochitosan-Nanosilica Hybrid Materials: Preparation and Application on Chili Plants for Resistance to Anthracnose Disease and Growth Enhancement. *Polym. J.* **2017**, *49*, 861–869.

(25) Yang, L.; Zhao, P.; Wang, L.; Filippus, I.; Meng, X. Synergistic Effect of Oligochitosan and Silicon on Inhibition of *Monilinia fructicola* Infections. *J. Sci. Food Agric.* **2010**, *90*, 630–634.

(26) Chen, J.; Wang, W.; Xu, Y.; Zhang, X. Slow-Release Formulation of a New Biological Pesticide, Pyoluteorin, with Mesoporous Silica. *J. Agric. Food Chem.* **2011**, *59*, 307–311.

(27) Lin, Y.-S.; Abadeer, N.; Hurley, K. R.; Haynes, C. L. Ultrastable, Redispersible, Small, and Highly Organomodified Mesoporous Silica Nanotherapeutics. *J. Am. Chem. Soc.* **2011**, *133*, 20444–20457.

(28) Chen, F.; Zhu, Y. Chitosan Enclosed Mesoporous Silica Nanoparticles as Drug Nano-Carriers: Sensitive Response to the Narrow PH Range. *Microporous Mesoporous Mater.* **2012**, *150*, 83–89.

(29) Schneider, C. A.; Rasband, W. S.; Eliceiri, K. W. NIH Image to ImageJ: 25 Years of Image Analysis. *Nat. Methods* **2012**, *9*, 671–675.

(30) Hang, M. N.; Hudson-Smith, N. V.; Clement, P. L.; Zhang, Y.; Wang, C.; Haynes, C. L.; Hamers, R. J. Influence of Nanoparticle Morphology on Ion Release and Biological Impact of Nickel Manganese Cobalt Oxide (NMC) Complex Oxide Nanomaterials. *ACS Appl. Nano Mater.* **2018**, *1*, 1721–1730.

(31) Elmer, W.; De La Torre-Roche, R.; Pagano, L.; Majumdar, S.; Zuverza-Mena, N.; Dimkpa, C.; Gardea-Torresdey, J.; White, J. C. Effect of Metalloid and Metal Oxide Nanoparticles on *Fusarium* Wilt of Watermelon. *Plant Dis.* **2018**, *102*, 1394–1401.

(32) Jeger, M. J.; Viljanen-Rollinson, S. L. H. The Use of the Area under the Disease-Progress Curve (AUDPC) to Assess Quantitative Disease Resistance in Crop Cultivars. *Theor. Appl. Genet.* **2001**, *102*, 32–40.

(33) Judy, J. D.; Unrine, J. M.; Rao, W.; Wirick, S.; Bertsch, P. M. Bioavailability of Gold Nanomaterials to Plants: Importance of Particle Size and Surface Coating. *Environ. Sci. Technol.* **2012**, *46*, 8467–8474.

(34) Lin, Y.-S.; Haynes, C. L. Impacts of Mesoporous Silica Nanoparticle Size, Pore Ordering, and Pore Integrity on Hemolytic Activity. *J. Am. Chem. Soc.* **2010**, *132*, 4834–4842.

Appendix I: Curriculum Vitae

Joseph Buchman

207 Pleasant Street SE, Minneapolis, MN 55455

Cell: (763) 412-0293 jbuchman@umn.edu

Work: (612) 626-5282 orcid.org/0000-0001-5827-8513

EDUCATION

Ph.D. in Chemistry, **University of MN,** Minneapolis, MN, Graduation: May 2019
Advisor: Christy L. Haynes
GPA: 3.529

M.S. in Chemistry, University of MN, Minneapolis, MN, Graduation: Feb 2015
Advisor: Christy L. Haynes
GPA: 3.529

B.S., Augsburg College, Minneapolis, MN, Graduation: May 2013
Majors: B.S. in Chemistry and B.S. in Biology with Minor in Mathematics
Honors: Summa cum Laude
GPA: 3.985

AWARDS & SCHOLARSHIPS

- MN ACS Travel Grant 2018
- University of MN Biotechnology Insititute Training Grant 2014 - 2016
- NSF Graduate Research Fellow 2013 - 2018
- AugSTEM Scholarship through National Science Foundation 2012 - 2013
- NASA Space Grant Scholarship for STEM students 2012 - 2013
- Courtland Agre Scholarship 2009 - 2013
- Wallin Education Partners Scholarship 2009 - 2013
- Goldwater Honorable Mention 2012
- ACS Undergraduate Award in Analytical Chemistry 2012
- Dr. Paul and Maxine Fridlund Scholarship 2012
- Chemistry Alumni Scholarship 2012
- Sundquist Scholar 2011
- CRC Press Chemistry Achievement Award 2010

RESEARCH EXPERIENCE

University of MN, Graduate Student Researcher Jun 2013 - Present
Mentor: Dr. Christy L. Haynes

Environmental Toxicity of Nanoparticles

- Develop high-throughput nanoparticle toxicity screening method with bacteria.
- Identify molecular mechanisms of nanotoxicity using an extensive suite of techniques.
- Design and synthesize nanoparticles to improve disease resistance of crop plants.
- Lead collaborative projects with multidisciplinary team across multiple universities.
- Mentor and train two undergraduate researchers.

Development of a Drug Delivery Platform

- Quantified the drug-loading capacity of mesoporous silica nanoparticles.
- Monitored drug release kinetics from mesoporous silica nanoparticles.

Abbott (St. Jude Medical), Graduate Student Intern Jun 2016 – Mar 2019
Mentor: Dr. Amanda J. DeGraw

Leachables & Extractables Analysis of Medical Devices

- Assisted in LC-MS method development for analysis of leachables and extractables.
- Wrote and edited standard operating procedures for a GLP laboratory.
- Tested stability of standards for LC-MS method.
- Aided in troubleshooting and maintenance of the LC-MS.

Mayo Clinic, Mayo Innovation Scholar Oct 2012 - Mar 2013
Mentor: Kelvyn Henderson

Analysis of a New Medical Device

- Tested the applications of a new implantable ventricular assist device.
- Used SWOT analysis to determine the marketability of the new device.
- Collaborated with an interdisciplinary team of scientists and economists.

Augsburg College, Student Researcher Mar 2011 - May 2013
Mentor: Dr. Vivian Feng

Green Synthesis of Novel Surfactants

- Created microfluidic devices from PDMS and glass slides.
- Developed microfluidic flow method for green synthesis of surfactants.
- Characterized purity and yield of surfactant products.
- Collaborated with the Aveda Corporation.

Environmental Remediation with Nanoparticles

- Obtained $4000 in internal funding for research.
- Synthesized dendrimer-encapsulated metal nanoparticles.
- Utilized nanoparticles for catalysis of PCB remediation.

Biodiesel Quantification in Commercial Diesel

- Developed methods for biodiesel analysis using FTIR, HPLC and NMR.
- Quantified biodiesel content in commercial diesel blends.
- Published a paper in *Journal of Chemical Education*.

Lupus Foundation of MN, Research Fellow Jun 2012 - Aug 2012
Mentor: Dr. Daniel Mueller

Development of a Diagnostic Platform

- Performed multiple direct ELISA assays to develop a diagnostic platform for SLE.
- Developed a peptide tetramer to improve sensitivity for autoreactive B cells.
- Distinguished phenotypes of autoreactive B cells with flow cytometry.

PUBLICATIONS

- **Buchman, J.T.**; Ma, C.; Landy, K.M.; Hudson-Smith, N.V.; Kang, H.; Elmer, W.; White, J.C.; Haynes, C.L. Tuning mesoporous silica nanoparticle size to optimize impact on watermelon plant health. *In Prep.*
- **Buchman, J.T.**; Elmer, W.; Ma, C.; Landy, K.M.; White, J.C.; Haynes, C.L. Coating mesoporous silica nanoparticles with chitosan improves watermelon plant defenses and growth. *In Prep.*
- Hudson-Smith, N.V.; **Buchman, J.T.**; Mitchell, S.L.; Krause, M.O.P. Do science blogs really promote reader engagement? An experimental comparison between blogs and traditional expository text. *In Prep.*
- Pandiakumar, A.K.; Stettnisch, M.; Hudson-Smith, N.V.; **Buchman, J.T.**; Haynes, C.L.; Klaper, R.; Hamers, R.J. Synthesis of nanoscale nickel cobalt aluminum oxide cathode material and its toxicity. *In Prep*.
- Robinson, M.E.; Evans, E.J.; Kim, K.; Melby, E.S.; Jones, Z.R.; **Buchman, J.T.**; Borgatta, J.; Haynes, C.L.; Orr, G.; Pedersen, J.A.; Hamers, R.J. Gram-scale synthesis of phosphorescent ruby nanoparticles as versatile, nanoscale optical probes. *In Prep*.
- **Buchman, J.T.**; Bennett, E.A; Wang, C.; Bennett, J.W.; Hudson, B.G.; Abbaspour Tamijani, A.; Clement, P.L.; Zhi, B.; Green, C.M.; Henke, A.H.; Laudadio, E.D.; Mason, S.E.; Hamers, R.J.; Klaper, R.D.; Haynes, C.L. The technologically relevant complex oxide battery material, Ni-enriched NMC, has differential toxicity to *S. oneidensis* MR-1 and *D. magna*. *In Prep*.
- **Buchman, J.T.**; Pho, T.; Rodriguez, R.S.; Feng, Z.V.; Haynes, C.L. Coating iron oxide nanoparticles with mesoporous silica reduces their interaction and impact on *S. oneidensis* MR-1. *Submitted*.
- Clement, P.L.; Kuether, J.E.; Borgatta, J.R.; **Buchman, J.T.**; Cahill, M.S.; Qiu, T.A.; Hamers, R.J.; Feng, Z.V.; Haynes, C.L. Cobalt release from a nanoscale multiphase

lithiated cobalt phosphate dominates interaction with *Shewanella oneidensis* MR-1 and *Bacillus subtilis*. *Submitted.*

- **Buchman, J.T.**; Hudson-Smith, N.V.; Landy, K.M.; Haynes, C.L. Understanding Nanoparticle Toxicity Mechanisms to Inform Redesign Strategies to Reduce Environmental Impact. *Acc. Chem. Res.*, *In Press*.
- Kang, H.; **Buchman, J.T.**; Rodriguez, R.S.; Ring, H.L.; He, J.; Bantz, K.C.; Haynes, C.L. Stabilization of silver and gold nanoparticles: preservation and improvement of plasmonic functionalities. *Chem. Rev.*, 2019, 119, 664-669.
- Mensch, A.C.; **Buchman, J.T.**; Haynes, C.L.; Pedersen, J.A.; Hamers, R.J. Quaternary-amine terminated quantum dots induce structural changes to supported lipid bilayers. *Langmuir*, 2018, 34, 12369-12378.
- Domínguez, G.A.; Torelli, M.D.; **Buchman, J.T.**; Haynes, C.L.; Hamers, R.J.; Klaper, R.D. Size dependent oxidative stress response of the gut of *Daphnia magna* to functionalized nanodiamond particles. *Environ. Research*, 2018, 167, 267-275*.*
- Gallagher, M.J.; **Buchman, J.T.**; Qiu, T.A.; Zhi, B.; Lyons, T.; Landy, K.M.; Rosenzweig, Z.; Haynes, C.L.; Fairbrother, D.H. Release, detection and toxicity of fragments generated during artificial accelerated weathering of CdSe/ZnS and CdSe quantum dot polymer composites. *Environ. Sci.: Nano*, 2018, 5, 1694-1710.
- **Buchman, J.T.**; Rahnamoun, A.; Landy, K.M.; Zhang, X.; Vartanian, A.M.; Jacob, L.M.; Murphy, C.J.; Hernandez, R.; Haynes, C.L. Using an environmentally-relevant panel of Gram-negative bacteria to assess the toxicity of polyallylamine hydrochloride-wrapped gold nanoparticles. *Environ. Sci.: Nano,* 2018, 5, 279-288. Best Paper of 2018 Nominee for the Royal Society of Chemistry's *Environmental Science* family of journals.
- Robinson, M.E.; Ng, J.D.; Zhang, H.; **Buchman, J.T.**; Shenderova, O.A.; Haynes, C.L.; Ma, Z.; Goldsmith, R.H.; Hamers, R.J. Optically detected magnetic resonance for selective imaging of diamond nanoparticles. *Anal. Chem.*, 2018, 90, 769-776.
- Allen, C.; Qiu, T.A.; Pramanik, S.; **Buchman, J.T.**; Krause, M.O.P., Murphy, C.J. Research highlights: investigating the role of nanoparticle surface charge in nano-bio interactions. *Environ. Sci.: Nano*, 2017, 4, 741-746. *Not Peer Reviewed
- Gallagher, M.J.; Allen, C.; **Buchman, J.T.**; Qiu, T.A.; Clement, P.L.; Krause, M.O.P.; Gilbertson, L.M. Research highlights: applications of life-cycle assessment as a tool for characterizing environmental impacts of engineered nanomaterials. *Environ. Sci.: Nano,* 2017, 4, 276-281*.* *Not Peer Reviewed
- Gunsolus, I.L.; Hang, M.N.; Hudson-Smith, N.V.; **Buchman, J.T.**; Bennett, J.W.; Conroy, D.; Mason, S.E.; Hamers, R.J.; Haynes, C.L. Influence of nickel manganese cobalt oxide nanoparticle composition on toxicity toward *Shewanella oneidensis* MR-1: redesigning for reduced biological impact. *Environ. Sci.: Nano*, 2017, 4, 636-646**.**
- Qiu, T.A.; Torelli, M.D.; Vartanian, A.M.; Rackstraw, N.B.; **Buchman, J.T.**; Jacob, L.M.; Murphy, C.J.; Hamers, R.J.; Haynes, C.L. Quantification of free polyelectrolytes present in colloidal suspension reveals source of toxic responses for polyelectrolyte-wrapped gold nanoparticles. *Anal. Chem*., 2017, 89, 1823-1830.
- **Buchman, J.T.**; Gallagher, M.J.; Yang, C.-T.; Zhang, X.; Krause, M.O.P.; Hernandez, R.; Orr, G. Research highlights: examining the effect of shape on nanoparticle interactions with organisms. *Environ. Sci.: Nano,* 2016, 3, 696-700. *Not Peer Reviewed
- Kim, D.; Finkenstaedt-Quinn, S.; Hurley, K.R.; **Buchman, J.T.**; Haynes, C.L. On-chip evaluation of platelet adhesion and aggregation upon exposure to mesoporous silica nanoparticles. *Analyst,* 2014, 139, 906-913.
- Feng, Z.V.; **Buchman, J.T.** Instrumental analysis of biodiesel content in commercial diesel blends: an experiment for undergraduate analytical chemistry. *J. Chem. Ed.*, 2012, 89, 1561-1565.

PRESENTATIONS

- **Buchman, J.T.**; Bennett, E.A; Wang, C.; Bennett, J.W.; Hudson, B.G.; Abbaspour Tamijani, A.; Clement, P.L.; Zhi, B.; Green, C.M.; Henke, A.H.; Laudadio, E.D.; Mason, S.E.; Hamers, R.J.; Klaper, R.D.; Haynes, C.L. The technologically relevant complex oxide

battery material, Ni-enriched NMC, has differential toxicity to *S. oneidensis* MR-1 and *D. magna*. Industrial Partnership for Research in Interfacial Materials and Engineering Annual Meeting, May 2019, Minneapolis, MN. Poster.

- **Buchman, J.T.**; Rahnamoun, A.; Landy, K.M.; Zhang, X.; Vartanian, A.M.; Jacob, L.M.; Murphy, C.J.; Hernandez, R.; Haynes, C.L. Using an environmentally-relevant panel of Gram-negative bacteria to assess the toxicity of polyelectrolyte-wrapped gold nanoparticles. Industrial Partnership for Research in Interfacial Materials and Engineering Annual Meeting, May 2018, Minneapolis, MN. Invited Talk.
- **Buchman, J.T.**; Rahnamoun, A.; Landy, K.M.; Zhang, X.; Vartanian, A.M.; Jacob, L.M.; Murphy, C.J.; Hernandez, R.; Haynes, C.L. Using an environmentally-relevant panel of Gram-negative bacteria to assess the toxicity of polyelectrolyte-wrapped gold nanoparticles. 255th ACS National Meeting, Mar 2018, New Orleans, LA. Oral.
- **Buchman, J.T.**; Rahnamoun, A.; Landy, K.M.; Zhang, X.; Vartanian, A.M.; Jacob, L.M.; Murphy, C.J.; Hernandez, R.; Haynes, C.L. Assessing the toxicity of polyelectrolyte-wrapped AuNPs to an environmentally-relevant panel of Gram-negative bacteria. Environmental Nanotechnology Gordon Research Conference, Jun 2017, Stowe, VT. Poster.
- **Buchman, J.T.**; Vartanian, A.M.; Jacob, L.; Zhang, X.; Murphy, C.J.; Haynes, C.L. The role of lipopolysaccharides in the toxicity of nanoparticles to Gram-negative bacteria. SciX, Sep 2016, Minneapolis, MN. Oral.
- **Buchman, J.T.**; Xiong, K.L.; Vartanian, A.M.; Jacob, L.; Zhang, X.; Murphy, C.J.; Haynes, C.L. Assessing the environmental impact of nanoparticles and evaluating a redesign strategy. 11th International Conference on the Environmental Effects of Nanoparticles and Nanomaterials, Aug 2016, Golden, CO. Poster.
- Pramanik, S.; **Buchman, J.T.**; Wu, J.; Vartanian, A.M.; Jacob, L.; Zhang, X.; Murphy, C.J.; Kortshagen, U.R.; Haynes, C.L. Assessing the environmental toxicity of nanomaterials. Industrial Partnership for Research in Interfacial Materials & Engineering Annual Meeting, May 2016, Minneapolis, MN. Poster.
- **Buchman, J.T.**; Qiu, T.A.; Forester, D.-C.B.; Frank, B.P.; Xiong, K.L.; Vartanian, A.M.; Jacob, L.; Zhang, X.; Caudill, E.R.; Pedersen, J.A.; Murphy, C.J.; Fairbrother, H.; Haynes, C.L. Nanoparticle screen for environmental impact and strategies for mitigation. Sustainability Symposium, April 2016, St. Paul, MN. Poster.
- **Buchman, J.T.**; Mueller, D.L. Developing a characterization method for autoreactive B cells in systemic lupus erythematosus. MN Academy of Science Winchell Symposium, April 2013, Minneapolis, MN. Poster.
- **Buchman, J.T.**; Mueller, D.L. Developing a characterization method for autoreactive B cells in systemic lupus erythematosus. Zyzzogeton Augsburg Research Symposium, April 2013, Minneapolis, MN. Poster.
- **Buchman, J.T.**; Mueller, D.L. Developing a characterization method for autoreactive B cells in systemic lupus erythematosus. Lupus Foundation of MN Presentation, August 2012, Minneapolis, MN. Oral.
- **Buchman, J.T.**; Feng, Z.V. Dendrimer encapsulated Pd nanoparticle catalyzed decomposition of polychlorinated biphenyls. MN Academy of Science Winchell Symposium, April 2012, Northfield, MN. Poster.
- **Buchman, J.T.**; Feng, Z.V. Dendrimer encapsulated Pd nanoparticle catalyzed decomposition of polychlorinated biphenyls. Zyzzogeton Augsburg Research Symposium, April 2012, Minneapolis, MN. Poster.
- **Buchman, J.T.**; Feng, Z.V. Dendrimer encapsulated Pd nanoparticle catalyzed decomposition of polychlorinated biphenyls. 243rd ACS National Meeting, March 2012, San Diego, CA. Poster.

INFORMAL SCIENCE COMMUNICATION

- **Buchman, J.T.** Nanoparticles can stick to bacteria, but does more nanoparticle sticking mean more toxicity? Apr 13, 2018. http://sustainable-nano.com/2018/04/13/nanoparticle-sticking-toxicity/

- **Buchman, J.T.** Using gold nanobullets for genetic engineering. Dec 15, 2016. http://sustainable-nano.com/2016/12/15/gold-nanobullets-for-genetic-engineering/
- **Buchman, J.T.** Why do scientists care about bacterial replication? Apr 8, 2016. http://sustainable-nano.com/2016/04/08/bacterial-replication/
- **Buchman, J.T.** How can you tell if bacteria are alive or dead? Sep 17, 2015. http://sustainable-nano.com/2015/09/17/livedead-baclight-assay/
- **Buchman, J.T.** Sustainable lamps powered by algae. Mar 3, 2015. http://sustainable-nano.com/2015/03/03/algae-lamps/
- **Buchman, J.T.** The chemical story behind non-petroleum-based plastics. Jun 26, 2014. http://sustainable-nano.com/2014/06/26/the-chemical-story-behind-non-petroleum-based-plastics/

TEACHING EXPERIENCE

University of MN, Teaching Assistant Aug 2013 - May 2014

- Demonstrated proper lab equipment usage to students.
- Used guided inquiry to help students develop their experimental methods.
- Graded students' lab notebooks and lab reports.

Augsburg College, Lab Assistant Sep 2012 - May 2013

- Taught proper instrument usage to students.
- Provided guidance with laboratory techniques.
- Assisted students with data analysis and calculations.

Augsburg College, Supplemental Instructor Sep 2011 - May 2012

- Hosted supplemental sessions to teach Organic Chemistry and Ecology.
- Strengthened important concepts from class.
- Reinforced good study habits.

Augsburg College, Tutor Sep 2010 - May 2013

- Tutored Chemistry (General, Organic, Analytical) and Biology (General, Cell).
- Offered support on homework and test preparation.

RELEVANT COURSEWORK

Analytical Spectroscopy	Analytical Separation & Chemical Equilibria
Materials Chemistry	Materials Characterization
Microbial Ecology	Mechanisms of Chemical Reactions
Medicinal Chemistry	Physical Chemistry
Instrumental Analysis	Quantitative Analytical Chemistry
Adv. Organic Chemistry	Adv. Inorganic Chemistry
General Chemistry	Biochemistry
Microbiology	Adv. Cellular and Molecular Biology
Genetics	Immunology
Plant Biology	Calculus-Based Physics
Calculus III	Probability and Statistics

TECHNICAL SKILLS

Lab: HRAM Orbitrap LC-MS, HPLC, UV-vis spectrometer, DLS, IR spectrometer, fluorescence spectrometer, TEM, fluorescent dye-based assays, qPCR, nitrogen physisorption, EDS, GC, cell culture, ELISA assays, SDS-PAGE, DNA/RNA & protein isolation, gel electrophoresis, rotary evaporation.
Data Analysis: Microsoft Word, Microsoft Excel, Microsoft PowerPoint, GraphPad Prism, ImageJ, ChemBioDraw, ChromPerfect, ChemStation, MestNOVA, Wolfram Mathematica, R.
Communication: Technical writing (SOPs, IBC, manuscripts), project management, conference presentations, contributor to Center for Sustainable Nanotechnology blog (author of 6 posts, editor of 17 posts), informal science communication, liaison between Haynes lab and DEHS for waste manifestation, scheduling coordinator.

LEADERSHIP & MEMBERSHIP

• Lab Safety Officer	2016 - 2019
Analysis & Compliance Committee Member	2016 - 2019
• Center for Sustainable Nanotechnology	2013 - Present
Standard Operating Procedures Subcommittee Chair	2016 - 2018
• Student Seminar Committee	2014 - 2018
• American Chemical Society	2011 - Present
• Augsburg Chemical Society	2010 - 2013
President	2012 - 2013
Treasurer	2011 - 2012
• Tri-Beta National Biology Honors Society	2011 - 2013
Treasurer	2012 - 2013